Etude de la violation de la symétrie *CP* dans l'expérience *BABAR*

présenté et soutenu publiquement le 28 Septembre 2007

pour l'obtention de l'

Habilitation à Diriger des Recherches de l'Université Pierre et Marie Curie (Paris VI)

(Spécialité Physique des Particules)

par

Serguei Ganjour

Composition du jury

Président: Jacques Chauveau *(Examinateur)*

Rapporteurs: Daniel Denegri
Simon Eidelman
Robert Fleischer

Examinateurs: Roy Aleksan
Ursula Bassler

Université Pierre et Marie Curie (Paris VI)

Abstract

This report of French "Habilitation à Diriger des Recherches" summarizes my scientific activities from 1995 to 2007. During this period of time, my research work was related to the particle physics experiment *BABAR*. The *BABAR* experiment has been running since 1999 at the PEP-II e^+e^- asymmetric B-factory located at SLAC. This experiment searches for CP violation in the system of B mesons and tests the Standard Model through the measurements of the angles and the sides of the Unitarity Triangle.

My research work is divided in five main topics: study of the *BABAR* magnet system and measurement of the magnetic field in the central tracking volume; project of the particle identification system based on aerogel counters for the forward region of the detector; conception of the magnetic shield and measurements of the fringe field in the region of photomultipliers of the DIRC system, the principal particle identification system of *BABAR*; development of the partial reconstruction technique of B mesons and study of the $B^0 \to D_s^{(*)+} D^{*-}$ decays; measurement of CP violation in the $B^0 \to D^{*\mp}\pi^{\pm}$ decays and constraint on the Unitary Triangle parameter $\sin(2\beta+\gamma)$ using these decays.

Keywords: CP Violation, *BABAR*.

Résumé

Ce mémoire d'habilitation à diriger les recherches, retrace mon activité scientifique de 1995 à 2007. Durant ces dix années environ, mon travail de recherche a été intimement lié à l'expérience de physique des particules *BABAR*. L'expérience *BABAR* en fonctionnement depuis 1999 au SLAC auprès de l'accélérateur PEP-II, recherche la violation de CP dans le système des mésons B qui sont produits à la résonance $\Upsilon(4S)$. En outre, *BABAR* a pour vocation de tester le Modèl Standard, notamment à travers la mesure des angles et des côtés du triangle d'unitarité, lié à la matrice de mélange des quarks du modèle standard électrofaible.

Mon activité de recherche s'est organisée autour de cinq axes majeurs: l'étude du système magnétique de *BABAR* et la mesure du champ dans le volume central du détecteur de trace; le projet du système d'identification des particules basée sur des compteurs aerogel dans la région avant; la conception du blindage magnétique et la mesure du champ dans la région des photomultiplicateurs du système principal d'identification des particules, le DIRC; le développement de la méthode de recon-stuction partielle des mésons B et l'étude des désintégrations $B^0 \to D_s^{(*)+} D^{*-}$; la mesure de la violation de CP dans les désintégrations $B^0 \to D^{*\mp}\pi^{\pm}$ et la contrainte des angles du trianle d'unitarité par la mesure de $\sin(2\beta+\gamma)$ avec ces désintégrations.

Mots-clés: Violation de CP, *BABAR*.

Contents

Introduction **1**

1 *CP* Violation Phenomenon **5**

1.1 Why do we study *CP* violation? 5
  1.1.1 Discrete symmetries C, P and T 5
  1.1.2 Matter-antimatter asymmetry in the Universe 6
  1.1.3 Conservation of the discrete symmetries 7
1.2 The B^0-$\overline{B}^0$ system 8
  1.2.1 Mixing of neutral B mesons 8
  1.2.2 Time evolution of B^0 mesons 10
1.3 Three types of *CP* violation 11
  1.3.1 Direct *CP* violation 11
  1.3.2 *CP* violation in mixing 12
  1.3.3 *CP* violation in interference 13
1.4 Standard Model and CKM matrix 14
1.5 The *BABAR* experiment 18
  1.5.1 Facility 18
  1.5.2 Method 19

2 *BABAR* Magnetic Field Map **21**

2.1 The *BABAR* detector 21
  2.1.1 Central tracker 22
2.2 Magnet system 24
  2.2.1 Field requirements 24
  2.2.2 Magnet coils 25
  2.2.3 Flux return 26
2.3 Magnetic field map 26
  2.3.1 Field computations 26
  2.3.2 Apparatus and data set 27
  2.3.3 Field model and data fitting 29
  2.3.4 Results 32
2.4 Conclusion 33

3 Particle Identification System ATC 35
3.1 Particle identification overview . . . 35
3.2 The Aerogel Threshold Counters . . . 36
3.3 Test-beam results with prototypes . . . 38
3.3.1 Beam line and apparatus . . . 38
3.3.2 Results . . . 39
3.3.3 Aerogel optical parameters . . . 41
3.4 Conclusion . . . 42

4 Particle Identification System DIRC 45
4.1 The Detector of Internally Reflected Cherenkov light (DIRC) . . . 45
4.2 Simulation and measurement of the fringe field . . . 47
4.2.1 Magnetic shielding . . . 47
4.2.2 Simulation of the *BABAR* magnetic circuit . . . 47
4.2.3 Design and construction of the shield . . . 49
4.2.4 Magnetic field mapper . . . 50
4.2.5 Probes . . . 51
4.2.6 Results . . . 53
4.3 Physics performances . . . 55

5 Method of Partial Reconstruction 59
5.1 Theoretical tools for quark flavor physics . . . 59
5.2 Reconstruction of B mesons . . . 61
5.2.1 Full reconstruction . . . 61
5.2.2 Partial reconstruction . . . 62
5.3 Study of $B^0 \to D_s^{(*)+} D^{*-}$ decays . . . 63
5.3.1 Event selection . . . 64
5.3.2 B meson reconstruction . . . 65
5.3.3 Background study . . . 66
5.3.4 Results . . . 67
5.3.5 Systematics . . . 70
5.4 Measurement of $\mathcal{B}(D_s^+ \to \phi\pi^+)$ . . . 71
5.5 Conclusion . . . 73

6 CP violation in $B^0 \to D^{*\mp}\pi^\pm$ decays 75
6.1 Measurements of CKM angle γ . . . 75
6.2 Measurement of $\sin(2\beta+\gamma)$ with $B^0 \to D^{*\mp}\pi^\pm$ . . . 77
6.2.1 $B^0 \to D^{*\mp}\pi^\pm$ decays . . . 77
6.2.2 Partial reconstruction of $B^0 \to D^{*\mp}\pi^\pm$ decays . . . 78
6.2.3 Backgrounds and event selection . . . 78
6.2.4 Decay time measurement and flavor tagging . . . 80
6.2.5 Probability density function . . . 80
6.2.6 Analysis procedure . . . 83

6.2.7 Results 84
6.2.8 Constraint on $\sin(2\beta+\gamma)$ 85
6.3 Status and perspectives 86

Conclusion 89

Bibliography 91

Publications 97

A Field Measurement of the *BABAR* Solenoid 99

B Particle identification with ATC 117

C Simulation and Measurement of the Fringe Field 127

D Study of $B^0 \to D_s^{(*)+} D^{*-}$ decays 161

E *CP* violation in $B^0 \to D^{*\mp}\pi^{\pm}$ decays 175
E.1 First measurement of *CP* asymmetries in $B^0 \to D^{*\mp}\pi^{\pm}$ decays 176
E.2 Precise measurement of *CP* asymmetries in $B^0 \to D^{*\mp}\pi^{\pm}$ decays 184
E.3 Status and prospects for *CP* asymmetry measurements: $\sin(2\beta+\gamma)$. 208

F CKM Phase Measurements 219

Introduction

This report of French “Habilitation à Diriger des Recherches” summarizes my scientific activities since the summer of 1995, when I joined the *BABAR* collaboration. During this period of time, my research work was related mostly to this experiment. This report does not include my scientific work in the period from summer 1999 to summer 2002 that has been devoted to the defense of my thesis of doctor in physics.

The *BABAR* experiment has been running since 1999 at the PEP-II e^+e^- asymmetric B-factory at SLAC operating at the energy of the $\Upsilon(4S)$ resonance. The main goal of this experiment is the search and the precise measurement of *CP* violation in the system of B mesons and the tests of the Standard Model through the measurements of the angles and the sides of the Unitarity Triangle.

Since its discovery in 1964 [1], the *CP* violation phenomenon remains one of the fundamental problems of modern physics. Although *CP* violation is an important ingredient to explain disappearance of antimatter in the Universe, neither its origin nor magnitude are yet well understood. In the framework of the current theory that explains different phenomena in particle physics, the Standard Model, *CP* violation is connected with the origin of the fermion masses. The search of the latter phenomenon is the most important task of the LHC experiments, where huge experimental efforts have been invested during the last years. The discovery of the Higgs boson, that could be the origin of the masses, is the main goal of the LHC experiments.

My first experimental work in the *BABAR* collaboration has been devoted to the project of the particle identification system. Several options for such a system were proposed at the early stage of the experiment. I have participated in the research and development of the particle identification system based on aerogel Cherenkov counters covering the forward region of the detector (Chapter 3). The prototypes of the aerogel counters have been successfully tested with a beam at CERN. Due to cost problems, the forward particle identification system has been excluded from the final design of *BABAR*. However, the results of these investigations have been published since they are of a broad interest for other researchers.

After the decision to use only the Detector of Internally Reflected Cherenkov Light, DIRC, as the principal particle identification system of *BABAR*, I have joined the DIRC group and contributed to the measurement of the fringe field of the *BABAR* solenoid in the region corresponding to the faces of the DIRC photomultipliers (Chapter 4). The first step of my work included calculations of the shielding components. The results of this study were used in the design of the magnetic shield. The second part of my research was related to the measurement of the field in the region of the DIRC photomultipliers. I have been responsible for the design and construction of the filed mapper that allowed us to perform such measurements before the commissioning of the experiment. A dedicated method of demagnetization, developed in this work, allowed us to guaranty a field magnitude of less then 1 G in the measured region. This provides a safe operation of the DIRC system at all time of detector operation.

In parallel, I took part in the studies of the *BABAR* magnet system by performing calculations of the magnetic field and of its precise measurement in the central tracking volume. Measurement and modelization of the solenoidal field (Chapter 2) have been performed at a precision as good as 1.7 G. This model of the magnetic field has successfully been applied for the reconstruction of the charged particles in the tracking system of *BABAR*.

Since the summer 1999 to the spring of 2002 my research was devoted to the study of the inclusive production of $D_s^{(*)+}$ mesons from B decays and the investigation of the feasibility of a partial reconstruction technique for the $B^0 \to D_s^{(*)+} D^{*-}$ decay channel. The results of this work have been included in my doctoral thesis [2] defended in April 2002. This study is not a part of the present report.

After the defense of my thesis, I performed a further study of the partial reconstruction technique that allowed the publication of a measurement of the $B^0 \to D_s^{(*)+} D^{*-}$ branching fractions and the polarization in $B^0 \to D_s^{*+} D^{*-}$ decays (Chapter 5). In the fall of 2003 I took the responsibility of the IHBD (Inclusive Hadronic B Decays) analysis group convener and stayed until summer 2005. This group analyzed the B meson decays with a partial reconstruction technique.

Since 2003 my scientific research has been related to the study of *CP* violation in the $B^0 \to D^{*\mp}\pi^{\pm}$ decays and measurement of the CKM parameter $\sin(2\beta+\gamma)$ with this decay channel (Chapter 6). At that time, *BABAR* had recorded approximately 80 fb^{-1} of integrated luminosity, and therefore, the measurement of small *CP* violation effects became feasible. In the first measurement of the *CP* asymmetry in $B^0 \to D^{*\mp}\pi^{\pm}$ decays, it was demonstrated that partial reconstruction is a very efficient method for the challenges of the time-dependent *CP* violation measurements. A remarkable constraint on the CKM parameter $\sin(2\beta+\gamma)$ has been obtained for the first time. An updated measurement based on 232 millions produced $B\overline{B}$ pairs, published about one year later, in 2005, represents the most precise *CP* violation measurement ($\sim 1.5\%$) in the decays of B mesons.

I have put a lot of efforts in the program of $\sin(2\beta+\gamma)$ CKM parameter determination in *BABAR*. In particular, I have played an active role (chair of the internal review committee) in the *CP* asymmetry measurements with $B^0 \to D^{(*)\mp}\pi^{\pm}/\rho^{\pm}$ using the method of full reconstruction. I have reported the combined constraint and the perspectives of the $\sin(2\beta+\gamma)$ measurements on the CKM workshops (Appendix E.3).

During my membership in the *BABAR* collaboration, I have actively participated in the scientific program of the experiment. I took the responsibility to serve in the review committees for several analyzes, for example, measurement of *CP* violation in the charmless penguin and the $B^0 \rightarrow D^{(*)+}D^{(*)-}$ decay channels. I have also reported the results of *CP* violation measurements at physics conferences and workshops. One example is given in Appendix F.

Chapter 1

CP Violation Phenomenon

The violation of *CP* symmetry is a fundamental property of nature which plays a key role in the understanding of the evolution of the Universe. Since neither its origin nor its magnitude are yet well established, it deserves particular studies.

This chapter gives an overview of *CP* violation phenomenon. The general formalism describing the B^0-$\overline{B}^0$ system, the implications of *CP* non conservation, and the generation of *CP* violation in the Standard Model are discussed. The detail discussion of this subject can be found in Ref. [3].

1.1 Why do we study *CP* violation?

The requirement of the conservation of various symmetries greatly simplifies the elaboration of the physical theories. The conservation of energy, momentum and spin involves invariance principles of the physical law under continuous transformations such as translation in time, space or rotation, respectively. An other category of conservation laws, for example conservation of electric, baryonic and leptonic charge and strong isospin is associated with the dynamics of the processes. They act on abstract spaces such as phases or isospin and also involve continuous transformations. The category of the discrete transformations which are also connected with the dynamics of the interaction plays a special role. These transformations are *charge conjugation, parity and time reversal.*

1.1.1 Discrete symmetries C, P and T

For a particle described by the wave function $\psi(\vec{p}, \vec{s})$ where $\vec{p}$ and $\vec{s}$ denote its momentum and spin, the action of the charge conjugation is to change the particle into its antiparticle without modifying $\vec{p}$ and $\vec{s}$. Thus the transformation of charge conjugation C can be expressed as

$$C|\psi(\vec{p}, \vec{s})\rangle = \eta_C|\overline{\psi}(\vec{p}, \vec{s})\rangle \tag{1.1}$$

where η_C is a phase factor. The antiparticle ($\overline{\psi}$) is defined by changing the sign of all the charges associated to the particle (electric, baryonic, leptonic...).

The parity transformation P changes the space vector $\vec{r}$ into $-\vec{r}$. This means that the momentum $\vec{p}$ becomes $-\vec{p}$, while orbital momentum remains unchanged ($\vec{L}=\vec{r} \times \vec{p}$). Hence

$$P|\psi(\vec{p},\vec{s})\rangle = \eta_P|\psi(-\vec{p},\vec{s})\rangle \tag{1.2}$$

where η_P is a phase factor.

Under time reversal transformation T, t is changed to $-t$ and therefore $\vec{p}$ is modified into $-\vec{p}$. Moreover the wave function is also replaced by its complex conjugate due to the fact that it should satisfy the Schrödinger equation. Thus

$$T|\psi(\vec{p},\vec{s})\rangle = \eta_T^s|\psi^*(-\vec{p},-\vec{s})\rangle \tag{1.3}$$

where η_T^s is a phase factor depending on the spin.

1.1.2 Matter-antimatter asymmetry in the Universe

There is one fundamental problem in modern cosmology that relates to *CP* violation, and that is the observed asymmetry between baryons and antibaryons in the Universe

$$n_{\overline{Bar}} << n_{Bar}, \; n_{Bar}/n_\gamma \sim 10^{-9} \div 10^{-10} \tag{1.4}$$

where $n_{\overline{Bar}}$, n_{Bar}, and n_γ are the densities of antibaryons, baryons and photons, respectively. In 1967, the necessary conditions to generate the Baryon Asymmetry in the Universe (BAU) have been postulated by Sakharov [4]:

- since the initial and final number of baryons are different, i.e. $\Delta n_{bar} \equiv n_{Bar} - n_{\overline{Bar}} \neq 0$, transitions violating the baryon number have to exist;
- C and the product of C and P parities, *CP*, have to be violated. Otherwise for any transition changing the baryon number $N \to f$ exists the conjugate process $\bar{N} \to \bar{f}$ which produces the same population of antibaryons;
- transitions satisfying the criteria above have to be active in the expending Universe, i.e. with deviation from thermal equilibrium. Otherwise the thermal equilibrium produces equal populations of particles and antiparticles.

In Grand Unified Theories (at scales of $\sim 10^{15\div16}$ GeV), or even in the Standard Model at sufficiently high temperatures, there are baryon number-violating processes. There is a class of theories [5] where the electroweak phase transition could have dramatic consequences on any baryon asymmetry generated at higher temperature. However, such theories must include *CP* violation from sources beyond the minimal Standard Model. Indeed, calculations made in that model show that generated matter-antimatter imbalance is not sufficient to produce the observed number of baryons to photon ratio (Equation 1.4). Since it is difficult to produce large enough BAU at the electroweak scale, one expects other sources of *CP* violation at large scales. Thorough studies of this phenomenon are therefore of a great interest.

1.1.3 Conservation of the discrete symmetries

Interaction between theory and experiment plays an essential role in all studies of discrete symmetries C, P and T. The fundamental property of these symmetries is described by *CPT* theorem [6], proposed by Lüders and Pauli in the early 50ties. Based on a very general hypothesis of locality and causality, all field theories that respect the Lorentz invariance are automatically invariant according to $C{\cdot}P{\cdot}T$ transformation [7]. This leads to very important consequences. For example, the lifetimes and masses of a particle and its antiparticle are equal. The experimental measurement of the mass difference for a particle and its antiparticle confirms the conservation of the *CPT* symmetry. As an illustration, some experimental mass differences are the following:

$$|m_{e^+} - m_{e^-}| \leq 0.02\,\mathrm{eV},\ |m_p - m_{\overline{p}}| \leq 1\,\mathrm{eV},\ |m_K - m_{\overline{K}}| \leq 3.6\ 10^{-10}\,\mathrm{eV} \qquad (1.5)$$

The conservation of C parity in the strong interactions is verified by comparing the angular distributions for the charged pions, for example in the reaction $p\overline{p} \to \pi^+\pi^-\pi^0$. It was shown that C parity is conserved at the percent level. It is easier to check the conservation of C parity in electromagnetic processes. For example the reaction $e^+e^- \to \mu^+\mu^-\pi^0$ is forbidden if C is conserved. Since this decay is not observed, one can set an upper limit at 5×10^{-6}. The reaction $p + F^{19} \to Ne^{20*} \to O^{16} + \alpha$ is forbidden if P is conserved. No such reaction is observed, which allows one to make very precise tests of P parity conservation in strong interactions. This leads to an upper limit of the order of 10^{-12}. Thus, C and P symmetries are conserved in the strong and electromagnetic interaction within experimental errors. Long time, it was thought that all processes in particle physics are invariant according to these transformations. However, as mentioned above, C has to be violated at some moment, because the world is made of matter. The weak interactions play a very special role in this context.

In 1957, Wu [8] has discovered the violation of P symmetry by studying the β decays of the ^{60}Co nucleus. Then another experiment confirmed the violation of P and C symmetries in weak interactions. The pion decays $\pi^+ \to \mu^+(-1)\nu(-1)$ and $\pi^- \to \mu^-(+1)\overline{\nu}(+1)$ (number in parentheses show the helicity) are governed by weak interaction since a neutrino is involved. The measurement of the muon helicity via the angular distributions of electron produced in its decay, shows that both Charge Conjugation and Parity are violated in a maximal way. However, the *CP* transformation where C and P applied consequently, seems to be conserved.

In 1964, Christenson, Cronin, Fitch and Turlay have discovered *CP* violation in the system of neutral kaons [1]. For almost 36 years, the neutral K^0 system has remained the only system where this phenomenon has been experimentally observed.

Further precision measurements of *CP* violation parameters, allowed us essentially to rule out a number of models that enable to explain this phenomenon. Indeed, only one model remained, the model of Kobayashi and Maskawa [9] based on 3 × 3 matrix of quark mixing. The study of *CP* violation in the system of B mesons was a great interest, since the first confirmation of the interpretation of *CP* violation in the Standard Model has been obtained. The first measurements of the Unitarity Triangle, discussed below, allowed building a coherent picture between *CP* violation and the weak decays of quarks.

1.2 The B^0-$\overline{B}^0$ system

This section describes the quantum mechanics of a charge conjugated system of two neutral mesons (for example, the $\overline{B}^0 = \bar{d}b$ is the antiparticle associated with the particle $B^0 = d\bar{b}$). It is important to note that the formalism defined here is independent on any theoretical model and particularly the Standard Model.

1.2.1 Mixing of neutral B mesons

In the early 50ties, in order to explain the phenomenon of associated production of K^0-mesons and Λ-baryons, Gell-mann proposed to introduce a new quantum number called Strangeness S associated with the kaon system. The Strangeness must be conserved in strong and electromagnetic interactions ($\Delta\mathrm{S} = 0$). Furthermore, one can predict that K^0 and $\overline{K}^0$ have to be mixed [10] since they have a common final state $\pi^+\pi^-$. Thus, if a K^0 propagates in space, it can oscillate into $\overline{K}^0$ and visa versa via virtual intermediate states, where for these decays are $|\Delta\mathrm{S}| = 1$. Consequently, the suggestion was made that K^0 and $\overline{K}^0$ are not the physical states, but instead are superpositions of the mass eigenstates K_1 and K_2. Like the kaons, which have an associated quantum number S, the neutral particle systems called the D^0 and B^0 mesons, have their own quantum numbers C (charm) and B (beauty), respectively.

There are two systems of neutral B mesons involving b quarks: B_d mesons consist of one $\bar{b}$-type antiquark and one d-quark. B_s mesons are made of one $\bar{b}$ and one s. Let us describe the B^0-$\overline{B}^0$ system with a formalism which can be transfered to any other system composed of a neutral particle and its antiparticle. As for the kaon system, the B^0 and $\overline{B}^0$ are not physical states. Therefore, the arbitrary state

$$\psi = a|B^0\rangle + b|\overline{B^0}\rangle \tag{1.6}$$

has to satisfy the Schrödinger equation

$$i\frac{d}{dt}\begin{pmatrix} a \\ b \end{pmatrix} = H\begin{pmatrix} a \\ b \end{pmatrix} = \left(M - i\frac{\Gamma}{2}\right)\begin{pmatrix} a \\ b \end{pmatrix}. \tag{1.7}$$

M and Γ are 2×2 Hermitian matrices, called dispersive (due to process involving intermediate virtual states) and absorptive (due to process involving intermediate real states) parts of the transition amplitude from B^0 and $\overline{B}^0$, respectively. The off-diagonal elements in these matrices are important for the discussion of *CP* violation. One can demonstrate [11] that imposing *CPT* invariance, one gets

$$H_{11} = H_{22}, \; H_{12} = H_{21}^* \tag{1.8}$$

In order to obtain the mass eigenstates, the matrix H has to be diagonalized. The eigenstates $|B_L\rangle$ and $|B_H\rangle$ can be written as

$$\begin{aligned} |B_L\rangle &= p|B^0\rangle + q|\overline{B^0}\rangle && (1.9) \\ |B_H\rangle &= p|B^0\rangle - q|\overline{B^0}\rangle && (1.10) \end{aligned}$$

The complex coefficients p and q obey the normalization condition $|q|^2 + |p|^2 = 1$. The eigenvalues λ_L and λ_H of the matrix H are obtained by solving the equation $Hv = \lambda v$. Assuming *CPT* invariance (Equation 1.8), they are

$$\begin{aligned} \lambda_L &= H_{11} + \sqrt{H_{12}H_{21}} = M_L - \frac{i}{2}\Gamma_L && (1.11) \\ \lambda_H &= H_{11} - \sqrt{H_{12}H_{21}} = M_H - \frac{i}{2}\Gamma_H && (1.12) \end{aligned}$$

Thus, the eigenstates have well defined masses and widths

$$\begin{aligned} M_L &= M_{11} + Re\sqrt{\left(M_{12} - \tfrac{i}{2}\Gamma_{12}\right)\left(M_{12}^* - \tfrac{i}{2}\Gamma_{12}^*\right)} \\ M_H &= M_{11} - Re\sqrt{\left(M_{12} - \tfrac{i}{2}\Gamma_{12}\right)\left(M_{12}^* - \tfrac{i}{2}\Gamma_{12}^*\right)} \\ \Gamma_L &= \Gamma_{11} - 2Im\sqrt{\left(M_{12} - \tfrac{i}{2}\Gamma_{12}\right)\left(M_{12}^* - \tfrac{i}{2}\Gamma_{12}^*\right)} \\ \Gamma_H &= \Gamma_{11} + 2Im\sqrt{\left(M_{12} - \tfrac{i}{2}\Gamma_{12}\right)\left(M_{12}^* - \tfrac{i}{2}\Gamma_{12}^*\right)} \end{aligned} \tag{1.13}$$

and hence

$$\begin{aligned} \Delta m_B &= M_H - M_L = -2Re\sqrt{\left(M_{12} - \frac{i}{2}\Gamma_{12}\right)\left(M_{12}^* - \frac{i}{2}\Gamma_{12}^*\right)} \\ \Delta\Gamma_B &= \Gamma_H - \Gamma_L = 4Im\sqrt{\left(M_{12} - \frac{i}{2}\Gamma_{12}\right)\left(M_{12}^* - \frac{i}{2}\Gamma_{12}^*\right)} && (1.14) \end{aligned}$$

The ratio q/p can be expressed in the terms of the M, Γ- matrix elements:

$$\frac{q}{p} = \sqrt{\frac{M_{12}^* - \frac{i}{2}\Gamma_{12}^*}{M_{12} - \frac{i}{2}\Gamma_{12}}} = -\frac{\Delta m_B - \frac{i}{2}\Delta\Gamma_B}{2(M_{12} - \frac{i}{2}\Gamma_{12})} \tag{1.15}$$

It is important to note that q/p is not an observable. Indeed, since the $|B^0\rangle$ and $|\overline{B}^0\rangle$ are only defined to a relative phase, one may change the convention by using $CP|B^0\rangle = e^{i\alpha}|\overline{B}^0\rangle$ This is equivalent of using $e^{i\alpha}|B^0\rangle$ for the B^0 wave function. Thus, $q/p \equiv \sqrt{\langle\overline{B}^0|H(\Delta B=2)|B^0\rangle/\langle B^0|H(\Delta B=2)|\overline{B}^0\rangle}$ is not invariant since q/p becomes $e^{i\alpha}q/p$. Therefore, only its modules can be measured.

1.2.2 Time evolution of B^0 mesons

The lifetime difference of two B_d mesons is expected to be negligible $\Delta\Gamma_B/\Gamma_B \simeq 10^{-2}$. It is rather safe and model independent assumption [12]. Indeed, an ideal mixing of B^0 and $\overline{B}^0$ is governed by the parameter x_d defined as

$$x_d = \Delta m_B/\Gamma_B \tag{1.16}$$

where $\Gamma_B = (\Gamma_H+\Gamma_L)/2$. This was measured for the B^0_d system to be $x_d = 0.73\pm0.05$. Thus, one obtains

$$\Delta\Gamma_B << \Delta m_B \tag{1.17}$$

For the further considerations in this report, the width Γ in B^0-$\overline{B}^0$ system is assumed to be the same for two mass states. Hence, the Equations 1.14, 1.15 can be simplified at a precision $\mathcal{O}(10^{-2})$:

$$\Delta m_B \;=\; 2|M_{12}|,\;\Delta\Gamma_B \;=\; 2Re(M_{12}\Gamma^*_{12})/|M_{12}|,\; q/p \;=\; -|M_{12}|/M_{12} \tag{1.18}$$

One notes that the mass difference of two B_d mesons has been also measured directly from the observation of the oscillation period between B^0_d and $\overline{B_d}^0$ to be $\Delta m_{B_d} = 0.507\pm0.005\,\mathrm{ps}^{-1}$ [13].

Starting with the time dependent equations for the physical states

$$|B_L(t)\rangle = e^{-(\Gamma_L/2+im_L)t}|B_L(0)\rangle,\; |B_H(t)\rangle = e^{-(\Gamma_H/2+im_H)t}|B_H(0)\rangle \tag{1.19}$$

let us examine the time evolution of B^0 and $\overline{B}^0$, once they are created. Taking into account Equation 1.17, one obtains

$$\begin{aligned}|B^0_{\text{phys}}(t)\rangle &= \frac{1}{2}e^{-(im+\frac{\Gamma}{2})t}[(e^{i\Delta mt/2}+e^{-i\Delta mt/2})\;|B^0\rangle\\ &+ (e^{i\Delta mt/2}-e^{-i\Delta mt/2})\;\frac{q}{p}|\overline{B}^0\rangle]\end{aligned} \tag{1.20}$$

$$\begin{aligned}|\overline{B}^0_{\text{phys}}(t)\rangle &= \frac{1}{2}e^{-(im+\frac{\Gamma}{2})t}[(e^{i\Delta mt/2}-e^{-i\Delta mt/2})\;\frac{p}{q}|B^0\rangle\\ &+ (e^{i\Delta mt/2}+e^{-i\Delta mt/2})\;|\overline{B}^0\rangle]\end{aligned} \tag{1.21}$$

Here, the following notations have been used:

$$\Gamma = (\Gamma_H+\Gamma_L)/2,\; m = (m_H+m_L)/2,\; \Delta m = m_H - m_L. \tag{1.22}$$

One can compute now the probability of the transition $B^0(t) \to f$ for the pure state B^0 at time $t = 0$:

$$\begin{aligned} |\langle f|H|B^0_{\text{phys}}(t)\rangle|^2 &= e^{-\Gamma t}|A_f|^2|\cos(\Delta mt/2) + i\lambda\sin(\Delta mt/2)|^2 \qquad (1.23) \\ &= e^{-\Gamma t}|A_f|^2|\Big[\frac{1}{2}(1+|\lambda|^2) + \frac{1}{2}(1-|\lambda|^2)\cos(\Delta mt) - Im\lambda\sin(\Delta mt)\Big] \end{aligned}$$

The time evolution for the initial $\overline{B}^0$ can be obtained in a similar way:

$$\begin{aligned} |\langle f|H|\overline{B}^0_{\text{phys}}(t)\rangle|^2 &= e^{-\Gamma t}|\bar{A}_f|^2|\cos(\Delta mt/2) + i\frac{1}{\lambda}\sin(\Delta mt/2)|^2 \qquad (1.24) \\ &= e^{-\Gamma t}|\bar{A}_f|^2|\Big[\frac{1}{2}(1+|\lambda|^2) - \frac{1}{2}(1-|\lambda|^2)\cos(\Delta mt) + Im\lambda\sin(\Delta mt)\Big] \end{aligned}$$

where

$$\lambda = \frac{q}{p}\frac{\bar{A}_f}{A_f} \qquad (1.25)$$

and $A_f = \langle f|H|B^0\rangle$, $\bar{A}_f = \langle f|H|\overline{B}^0\rangle$. Thus, the comparison of these transition probabilities may exhibit *CP* violation.

1.3 Three types of *CP* violation

It is very important to note that manifestation of *CP* violation can be elaborated without involving any particular theory. The *CP* violation effects can be classified in the following three model independent ways:

1. **Direct *CP* violation**, which occurs in both charged and neutral decays. The final state f can only originate from the flavor of the initial B, i.e. it is possible to determine unambiguously the nature of the B. *CP* violation is observed, if $Pr(B \to f) \neq Pr(\bar{B} \to \bar{f})$
2. ***CP* violation in mixing**, which occurs when two neutral mass eigenstates are not *CP* eigenstates. *CP* violation due to the B^0-$\overline{B}^0$ mixing is observed if $Pr(B^0 \to \overline{B}^0) \neq Pr(\overline{B}^0 \to B^0)$.
3. ***CP* violation in the interference between decays with and without mixing**, which occurs in the decays into final states that are common for B^0 and $\overline{B}^0$.

1.3.1 Direct *CP* violation

The interference of several decay amplitudes may result into *CP*-violating effects. Let us assume two amplitudes A_1 and A_2 contribute to the decay $B \to f$, where f

is a particular final state. Two amplitudes A_f and $\bar{A}_{\bar{f}}$ that correspond to two *CP* conjugated processes can also be defined as

$$A_f = \langle f|H|B\rangle, \ \bar{A}_{\bar{f}} = \langle \bar{f}|H|\bar{B}\rangle \tag{1.26}$$

If the probability of $B \to f$ process is not equal to the probability of $\bar{B} \to \bar{f}$ transition, the *CP* violation occurs. This yields the following requirement independent of phase conventions:

$$\left|\frac{\bar{A}_{\bar{f}}}{A_f}\right| \neq 1 \Rightarrow \text{Direct } CP \text{ violation} \tag{1.27}$$

Taking into account that only the weak CKM phases ϕ_1 and ϕ_2 are modified by *CP* transformation, the total amplitudes of two processes are

$$\begin{aligned} A_f &= A_1 + A_2 = |A_1|e^{i\phi_1}e^{i\delta_1} + |A_2|e^{i\phi_2}e^{i\delta_2} \\ \bar{A}_{\bar{f}} &= \bar{A}_1 + \bar{A}_2 = |A_1|e^{-i\phi_1}e^{i\delta_1} + |A_2|e^{-i\phi_2}e^{i\delta_2} \end{aligned} \tag{1.28}$$

where δ_1 and δ_2 are the *CP* conserving phases due to the strong interactions in the final state. Thus, the asymmetry of two *CP* conjugated processes is

$$\begin{aligned} a_f &= \frac{Pr(B \to f) - Pr(\bar{B} \to \bar{f})}{Pr(B \to f) + Pr(\bar{B} \to \bar{f})} \\ &= \frac{2|A_1||A_2|\sin(\phi_1 - \phi_2)\sin(\delta_1 - \delta_2)}{|A_1|^2 + |A_2|^2 + 2|A_1||A_2|\cos(\phi_1 - \phi_2)\cos(\delta_1 - \delta_2)} \end{aligned} \tag{1.29}$$

This asymmetry is significantly different from zero if the following conditions are satisfied:

- the magnitudes of the two amplitudes are of the same order, $|A_1| \simeq |A_2|$;
- the two amplitudes have different CKM phases, $\phi_1 - \phi_2 \neq 0$;
- the two amplitudes have different strong phases, $\delta_1 - \delta_2 \neq 0$.

1.3.2 *CP* violation in mixing

Another quantity (see Equation 1.15) that is independent of phase conventions is

$$\left|\frac{q}{p}\right|^2 = \left|\frac{M_{12}^* - \frac{i}{2}\Gamma_{12}^*}{M_{12} - \frac{i}{2}\Gamma_{12}}\right| \tag{1.30}$$

It implies

$$\left|\frac{q}{p}\right| \neq 1 \Rightarrow CP \text{ violation in mixing} \tag{1.31}$$

The B^0-$\overline{B}^0$ mixing may exhibit an asymmetry in the transition $B^0 \to \overline{B}^0$ and $\overline{B}^0 \to B^0$ In this case, one can write the asymmetry as

$$a_{CP} = \frac{Pr(\overline{B}^0 \to B^0) - Pr(B^0 \to \overline{B}^0)}{Pr(\overline{B}^0 \to B^0) + Pr(B^0 \to \overline{B}^0)} = \frac{|\frac{p}{q}|^2 - |\frac{q}{p}|^2}{|\frac{p}{q}|^2 + |\frac{q}{p}|^2} \tag{1.32}$$

Once B^0-$\overline{B}^0$ pairs are produced, this asymmetry can be observed, for example, by measuring the difference between the number of same sign positive leptons ($B^0\overline{B}^0 \to l^+l^+ + X$) and negative leptons ($B^0\overline{B}^0 \to l^-l^- + X$). One notes that a_{CP} asymmetry is also an indication of T violation.

1.3.3 *CP* violation in interference

In the third type of *CP* violation, which occurs in the interference between decays with and without mixing, the final states can be produced from both B^0 and $\overline{B}^0$:

$$B^0 \to f,\ \overline{B}^0 \to f$$

The condition above holds for several final states, but particularly for *CP* eigenstates:

$$CP|f_{CP}\rangle = \eta_{CP}|f_{CP}\rangle,$$

where η_{CP} is the *CP* parity of the final state ($\eta_{CP} = \pm 1$). In this case, *CP* violation can be observed by interplay between mixing and decays, e.g.:

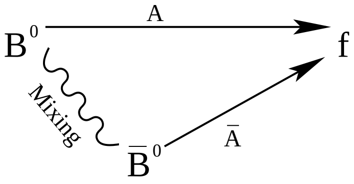

The quantity of interest here is an invariant λ of Equation 1.25, that is independent of phase conventions:

$$\lambda_{CP} \equiv \frac{q}{p}\frac{\bar{A}_{f_{CP}}}{A_{f_{CP}}} = \eta_{CP}\frac{q}{p}\frac{\bar{A}_{\bar{f}_{CP}}}{A_{f_{CP}}} \tag{1.33}$$

When both direct (Equation 1.27) and mixing (Equation 1.31) *CP* is conserved, the relative phase between (q/p) and $(\bar{A}_{f_{CP}}/A_{f_{CP}})$ becomes important. It implies

$$\lambda_{CP} \neq \pm 1 \Rightarrow CP \text{ violation in interference} \tag{1.34}$$

In this report, we assume the Standard Model prediction $|q/p| \simeq 1$. Indeed, the magnitude of $|q/p| - 1$ is expected to be of the order of 10^{-3}. Hence, one gets:

$$|\langle f_{CP}|H|B^0\rangle| = |\langle f_{CP}|H|\overline{B}^0\rangle| \tag{1.35}$$

Thus, the time dependent asymmetry can be expressed using Equations 1.23, 1.24 as

$$\begin{aligned} a_{f_{CP}}(t) &= \frac{Pr(\overline{B}^0(t) \to f_{CP}) - Pr(B^0(t) \to f_{CP})}{Pr(\overline{B}^0(t) \to f_{CP}) + Pr(B^0(t) \to f_{CP})} \\ &= \frac{(1-|\lambda_{CP}|^2)\cos\Delta(m_B t) - 2Im\lambda_{CP}\sin(\Delta m_B t)}{1+|\lambda_{CP}|^2} \end{aligned} \tag{1.36}$$

This asymmetry will be significant if any of the three types of *CP* violation are present. However, neglecting the direct *CP* violation $|\lambda_{CP}| = 1$, the equation above can be considerably simplified:

$$a_{f_{CP}}(t) = -Im\lambda_{CP}\sin\Delta(m_B t) \tag{1.37}$$

One notes, it is possible that $|q/p| = 1$ and $|\lambda_{CP}| = 1$, i.e. there is no *CP* violation in either mixing or decay, while the *CP* asymmetry in Equation 1.37 is non zero due to $Im\lambda_{CP} \neq 0$.

1.4 Standard Model and CKM matrix

Non conservation of *CP* symmetry has been introduced in the Standard Model (SM) in 1973 [9], by requiring three families of quark and lepton doublets

$$\begin{pmatrix} u \\ d \end{pmatrix} \quad \begin{pmatrix} c \\ s \end{pmatrix} \quad \begin{pmatrix} t \\ b \end{pmatrix} \\ \begin{pmatrix} \nu_e \\ e \end{pmatrix} \quad \begin{pmatrix} \nu_\mu \\ \mu \end{pmatrix} \quad \begin{pmatrix} \nu_\tau \\ \tau \end{pmatrix} \tag{1.38}$$

Amongst other things, the remarkable success of the SM is demonstrated by the fact, that the measured mass of the t quark ($m_t = 174.2 \pm 3.3$ GeV/c^2 [13]) is consistent with the SM prediction derived from the measured mass ratio of the Z and W bosons. The introduction of the spontaneous $SU(2) \times U(1)$ symmetry breaking by the Higgs mechanism [15] allows one to generate the mass of each fermion through a Yukawa type coupling. Its interaction Lagrangian can be written as

$$\mathcal{L}_{Yukawa} = -\left(\overline{\mathbf{u}}'_{\mathbf{L}}\ \mathbf{m}\ \mathbf{u}'_{\mathbf{R}} + \overline{\mathbf{d}}'_{\mathbf{L}}\ \tilde{\mathbf{m}}\ \mathbf{d}'_{\mathbf{R}} + h.c.\right)\left(1 + \frac{\Phi_0}{v}\right), \tag{1.39}$$

where Φ_0 is the scalar field of the neutral Higgs and v is its value in the new vacuum. The quark fields $\mathbf{u}'_{\mathbf{L,R}}$ and $\mathbf{d}'_{\mathbf{L,R}}$ are vectors in flavor space for the left- and right-handed up- and down-type quarks, respectively,

$$\overline{\mathbf{u}}'_{\mathbf{L,R}} = \frac{1 \mp \gamma_5}{2}\begin{pmatrix} u' \\ c' \\ t' \end{pmatrix}, \ \overline{\mathbf{d}}'_{\mathbf{L,R}} = \frac{1 \mp \gamma_5}{2}\begin{pmatrix} d' \\ s' \\ b' \end{pmatrix}, \tag{1.40}$$

$\mathbf{m}$ and $\widetilde{\mathbf{m}}$ are 3×3 matrices of arbitrary complex numbers. Since $\mathbf{m}$ and $\widetilde{\mathbf{m}}$ are not diagonal, one needs to define the *physical* fermion fields $\mathbf{u_{L,R}} = V_{L,R}\mathbf{u'_{L,R}}$ and $\mathbf{d_{L,R}} = \widetilde{V}_{L,R}\,\mathbf{d'_{L,R}}$, where $V_{L,R}$ and $\widetilde{V}_{L,R}$ are unitary matrices. The mass matrices in Equation 1.39 are diagonalized in terms of these new fields with $\mathbf{m_D} = V_L\mathbf{m}V_R^\dagger$ and $\widetilde{\mathbf{m}}_\mathbf{D} = \widetilde{V}_L\,\widetilde{\mathbf{m}}\,\widetilde{V}_R^\dagger$. The coupling to the charged $W^\pm$ introduces the mixing between families, while the observed absence of the flavor changing neutral currents means that the coupling of the physics quarks to the neutral Z preserves the flavor. Thus, the interaction Lagrangian for the charged coupling is

$$\mathcal{L} = \frac{g}{\sqrt{2}}\left(\overline{\mathbf{u}}_\mathbf{L}\gamma^\mu W_\mu^+\mathbf{V}\mathbf{d_L} + \overline{\mathbf{d}}_\mathbf{L}\gamma^\mu W_\mu^+\mathbf{V}^\dagger\mathbf{u_L}\right) \tag{1.41}$$

where $\mathbf{V} = V_L\,\widetilde{V}_L^\dagger$ is a unitary matrix called Cabibbo-Kobayashi-Maskawa (CKM) or quark-mixing matrix [9, 14]:

$$V = \begin{pmatrix} V_{ud} & V_{us} & V_{ub} \\ V_{cd} & V_{cs} & V_{cb} \\ V_{td} & V_{ts} & V_{tb} \end{pmatrix}. \tag{1.42}$$

The elements of the CKM matrix are related to the mass of the fermions. There were several attempts to explain this connection, but none is able to describe the experimental data. Since there exists no obvious way to deduce the values of these elements from theory, it is necessary to measure them in order to verify the predictions.

Let us see how the CKM matrix can be constructed and what are its properties. Being unitary this matrix can be constructed from a product of rotation matrices. The general expression of V can be deduced from $n(n-1)/2$ mixing angles and $(n-1)(n-2)/2$ phases, where n is the number of fermion families. It is interesting to note that only with more than two families the elements of CKM matrix can be complex. Therefore, only in this case *CP* violation can be generated through the interference of two diagrams involving different matrix elements. In particular, three mixing angles and a single phase are the fundamental parameters of the theory with three families.

There exist many different parameterizations of the CKM matrix. The most famous parameterization was proposed by Wolfenstein [16] with parameters (λ, A, ρ, η):

$$V = \begin{pmatrix} 1-\frac{\lambda^2}{2} & \lambda & A\lambda^3(\rho+i\eta) \\ -\lambda & 1-\frac{\lambda^2}{2} & A\lambda^2 \\ A\lambda^3(1-\rho-i\eta) & -A\lambda^2 & 1 \end{pmatrix} + \mathcal{O}(\lambda^4), \tag{1.43}$$

where η carries the *CP* violating phase information and $\lambda = \sin\theta_C$. The angle θ_C is the Cabibbo angle ($\lambda = 0.2205 \pm 0.0018$). This approximation is at the order of λ^3, which is good enough at the present experimental sensitivity.

The unitarity of the CKM matrix leads to six independent relations, which imply the sum of three complex quantities to be equal zero. Each of them can be geometrically presented in the complex plane as a triangle. Knowing the experimental values for the various $|V_{ij}|$, only one

$$V_{ud}V_{ub}^* + V_{cd}V_{cb}^* + V_{td}V_{tb}^* = 0 \tag{1.44}$$

has 3 sides of the same order. This triangle is commonly called the "Unitarity Triangle". Figure 1.1 shows the rescaled Unitarity Triangle (UT) derived from Equation 1.44 choosing a phase convention with $V_{cd}V_{cb}^*$ being real and dividing the length of all sides by $|V_{cd}V_{cb}^*|$. Thus, two vertices of the triangle are fixed at (0,0) and (1,0) while the remaining vertex is placed at (ρ, η). Three angles of the UT are denoted by $\alpha(\phi_2)$, $\beta(\phi_1)$ and $\gamma(\phi_3)$. They can be expressed via matrix elements of the CKM matrix as

$$\alpha(\phi_2) \equiv \arg\left[-\frac{V_{td}V_{tb}^*}{V_{ud}V_{ub}^*}\right],\ \beta(\phi_1) \equiv \arg\left[-\frac{V_{cd}V_{cb}^*}{V_{td}V_{tb}^*}\right],\ \gamma(\phi_3) \equiv \arg\left[-\frac{V_{ud}V_{ub}^*}{V_{cd}V_{cb}^*}\right]. \tag{1.45}$$

These physical quantities can be extracted from the measurement of *CP* asymmetry in the different *B* decay modes. The consistency of various measurements provide tests of the SM.

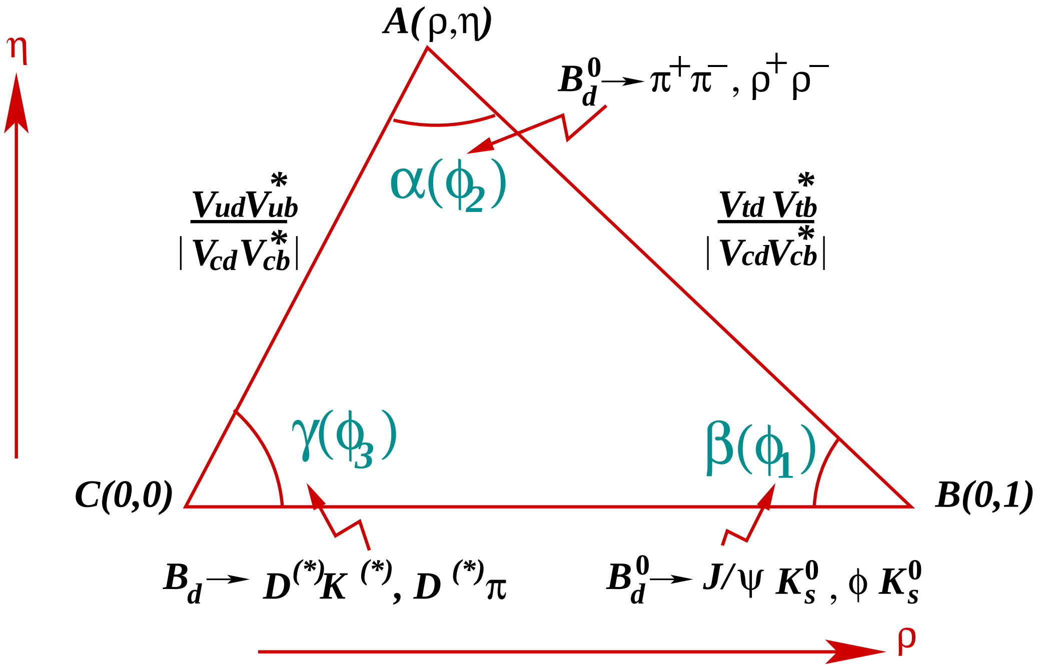

Figure 1.1: *The unitarity triangle. Some B decay modes, which allow one to measure the angles are shown.*

In order to estimate the feasibility to measure the three angles, it is useful for experimentalists to know what might be their potential values. Using the experimental results of *CP* violation in the neutral K^0 system (ϵ_K), neutral B-meson mixing ($|V_{td}|$, $|V_{ts}|$), and CKM matrix elements form semileptonic decays ($|V_{ub}|$, $|V_{cb}|$), the region of the apex of the UT can be constrained in the imaginary plane. Figure 1.2 illustrates the allowed region of (ρ, η) constrained from the experimental results in 1999, i.e. before commissioning of the B-Factories. The predicted values for the unitarity angles are [11]:

$$-0.6 \leq \sin 2\alpha \leq 0.9, \; 0.45 \leq \sin 2\beta \leq 0.82, \; -0.60 \leq \sin 2\gamma \leq 1 \tag{1.46}$$

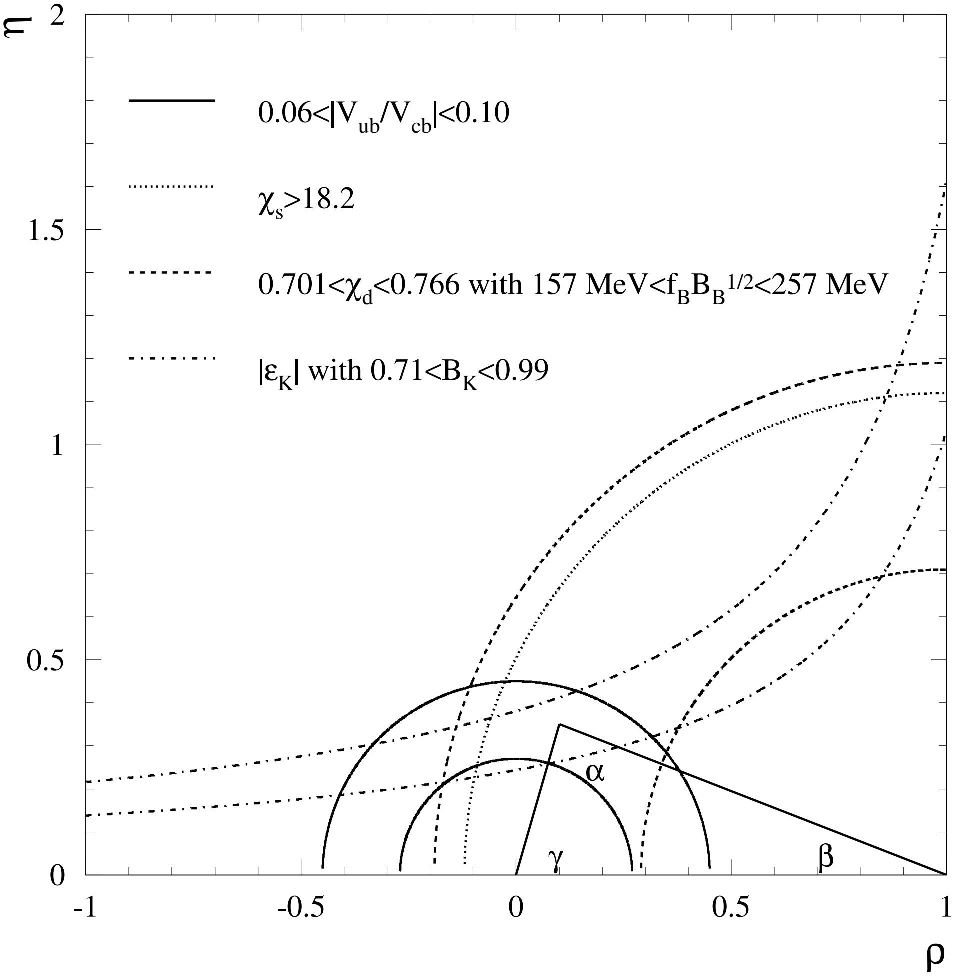

Figure 1.2: *Experimental constraints of the unitarity triangle before observation of CP violation in the B^0 system.*

1.5 The *BABAR* experiment

The primary goal of the *BABAR* experiment is a systematic study of *CP* violation in the decays of B mesons. The experimental program of this experiment implies the answers to the following questions:

1. does the *CP* violation phenomenon exist in the B meson system?
2. can we describe this phenomenon by the parameters of the CKM matrix in the SM? In particular, will high precision measurements of the CKM matrix elements coincide with the parameters of the UT?
3. are any signatures of the New Physics (NP) beyond the SM in the rare decays of the B mesons?

Since *CP* violating effects in the B system are large enough, a relatively small sample of events allows one to perform significant measurement. Unfortunately, the decay channels which are interesting for *CP* violation have very small branching fractions (of the order of 10^{-4} or less). Therefore, a large sample of B's (about 10^7) is necessary to perform these measurements. Thus, the accelerator luminosity must be a few $10^{33}\,\mathrm{cm}^{-2}\,\mathrm{s}^{-1}$, which has been realized in the last generation of B-factories [17, 18].

Observation of *CP* violation in $B_d^0-\overline{B}_d^0$ system has been reported in 2001 [19, 20]. Measurement of $\sin 2\beta$ quantity exploited the decays of B mesons to charmonium final state such as $B_d^0 \rightarrow J/\psi K_S^0$. Since this great discovery *BABAR* and *BELLE* performed precision tests of the SM by measuring the angles and the sides of the UT.

1.5.1 Facility

The $\Upsilon(4S)$ resonance produced in e^+e^- collisions is a very good laboratory for studying B mesons. Although the cross section $\sigma(e^+e^- \rightarrow \Upsilon(4S))$=1.1 nb (Figure 1.3) is not so large, the $\Upsilon(4S)$ mass is just above the $B\bar{B}$ threshold, so it is the cleanest source of $B\bar{B}$ pairs. It consists of about 50% of B^+ B^- and 50% of $B_d^0\overline{B}_d^0$. It is also important to say that no other particles are produced which allows one to get a good tagging efficiency. Due to the limited phase space, the B mesons from $\Upsilon(4S) \rightarrow B\bar{B}$ decay are produced almost at rest in the center of mass frame. Thanks to the asymmetry in the beam energies, the B mesons are boosted with a significant momentum in the laboratory frame. This enables the measurement of the time-dependent *CP* asymmetry in the decays of neutral B mesons.

The accelerator complex PEP-II used by the *BABAR* experiment is located at the Stanford Linear Accelerator Center (SLAC). PEP-II [21, 22] is an e^+e^- storage ring system designed to produce a luminosity of at least $3\times10^{33}\,\mathrm{cm}^{-2}\,\mathrm{s}^{-1}$. It operates at a center of mass energy corresponding to the $\Upsilon(4S)$ resonance at $\sqrt{s} = 10.58\,\mathrm{GeV}$ since 1999. PEP-II consists of a High Energy Ring (HER) for electrons and a Low Energy Ring (LER) for positrons. The asymmetric energies of 9 GeV for the electron and of 3.1 GeV for the positron beam provide a boost in the laboratory frame of $\beta\gamma$=0.56.

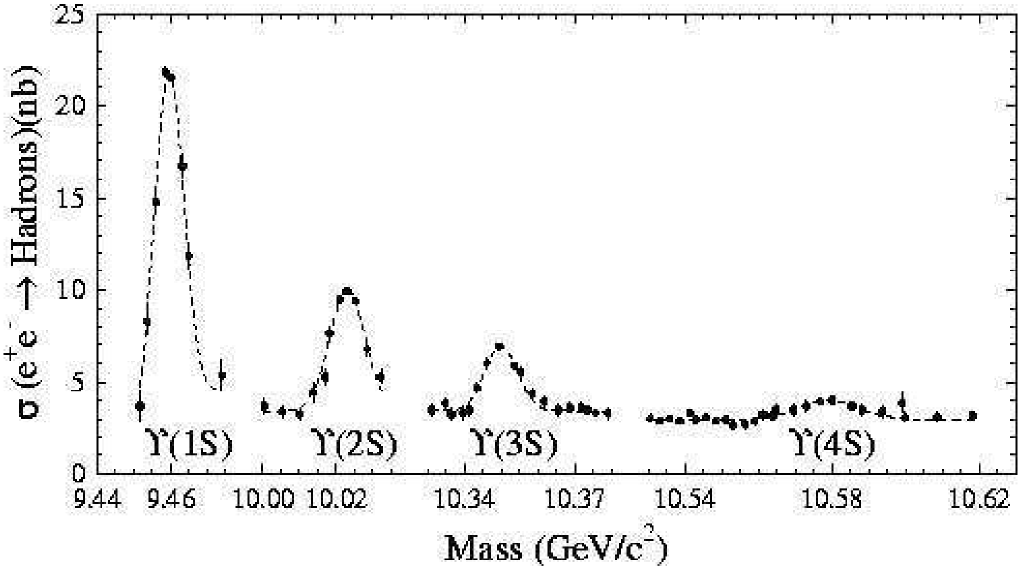

Figure 1.3: *Hadronic cross section in the $\varUpsilon$ region.*

1.5.2 Method

In e^+e^- collisions at the $\varUpsilon(4S)$ energy (the quantum numbers of this resonance are $J^{PC} = 1^{--}$) $B\bar{B}$ pairs are produced in a coherent $L = 1$ state. For the neutral B's that means that at any time there is always exactly one B^0 and one $\overline{B}^0$ until one of them decays. Thus, only at that time the nature of the second meson (B^0 or $\overline{B}^0$) is defined. However, if one of the particles decays, the other continues to evolve due to B^0-$\overline{B}^0$ mixing, and therefore events with two B^0 or two $\overline{B}^0$ decays may happen. Thus, one should consider the $B\bar{B}$ system as a whole instead of individual B mesons. Since the wave function of the $B\bar{B}$ pair is antisymmetric, the time-dependent asymmetry as defined in Equation 1.36 is governed by the time between the two B decays $\Delta t = t_2 - t_1$. Thus, the reference time (t_0) is not the $\varUpsilon(4S)$ decay time anymore, but the time at which one of the B mesons is identified. The consequence of this is that it is mandatory to measure Δt if one wants to use the interference between B decays with and without B^0-$\overline{B}^0$ mixing for CP violation search.

The time between two B decays has to be measured as the flight distance of the B meson using $L = \beta\gamma ct$. Assuming that the $\varUpsilon(4S)$ resonance is produced with a boost $\beta\gamma$, the distance Δz can be expressed as

$$\Delta z = \beta\gamma c\tau \left[\frac{t_2 - t_1}{\tau}\right] + \gamma\beta_{cm} c\tau \cos\theta^*_B \left[\frac{t_2 + t_1}{\tau}\right], \tag{1.47}$$

where $\beta\gamma$ is the boost of the $\varUpsilon(4S)$, $c\tau$ is the average flight distance of a B meson and β_{cm} is its velocity in the $\varUpsilon(4S)$ center of mass ($\beta_{cm} \simeq 0.07$), θ^*_B is the angle between B meson produced in the $\varUpsilon(4S)$ rest frame with respect to the beam direction. For most studies the last term in Equation 1.47 can be neglected. Thus, assuming $\beta\gamma \simeq 0.56$, one obtains $\beta\gamma c\tau \approx 250\mu m$, which is measurable with today's technique.

Besides the measurement of Δz, the flavor of the B^0 at time $t = t_0$ has to be determined. There are several techniques for *tagging* the initial flavor of a B meson. They are based on the determination of the charge of the b quark. The most useful methods are tagging using leptons and kaons.

- *The Lepton Tagging.* The charge of the b quark in the decays $b \to cl\nu$ can be deduced from the charge of the lepton. Since the total inclusive branching fraction $(\mathcal{B}(B \to X_c e\nu_e) + \mathcal{B}(B \to X_c \mu\nu_\mu))$ is about 20%, this is very attractive.

- *The Kaon Tagging.* In the direct cascade $b \to c \to s$, the charge of the s quark is the same as the charge of b, and therefore, if the s quark produces a charged kaon, its charge should have the same sign as the charge of the initial b.

To conclude, measurements of *CP* violation require the ability to tag the quark content of one of the B mesons, and to reconstruct exclusively the second B decay, and to measure the time between these two B decays.

Chapter 2

BABAR Magnetic Field Map

This chapter describes my scientific activity for the magnet system of the *BABAR* experiment, where I am collaborating since 1995. The first part gives a brief overview of the *BABAR* detector with emphasis to the central tracker. Then, I describe in details the magnet system and the field requirements. The main part of this chapter presents the results of the field computation and the field mapping of the central tracking volume of *BABAR*. The magnetic field calculations have been performed in the period 1996-1998, while the major work for the mapping of the *BABAR* solenoid took place in spring 1998 at SLAC. The results of this work are described in Appendix A and [23, 24].

2.1 The *BABAR* detector

The *BABAR* detector (Figures 2.1, 2.2) [25] measures the charged particles by a combination of a five-layer (double-sided) silicon vertex tracker (SVT), which provides the measurements of the impact parameters and the track angles, and of a 40-layer central drift chamber (DCH) used for the measurements of the track momentum and its energy loss. The tracking system is embedded in a 1.5 T solenoidal field produced by a superconducting magnetic coil and provides good momentum resolution. The DCH is surrounded by the Detector of Internally Reflected Cherenkov Light (DIRC). It consists of 12 sectors of quartz bars readout by a matrix of about 11000 phototubes arranged on the internal surface of a water tank. The electromagnetic showers are measured by the Electromagnetic Calorimeter (EMC) composed of CsI(Tl) crystals. The Instrumented Flux Return (IFR) with resistive plate chambers provides the identification of the muons and neutral hadrons. Charged hadrons are identified using the ionization energy loss (dE/dx) measured in the DCH and SVT, and the Cherenkov radiation detected in the DIRC.

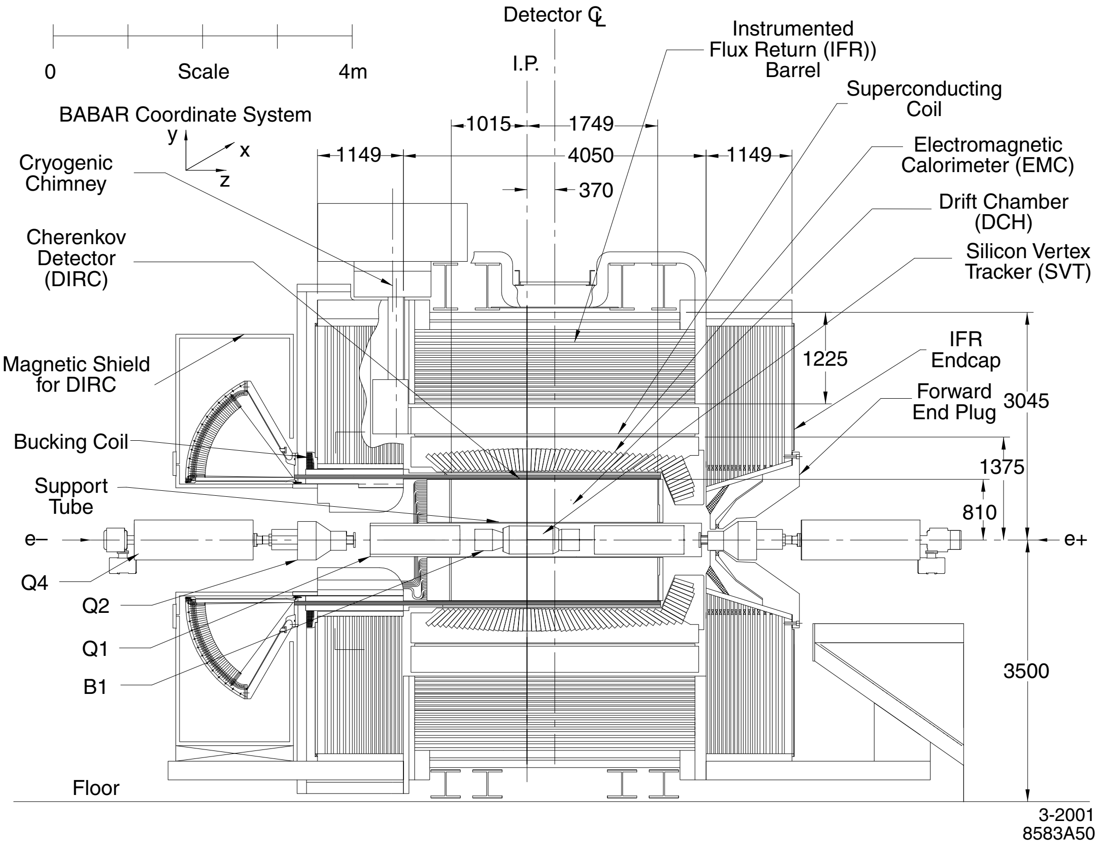

Figure 2.1: *The BABAR Detector (side view).*

2.1.1 Central tracker

The tracking system of the *BABAR* detector consisting of the central drift chamber and the vertex tracker is arranged inside a magnetic field of 1.5 T produced by a superconducting magnet. It provides a typical momentum resolution of

$$\delta p_T/p_T = (0.13 \pm 0.01)\% \cdot p_T + (0.45 \pm 0.03)\%, \tag{2.1}$$

where p_T is given in GeV/c.

The SVT provides the required vertex resolution for the measurement of the *CP* violation and other decay-time-dependent measurements. In addition, when the charged particles have a low transverse momentum ($p_T < 120\,\mathrm{MeV}/c$) and cannot be measured by the central drift chamber, the SVT is capable to act as an independent tracker.

The SVT design has been studied in order to minimize the multiple scattering. It takes into account the physical constraints imposed by the PEP-II geometry, such as the presence of the permanent magnets nearby the interaction point, which are necessary to separate the beams shortly after the interaction point. The polar angle

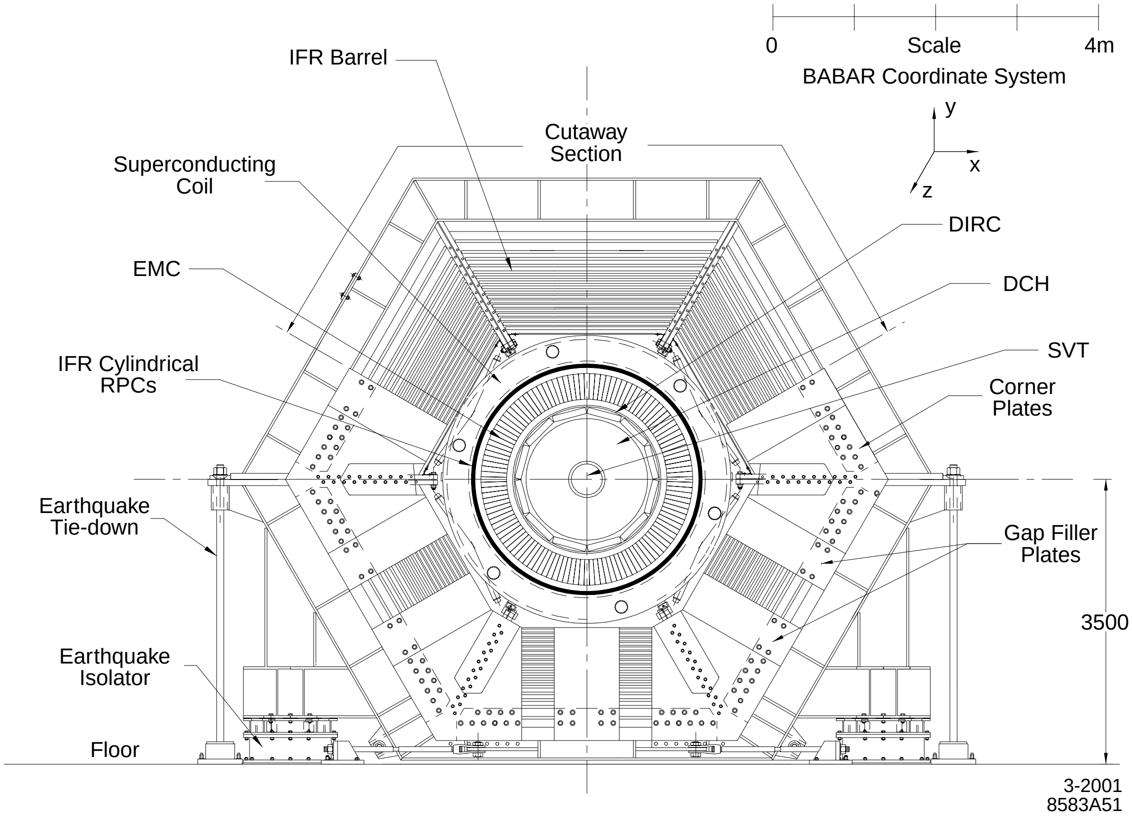

Figure 2.2: *The BABAR Detector (front view).*

acceptance is $-0.87 < \cos\theta_{lab} < 0.96$ ($-0.95 < \cos\theta_{cm} < 0.87$) and is limited by the beamline elements. The SVT consists of five double-sided layers of silicon detectors assembled on carbon fiber support cones. The first three layers provide the tracking resolution while the last two are necessary to measure the low momentum tracks independently from the drift chamber information. The single hit resolution in azimuthal and longitudinal planes depends on the angle of incidence of the tracks and varies from 20 to $40\,\mu$m. The achieved average hit reconstruction efficiency is above 98%. The SVT precision determines the impact parameter resolution for the measurement of high transverse momentum tracks, where the distance between two vertices is reconstructed with a resolution of about $50\,\mu$m. Two B decay vertices are separated with a typical accuracy of $110\,\mu$m. A detailed description of the SVT and its components can be found in [26].

The main purpose of the DCH is the precise and efficient measurement of charged particle parameters such as momenta and angles, for particles with transverse momenta p_T above about $120\,\mathrm{MeV}/c$. The DCH complements the information about the impact parameter and the direction of the track measured by the SVT. The reconstruction of decay vertices, for example K_S^0, outside of the SVT requires, in addition to the transverse momenta and position, the measurement of the longitudinal position with an accuracy of about 1 mm. The DCH has also to provide the particle identification at relatively low momenta by measuring the ionization loss (dE/dx) and has to supply information for the charged particle trigger.

The DCH has an outer radius of 809 mm and a length of 2800 mm. The interaction point is shifted by 367 mm relatively to the center of the chamber, in order to improve the forward acceptance, given the boost for the $\Upsilon(4S)$ events. The acceptance of the DCH covers the polar angle range $-0.92 < \cos\theta_{lab} < 0.96$. Forty layers of small hexagonal cells provide spatial and amplitude measurements. The longitudinal position is measured by placing the wires in 24 layers at a small angle with respect to the z-axis. The design of the drift chamber has been studied to minimize the amount of material in front of the calorimeter. By choosing low-mass aluminum field wires and helium based gas (80%He+20%C_4H_{10}) the material thickness is less than $0.2\%X_0$. The DCH provides an average single point resolution of 125 μm.

2.2 Magnet system

The *BABAR* magnet system provides the magnetic field which enables charged particle momentum measurement, serves as a hadron absorber for hadron/muon separation and provide the overall structure and support for the detector components. To provide a designed momentum resolution for the charged tracks, the magnetic field mapping and subsequent corrections have to be determined in the tracking volume to a precision of 2 G.

2.2.1 Field requirements

The *BABAR* magnet system consists of a superconducting solenoid, a segmented flux return and a field compensating or bucking coil. Detector performance criteria and geometry considerations drive the design of the solenoid and the flux return. The magnitude, uniformity and map precision specifications for the magnetic field are derived from drift chamber track finding and momentum resolution requirements. Studies of $B^0 \to \pi^+\pi^-$ show that a magnetic field of 1.5 T is necessary to achieve a mass resolution of about 20 MeV/c^2. A field uniformity in the tracking volume is an important parameter of the detector magnet system. To simplify track finding and fast and accurate track fitting, the magnitude of the magnetic field within the tracking volume is required to be uniform within a few percent. To meet the momentum resolution of the drift chamber (see Equation 2.1) it is sufficient that the random errors in the field determination are about a tenth of a percent, i.e. of about 15 G. However, the systematic errors (correlated from point to point) can lead to momentum uncertainty significantly larger than the statistical error. Simulation studies show that such a systematic precision has to be as good as 2 G.

To produce the high luminosity of PEP-II, high beam currents and a large number of closely spaced beam bunches are required. The bunches are separated magnetically in the horizontal plane by a pair of dipoles (B1) and a series of offset quadrupoles (Q1, Q2, Q4 and Q5), as shown in Figure 2.1. The *BABAR* magnet was designed to minimize disturbance of operation of the PEP-II beam elements.

The samarium-cobalt B1 dipole and Q1 quadrupole magnets are located inside the solenoid. Although these magnets can maintain the high longitudinal field of 1.5 T, they can not tolerate a large radial component B_r. Assuming linear dependence of B_r on r, the radial field can not exceed 0.25 T at $r = 200\,\mathrm{mm}$. Otherwise, their field properties are degraded due to partial demagnetization. The conventional iron Q2, Q4 and Q5 quadrupole magnets are placed outside the field of the *BABAR* solenoid. Consequently, they are exposed to the solenoidal stray fields. The Q2 quadrupole is situated within the forward end of the instrumented end door flux return. Since it is most acted by the solenoid fringe field, a skew octupole moment is induced resulting from the magnetic field in its vicinity. The luminosity is critically dependent upon the Q2 field quality. Hence, an adequate shielding of the *BABAR* central field becomes important to ensure the quality of the quadrupole field.

2.2.2 Magnet coils

The *BABAR* magnet is a thin superconducting solenoid within a hexagonal barrel flux return (Figure 2.2). The magnetic field of 1.5 T is obtained by injecting a constant current of 4596 A in the solenoid. The conductor is operated at 45% of the critical current, with a peak field in the conductor of 2.5 T. This gives a large safety margin.

The combined thickness of the vertex detector, drift chamber, particle identification system, electromagnetic calorimeter, and appropriate clearances set the solenoid diameter to be 3060 mm. Solenoid length of 3513 mm is also determined by the length of the nested subsystems. The designed thickness of 350 mm limits the momentum threshold for detecting muons and the efficiency of K_L^0 detection within the instrumented flux return.

Magnetic uniformity is achieved by increasing the current density in regions at both ends of the solenoid. This is done by adding more aluminum stabilizer to the central region conductor, which reduces the current density there. To optimize the detector acceptance due to unequal beam energies, the center of the *BABAR* detector is offset by the 367 mm in the electron beam direction with respect to the Interaction Point (IP). As a result of the symmetry of the solenoid and this offset the designed field uniformity in the region of the drift chamber is within a few percents.

As it will be described in Section 4.2.1, to reduce the stray field to an acceptable level for the DIRC photomultipliers and the PEP-II quadrupoles, a bucking coil, mounted at the face of the backward door and surrounding the DIRC strong support tube, is designed. To optimally control the fringe fields and avoid a magnetization of the DIRC magnetic shield, the currents in the solenoid and bucking coil are ramped together. Although the optimal operating current is 200 A, a current of up to 575 A is reachable to demagnetize the DIRC shield (see Section 4.2.6).

2.2.3 Flux return

The flux return assembly supports the detector components on the inside and provides an external flux path for the 1.5 T magnetic field of the superconducting solenoid. It consists of the barrel and the end doors which are connected by a structural steel and filler plates. A room for cables and utilities from the inner detector is reserved in this interface. Subsequently, separation and movement of the end doors are required by beam line components and by the need to provide ready access to inner detectors.

The segmented geometry of the flux return allows tracking of muons and provides for detection of K_L^0 mesons. The total thickness of the steel layers in the barrel and end door is determined both by the minimum steel required to avoid magnetic saturation and by the need for sufficient thickness to ensure that most of the pions interact in the steel. The minimal steel thickness to prevent pion punch-through is 550 mm (∼3.6 interaction lengths). Plate segmentation and thicknesses are specified both for efficient identification of K_L^0 mesons and for distinguishing muons from pions based on range measurements.

2.3 Magnetic field map

The goal of the magnetic field mapping and subsequent corrections is to determine the magnetic field in the tracking volume to a precision of 2 G.

2.3.1 Field computations

Extensive calculations of the magnetic field were performed to develop the detailed design of the flux return, solenoid coil, and the bucking coil. The fields were modeled in great detail in two and three dimensions. Although most of the basic design work was performed in two dimensions, several three dimensional calculations were necessary to assure the accuracy of the model. These studies have been performed using a commercial software [27].

Great demands are placed on the detector design by the magnetic forces. There are three kinds of such forces:

- symmetric magnetic force on the end doors;
- axial force on the solenoid due to the forward-backward asymmetry of the steel;
- superconducting coil quench induced forces.

These forces were analyzed for the components such as endplates of the DCH and the EMC and were found not to be a problem [23].

Calculations of the leakage of field into the PEP-II magnets, the impact of that leakage on the multipole purity, and the shield design of the quadrupoles have been performed with two and three dimensional models of the quadrupoles [23, 28].

Three-dimensional studies were made to examine the effects of the different non-axisymmetric aspects of the detector iron. These ϕ asymmetric elements in the doors and barrel iron are:

1. holes for cable access, rails, and lead screws of the plug removal mechanism;
2. vertically running channels for services to the liquid helium cryostat;
3. iron spacers along the door boundaries and interior parts for the RPC detectors;
4. warped shape of one of the front doors as a manufacture effect;
5. vertically running channels at the top half of the front doors;
6. hexagonal shape of the barrel iron;
7. access slots for cables in each hexagonal side of the barrel iron.

Before starting detailed three-dimensional calculations of *BABAR*, a thorough comparison between two- and three-dimensional axisymmetrical models has been performed. This comparison gave a comforting assurance of the model consistency in the regions of interest. The maximal difference is about 5 G in front of the edge of Q2, where the gradient of the field is also maximal. In the other regions such as the central tracking volume and the region of DIRC photomultipliers the consistence is better than 1 G. It was verified that the difference between the two models becomes smaller with condensation of the mesh.

Due to the complexity of the *BABAR* design, two three-dimensional models are considered, one with left-right symmetry and another with top-bottom symmetry. Each ϕ asymmetric element has been included at least in one of the model. These models were used to compute the field in the central tracking volume and the region of the DIRC photomultipliers (see Section 4.2.2).

2.3.2 Apparatus and data set

A filed mapping device was built specifically for the *BABAR* magnet based on a design concept developed at Fermilab [29]. It consists of a transport mechanism that could move a set of Hall probes throughout the inside volume of the solenoid. This mechanism consists of a long spindle with a rotating inner shaft held inside a pipe. One end of the pipe is rigidly attached to a cart on wheels. The cart moved on precision rails along the spindle axis such that the spindle could travel through the central hole of the front end plate. This allowed the tip of the spindle to be positioned anywhere along the axis inside the solenoid when the end plate doors are closed. The magnetic probes were mounted on a narrow plate (propeller) at right angles to the rotating shaft at the tip end.

Measurements were obtained from five sets of B_z, and B_r and two B_ϕ Hall probes. These probes were equally spaced along a radial direction, each having the same ϕ. Each pair of high accuracy B_z and B_r probes were encapsulated together in one unit, while the less accurate B_ϕ probe was an individual unit. In addition to the Hall probes, one NMR probe was placed at a fixed radius of $89\,\mathrm{mm}$ and a ϕ value of 180° away from the other probes. It provides a very precise field reference near the z-axis as a function of z for $|z| < 1\,\mathrm{m}$ ($z = 0$ at the magnet center). The NMR measurements set the absolute scale of the magnetic field. The probes were mounted rigidly on a separate plate that was attached at the propeller plate. The z coordinate of the probes was controlled by the cart position on the rails, the ϕ coordinate by the rotation of the spindle shaft, and the r coordinate by the placement of the probe plate along the propeller arm. The z and ϕ placement was done under computer control. The probe plate could be manually installed to one of three radial positions. The radial placement of the probe plate and the nominal coordinates of each probe on the plate are shown in Figure 2.3.

Knowing the placement and the alignment of the probes is crucial for measuring the magnetic field. For example, a 1 mrad rotation of a B_r probe in the (r, z) plane results in an error of 15 G in that probe from the 1.5 T B_z field. Precision optical alignment tools were used to determine the position and orientation of the sensors transverse to the z-axis. These alignment corrections were attributed both to the probe coordinates as well as the probe field measurements.

The data sets were taken at field settings of 1.5 T and 1.0 T. As a cross check, data sets at the nominal field of $1.5T$ and two outermost positions of the propeller were repeated. Control measurements were made at a standard reference point at $z = 0$ and $\phi = 0$ between each grid movements in z. This provides a quality check of the data.

Measurements ranged from -1.8 m to +1.8 m in intervals of 0.1 m in z, and in 15° azimuthal steps from 0° to 345° for each of three different radial positions of the Hall probe plate. At each $z - \phi$ grid point, the field readings from the 13 probes ($5 - B_z$, $5 - B_r$, $2 - B_\phi$, and 1−NMR) were recorded, together with the coil current and environmental temperatures. A data set consists of a full range over the z grid points, and a full range of the 24 ϕ-grid points at each z setting and three different radial positions of the Hall probe plate. This sums to 46320 points of the full field map used in the fit model.

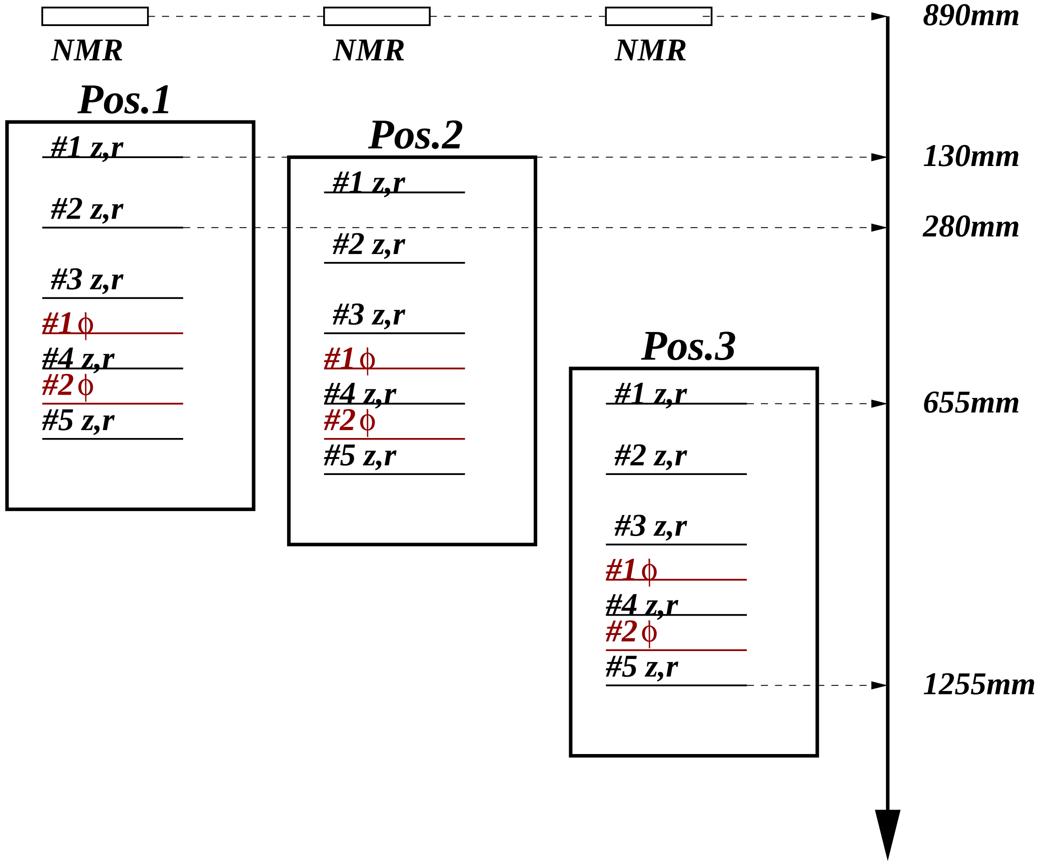

Figure 2.3: *The nominal radial coordinates of the B_z, B_r and B_ϕ Hall probes at each of three positions of the probe plate. The NMR probe is fixed to the spindle away from the other probes at a fixed radius as described in the text.*

2.3.3 Field model and data fitting

The magnetic field in a source-free region can be described by a scalar magnetic potential ψ satisfying the Laplace equation

$$\bigtriangledown^2\psi = 0 \tag{2.2}$$

The solution of this equation expressed in cylindrical coordinates, $\psi(z, r, \phi)$ applicable to the inner volume of a solenoid is a linear combination of the terms containing trigonometric, hyperbolic, and Bessel (I_n or J_n) functions. The magnetic fields is given by the gradient of the magnetic scalar potential, $\vec{B} = -\bigtriangledown \psi$.

Polynomial field functions

The ϕ-symmetric field functions derived from the ϕ-symmetric Laplace potential function are written as

$$\begin{aligned} B_z(z,r) &= \sum_i (s_i\cos(k_i z) - c_i\sin(k_i z)) I_0(k_i r) \\ B_r(z,r) &= \sum_i (s_i\sin(k_i z) + c_i\cos(k_i z)) I_1(k_i r) \\ B_\phi(z,r) &= 0 \end{aligned} \tag{2.3}$$

These equations can be used to fit measured B_z, B_r, B_ϕ field values by choosing appropriate values for the k variables and fitting for the c and s coefficients. However, since the k values are arbitrary, it is difficult to pick an appropriate set that would minimize the number of terms required to fit the data.

An alternate method uses a set of polynomials to fit the data. Polynomials may be derived from the above set of equations by expanding each trigonometric or Bessel term into a series, collecting terms of equal rank, and replacing the resulting factors $\sum s_i k_i^n$ and $\sum c_i k_i^n$ by new fitting parameters P_n. Then, one can fit these parameters for as many terms as required to describe the data to a certain level of accuracy. The series expansion of the ϕ-symmetric Laplace field functions gives the following polynomial field functions, shown for terms up to order n

$$\begin{aligned} B_Z(z,r) &= \sum_{i=0}^{n} P_i(i!)(-1)^{\frac{i+1}{2}} \sum_{k=0(2)}^{i} \frac{(-1)^{k/2} z^{i-k} r^k}{(i-k)!2^k((k/2)!)^2} \\ B_R(z,r) &= \sum_{i=1}^{n} P_i(i!)(-1)^{\frac{i+1}{2}} \sum_{k=1(2)}^{i} \frac{(-1)^{k/2} z^{i-k} r^k}{(i-k)!2^k((k/2)!)((k+1)/2)!} \\ B_\phi(z,r) &= 0 \end{aligned} \tag{2.4}$$

The $(i+1)/2$, $k/2$, and $(k+1)/2$ terms must be truncated to whole integers in the above expressions, and the k-summation is stepped by 2. Note, the same P_i fitting parameters appear in B_z and B_r in order to satisfy Maxwell's equations, since both equations are derived from the same magnetic potential. As we demonstrate later, the fit was improved by using terms up to P_{40}.

Angular dependent fields

Since the *BABAR* magnet iron is not ϕ symmetric it is required that ϕ dependent field terms be added to the fitting model. According to the presence of ϕ asymmetric elements described in Section 2.3.1, the following functional terms were added to the field model:

- A *magnetic dipole* term oriented along the Z-axis at each hole on the end plate gives an approximate representation of the field from the missing magnetized iron.

- For extended objects such as the linear RPC spacers, a rectangular shaped pole was used instead. A *rectangular pole* is achieved by placing a rectangular loop of current in the plane of the end plate that circumvents the object, giving a pole pointing along the Z-axis over the length of the rectangle.

- The asymmetry due to the warped doors can be modeled in part by an *annular dipole* of varying width along its circumference. An annular dipole consists of two current loops in the plane of the end plate having opposite currents and origins slightly displaced from each other.

- The barrel iron surrounding the solenoid coil is in the shape of a hexagon, so a field component with six-fold symmetry in ϕ would be expected at large radii. This six-fold asymmetry can be modeled with a few *trigonometric-Bessel terms* (with $n = 6$) added to the fitting model. It was also found necessary to include trigonometric-Bessel terms with $n = 2$ and $n = 1$. The source for these fields is not precisely known, but a slightly flattened hexagonal barrel would give an $n = 2$ component, while a slightly off-centered component (coil or iron) could give an $n = 1$ component.

Data fitting

A non-linear least squares fitting program was used to fit the model to the measured data. Assumed errors of measurement for data points within the tracking volume are presented in Table 2.1.

Probe	Precision
NMR	0.1 G
B_z Hall	1.0 G
B_r Hall	1.0 G
B_ϕ Hall	3.0 G

Table 2.1: *Precision of probes used in the field mapping.*

Fits were done with a varying number of polynomial terms to establish the minimum order. The χ^2 per degree of freedom decreases with the number of polynomial terms below 40 terms. Forty terms were used in the final fits. The final configuration includes 80 floating parameters summarized in Table 2.2.

Number of parameters	Type of term
4	Magnetic axis terms ($X_0,\ Y_0,\ \theta_{XZ},\ \theta_{YZ}$)
40	Polynomial strength
1	Bessel (n=1)
2	Bessel (n=2)
3	Bessel (n=6)
9	Dipole, (22 total)
14	Rectangular pole, (20 total)
7	Annular pole

Table 2.2: *Fitting parameters used in the filed model.*

2.3.4 Results

A resulting χ^2 per degree of freedom of 2.89 is found in the final fit. This implies that the product of two effects: the model is not yet complete, and the assumed errors are too small, deteriorate the obtained χ^2. We increase all the measuring errors by a factor of 1.7. This allows us to obtain the ideal fit with a χ^2 per degree of freedom of 1.0. We find the root mean square of the residuals to be 1.7 G for points within the tracking fiducial volume and 4.8 G for all the measured points. In the tracking region the field is very uniform, the measured B_ϕ component is about 10 G. As a result, the variation of the field transverse to the trajectory, along the path of a high momentum track is at most 2.5% from maximum to minimum within the tracking volume [25].

Figure 2.4 shows the results of the measurements and two dimensional calculations of B_z component at $r = 805$ mm which is outer radius of the DCH. The agreement is at that level of 10 G. Figure 2.5 presents the variation of B_r with ϕ. Three dimensional Mermaid calculations allow us to estimate the major effects and to predict the angular behavior of the field. The bumps at $\phi = 90°$ and 270° can be associated with the vertical chimney cut-out in the BABAR doors. One sees, the simulation reproduces very well the shape of the field, while its magnitude is slightly shifted. We have also observed about 15 G variation of B_r component at $z = 0$ due to the magnetic axis being tilted with respect to the geometrical axis of the BABAR yoke. One can estimate an angle between these two axes of about 1 mrad. Note that this effect has not been taken into account in the Mermaid calculations. This explains the difference of the field magnitude in data and simulation.

It is important to note that, during the mapping process, the permanent magnet dipoles (B1) and quadrupoles (Q1) were not installed yet. Their presence inside the

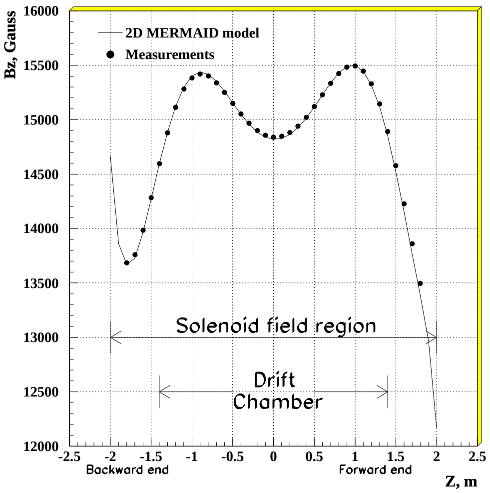

Figure 2.4: *Measured* B_z *as a function of* z *at* $r = 805$ mm. *The results of Mermaid calculations with 2D model are overlaid.*

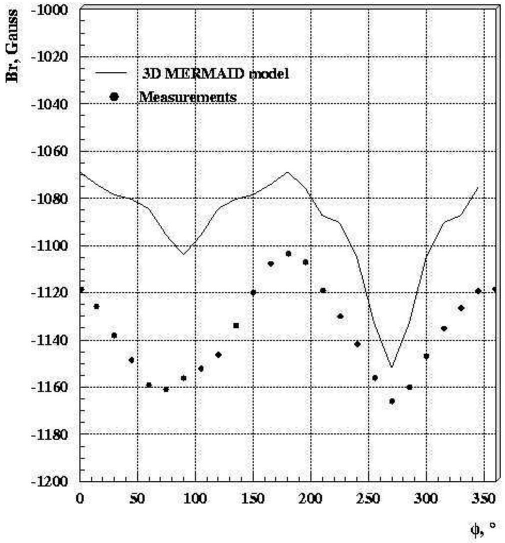

Figure 2.5: *Measured* B_r *as a function of* ϕ *angle at* $z = -1.4$ m *and* $r = 805$ mm. *The results of Mermaid calculations with 3D model are overlaid.*

solenoid leads to field perturbations. One source of such perturbations is the fringe fields of the B1 and Q1 permanent magnets and the dipole and quadrupole trim coils mounted on Q1. The fields associated with the trim coils were measured and parameterized before the installation. Another source of field perturbation is due to the permeability of the permanent magnet material which ranges from 1.11 to 1.13 in the z direction. The NMR (Hall) probes were installed between the forward (backward) B1 and Q1 to measure the effect of the permeability. The induced magnetization increases the B_z by about 90 G at the IP and decreases slowly with increasing radius. These perturbations were included in the *BABAR* field model.

2.4 Conclusion

Since its successful commissioning, the magnet system has been operated without problems. The magnetic field within the *BABAR* super conducting solenoid (3.8 m long by 3 m diameter, at a field of 1.5 T) has been measured with a set of Hall probes mounted on the specially built field mapping device. The measurements were fit to a functional model which contains polynomial terms to order 40 for the B_z and B_r field components, a few trigonometric-Bessel terms having one-, two-, and six-fold ϕ symmetry, and 24 dipole terms positioned on the end plates to describe the non-uniform iron distribution of these plates. The measurements and the model agree to 1.7 G (rms) within the *BABAR* tracking volume, and to 4.8 G in the fully mapped volume ($-1.8 < z < 1.8$ m, $r < 1.3$ m). In the tracking region, the magnetic field meets the specifications, both in magnitude and uniformity. Predictions of the fields in the *BABAR* magnet were made using the Mermaid computer program. Comparisons of the measurements with the predictions gave comforting assurance that there were no significant errors in the measurements.

Chapter 3

Particle Identification System ATC

Powerful particle identification for hadrons and leptons over a large range of solid angle and momentum is an essential requirement to meet the physics objectives of *BABAR*. This chapter presents my contribution to the research and development of the forward particle identification system based on *Aerogel Threshold Counters* (ATC) for the *BABAR* experiment in the period of the detector design [30]. I summarize the results obtained with the prototypes of the 4-layer design of the ATC system developed by the Novosibirsk group, where I was working at that time. This work has been done in collaboration with A. Buzykaev and E. Kravchenko. The other design versions of the ATC system proposed by LAPP and INFN groups were tested together with 4-layer option at the same test beam setup. The common papers with the results of this experiment were published in Ref.[31].

First, I briefly overview the project of the particle identification system in *BABAR*. The main part of this chapter is devoted the test beam results with prototypes of the forward particle identification system. These counters have been tested with the PS T10 beam line at CERN in 1995. Research and development of threshold Cherenkov counters which include analysis of the test beam data for the 4-layer option of the ATC system, study of aerogel and light reflector properties have been a significant part of my research in 1995-1997 (Appendix B).

3.1 Particle identification overview

As described above (Section 1.5), the study of CP violation requires particle identification, both to reconstruct exclusive final states and to tag the flavor of the other B in the event. Information from the drift chamber, electromagnetic calorimeter, and muon chambers allow us to identify most of the leptons and many of the hadrons. However, this information is not sufficient to discriminate charged pions and kaons with momenta above $0.7\,\mathrm{GeV}/c$, or protons from pions and kaons above $1.3\,\mathrm{GeV}/c$. The maximal momenta of the kaons used for the tagging of B via decay cascade $b \to c \to s$ are about $2\,\mathrm{GeV}/c$. In contrast, the pions and kaons from the rare two-body decays

$B^0 \to \pi^+\pi^-, K^+\pi^-$ have momenta between 1.7 and 4.2 GeV/c.

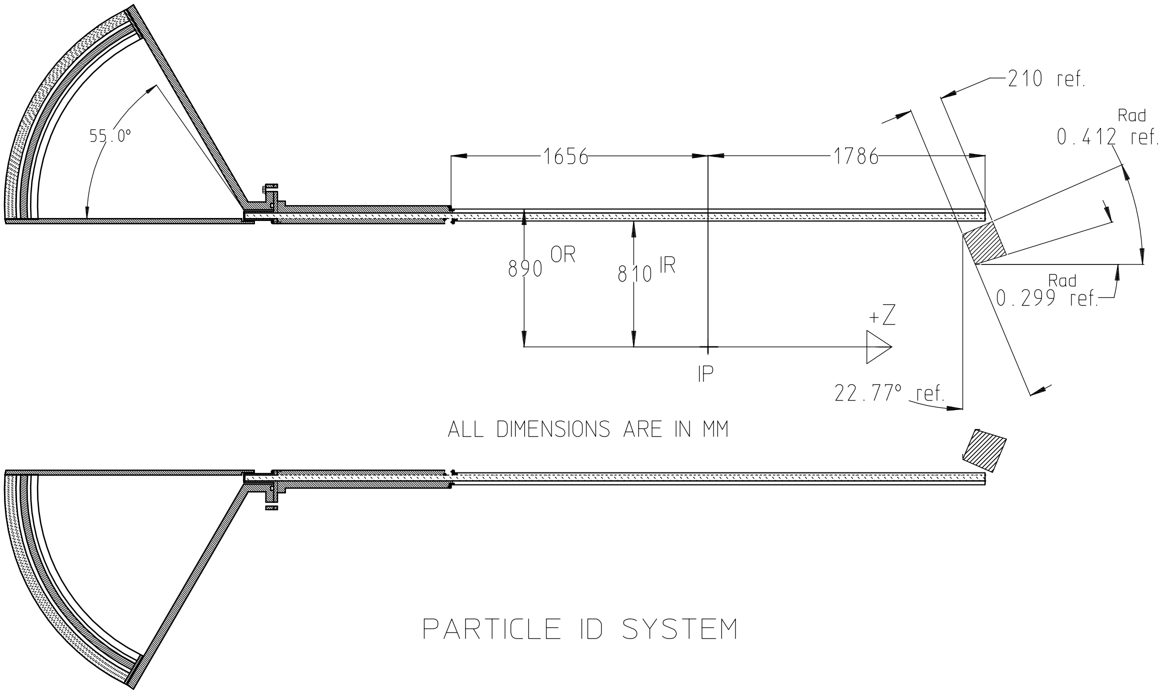

Figure 3.1: *Project of the particle identification system for the BABAR experiment. It consists of the barrel DIRCand forward ATC systems [30].*

To meet these requirements a system containing two types of Cherenkov detectors has been designed for *BABAR* [30]. The barrel region ($25.5° < \theta < 147°$) is covered by a DIRC [32], which provides good performance over the whole momentum range while occupying only a thin radial region. An ATC covers the forward region ($17.1° < \theta < 23.6°$) enlarging the kaon tagging acceptance and providing π/K separation up to 4.3 GeV/c. Figure 3.1 shows the layout of the main components of the particle identification system designed for *BABAR*. The boundary between the systems was chosen to maximize the acceptance for particle identification within the constraints of magnet length and calorimeter position and angle. Both systems maintain low mass in order to minimize a deterioration of energy resolution of photons detected in the EMC.

3.2 The Aerogel Threshold Counters

The forward PID detector is a silica aerogel Cherenkov counter covering the polar angle range $17.1° < \theta < 23.6°$. Both kaon tagging and pion identification are achieved with two refractive indices, $n \simeq 1.0065$ (low) and $n \simeq 1.05$ (high).

There are two key components in the ATC system: the aerogel radiator and the readout device. Aerogel with good optical quality is produced by Airglass, Jet Propulsion Laboratory (JPL), and the Boreskov Catalysis Institute at Novosibirsk [33].

In order to collect Cherenkov photons efficiently inside the solenoid, the photon detector must work in magnetic fields up to 1.5 T, have a large UV-sensitive area with high quantum efficiency, and have low noise. The baseline design uses bialkali fine mesh photomultiplier tubes (FM PMT) from Hamamatsu with a high quantum efficiency photocathode. The average thickness in front of the endcap calorimeter is 9.5% of a radiation length.

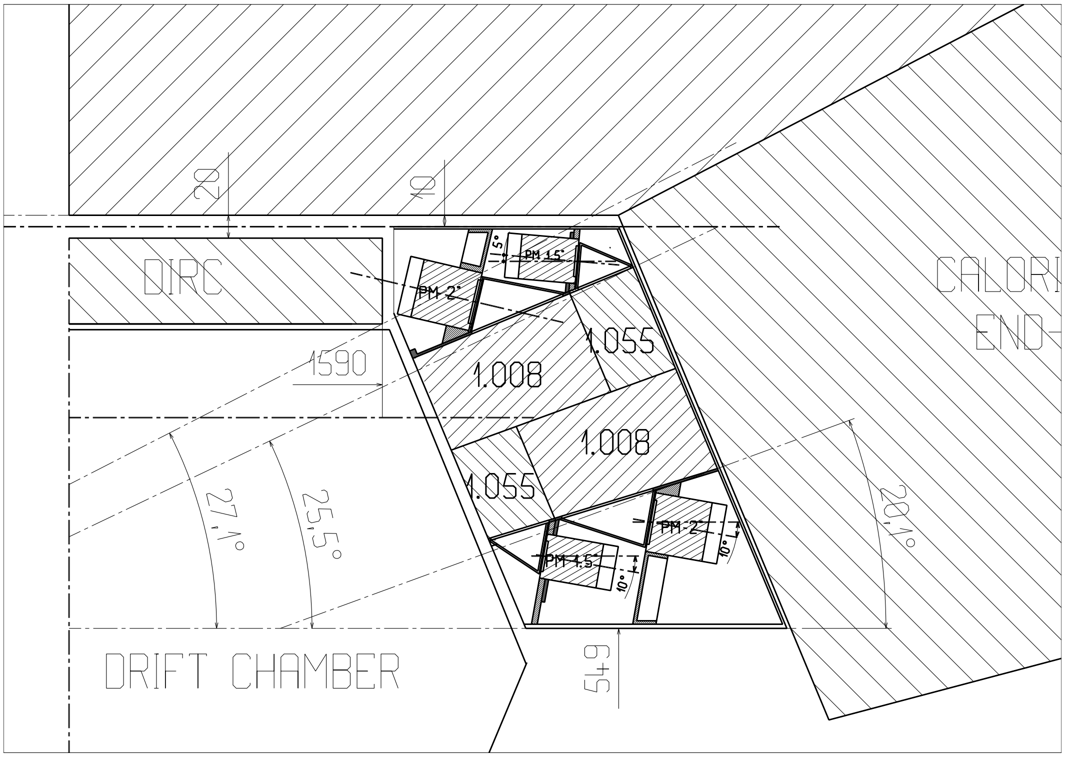

Figure 3.2: *Schematic view of ATC detector.*

Two geometrical designs covering the forward region of the *BABAR* detector have been considered:

- The first one, is a 2-layer, 2 ring design. There is one layer of high index aerogel and one layer of low index aerogel in each ring. The counters are readout by Hamamatsu, 1.5" (2") for the high (low) index, fine mesh photomultipliers (FM), or by Hybrid-Photo-Diodes (HPD). These photo-detectors are attached at the aerogel containers with a pyramidal shaped air light guide located on the top and on the bottom of the rings, as shown in Figure 3.2.

- The second design consists of 4 layers (2 super-layers). Each super-layer includes two counters: one with low, another with high aerogel indices. The second super-layer is shifted with respect to the first one by half of the counter size. This allows us to prevent a loss of signal when a particle crosses the phototube in one of the layers. Each high (low) index cell is readout by 2 (3) 2" Hamamatsu FM phototubes (Appendix B.1).

The 2-layer design with FM PMT readout has been chosen as the baseline option of the ATC system. This decision has been approved based on the results of the test beam, described in the next section.

3.3 Test-beam results with prototypes

3.3.1 Beam line and apparatus

The prototypes of the *BABAR* ATC system have been tested in the PS T10 beam line at CERN. The beam provides positive and negative particles with momenta between 1 and 5 GeV/c. The beam components are mainly pions and protons. The beam line shown in Figure 3.3, was equipped with two gas Cherenkov counters filled by CO_2 at a 4.3 bar pressure. It was triggered by the coincidence of three scintillator counters, where the extension of the latter one ($1 \times 1\,\text{cm}^2$) has limited the beam size. In addition, 1 cm thick veto scintillator counter readout by CAMAC scaler, was used to count the number of particles crossing the setup in a 1μ m gate.

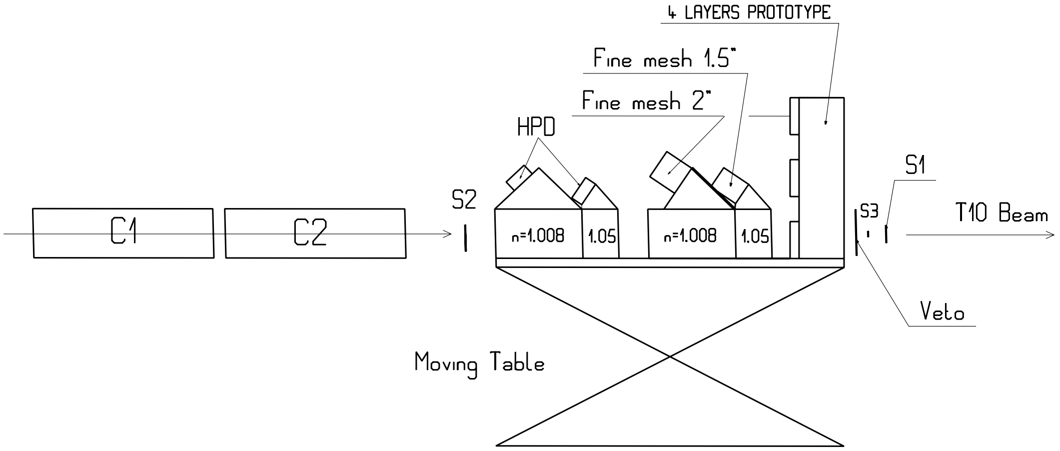

Figure 3.3: *The T10 beam line with the apparatus*

The following 2-layer design prototypes were placed on a moving table:

- The low index cell had a dimension of $10 \times 10 \times 14\,\text{cm}^3$. It was filled with 5 aerogel blocks of 9.5×9.5 cm^2 front face and 2.6 cm thick. The aerogel produced by Jet Propulsion Laboratory (JPL), had a nominal refractive index of 1.008. It is readout by either one 2" Hamamatsu fine mesh (FM) phototubes or two 1" Hybrid Photo-Diodes (HPD).

- The high index cell had a dimension of 10 × 10 × 6 cm^3. Two sets of aerogel produced by the different manufactures such as Airglass with an index n=1.055 and Boreskov Catalysis Institute in Novosibirsk with an index n=1.050 have been tested. The counter was readout by either a 1.5" Hamamatsu FM photomultipliers or one 1" HPD device.

The following 4-layer prototypes were placed nearby:

- The low index prototype with an aerogel thick of 69 mm was readout by three 2" Hamamatsu FM photomultipliers. Two sets of aerogel were tested: one set with n=1.012 produced by the Boreskov Catalysis Institute in Novosibrsk, and a second one with n=1.008 produced by the Jet Propulsion Laboratory (JPL).
- The high index prototype was readout by two 2" Hamamatsu FM photomultipliers. It was filled with 21 mm thick aerogel produced in Boreskov Catalysis Institute in Novosibrsk (SAN-95) with the refractive index of 1.05.

The walls of counters were wrapped with three layers of $250\mu\,\mathrm{m}$ PTFE film on top of aluminized mylar. In order to remove water from the aerogel, all the blocks were baked before being exposed to the beam.

3.3.2 Results

The prototypes were exposed to a 5 GeV/c negative pion beam ($\beta \simeq 1$). The events were selected by requiring a clean signal in both gas Cherenkov counters and only 1 count withing $1\mu\,\mathrm{s}$ in the veto counter to reduce pile up events. As an example, Figure 3.4 shows the observed number of photoelectrons in the high index (1.050) prototype of the 4-layer option of the ATC system. To study the inhomogeneity of the light collection of the counter, four different points were exposed. The Monte Carlo simulation that uses the measured aerogel and reflector optical quantities have also been performed. One observes that the results are in good agreement. We have also studied the signal induced by below threshold particles. To select the protons, the absence of signal in both gas Cherenkov counters was required instead. Figure 3.5 show the detected number of photoelectrons as a function of the beam momentum for both pion and proton beams. We use a theoretical curve [13] normalized on the number of photoelectrons measured with pions ($\beta \simeq 1$) to fit the proton data (circles). Dashed lines correspond to a $\pm 1\sigma$ variation of such a normalization. A non-zero signal corresponding to protons with momentum below Cherenkov threshold ($p_{th} = 2.93\,\mathrm{GeV}/c$) is due to δ-electrons, Cherenkov light from the reflector and scintillations in the aerogel.

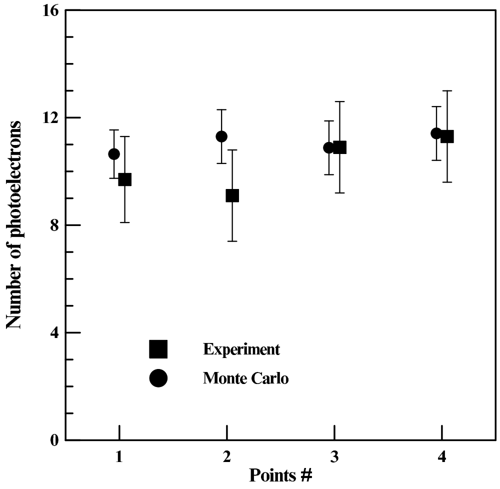

Figure 3.4: *Detected number of photoelectrons for the "high" index prototype (4-layer option) for the different positions of the pion beam ($\beta \simeq 1$).*

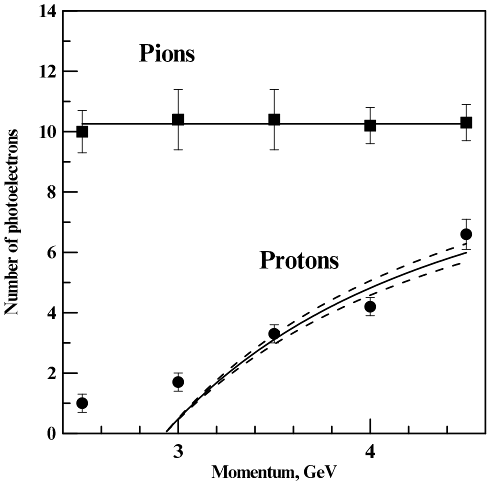

Figure 3.5: *Detected number of photoelectrons for the high aerogel index prototype (4-layer option) as a function of momentum. The result obtained with a pion beam (squares) is fitted with a straight line, while a theoretical curve (see the text) is used to fit the proton data (circles).*

Enhancement of the signal in an aerogel counter is possible by shifting the photon spectrum to the red region, where the transparency of aerogel, the reflection of PTFE, and the quantum efficiency of the photocathode are essentially advanced. The low index prototypes of the 2-layer option were tested with the use of PMP-420 wavelength shifter. The last layer of PTFE covering the walls parallel to the beam direction was impregnated with this shifter dissolved in acetone. The wavelength shift from $\simeq 350$ nm to $\simeq 420$ nm has increased the signal by about 35% (65%) in the center (farthest) point and weakened its dependence on the distance to the light detection device.

Measured numbers of photoelectrons for all prototypes involved in this test beam experiment are summarized in Table 3.1. The numbers for the 4-layer options in this table are corrected for the difference in the low aerogel indices and the thickness of the aerogel in the high index counter between the prototype and the project. The low index prototypes of 2-layer option have been equipped with PMP wavelength shifter. Based on experimental spectra obtained with pion and proton beams, we have calculated the probability $\mathcal{P}(p \rightarrow \pi)$ for a proton to emit light in the counter and to be identified as a pion, and the probability $\mathcal{P}(\pi \rightarrow p)$ for a pion, not to emit light in the counter and to be identified as a proton. We choose the point at the optimal threshold (the one where these two probabilities are equal) as a figure of

	Low (n=1.008)			High (n=1.05)
Prototype	Background	Signal ($\beta = 1$)	$\mathcal{P}(p \to \pi)$, %	Signal ($\beta = 1$)
2-layer FM PMT	0.9	13.4	4.0	10.0
2-layer HPD	0.6	8.6	3.3	9.7
4-layer FM PMT	0.3(0.5)	7.8(11.4)	3.2(5.6)	11.0

Table 3.1: *Number of photoelectrons detected in the prototypes in the different conditions. Proton contamination at the optimal threshold* $\mathcal{P}(p \to \pi)$ *is also indicated for low index prototypes. The light yield of the 2-layer design counters (n=1.008) has been enhanced by using the PMP-420 wavelength shifter. The actual measured numbers for 4-layer option counter (n=1.012) is indicated in parenthesis, while the main numbers are estimated for the project aerogel index (n=1.008).*

merit of our detector performances (see Appendix B.6).

3.3.3 Aerogel optical parameters

A powerful $\pi/K/p$ separation requires maximizing the Cherenkov light collection in the counter. To meet this requirement, a high transparency of the aerogel blocks becomes a key property of the radiator. The direct comparison of two aerogel manufacturers has been done using the high aerogel index prototype (2-layer option with fine-mesh PMT readout). Figure 3.6 shows the observed number of photoelectrons as a function of vertical distance to the center of the box for the aerogel samples produced by Boreskov Catalysis Institute (SAN-95) and Airglass. The latter one has significantly smaller signal amplitude that is diminishing very rapidly with the distance from the PMT window.

It is very difficult to measure correctly the aerogel absorption length independently of the scattering length. However, a specially developed method, described in [34] allows us to perform such a measurement in the laboratory without the beam. Figure 3.7 shows the measured absorption length of the SAN-95 sample as a function of wavelength. This allowed us to perform the Monte Carlo simulation of the light collection in the counter. The results of such a simulation were described in Section 3.3.2. In year after the test beam experiment with prototypes of the *BABAR* ATC system at CERN, Boreskov Catalysis Institute has tested a new technology of aerogel production. The absorption length of the produced samples with such a technology has significantly improved. The result for SAN-96 blocks are also included in Figure 3.7.

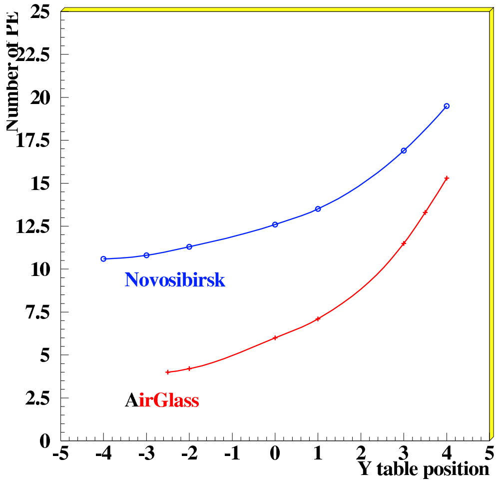

Figure 3.6: *Number of photoelectrons versus the vertical distance to the center of the counter box (2-layer option). The photomultiplier is located at y=5* cm. *The solid line corresponds to the SAN-95 (Novosibirsk) aerogel, while the dashed line corresponds to the Airglass aerogel.*

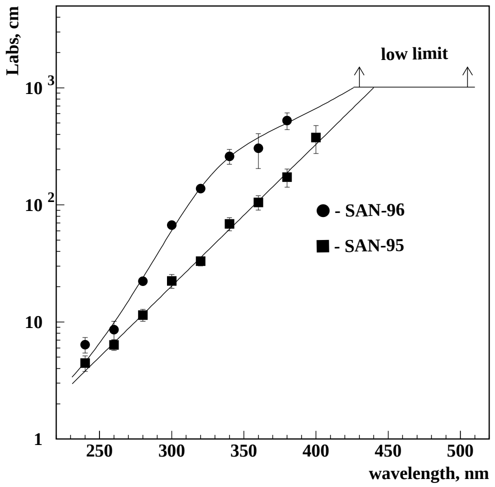

Figure 3.7: *The absorption length of aerogel produced in Boreskov Catalysis Institute (n=1.05). The prototypes of the ATC system were filled with SAN-95. New technology of the aerogel production (SAN-96) allowed an essential improvement of its absorption length after the test beam experiments.*

3.4 Conclusion

Several prototypes of the *BABAR* ATC system have been tested in a beam line at CERN. Counters equipped with aerogel blocks of low (1.008) and high (1.050) refractive indices have been exposed to pion and proton beams. The observed average number of photoelectrons for $\beta = 1$ particles is greater then 10 p.e. for the high aerogel index and about 8 p.e. for the low index. The study of background induced by particles with momentum below the Cherenkov threshold shows that one can reach a pion efficiency of about 96% for a proton misidentification as low as 4%. This corresponds to about 3.2σ separation power between pions and protons. We conclude that aerogel counters can be used to construct a powerful and compact particle identification device in the momentum range of 0.4-4.3 GeV/c.

Taking into account a combination of several parameters such as detector performances, amount of material, cost, complexity, we selected a 2-layer option with fine mesh photomultiplier readout as a baseline design for *BABAR*.

However, due to the cost problem, the forward particle identification system, based on aerogel counters has been excluded in the final design of *BABAR*. This has also allowed us to bring the endcap EMC closer to the interaction point and, consequently, diminish the number of crystals. One has to note that the other B-factory experiment *BELLE* has used the aerogel Cherenkov counters as a principal particle identification system of the detector [35].

Chapter 4

Particle Identification System DIRC

This chapter describes my contribution to the DIRC system of the *BABAR* detector. The *Detector of Internally Reflected Cherenkov light* (DIRC) [36] is the principal particle identification system of the *BABAR* detector. Due to the complex non-symmetrical geometry of *BABAR*, the external detector components, like the final focus elements and the photon detectors of the DIRC, are placed in a very strong fringe field. Thus, the shielding of these components for detector operation is an important challenge of the experiment. The first step of my work included calculations of the shielding components that were accounted in the design of the magnetic shield. Then my research was related to a measurement of the field in the region of the DIRC photomultipliers. I have been responsible for the design and construction of the field mapper that allowed us to perform such measurements before commissioning of the experiment. This work was my main activity in 1996-1998. The results of this work have been published in [37] (Appendix C).

First part of this chapter gives a brief overview of the DIRC system of the *BABAR* detector. The main part describes in details the results of simulation and measurement of the fringe field of the *BABAR* 1.5 T solenoid. Finally, I discuss the physics highlights related to the performances of the DIRC system.

4.1 The Detector of Internally Reflected Cherenkov light (DIRC)

Figure 4.1 shows the basic principle of the DIRC. Charged particles, produced at the interaction point inside the detector, traverse the quartz bars in which Cherenkov radiation is produced. The angle θ_c of this radiation with respect to the incident particle is a measure of the velocity v of these particle from the equation $\cos\theta_c = 1/n\beta$ with $\beta = v/c$, where c is the velocity of light and n=1.473 is the mean refractive index of the quartz radiator. The Cherenkov photons propagate along the rectilinear bars by total internal reflection, preserving the angular information and exiting outside the detector into a large pure water tank, called the standoff box. Using the position of the photo-tube and the arrival time of the signals, the DIRC is a three-dimensional imaging device. Since the tracking system provides the track position and angles, the measured photon propagation angles are used to determine the Cherenkov angle. The arrival time of the signal can be also related to the propagation angles and provides an additional constraint, which is very useful to avoid ambiguities in the signal association due to high background rates.

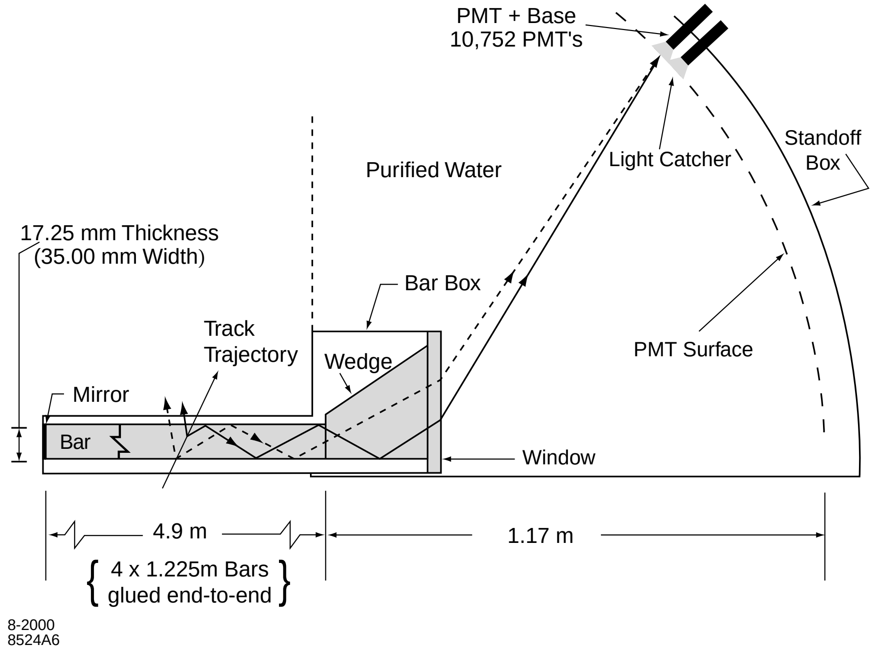

Figure 4.1: *Schematic view of DIRC quartz radiator bar and the photon detection region.*

The DIRC consists of quartz bars inside the detector and of the standoff box, supporting photomultipliers outside the detector at the backward end. The bars are supported by a mechanical structure which is attached to the barrel iron via special structural elements. The water tank is composed of a cylinder, a cone and 12 cylindrical sections. 10752 photomultipliers are mounted on the sectors placed at about 1.17 m from the quartz bar exit point to permit a precise measurement of the angle for each photon. The standoff box is arranged inside a special low magnetic field volume, which diminishes the value of the fringe fields from the main solenoid.

A single photon angular resolution of about 10.2 mrad is obtained with an average of 30 photons per track which corresponds to about 2.8 mrad for the Cherenkov angle. A timing precision of 1.7 ns is measured. The separation between charged kaons and pions is approximately three standard deviation at 3.5 GeV/c.

4.2 Simulation and measurement of the fringe field

4.2.1 Magnetic shielding

Due to the asymmetric beam energies, the detector is not forward-backward symmetrical with respect to the interaction point, as can be seen in Figure 2.1. Potentially, this places crucial final focus elements in a very strong fringe field of the *BABAR* flux return. Such a field would degrade the performance of the quadrupoles, reducing the luminosity significantly. The solution in the backward (negative z) region, as indicated in the figure, is to mount a bucking coil on the flux return steel encircling quadrupole Q2. This reduces the B_Z component field at Q2 to less than 100 G.

In addition to the potential effect on the accelerator, the operation of the DIRC PMTs is also challenged by these fringe fields. Even though they are mounted more than a meter from the outside surface of the flux return they could not operate in the ambient magnetic fields, which far exceed the few Gauss limit for efficient operation. Although it would have been possible to shield each PMT with mu-metal individually, this approach would have reduced the overall photon detection efficiency [36]. An alternative method is to surround the entire SOB with an iron enclosure to shield against stray fields.

Due to the lack of simple symmetries and the superposition of the fringe fields of the *BABAR* flux return and the bucking coil field, the design of an optimal shielding configuration was a considerable challenge. Nevertheless, the solution described here reduces the fringe field at the photomultipliers to an acceptable level of less than 1 G.

4.2.2 Simulation of the *BABAR* magnetic circuit

In order to satisfy the PMT and Q2 requirements, it was soon recognized that a combination of active (bucking coil) and passive elements (iron) was necessary.

The *BABAR* magnetic circuit consists of two active elements: a thin cryogenic solenoidal magnet, generating a 1.5 T magnetic field, and the bucking coil in the backward direction. The passive elements are also grouped into two parts. The first are those elements with a geometry determined by the central apparatus of *BABAR* such as the barrel and endcaps (forward and backward) of the IFR, the flux return plugs (forward and backward), along with part of the DIRC support structure. The second part is the DIRC magnetic shield (Figure 2.1), whose design had to accommodate the existing geometry and magnetic fields due to the other elements. The shield geometry is most strongly determined by the position and shape of the SOB, which is cantilevered from the Support Gusset. In the backward plug region, the DIRC support structure is part of the magnetic circuit, but the fused silica bars and bar boxes require holes in this part of the circuit, increasing the fringe field in the backward direction significantly. This ensemble of elements makes calculation of the resulting magnetic field extremely complicated, even if an axisymmetric (or 2D) approximation is used.

The primary mechanical constraints considered during the design of the DIRC shield were:

- that the beam elements must be contained within the shield cylinder;
- that access to the drift chamber is made inside the shield cylinder;
- that the magnetic shield and its support, resting on the skid plates, should also provide a counterweight for the *BABAR* IFR backward doors, when opened;
- that the shield should provide a stop for the backward plug against movements in the -z direction due to a potential seismic event.

To minimize the maximum transverse field at the photomultipliers an iterative series of axisymmetric studies of the structure were performed to determine optimum bucking coil current that would allow accelerator Q2 magnet operation. The principle parameters investigated were: the position of the bucking coil; the thickness, shape and permeability of the iron shield; the size of the magnetic gap between the shield iron, and the plug and SST; the dimensions of the support gusset; and the radius at which the shield inner cylinder connects to the outer shield.

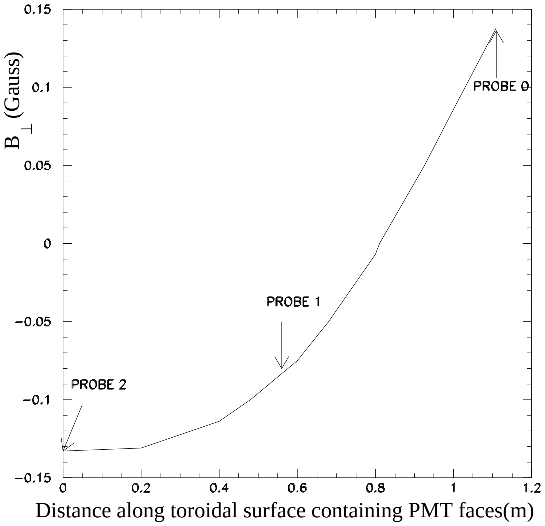

Figure 4.2: *Results of the 2D model of BABAR using the measured permeability. The figure displays the* $B_\perp$ *along a surface containing the PMT faces from probe 2 to probe 0.*

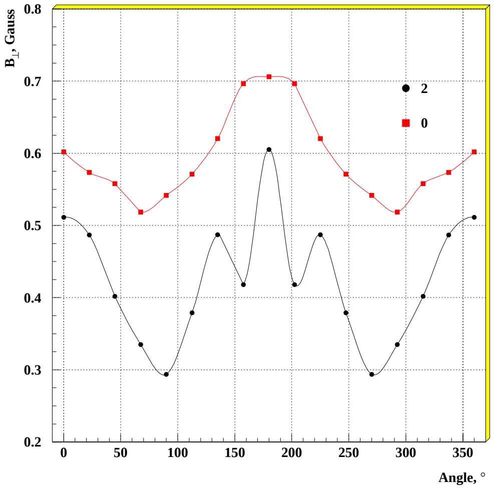

Figure 4.3: $B_\perp$ *vs. azimuthal angle calculated in the left-right symmetry model of BABAR. The coordinate system has the downward direction at 0°.*

A set of shield design parameters was derived from this exercise that predict that the magnetic field transverse to the PMT axis $B_\perp$ at the PMT faces would be less than 0.2 G, as seen in Figure 4.2 (the three probe positions are defined in Section 4.2.4). This configuration requires a bucking coil current of about 30.7 kA-turns. The optimum to produce the lowest field at Q2 is higher by about 15 %, requiring a modest compromise.

Three-dimensional studies were made to examine the effects of the different non-axisymmetric aspects of the *BABAR* iron (Appendix C.3.3). Due to the complexity of the *BABAR* magnetic circuit, it was not possible to make a 360° model within the computer memory limitations. Therefore, two models are considered, one with left-right symmetry and another with top-bottom symmetry.

The results of the 3D simulations show that the expected $B_\perp$ inside the DIRC shield is less than 1 G with angular variations of about ± 0.2 G. The $B_\perp$ for the left-right symmetric model varies between 0.3 G and 0.7 G as seen in Figure 4.3. Since a possible residual field was not included in the model, the measured azimuthal dependence can be different in detail from the prediction.

In addition, the calculations show that in the case of a quench of the main solenoid or if power to the bucking coil is lost, the field in the shield iron can reach 7000 G instead of 500 G when both coils are on. The resulting coercive force is about 1 Oe for the very pure iron used in the shield construction. Therefore, the residual field of the iron would give an additional contribution to the fringe field in the PMT region.

The residual field distribution inside the shield was estimated using a simplified simulation. The value of the maximum perpendicular component at the PMT reaches about 3 G on the uppermost PMT and about 2 G on the lowermost PMT. In this model, the residual field due to the coercive force exceeded the expected fringe field inside the shield. This result led to a special effort to consider the use of the bucking coil to demagnetize the shield. In this method, the amplitude of the bucking coil current should vary about zero. It was predicted that about ten cycles of bucking coil current would be enough to decrease the residual fields to acceptable levels in a reasonable time.

4.2.3 Design and construction of the shield

The magnetic shield has been designed at Saclay. It is based on the following considerations:

- All connections are welded including the support structure, except for the cover plate and the flange on the fixed part of the inner cylinder to allow the opening of the SOB;
- since bending of the iron (required for some components) strongly affects permeability, especially at low H, the entire structure must be annealed after construction; the best results were obtained by using a temperature of 850 °C for 4 hours.

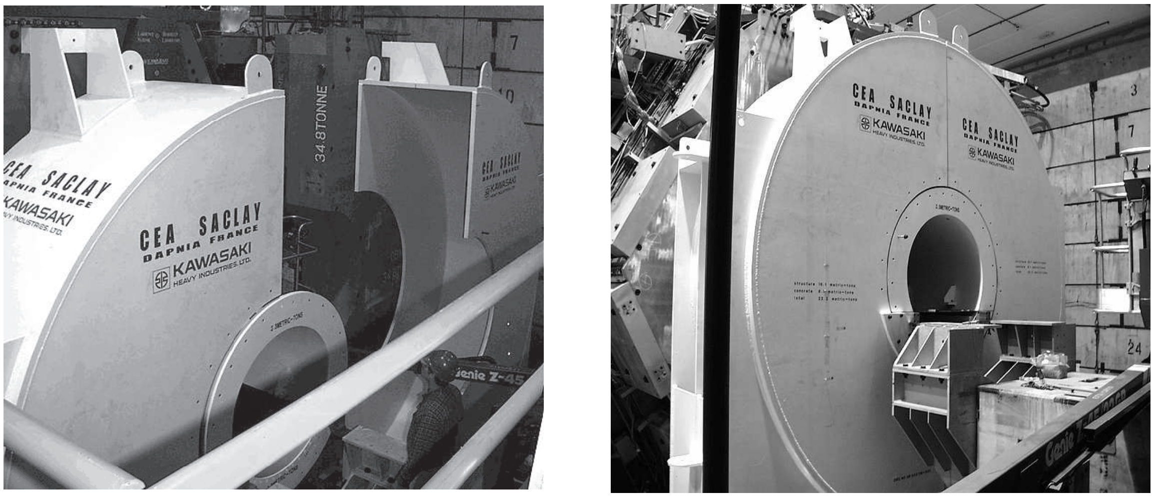

Figure 4.4: *DIRC shield in the process of being adjusted (left). Shield fully mounted, except for the top of cover plate (right).*

The construction of the shield was the responsibility of KHI. The ultra low carbon steel used was the proprietary material EFE, manufactured at Kawasaki Steel Corporation (KSC). The permeability and coercive force of the completed structure were measured at KSC and exceeded the specifications. Figure 4.4 shows the shield as it is being aligned and mounted, before mounting the *SOB*.

4.2.4 Magnetic field mapper

The aim of the DIRC magnetic field mapper is to measure the field components inside the shield at positions corresponding to the faces of the PMTs. It consists of a rigid support structure, mounted on the horsecollar, which can rotate about the beam axis.

The mechanical design of the mapper is shown in Figure 4.5. Three-dimensional probes are placed at three positions along the PMT rows, at the two extremes and in the middle. Figure 4.6 shows the functional diagram of the magnetic field measurement system.

A rigid frame is attached to the platform moving around the circular rail mounted on the horsecollar. All elements, such as frame, removable platform and circular rail are fabricated from aluminum alloy. The movement of the platform along the rail is provided by three rollers. Three 3D probes are fixed on the arc of the frame.

The step motor mounted on the platform provides the motion of the frame. The motor has no permanent magnet inside. A worm gear is used to transfer the rotation momentum of the rotor.

The potentiometric method with the use of nichrome wire resistor of 0.8 mm diameter is used to measure the azimuthal angle ϕ. This wire is located in the groove on the rail. An electric contact attached to the platform moves along the rail together

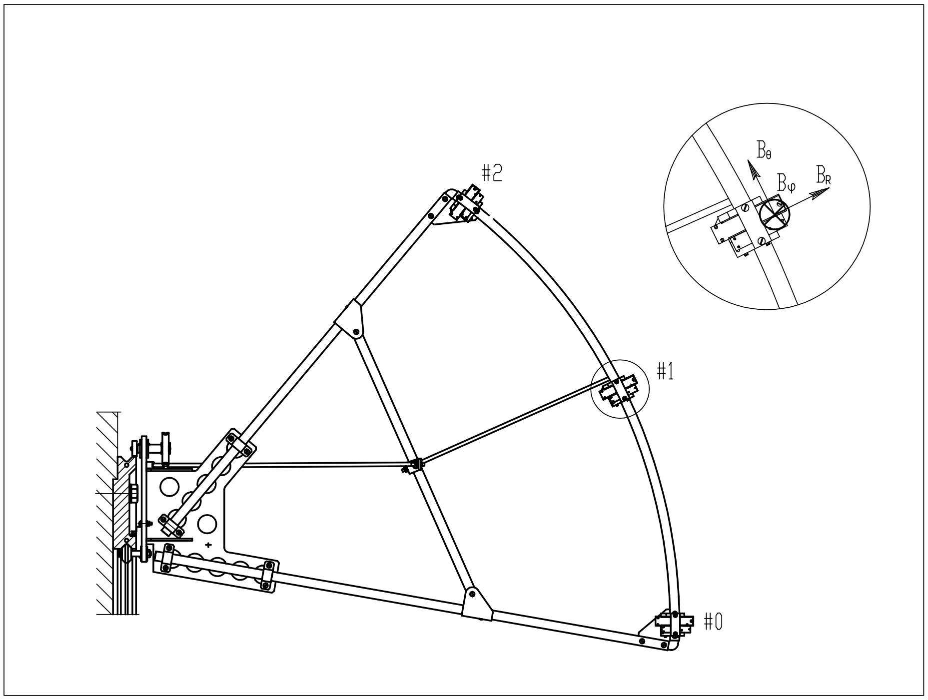

Figure 4.5: *Location of the probes on the rigid frame.*

with the platform. The wire resistor is supplied by 100 mA current. The accuracy of the azimuthal angle measurement is about 0.2° Figure 4.6 shows the functional diagram of the fringe field mapping.

4.2.5 Probes

Both ferro-probes (Magnetically Modulated Permalloy Probes or MMPP) and Hall probes are used. Each set of 3D probes consists of one 3D ferro-probe and one 3D Hall probe located next to each other. The sensitive volume of a set is a cube of $20 \times 20 \times 20$ mm^3. The locations of the 3D probes on the rigid frame correspond to the faces of the PMTs as shown in Figure 4.5. The measurement coordinate system has 0° as the downward direction, rotating in the clockwise direction as viewed from the rear of *BABAR*.

Ferro-probes are used to measure relatively low fields up to about 10 G. The ferro-probe is supplied with a measuring electronic unit which transforms magnetic field into voltage with coefficient of about 0.5 V/G. Each 3D ferro-probe is arranged inside a cube of $10 \times 10 \times 10$ mm^3.

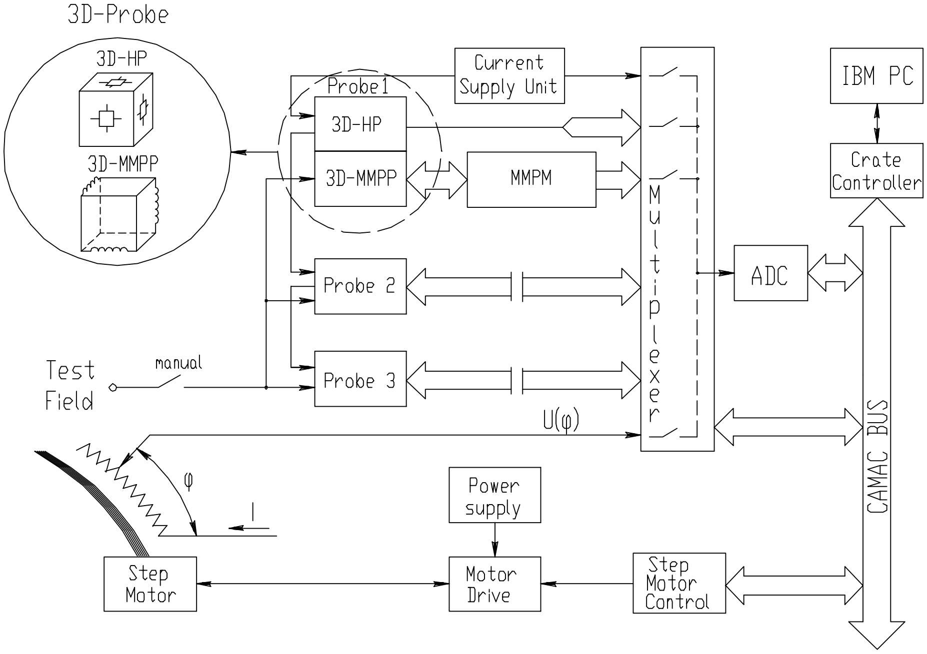

Figure 4.6: *Functional diagram of the magnetic field measurement system*

The design of one coordinate ferro-probe is shown in Figure 4.7. It consists of permalloy core of 20 μm diameter and 7 mm long located in the quartz tube. This core was annealed in advance and has very small coercive force. The common excitation and compensation coils are wound along the quartz tube. The signal coil is wound at the middle of the tube. Figure 4.8 shows the electronic block diagram of MMPM. Rectangular 16 kHz impulses from generator are applied to the excitation circuit. The signal in the signal coil is proportional to B derivative in the core. The second harmonic (2f=32 kHz) of this signal is proportional to the measured B_{ext}. An integrating ADC with a multiplexer is used to read out the probes with 14-20 bit resolution for two scales: 8 V and 0.5 V. The long-term zero drift is less than 0.02 G within a 20-30° temperature range.

Hall probes are used to measure relatively high fields exceeding 5 G, thus overlapping the ferro-probe sensitive region. One 3D set of Hall probes consists of three probes glued on the sides of an aluminum cube, $3 \times 3 \times 3$ mm^3. This unit is assembled in a box $9 \times 15 \times 62$ mm^3. The stabilized DC current source which is used to supply the Hall probes has a stability of 10^{-5}.

A special calibration system is used to measure the zero offset and sensitivities

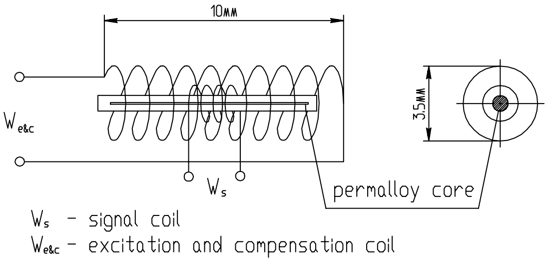

Figure 4.7: *One-coordinate ferro-probe or MMPP*

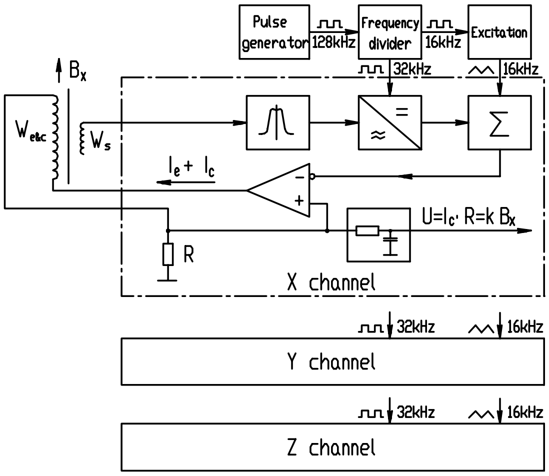

Figure 4.8: *Electronic block diagram of MMPM*

of the probes. The calibration is performed with the help of Helmholtz coils located inside a zero field box manufactured from annealed permalloy. It can produce magnetic fields up to 50 G. A Hall probe calibrated by an NMR probe has been used to measure the coefficient between the current and magnetic field of this coils. The estimated error is 0.1%.

4.2.6 Results

To establish a baseline, mapper measurements were made with no solenoid field. The maximum remnant field in the *BABAR* doors, support gusset and skid plates was about 0.9 G. The mounting of the shield greatly reduced the influence of the remnant field at the PMT positions due to the *BABAR* doors. More importantly, a very low measured field (less than 0.2 G) demonstrated that the iron used in the shield construction had a very low residual field.

The solenoid and bucking coils were ramped together in 5 steps to the nominal operating currents. Measurements were made at each step.

At the nominal currents, the maximum component of the field at the PMT perpendicular to its long axis is 0.8 G, which is acceptable for PMT operation. The bucking coil current was varied to determine the optimum currents for PMT and quadrupole operation. It was increased to 230 A in 10 A steps and then was reduced back to 200 A. The current was then reduced to 170 A in 10 A steps. The optimum current for Q2 operation is near 200 A, and this value was chosen for the operating point.

The maximum value of $B_\perp$ at the PMTs differed in the two 200 A measurements due to hysteresis effects; in fact, it was reduced from 0.8 G to 0.6 G. At 170 A, the

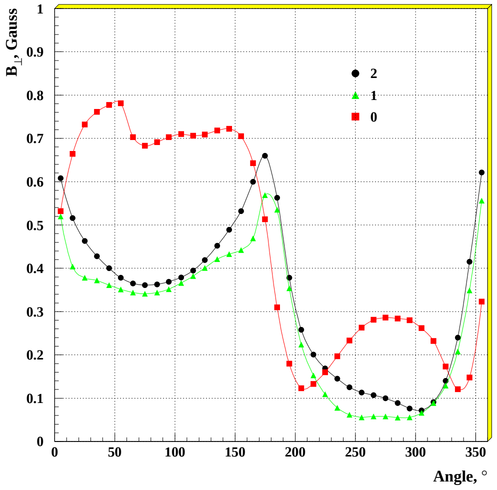

Figure 4.9: *$B_\perp$ vs. azimuthal angle with the solenoid at its nominal current and the bucking coil at the optimum current for Q2, 200 A.*

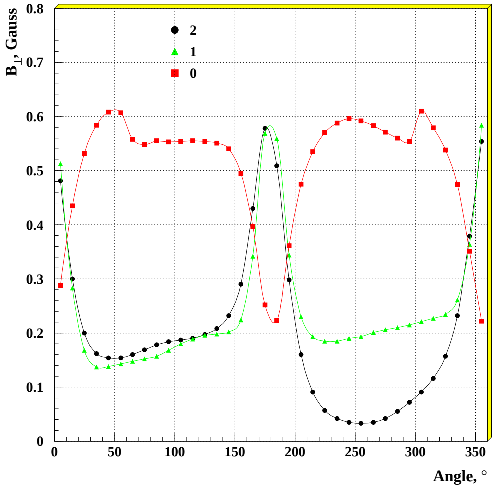

Figure 4.10: *$B_\perp$ vs. azimuthal angle with the solenoid at its nominal current and the bucking coil at the optimum current for Q2, obtained with overshoot current 260 A.*

three probes had the same maximum value of 0.5 G, which is the optimum for the PMT. This value is about 15 % lower than that at 200 A, in good agreement with the calculation.

The bucking coil current was cycled back to 200 A as follows: 170 A → 230 A → 180 A → 220 A → 190 A → 210 A → 200 A at which point a reduction in the hysteresis was observed. Figure 4.9 shows the scan at the final 200 A current. The maximum $B_\perp$ is about 0.8 G and a left-right asymmetry is observed, probably due to residual shield magnetization. Various demagnetization schemes were developed successfully for the cases when either the main solenoid quenches or the bucking coil power is lost. The residual magnetization can be compensated by raising the bucking coil to a current above 200 A, called the overshoot current, and then lowering the current to the nominal 200 A current. It was found that this was not only possible, but optimum in that the apparent *BABAR* left-right asymmetry could be compensated. In Figure 4.10 we see the compensation of left-right, around the optimum value of I_{over}=260A. This result is in relatively good agreement with the calculations (Figure 4.3) though some residual field probably still influences the probe 0 result.

During normal *BABAR* operation the magnetic field in the *SOB* is monitored continuously by 12 probes in 4 locations.

4.3 Physics performances

The DIRC plays a central role in B meson selection and its flavor tagging. The $D^0 \to K^-\pi^+$ coming from $D^{*+} \to D^0\pi^+ \to (K^-\pi^+)\pi^+$ decay is a good control sample to study the pion and kaon identification capabilities of the DIRC. Figure 4.12 shows the $K^-\pi^+$ invariant mass spectrum from inclusive D^* production. The comparison of the D^0 yield with and without positive kaon identification allows us to extract the efficiency of the particle identification of the single kaon. Figure 4.12 shows the measured selection efficiency and misidentification for kaon tracks from such a sample, as a function of track momentum in laboratory frame.

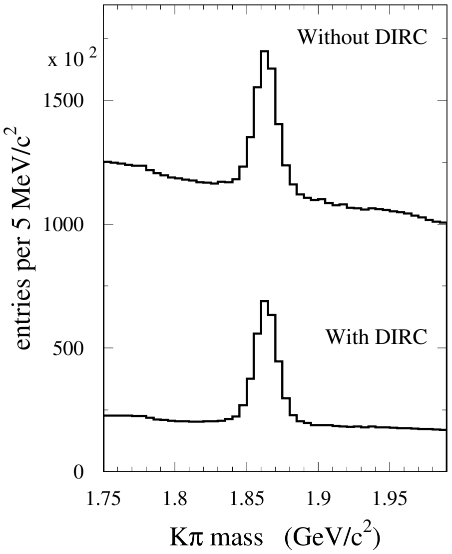

Figure 4.11: *Invariant $K^+\pi^-$ mass spectrum for kinematically reconstructed D^0 mesons in the decay $D^* \to D^0\pi$, without (top) and with (bottom) the use of the DIRC to identify the kaon.*

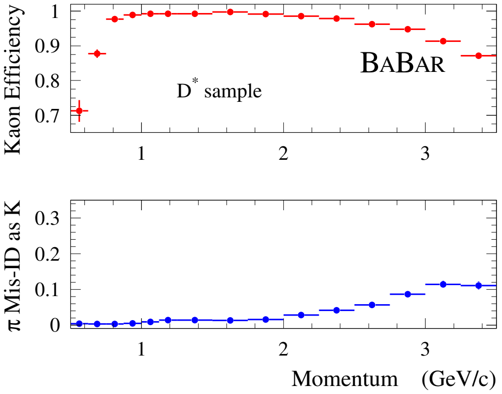

Figure 4.12: *The efficiency and misidentification for kaon tracks*

To illustrate the quality of the hadron particle identification, the charmless $B \to h^+h'^-$ $(h,\ h' = \pi,\ K)$ decays can be considered. The *CP* asymmetry in the tree level contribution to the decay $B^0 \to \pi^+\pi^-$ is related to the CKM angle α of the unitarity triangle. Furthermore, the ratios of B branching fractions to various $\pi\pi$ and πK states are sensitive to the angle γ. In the Standard Model $B^0 \to K^+\pi^-$ occurs through two different mechanisms ("penguin" and "tree"), which carry different weak phases and, in general, strong phases. Thus, one predicts a large direct *CP* violation of about 10% in this decay. *BABAR* has performed measurements of the branching fractions and *CP* asymmetries in $B \to \pi^+\pi^-$, $K^+\pi^-$ and K^+K^- decays [38].

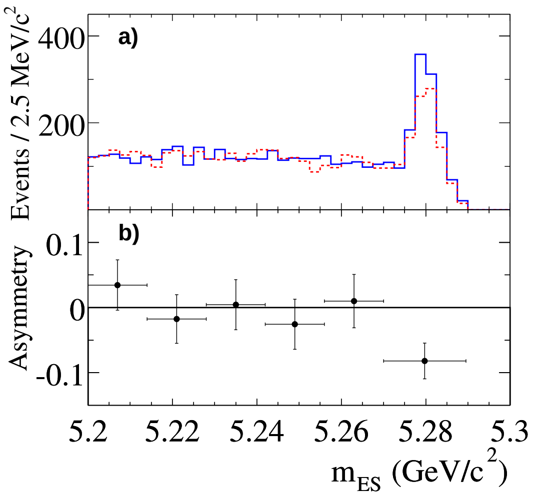

Figure 4.13: *Distribution of B meson mass enhanced in $K^+\pi^-$ (solid histogram) and $K^-\pi^+$ (dashed histogram) (a),asymmetry $A_{K\pi}$ calculated for ranges of the reconstructed B mass.*

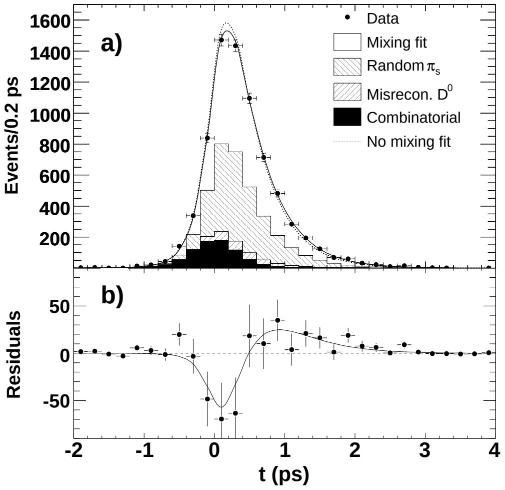

Figure 4.14: *a) The proper-time distribution of combined D^0 and $\overline{D}^0$ WS candidates in the signal region. The result of the fit allowing (not allowing) mixing but not CP violation is overlaid as a solid (dashed) curve. Background components are shown as shaded regions. b) The points represent the difference between the data and the no-mixing fit. The solid curve shows the difference between fits with and without mixing.*

Since the charged particles from two-body decays $B \to h^+h'^-$ are in the momentum range $1.75 < p < 4.25$ GeV/c, dE/dx has a little discrimination power for particle identification. However, the Cherenkov angle θ_c measured in the DIRC provides separation between kaons and pions about 4σ at 3 GeV/c declining to about 2.5σ at 4.1 GeV/c. The maximum-likelihood fit uses θ_c as one of the variables to determine the event yield of the four $\pi^+ \pi^-$, $K^+\pi^-$, $K^-\pi^+$ and K^+K^- simultaneously. The measured yields of $K^+\pi^-$ and $K^-\pi^+$ allowed us to observe the direct CP asymmetry

$$\mathcal{A}_{K\pi} = \frac{n_{K^-\pi^+} - n_{K^+\pi^-}}{n_{K^-\pi^+} + n_{K^+\pi^-}} = -0.133 \pm 0.030(\text{stat}) \pm 0.009(\text{syst}) \qquad (4.1)$$

at the level of 4.2 standard deviations using a data sample of 227 million $B\overline{B}$ pairs. Figure 4.13 shows the distributions of the reconstructed B meson mass (m_{ES}) for data samples enhanced in signal $K\pi$ decays using a probability ratios, and $\mathcal{A}_{K\pi}$ as a function of m_{ES}.

One more example of excellent hadron identification performances of *BABAR* can be illustrated by a recent evidence of the D^0-$\overline{D}^0$ mixing [39]. The wrong-sign (WS) decay $D^0 \to K^+\pi^-$ can be produced via the doubly Cabibbo-suppressed (DCS) decay $D^0 \to K^+\pi^-$ or via mixing followed by a Cabibbo-favored (CF) decay $D^0 \to \overline{D}^0 \to K^+\pi^-$. The DCS decay has a small rate of order $\tan^4\theta_C \approx 0.3\%$ relative to the CF decay. We distinguish D^0 and $\overline{D}^0$ by their production in the decay $D^{*+} \to \pi^+ D^0$. In RS decays the slow pion π^+ and kaon have opposite charges, while in WS decays the charges are the same. The time dependence of the WS decay rate is used to separate the contributions of DCS decays from D^0-$\overline{D}^0$ mixing. Figure 4.14 shows the proper-time distribution for WS data. The fit results with and without mixing are shown as the overlaid curves. The fit with mixing provides a substantially better description of the data than the fit with no mixing. This result is inconsistent with the no-mixing hypothesis at a significance of 3.9 standard deviations.

Thus, the DIRC is a ring-imaging Cherenkov detector that is very well-matched to the hadronic particle identification requirements of *BABAR*. The detector performance provides an excellent possibility to perform the physics program of the experiment.

Chapter 5

Method of Partial Reconstruction

This chapter describes my contribution to the study and development of a partial reconstruction technique used for the B meson reconstruction. The preliminary study of the $B^0 \to D_s^{(*)+} D^{*-}$ decays with this technique has been performed and included in my thesis work [2]. The final measurement has been done one year after and published in Physical Review D (see Appendix D, [40]). Several precision measurements using this technique were published in the period of my convenership of the Inclusive Hadronic B Decays (IHBD) analysis working group in 2003-2005. They are also discussed in this chapter.

I briefly describe the methods of full and partial reconstruction of B mesons. The main section summarizes the analysis highlights and the results obtained for the $B^0 \to D_s^{(*)+} D^{*-}$ decays. A measurement of the $D_s^+ \to \phi\pi^+$ branching fraction is then reported. A set of precise measurements conducted with the partial reconstruction is discussed in conclusion.

5.1 Theoretical tools for quark flavor physics

The experimental observables, except the direct measurements of the angles of the UT, that are presently used to constrain ρ and η (see Section 1.4) depend on hadronic matrix elements. The QCD, theory of strong interaction, has been tested to high precision in the perturbative regime, where the coupling constant α_s is small. However, quantitative predictions in low-energy regime remain difficult. There exist several approaches to non-perturbative QCD which allow an application of a few general techniques to evaluate the matrix elements that are relevant for quark flavor physics. Most of the model independent theoretical tools, effective theories, exploit that some quark masses are smaller while the the others are greater than Λ_{QCD}, a typical hadronic scale, of order of 500 MeV. This allows one to construct small parameters, expending in which provides perturbative calculations of hadronic physics. However, in many cases the relevant hadronic scale may not be much smaller than the mass of the b quark. Thus, experimental inputs are required to verify how well these expansions work.

There exist two basic approaches: one approach, chiral symmetry, is derived from the limit of small u, d, and s-quark masses compared to Λ_{QCD} ($m_q \to 0$, where $q = u, d, s$), another approach, heavy quark symmetry (HQS) [41], is constructed from the heavy-quark limit, where c and b-quark masses are larger than Λ_{QCD} ($m_q \to \infty$, where $q = c, b$). Since the u and d-quark masses are small, the SU(2) isospin symmetry between u and d is a very good approximation. The expected corrections to the chiral limit are suppressed by $(m_d - m_u)/\Lambda_{\chi SB}$, where $\Lambda_{\chi SB} \simeq 1\,\mathrm{GeV}$ is the chiral symmetry-breaking scale, and are usually of the order of a few percent at the amplitude level. However, the full SU(3) symmetry is broken by $m_s/\Lambda_{\chi SB}$, and is expected to have typically 20-30% corrections. Deviation from the heavy quark limit can be estimated using heavy-quark effective theory (HQET) [42], which provides a systematic expansion in powers of $\alpha_s(m_Q)$ and $\Lambda_{\mathrm{QCD}}/m_Q$ ($Q = b, c$).The former type of corrections are calculable perturbatively, while the latter ones can be parameterized by a minimal set of hadronic matrix elements that can be extracted from data or estimated using non-perturbative techniques.

Factorization hypothesis plays a special role in the understanding and the predictions of relations between amplitudes of two-body decays of the B mesons. Traditionally, naive factorization assumes that the decay amplitude of $B \to M_1 M_2$ transition can be estimated as a product of two independent currents: one can mediate the $B \to M_1$ transition, and another describes the vacuum $\to M_2$ transition. In other words, the matrix element factorizes as

$$\langle M_1(p'), M_2(q)|j^\mu A_\mu|\overline{B}(p)\rangle = \langle M_1(p')|j^\mu|\overline{B}(p)\rangle \times \langle M_2(q)|A_\mu|0\rangle, \tag{5.1}$$

where p, p', and q are the four-momenta of B, M_1 and M_2, respectively. Most of the calculations based on the factorization approach exploit the Lorentz invariant form factor motivated by HQET to parametrize the hadronic matrix element of the $B \to M_1$ transition. The value of the form factor is given for the minimum or maximum value of the transfered momentum, $q^2 = 0$ or $q^2 = q^2_{max}$, and then extrapolated to an intermediate value using different phenomenological models. The decay constant is involved in the matrix element of the axial-vector or vector current between M_2 and vacuum:

$$\langle P(q)|A_\mu|0\rangle = iq_\mu f_P \tag{5.2}$$

for a pseudoscalar meson P with four-momentum q, and

$$\langle V(q,\epsilon)|V_\mu|0\rangle = \epsilon_\mu M_V f_V \tag{5.3}$$

for a vector meson V with the four-momentum q and the polarization vector ϵ_μ.

Indeed, the "color transparency" can justify factorization [43], only if the meson M_1 that inherits the spectator-quark from the B is heavy, while M_2 is light. In the limit that the mass of the heavy quark is infinitely large, the recoil of the light quark does not change the velocity of the heavy quark. In this picture, the QCD interactions of the light quark are not perturbed by the transition of one heavy quark to another. An important consequence of this theory is that all heavy meson decays are governed by one single form factor. The dominance of the factorizable amplitude can also be confirmed by the QCD limit, where number of colors N_c is very high. One concludes that the non-factorizable corrections are suppressed by a factor of $1/N_c^2$.

Factorization hypothesis is a very powerful phenomenological tool for the quark flavor physics. It provides the framework to understand a large number of two-body decays of the B mesons. Recently, this approach has been expended for several specific cases. For example, the heavy-quark limit allowed calculations of the second order corrections in the loop diagrams for the $B \to D\pi$ transitions [44]. However, several questions still remain. They basically include the study of application field of the factorization and importance of the non-factorizable corrections [45].

5.2 Reconstruction of B mesons

Two different analysis techniques, full reconstruction and partial reconstruction, are used for the B meson reconstruction in *BABAR*. The full reconstruction technique is the standard method which employs the exclusive reconstruction of all decay products. This allows one to obtain a very clean B sample using beam energy constraint which significantly improves the B mass resolution. In the partial reconstruction technique, only one meson from the B decay and the soft (low-momentum) particle from the decay of another non-reconstructed, “missing”, meson are used. Applying kinematic constraints consistent with the signal decay mode, the four-momentum of the “missing” meson is calculated. Signal events are peaked in the m_{miss} distribution at the nominal mass of the non-reconstructed meson. This method eliminates the efficiency loss associated with the missing meson reconstruction, although an ambiguity relative to the B direction increases the combinatorial background.

5.2.1 Full reconstruction

When all decay products of the B meson are reconstructed in the detector, the full reconstuction technique provides a complete information on the kinematic of the original particle, i.e. its momentum $\mathbf{p}_B$ and energy E_B. Two almost uncorrelated kinematic variables, are used for background rejection. The beam-energy substituted mass

$$m_{\text{ES}} = \sqrt{E_{\text{CM}}^2/4 - \mathbf{p}_B^2} \tag{5.4}$$

where p_B is the center-of-mass (CM) B momentum and E_{CM} is the total CM energy of the beams. The signal m_{ES} has a typical resolution of about 2.5-3 MeV, which is about 10 times more accurate than the invariant mass computed by a simple sum of the 4-momenta of the measured decay products. The background shape in m_{ES} is described by an ARGUS function [47]

$$A(y) = \alpha y\sqrt{1-y^2}\exp(s_f(1-y^2)), \tag{5.5}$$

where $y = 2m_{\rm ES}/E_{\rm CM}$. The second discriminative variable is the difference between the CM energy of the reconstructed B meson E_B and the beam energy in the center-of-mass frame $E_{\rm CM}/2$:

$$\Delta E = E_B - E_{\rm CM}/2 \tag{5.6}$$

ΔE is insensitive to the boost and peaks at zero for $e^+e^- \to B\overline{B}$ events. The signal can be fitted with a Gaussian on the top of the background which is usually a linear function.

5.2.2 Partial reconstruction

Examples of the modes, which can be reconstructed partially are $B \to D^{*-}X$, where $X = \pi^+,\ \rho^+,\ a_1,\ D^{(*)},\ D_s^{(*)+}$. Let us consider the method of partial reconstruction based on the $B^0 \to D_s^{(*)+}D^{*-}$ decay mode[1] since it is connected to the analysis being presented in this chapter. In selecting candidates for the decays $B^0 \to D_s^{(*)+}D^{*-}$, no attempt is made to reconstruct the $\overline{D}^0$ from $D^{*-} \to \overline{D}^0\pi_s^-$ decays. A soft pion from D^{*-} decay is combined with the fully reconstructed $D_s^{(*)+}$, where the total $D_s^{(*)+}$ and π_s charge is required to be zero. Given the four-momenta of the $D_s^{(*)+}$ and π_s^-, and assuming they originate from a $B^0 \to D_s^{(*)+}D^{*-}$ decay, energy and momentum conservation yields the following equations:

$$\mathrm{P}_{B^0} = \mathrm{P}_{D_s^{(*)+}} + \mathrm{P}_{D^*} \tag{5.7}$$

$$\mathrm{P}_{B^0} = \mathrm{P}_{D_s^{(*)+}} + \mathrm{P}_{\pi_s} + \mathrm{P}_X \tag{5.8}$$

Here, where P_B, $\mathrm{P}_{D_s^{(*)+}}$, P_{D^*}, P_{π_s} and P_X are the four-momenta of the B^0, $D_s^{(*)+}$, D^*, the soft pion, and the missing particle X, respectively. In the CM frame, the B mesons are monoenergetic. Therefore, assuming that the decay is two-body like as in Equation 5.7, it is straightforward to calculate the angle of the B direction relative to the $D_s^{(*)+}$:

$$\cos\theta_{B^0} = \frac{M_{D^{*-}}^2 - M_{B^0}^2 - M_{D_s^{(*)+}}^2 + E_{\rm CM}E_{D_s^{(*)+}}}{2p_{B^0}p_{D_s^{(*)+}}}, \tag{5.9}$$

where M_x is the nominal mass of particle x [52], $E_{D_s^{(*)+}}$ and $\mathbf{p}_{D_s^{(*)+}}$ are the measured CM energy and momentum of the $D_s^{(*)+}$ meson, and $p_{B^0} = \sqrt{E_{\rm CM}^2/4 - M_{B^0}^2}$. Thus, the four-momentum of the B^0 can be calculated up to an unknown azimuthal angle ϕ around the $D_s^{(*)+}$ flight direction, as shown in Figure 5.1. This calculation uses the constraint of the known CM energy and the masses of the B^0 and D^{*-} mesons.

---

[1] Reference to a specific decay channel or state also implies the charge conjugate decay or state. The notation $D_s^{(*)+}$ refers to either D_s^+ or D_s^{*+}.

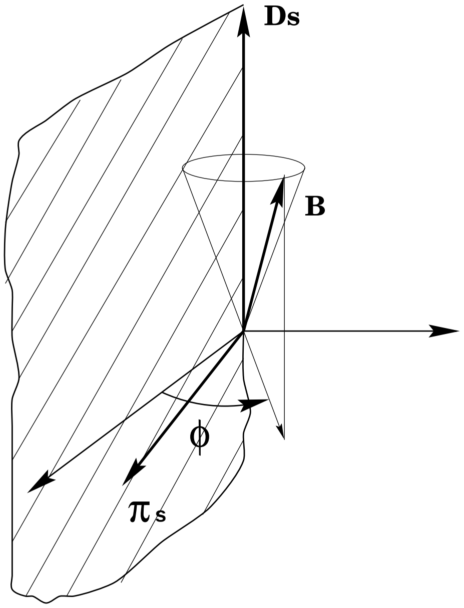

Figure 5.1: *Definition of the arbitrary angle ϕ.*

At this point, the angle ϕ around the $D_s^{(*)+}$ is degenerated as we have no means of determining it without any further assumption. A possibility is to postulate $X = D^0$. In that case, one can solve the Equations 5.7, 5.8 and extract the angle ϕ with a 4-fold ambiguity. However, it was decided not to do so as one prefers to deduce the ϕ-dependent missing mass using $\cos\theta_{B^0}$ and the measured momenta of the $D_s^{(*)+}$ and soft pion as

$$m_X \equiv \sqrt{|\mathrm{P}_X(\phi)|^2} = \sqrt{(\mathrm{P}_{B^0} - \mathrm{P}_{D_s^{(*)+}} - \mathrm{P}_{\pi_s})^2}\ , \tag{5.10}$$

The missing mass should be the D^0 mass if the $B^0 \to D_s^{(*)+} D^{*-}$ decay occurs. This variable is used to determine the background by studying both side bands and wrong sign combination as well as Monte Carlo as will be shown later. However, to derive the missing mass m_X, one needs to fix the angle ϕ. In this analysis the missing mass is defined with an arbitrary choice for the angle ϕ, such that the B^0 momentum $\mathbf{p}_B$ lies in the same plane as $\mathbf{p}_\pi$ and $\mathbf{p}_{D_s^{(*)+}}$ momenta. It is important to note that signal discrimination against background is independent of the choice of the value of ϕ.

5.3 Study of $B^0 \to D_s^{(*)+} D^{*-}$ decays

It has been verified experimentally that the factorization hypothesis describes well the semileptonic decays and non leptonic modes of the B mesons with relatively low q^2. For example, $B \to D^*\pi$, $D^*\rho$ branching fractions and polarization for $D^*\rho$ are well described by this approach. The $B^0 \to D_s^{(*)+} D^{*-}$ decays can only occur via $c\bar{s}$ quarks pair coupling with a W boson emitted externally in $b \to cW$ transition. Thus, these decay modes are well suited to test factorization for final states with two heavy quarks. The factorization assumption in these decays would also allow further extraction of the values of the decay constants $f_{D_s^{(*)}}$. Thus, precise knowledge of the $B^0 \to D_s^{(*)+} D^{*-}$ branching fractions and the polarization in decays of B mesons to vector-vector final states $B^0 \to D_s^{*+} D^{*-}$ provide a test of the details of the factorization assumption in the relatively high q^2 regime [46].

Reported measurements of the $B^0 \to D_s^{(*)+} D^{*-}$ branching fractions and polarization in the decay $B^0 \to D_s^{*+} D^{*-}$ exploit the method of partial reconstruction. The data used in this analysis correspond to an integrated luminosity of 20.8 fb^{-1} recorded by *BABAR* in 1999 and 2000 at the $\Upsilon(4S)$ resonance. This data set corresponds to about 22.7 million produced $B\overline{B}$ pairs.

5.3.1 Event selection

For each event, the ratio of the second to the zeroth order Fox-Wolfram moment [48], using all charged tracks and neutral clusters in the event, is computed. This ratio is required to be less than 0.35 in order to suppress continuum $e^+e^- \to q\overline{q}$ events, where $q = u, d, s, c$.

We reconstruct D_s^+ mesons in the decay modes $D_s^+ \to \phi\pi^+$, $D_s^+ \to \overline{K}^{*0} K^+$ and $D_s^+ \to K_S^0 K^+$, with subsequent decays $\phi \to K^+K^-$, $\overline{K}^{*0} \to K^-\pi^+$ and $K_S^0 \to \pi^+\pi^-$. These modes were selected since they offer the best combination of branching fraction, detection efficiency and signal-to-background ratio. The charged tracks are required to originate from the interaction point within ±10 cm along the beam direction and ±1.5 cm in the transverse plane, and leave at least 12 hits in the DCH.

Kaons are identified using dE/dx information from the SVT and DCH, and the Cherenkov angle and the number of photons measured with the DIRC. For each detector component $d = \{\text{SVT, DCH, DIRC}\}$, a likelihood L_d^K (L_d^π) is calculated given the kaon (pion) mass hypothesis. A charged particle is classified as a "loose" kaon if it satisfies $L_d^K / L_d^\pi > 1$ for at least one of the detector components. A "tight" kaon classification is made if the condition $\prod_d L_d^K / L_d^\pi > 1$ is satisfied.

Three charged tracks consistent with originating from a common vertex are combined to form a D_s^+ candidate. In the case of the decay $D_s^+ \to \phi\pi^+$, two oppositely charged tracks must be identified as kaons with the loose criterion, with at least one of them also satisfying the tight criterion. No identification criteria are applied to the pion from the D_s^+ decay. The reconstructed invariant mass of the K^+K^- candidates must be within 8 MeV/c^2 of the nominal ϕ mass [13]. In the decay $D_s^+ \to \phi\pi^+$, the ϕ meson is polarized longitudinally, resulting in the kaons having a $\cos^2\theta_H$ distribution, where θ_H is the angle between the K^+ and D_s^+ in the ϕ rest frame. It is required that $|\cos\theta_H| > 0.3$, which retains 97% of the signal while rejecting about 30% of the background.

In the reconstruction of the $D_s^+ \to \overline{K}^{*0} K^+$ mode, the $K^-\pi^+$ invariant mass is required to be within $65\,\mathrm{MeV}/c^2$ of the nominal $\overline{K}^{*0}$ mass [13]. This wider window leads to a fraction of combinatorial background much larger than in the $D_s^+ \to \phi\pi^+$ mode. To reduce this background, as the $\overline{K}^{*0}$ is also polarized longitudinally, we require $|\cos\theta_H| > 0.5$. In addition, substantial background arises from the decays $D^+ \to \overline{K}^{*0}\pi^+$ and $D^+ \to \overline{K}^0\pi^+$, which tends to peak around the nominal D_s^+ mass. This background is suppressed by requiring that the kaon daughter of the $\overline{K}^{*0}$ satisfy the loose kaon identification criterion, and that the other kaon satisfy the tight criterion.

For the decay mode $D_s^+ \to K_S^0 K^+$, the $\pi^+\pi^-$ invariant mass must be within $15\,\mathrm{MeV}/c^2$ of the nominal K_S^0 mass, and the charged kaon is identified using the tight criterion. To improve the purity of the K_S^0 sample, the angle α between the K_S^0 momentum and the flight direction defined by its decay vertex and the primary vertex of the event is determined. It is required that $\cos\alpha > 0.98$ to reject the combinatorial background.

The invariant mass M_{D_s} of all D_s^+ candidates is required to be within three standard deviations (σ_{D_s}) of the signal distribution peak $M_{D_s}^{\mathrm{peak}}$ seen in the data. D_s^+ candidates satisfying all the above selection criteria are combined with photon candidates to form $D_s^{*+} \to D_s^+\gamma$ candidates. The candidate photons are required to satisfy $E_\gamma > 50\,\mathrm{MeV}$, where E_γ is the photon energy in the laboratory frame, and $E_\gamma^* > 110\,\mathrm{MeV}$, where E_γ^* is the photon energy in the CM frame. When the photon candidate is combined with any other photon candidate in the event, the pair must not form a good π^0 candidate, defined by a total CM energy $E_{\gamma\gamma}^* > 200\,\mathrm{MeV}$ and an invariant mass $115 < M_{\gamma\gamma} < 155\,\mathrm{MeV}/c^2$.

5.3.2 B meson reconstruction

D_s^{*+} candidates used in the partial reconstruction of the decay $B^0 \to D_s^{*+}D^{*-}$ must satisfy $|\Delta M - \Delta M^{\mathrm{peak}}| < 2.5\,\sigma_{\Delta M}$, where ΔM^{peak} is the peak of the signal $\Delta M = M(D_s^+\gamma) - M(D_s^+)$ distribution observed in the data. The CM momentum of the $D_s^{(*)+}$ candidate is required to be greater than $1.5\,\mathrm{GeV}/c$. $D_s^{(*)+}$ candidates satisfying these criteria, in addition to those described in Section 5.3.1, are then combined with π^- candidates to form partially reconstructed $B^0 \to D_s^{(*)+}D^{*-}$ candidates. Since the transverse momentum of the pion in signal events is less than $210\,\mathrm{MeV}/c$, no specific criteria of the number of DCH hits are required for the pion candidate.

Due to the high combinatorial background in the ΔM distribution, more than one $D_s^{*+}\pi^-$ candidate pair per event is found in 20% of the events. To select the best candidate in the event, the following χ^2

$$\chi^2 = \left(\frac{M_i - M_i^{\mathrm{peak}}}{\sigma_i}\right)^2 + \left(\frac{M_{D_s} - M_{D_s}^{\mathrm{peak}}}{\sigma_{D_s}}\right)^2 + \left(\frac{\Delta M - \Delta M^{\mathrm{peak}}}{\sigma_{\Delta m}}\right)^2 \tag{5.11}$$

is calculated for each D_s^{*+} candidate, where M_i is the invariant mass of the intermediate ϕ, K^{*0}, or K_S^0 candidate, depending on the D_s^+ decay mode, M_i^{peak} is the

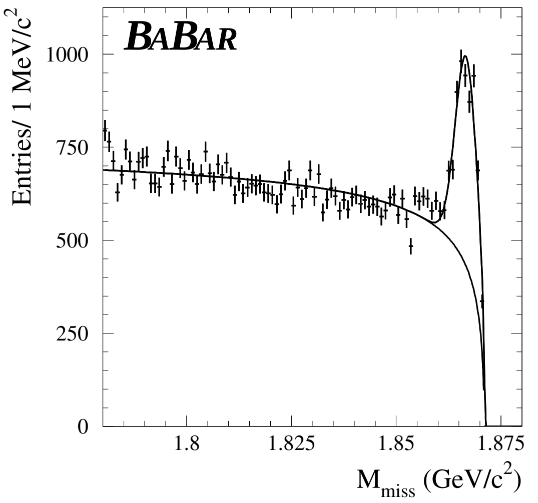

Figure 5.2: $D_s^+\pi^-$ *missing mass distributions of data events. All the* D_s^+ *decay modes have been combined in this plot. The curves show the result of the fit (see text) indicating the signal and background distributions.*

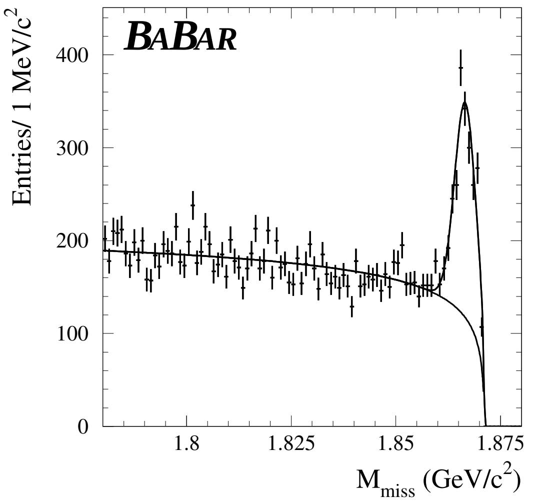

Figure 5.3: $D_s^{*+}\pi^-$ *missing mass distributions of data events. All the* D_s^+ *decay modes have been combined in this plot. The curves show the result of the fit (see text) indicating the signal and background distributions.*

corresponding peak of the signal M_i distribution, and σ_i is its width. Only the candidate with the smallest value of χ^2 in the event is accepted.

The missing mass distributions of partially reconstructed $B^0 \to D_s^{(*)+}D^{*-}$ decays are shown in Figures 5.2 and 5.3. A clear signal peak is observed. We perform a binned maximum likelihood fit of these distributions. The fit function is the sum of a Gaussian distribution and a background function f_B given by

$$f_B(m_{\text{miss}}) = \frac{C_1\left(M_0-m_{\text{miss}}\right)^{C_2}}{C_3+\left(M_0-m_{\text{miss}}\right)^{C_2}}\ , \tag{5.12}$$

where C_i are parameters determined by the fit, and $M_0 = M_{D^*} - M_\pi = 1.871\,\text{GeV}/c^2$ is the kinematic end point. The fits find 3704±232 and 1493±95 peaking events under the Gaussian peak in the sum of the $D_s^+\pi^-$ and $D_s^{*+}\pi^-$ plots, respectively. However, due to the presence of peaking backgrounds, discussed below, further calculation is needed in order to extract the signal yields and the branching fractions.

5.3.3 Background study

The missing mass distribution of the backgrounds has been studied in great details with a Monte Carlo simulation. It includes both $B\overline{B}$ and $q\bar{q}$ continuum events. Two kinds of backgrounds are considered: "peaking" background is enhanced under the signal peak at the high end of the missing mass spectrum, and "non-peaking" background has a more uniform missing mass distribution. There are two sources of the peaking background:

- *Cross Feed (CF):* If the soft photon from $D_s^{*+} \to D_s^+ \gamma$ decay is not reconstructed, $B^0 \to D_s^{*+} D^{*-}$ decays may lead to an enhancement under the signal peak of the $D_s^+ \pi^-$ missing mass spectrum. Similarly, the $B^0 \to D_s^+ D^{*-}$ decays may lead to a peaking enhancement in the $D_s^{*+} \pi^-$ m_{miss} spectrum, due to the combination of a D_s^+ with a random photon.
- *Self-Cross Feed (SCF):* This is due to true $B^0 \to D_s^{*+} D^{*-}$ decays in which the D_s^+ is correctly reconstructed, but combined with a random photon to produce the wrong D_s^{*+} candidate, resulting in a peaking enhancement in the $D_s^{*+} \pi^-$ spectrum.

We compute the reconstruction efficiency of correctly reconstructed signal $B^0 \to D_s^{(*)+} D^{*-}$ decays, as well as cross feed and self-cross feed, for events in the signal region $m_{\mathrm{miss}} > 1.86\,\mathrm{GeV}/c^2$.

In addition to the above backgrounds, we also considered a possible contribution from the charged and neutral B decays $B \to D_s^{(*)+} \overline{D}^{**}$. These backgrounds were simulated with four $\overline{D}^{**}$ states: $\overline{D}_0^*(j = 1/2)$, $\overline{D}_1(2420)$, $\overline{D}_1(j = 1/2)$ and $\overline{D}_2^*(2460)$, and their contribution has been determined to be negligible, due mainly to the $D_s^{(*)+}$ CM momentum cut. Figure 5.4 shows a comparison of the missing mass distributions in data and Monte Carlo events.

5.3.4 Results

The signal yields in the $D_s^+ \pi^-$ and $D_s^{*+} \pi^-$ m_{miss} peaks are obtained from the fits described above. In calculating the branching fractions from these yields, one has to take into account the fact that the peaks consist not only of correctly reconstructed signal, but also of cross feed and self-cross feed. This is done by inverting the 2 × 2 efficiency matrix. Its diagonal elements correspond to the sum of signal and self-cross feed efficiencies, while off-diagonal terms are the cross-feed efficiencies.. The efficiencies corresponding to transverse and longitudinal polarization of $B^0 \to D_s^{*+} D^{*-}$ have been weighted according to the measured polarization as described below. With this procedure, the $B^0 \to D_s^{(*)+} D^{*-}$ branching fractions are determined to be

$$\begin{aligned} \mathcal{B}(B^0 \to D_s^+ D^{*-}) &= (1.03 \pm 0.14 \pm 0.13 \pm 0.26)\% , \\ \mathcal{B}(B^0 \to D_s^{*+} D^{*-}) &= (1.97 \pm 0.15 \pm 0.30 \pm 0.49)\% \end{aligned} \tag{5.13}$$

and their sum is

$$\Sigma\mathcal{B}(B^0 \to D_s^{(*)+} D^{*-}) = (3.00 \pm 0.19 \pm 0.39 \pm 0.75)\%, \tag{5.14}$$

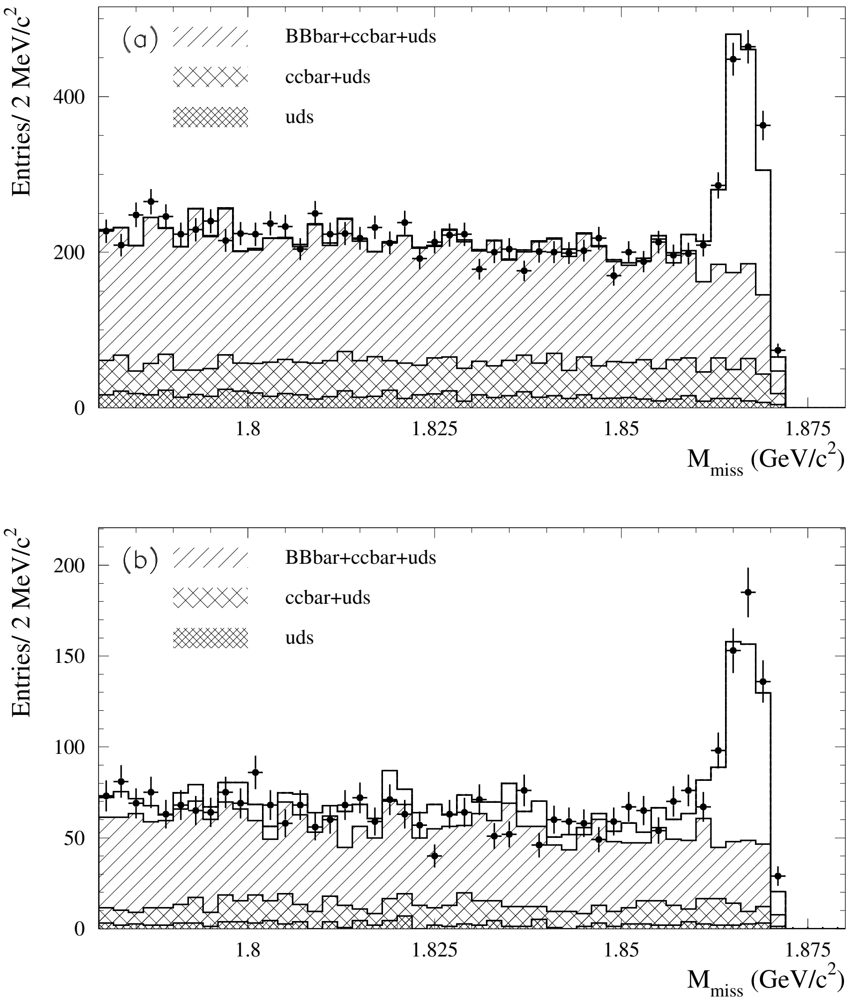

Figure 5.4: *The missing mass distribution of (a) $D_s^+\pi^-$ and (b) $D_s^{*+}\pi^-$ combinations for data (data points) and Monte Carlo (histogram). The contributions from the $B\bar{B}$, $c\bar{c}$ and uds are shown separately. The CF and SCF backgrounds are included in the total histogram, not in the hatched $B\overline{B}$ histogram.*

where the first error is statistical, the second is the systematic error from all sources other than the uncertainty in the $D_s^+ \to \phi\pi^+$ branching fraction, and the third error, which is dominant, is due the uncertainty in the $D_s^+ \to \phi\pi^+$ branching fraction $\mathcal{B}(D_s^+ \to \phi\pi^+) = (3.6 \pm 0.9)\%$ [13].

The measurement of the fraction of the longitudinal polarization Γ_L/Γ in the $B^0 \to D_s^{*+}D^{*-}$ decay mode is performed using the events reconstructed in the signal region ($M_{miss} > 1.86\,\mathrm{GeV}/c^2$). To reduce the systematic error due to large backgrounds, the polarization measurement is done with only the channel $D_s^+ \to \phi\pi^+$, which has the best signal to background ratio. Figure 5.5 shows the missing mass distribution for such a decay. Two angles are used: the helicity angle θ_γ between the D^{*-} and the soft photon direction in the D_s^{*+} rest frame, and the helicity angle θ_π between the D_s^{*+} and the soft pion direction in the D^{*-} rest frame. Since the B meson is not fully reconstructed, we compute θ_γ and θ_π by constraining m_{miss} to the nominal D^0 mass [13] to obtain a unique kinematical solution for the azimuth ϕ.

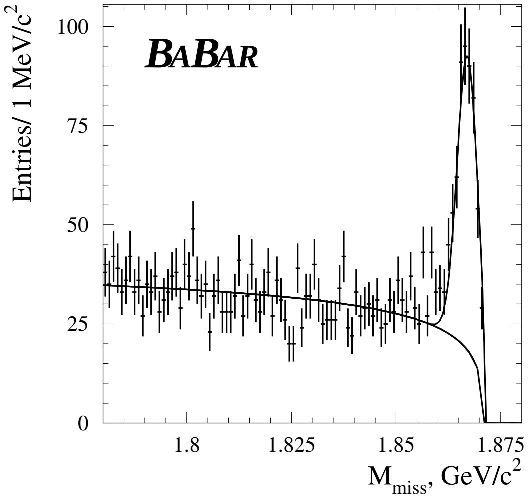

Figure 5.5: *$D_s^{*+}\pi^-$ missing mass distribution of data events. Only D_s^+ decays into $\phi\pi^+$ final state are included in the polarization measurement. The curves show the result of the fit (see text) indicating the signal and background distributions.*

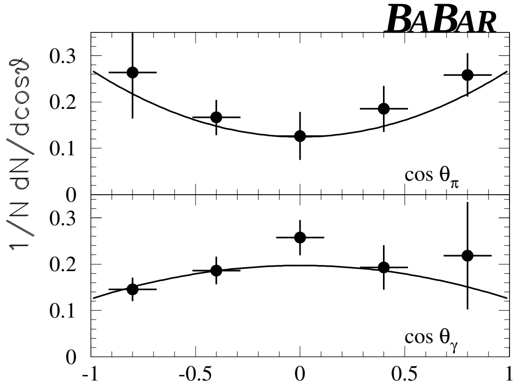

Figure 5.6: *Projections of the number of background-subtracted data events on the $\cos\theta_\gamma$ and $\cos\theta_\pi$ axes. The result of the two-dimensional fit is overlaid.*

The two dimensional distribution $(\cos\theta_\gamma,\ \cos\theta_\pi)$ is divided in five bins in each dimension. The combinatorial background, as well as the cross feed and the self-cross feed obtained using the Monte Carlo simulation, are subtracted. The resulting signal distribution is corrected bin-by-bin for the detector efficiency, which is obtained from the simulation. Finally, a two-dimensional binned minimum-χ^2 fit is performed on the efficiency-corrected signal distribution using the following function:

$$\frac{d^2\Gamma}{d\cos\theta_\pi\ d\cos\theta_\gamma} \propto \frac{\Gamma_L}{\Gamma}\cos^2\theta_\pi\sin^2\theta_\gamma + (1 - \frac{\Gamma_L}{\Gamma})\sin^2\theta_\pi\frac{1+\cos^2\theta_\gamma}{4}. \qquad (5.15)$$

The resulting fit has a χ^2 of 23.1 for 25 bins with two floating parameters (Γ_L/Γ and total normalization). Figure 5.6 shows the data and the result of the fit projected on the $\cos\theta_\gamma$ and $\cos\theta_\pi$ axes.

From the fit, the fraction of a longitudinal polarization is determined to be

$$\Gamma_L/\Gamma = (51.9 \pm 5.0 \pm 2.8)\%, \tag{5.16}$$

where the first error is statistical and the second is systematic. The polarization measurement is consistent with theoretical prediction assuming factorization ranging from 50 to 55% [49]. The results listed above are also in a good agreement with previous experimental results [50, 51].

5.3.5 Systematics

Table 5.1: *Sources of systematic error (%) for $B^0 \to D_s^{(*)+} D^{*-}$ branching fractions and $B^0 \to D_s^{*+} D^{*-}$ polarization. The uncertainty in the $D_s^+ \to \phi\pi^+$ branching fraction is not included in this table.*

Source	$B^0 \to D_s^+ D^{*-}$	$B^0 \to D_s^{*+} D^{*-}$	$\sigma(\Gamma_L/\Gamma)$
Background subtraction	2.7	5.9	0.5
Monte Carlo statistics	4.2	6.0	2.7
Polarization uncertainty	0.8	0.5	-
Cross Feed	3.2	2.4	-
$\mathrm{N}_{B\overline{B}}$	1.6	1.6	-
$\mathcal{B}(\phi \to K^+K^-)$	1.6	1.6	-
Particle identification	1.0	1.0	0.1
Tracking efficiency	3.6	3.6	0.5
Soft pion efficiency	2.0	2.0	0.2
Relative branching fractions	10.2	10.2	-
$\mathcal{B}(D_s^{*+} \to D_s^+\gamma)$	-	2.7	-
Photon efficiency	-	1.3	0.1
π^0 veto	-	2.7	0.3
Total systematic error	13.1	15.1	2.8

The various contributions to the systematic errors of the branching fractions and polarization measurement are summarized in Table 5.1. The dominant systematic error is due to the uncertainty in our knowledge of the three D_s^+ decay branching fractions. To evaluate the uncertainty due to the background subtraction, the signal yield is determined in an alternative way, by counting the number of events in the histogram after a bin-by-bin subtraction of the background, determined from the Monte Carlo simulation. The difference of the signal yields is taken as a systematic error. This also accounts for the systematic error due to a possible deviation of the signal shape from a Gaussian.

The Monte Carlo statistical errors in the determination of the signal and the cross feed efficiencies are propagated to the systematic error. The uncertainty in the calculation of the $B^0 \to D_s^{*+} D^{*-}$ polarization is propagated to the branching fraction systematic error. The systematic error due to charged particle reconstruction efficiency error is 1.2% times the number of charged particles in the decay. An additional error of 1.6% is added in quadrature to account for the uncertainty in the reconstruction efficiency of the soft pion. This error results as 2% in total error.

The systematic error due to the excluding π^0 overlap (π^0 veto) requirement was studied by measuring the relative yield of inclusive D_s^{*+} production in data and Monte Carlo events. To evaluate this error, the selection with and without the π^0 veto was applied for the final photon from $D_s^{*+} \to D_s^+\gamma$ decay.

For the polarization measurement, the level of the various backgrounds depends on the charged, neutral and particle identification efficiencies. The fit was repeated varying the background according to the errors in these efficiencies, and the resulting variations in Γ_L/Γ were taken as the associated systematic error.

To check that the simulation accurately reproduces the background $m_{\rm miss}$ distributions in the data, a systematic data-Monte Carlo comparison is made in control samples containing no signal events. These samples are events with $1.78 < m_{\rm miss} < 1.85\,{\rm GeV}/c^2$; events in the D_s^+ sideband $1.89 < M_{D_s} < 1.95\,{\rm GeV}/c^2$ or $1.985 < M_{D_s} < 2.05\,{\rm GeV}/c^2$; events in the D_s^{*+} sideband $170 < \Delta M < 300\,{\rm MeV}/c^2$; wrong sign $D_s^{(*)+}\pi^+$ combinations in either the M_{D_s} and ΔM sidebands or signal regions; and candidates in which $m_{\rm miss}$ was calculated using the negative of the CM $D_s^{(*)+}$ momentum $p^*_{D_s^{(*)+}}$. The difference between the data and the Monte Carlo simulation of these control samples is consistent with zero withing statistical errors.

5.4 Measurement of $\mathcal{B}(D_s^+ \to \phi\pi^+)$

As it was demonstrated above, measurements of $\mathcal{B}(B^0 \to D_s^{(*)+} D^{*-})$ are limited by the uncertainties on the D_s^+ partial decay rates. A substantial improvement can therefore be obtained using a partial reconstruction technique where the D_s^+ is not explicitly reconstructed. Partial reconstruction allows an unbiased measurement of the $D_s^+ \to \phi\pi^+$ branching fraction, which has important implications for a wide range of $D_s^{(*)+}$ and B physics, as most of the D_s^+ decay branching fractions are normalized to it [52]. As an example, an improved measurement of $\mathcal{B}(D_s^+ \to \phi\pi^+)$ would reduce the experimental uncertainty on the constraint on the Unitary Triangle parameter $\sin(2\beta+\gamma)$ from the measurement of the *CP* violating asymmetry in $B^0 \to D^{(*)\mp}\pi^{\pm}$ decays (see Section 6.2.8).

Indeed, the $B^0 \to D_s^{*+}D^{*-} \to (D_s^+\gamma)(\overline{D}^0\pi^-)$ decay can be reconstructed in two different ways. The first method implies a combination of the fully reconstructed D^{*-} decay with the photon from the $D_s^{*+} \to D_s^+\gamma$ decay, without explicit D_s^+ reconstruction. The measured event yield which is independent on the $D_s^+ \to \phi\pi^+$ branching fraction, allows us to compute $\mathcal{B}(B^0 \to D_s^{*+}D^{*-})$. The second method uses a combination of the fully reconstructed D_s^{*+} with the soft pion from $D^{*-} \to \overline{D}^0\pi^-$ decay, without explicit $\overline{D}^0$ reconstruction. From the measured event yield the product of $\mathcal{B}(B^0 \to D_s^{*+}D^{*-})$ and $\mathcal{B}(D_s^+ \to \phi\pi^+)$ can be extracted. First, improved measurement of $D_s^+ \to \phi\pi^+$ branching fraction exploits a combination of these two methods of the partial reconstruction. Preliminary result of this measurement has been reported on LP 2003 conference in Fermilab [53]. This result has been obtained based on about 20 fb^{-1} of integrated luminosity data set.

Further improvement has been achieved by increasing the analyzed data sample about a factor six. Figure 5.7 shows the missing mass distribution recoiling against the $D^{*-}\gamma$ system based on 123 million $B\overline{B}$ events, assuming that a $B^0 \to D^{*-}\gamma X$ decay took place. To extract the signal yield an unbinned maximum-likelihood fit to the m_{miss} distribution is applied. The signal peak is well modeled by a Gaussian, while the combinatorial background is described with the threshold function given in Equation 5.12. From the measured event yield, the $B^0 \to D_s^{*+}D^{*-}$ branching fraction is computed to be [54]

$$\mathcal{B}(B^0 \to D_s^{*+}D^{*-}) = (1.88 \pm 0.09 \pm 0.17)\%, \tag{5.17}$$

where the first uncertainty is statistical and the second is systematic. This result is independent of the partial decay rates of the D_s^+ mesons and consistent with Equation 5.13. Although, it reduces the total uncertainty by a factor of about three.

Full reconstruction of the $B^0 \to D_s^{*+}D^{*-}$ decay via $D_s^+ \to \phi\pi^+$ ($\phi \to K^+K^-$) measures the branching fraction product $\mathcal{B}(B^0 \to D_s^{*+}D^{*-}) \times \mathcal{B}(D_s^+ \to \phi\pi^+)$. The number of fully reconstructed B^0 candidates is obtained from a fit to the m_{ES} spectrum. Fit is performed with the sum of a Crystal Ball [55] function, and a threshold ARGUS function [47]; the latter accounts for the combinatorial background. Figure 5.8 shows the fit of the fully reconstructed data sample. Combination of the yields of two methods results:

$$\mathcal{B}(D_s^+ \to \phi\pi^+) = (4.81 \pm 0.52 \pm 0.38)\%, \tag{5.18}$$

where the first uncertainty is statistical and the second is systematic. The main source of the systematic uncertainty is due to modeling of the signal and background shapes. This result represents an improvement by about a factor of two over previous measurements [52, 56].

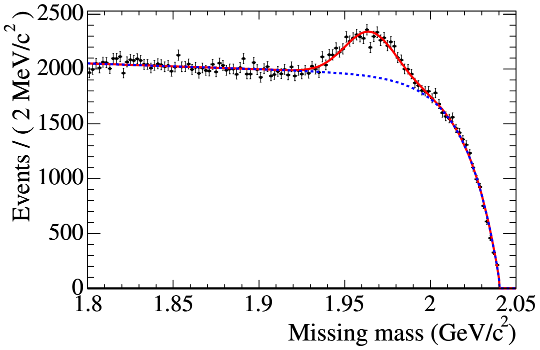

Figure 5.7: *$D^{*-}\pi^+$ missing mass distributions of data events. The curves show the result of the fit (see text) indicating the signal and background distributions.*

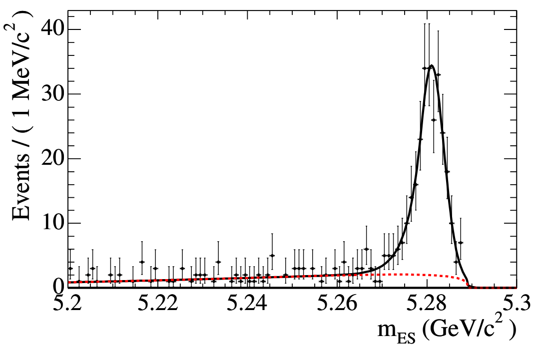

Figure 5.8: *Fit (solid line) to the measured m_{ES} distribution. The background component is shown as the dashed line.*

5.5 Conclusion

The first *BABAR* data allowed one to develop a dedicated technique of partial reconstruction for many decay channels. Although not all B decay channels can be studied by this method, an unique opportunity of precise measurements of important quantities occurs due to high selection efficiency enhanced by non reconstructed meson. Asides branching fractions, such fundamental quantities as the B^0 lifetime τ_{B^0} and the $B^0 - \overline{B}^0$ mixing frequency Δm_d were measured [57, 58].

Bunches of unique measurements have been performed with the partially reconstructed $\overline{B}^0 \to D^{*+} l^- \bar{\nu}_l$ decay mode. The first direct measurement of the branching fraction f_{00} for $\Upsilon(4S) \to B^0 \overline{B}^0$ reported in Ref. [59]

$$f_{00} = 0.487 \pm 0.010(\mathrm{stat}) \pm 0.008(\mathrm{syst}) \tag{5.19}$$

does not depend on the branching fractions of $\overline{B}^0 \to D^{*+} l^- \bar{\nu}_l$ and $D^{*+} \to D^0 \pi^+$, on the ratio of the charged and neutral B meson lifetimes, nor on the assumption of isospin symmetry. The most precise measurement of τ_{B^0} and Δm_d exploits the partial reconstruction of $\overline{B}^0 \to D^{*+} l^- \bar{\nu}_l$ decays. With a sample of about 50 000 lepton-tagged signal events the following results are obtained [58]:

$$\begin{aligned} \tau_{B^0} &= (1.504 \pm 0.013 \ (\mathrm{stat}) \ {}^{+0.018}_{-0.013} \ (\mathrm{syst})) \ \mathrm{ps}, \\ \Delta m_d &= (0.511 \pm 0.007 \ (\mathrm{stat}) \ {}^{+0.007}_{-0.006} \ (\mathrm{syst})) \ \mathrm{ps}^{-1}. \end{aligned} \tag{5.20}$$

Dedicated studies using a partial reconstruction technique with the *BABAR* detector allowed a reliable application of this method for precision measurements of *CP* violation which are discussed in the next chapter.

Chapter 6

CP violation in $B^0 \to D^{*\mp}\pi^{\pm}$ decays

This chapter describes my activity in the analysis of *BABAR* data since 2003. At that time, *BABAR* had recorded approximately 80 fb^{-1} of integrated luminosity, and therefore, a measurement of small *CP* violation effects become feasible. Previous thorough investigations of the method of partial reconstruction for the B decays allowed us to apply reliably this method for the challenges of time-dependent *CP* violation measurements in $B^0 \to D^{*\mp}\pi^{\pm}$ channel.

The first measurement of *CP* asymmetry in the $B^0 \to D^{*\mp}\pi^{\pm}$ decays has been presented at the EPS 2003 conference in Aachen and, then, published in "Physical Review Letter" [60]. As a next step of this program, an updated result using 232 millions of $B\overline{B}$ events recorded by the *BABAR* experiment, has been published in "Physical Review D" [61]. This work has been performed in collaboration with Marco Zito, Marie Legendre and Abi Soffer. I have also presented the complete review and perspectives of $\sin(2\beta+\gamma)$ measurement for the CKM workshops [62, 63]. The publications and workshop proceedings are presented in Appendix E.

In the first part of this chapter I briefly summarize the experimental methods that allow the measurement of the UT angle γ. The main section presents the analysis highlights and the results of *CP* violation measurement in the $B^0 \to D^{*\mp}\pi^{\pm}$ decays with a partial reconstruction technique. I also describe the frequentistic method used to constrain $\sin(2\beta+\gamma)$. Finally, the current experimental status and the future perspectives of $\sin(2\beta+\gamma)$ measurement are discussed.

6.1 Measurements of CKM angle γ

Measuring the angles of the Cabibbo-Kobayashi-Maskawa (CKM) unitarity triangle [9] allow us to overconstrain this triangle and to test the Standard Model interpretation of *CP* violation in the quark sector. A crucial step in this scientific program is the measurement of the angle $\gamma = \arg\left(-V_{ud}V_{ub}^{*}/V_{cd}V_{cb}^{*}\right)$ of the unitarity triangle (UT) related to the CKM matrix. The experimentalists concentrate on two major methods to measure the UT angle γ. One method exploits the time-dependent analysis of the $B^0 \to D^{(*)\mp}\pi^\pm$ decays. Another method utilizes the measurement of direct *CP* violation in $B^+ \to DK^+$, where the neutral D can be both D^0 and $\overline{D}^0$ (and where D^0 also stands for D^{*0}).

The neutral B meson decay modes $B^0 \to D^{*\mp}h^\pm$, where h is a light hadron (π, ρ, a_1), have been proposed for use in measurements of $\sin(2\beta+\gamma)$ [64], where $\beta = \arg\left(-V_{cd}V_{cb}^*/V_{td}V_{tb}^*\right)$. Indeed, the decay $B^0 \to D^{(*)\mp}\pi^\pm$ can proceed either via the doubly-Cabibbo-suppressed $b \to u\bar{c}d$ (A_u) transition, or by B^0–$\overline{B}^0$ mixing followed by the Cabibbo-favored $\bar{b} \to \bar{c}u\bar{d}$ (A_c) transition, as shown in Figure 6.1. The interference of these two amplitudes results in sensitivity to $\sin(2\beta+\gamma)$, and the size of the interference effect depends on the ratio of the magnitudes of the two amplitudes (usually denoted $r_{D^{(*)}\pi}$). Since A_u is doubly CKM-suppressed with respect to A_c, one expects $r_{D^{(*)}\pi}$ to be small of order 2%. Although the $D^{(*)\mp}\pi^\pm$ final states are abundant, the smallness of $r_{D^{(*)}\pi}$ makes the *CP* violation effect hard to measure and, since it must be extracted from a large number of events, sensitive to systematic errors. Furthermore, while there are two observables for each final state, there are also two hadronic parameters ($r_{D^{(*)}\pi}$ and $\delta_{D^{(*)}\pi}$, the strong phase difference between the decay amplitudes), and therefore it is difficult to cleanly extract the weak phase information, although approaches based on, e.g. SU(3) symmetry exist.

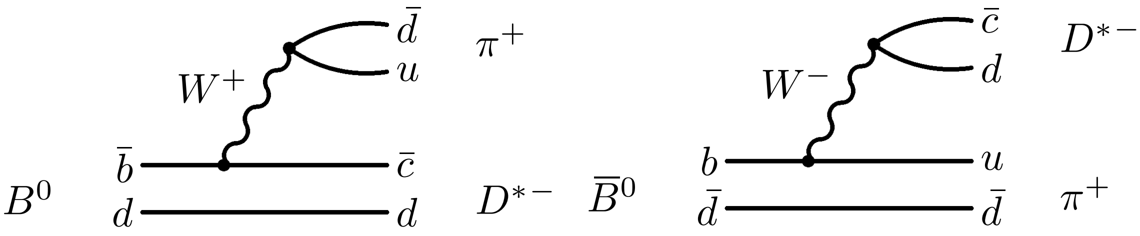

Figure 6.1: *Feynman diagrams for the Cabibbo-favored decay $B^0 \to D^{*-}\pi^+$ (left), corresponding to the decay amplitude A_c, and the Cabibbo-suppressed decay $\overline{B}^0 \to D^{*-}\pi^+$ (right), whose amplitude is A_u.*

The decays $B \to D^{(*)}K^{(*)}$ provide the cleanest method to determine γ. The method employs the interference between $b \to c\bar{u}s$ and $b \to u\bar{c}s$ when the final state is accessible to both D^0 and $\overline{D}^0$ mesons. The theoretical uncertainty is completely negligible, and effects due to mixing and *CP* violation in the neutral D sector can be taken into account. There are important hadronic parameters: the ratio of the magnitudes of the two amplitudes and the strong phase difference between them (these are usually denoted r_B and δ_B), that can be extracted from the data. The B decay modes which have been exploited up to date are $B^\pm \to DK^\pm$, $D^*K^\pm$ and $DK^{*\pm}$, and in each case the D decay modes to *CP* eigenstates (principally K^+K^- for CP-even and $K_S\pi^0$ for CP-odd) [65] (GLW), doubly-Cabibbo-suppressed final states $(K^\mp\pi^\pm)$ [66] (ADS), and multibody final states $(K_S^0\pi^+\pi^-)$ [67] (GGSZ) can be used to constraint the CKM angle γ. One of the major developments of the B factories over the past few years has been the use of the multibody decay $D \to K^0_S\pi^+\pi^-$. The rich interference pattern across the Dalitz plot results in regions which are highly sensitive to γ; in addition this mode is reasonably clean experimentally, due to its large product branching fraction and clean signal. However, in order to perform an unbinned fit it is necessary to make an assumption about the strong phase variation across the Dalitz plot which results in model uncertainty, currently estimated to be $\sim 10^\circ$ on γ. To reduce this, additional studies of the Dalitz plot structure are necessary, and the results using D mesons coherently produced in $\psi(3770) \to D\bar{D}$ at charm-tau factories play a particularly crucial role.

6.2 Measurement of $\sin(2\beta+\gamma)$ with $B^0 \to D^{*\mp}\pi^\pm$

The data sample used in this analysis consists of 211 fb^{-1} collected on the Υ(4S) resonance (on-resonance sample), and 21 fb^{-1} collected at an e^+e^- center-of-mass (CM) energy approximately 40 MeV below the resonance peak (off-resonance sample).

6.2.1 $B^0 \to D^{*\mp}\pi^\pm$ decays

The time-dependent decay rates for $B \to D^{*\pm}\pi^\mp$ decays can be written as

$$\begin{aligned}
\mathcal{P}(B_{\rm tag}=B^0, D^{*-}\pi^+) &= \frac{e^{-|\Delta t|/\tau}}{4\tau} \times \left[1 - C\cos(\Delta m\Delta t)\ - S^+\sin(\Delta m\Delta t)\right], \\
\mathcal{P}(B_{\rm tag}=B^0, D^{*+}\pi^-) &= \frac{e^{-|\Delta t|/\tau}}{4\tau} \times \left[1 + C\cos(\Delta m\Delta t)\ - S^-\sin(\Delta m\Delta t)\right], \\
\mathcal{P}(B_{\rm tag}=\overline{B}^0, D^{*-}\pi^+) &= \frac{e^{-|\Delta t|/\tau}}{4\tau} \times \left[1 + C\cos(\Delta m\Delta t)\ + S^+\sin(\Delta m\Delta t)\right], \\
\mathcal{P}(B_{\rm tag}=\overline{B}^0, D^{*+}\pi^-) &= \frac{e^{-|\Delta t|/\tau}}{4\tau} \times \left[1 - C\cos(\Delta m\Delta t)\ + S^-\sin(\Delta m\Delta t)\right] \quad (6.1)
\end{aligned}$$

where τ is the B^0 lifetime averaged over the two mass eigenstates, Δm is the $B^0 - \overline{B}^0$ mixing frequency, and Δt is the difference between the time of the $B \to D^{*\pm}\pi^\mp$ ($B_{\rm rec}$) decay and the decay of the other B ($B_{\rm tag}$) in the event. The parameters C and $S^\pm$ are given by

$$C \equiv \frac{1-r^{*2}}{1+r^{*2}}, \qquad S^\pm \equiv \frac{2(-1)^L r^*}{1+r^{*2}}\sin(2\beta+\gamma\pm\delta). \tag{6.2}$$

Here δ is the strong phase difference between A_u and A_c [1] and $r \equiv |A_u/A_c|$, $L = 1$ is the angular momentum of the $D^*\pi$ final state [68]. As mentioned above, due to the

---

[1] The definition of δ is subject to additional π terms, which are redundant with the discrete ambiguity $2\beta+\gamma \to 2\beta+\gamma+\pi$, $\delta \to \delta+\pi$. For consistency in the PDF definitions between different BABAR publications, the angular momentum factor $(-1)^L$ is neglected. However, if the sign of $\cos\delta$ is fixed, for example, through factorization arguments, it becomes important since the sign of $\sin(2\beta+\gamma)$ can be determined.

small value of $r \sim 10^{-2}$, large data samples are required for a statistically significant measurement of S. With this respect, extraction of r^* from the data by fitting the cosine term is impossible with the current statistics. The interpretation of the measured asymmetries in terms of $\sin(2\beta+\gamma)$ requires an assumption regarding the value of r^*, discussed in Section 6.2.8.

6.2.2 Partial reconstruction of $B^0 \to D^{*\mp}\pi^{\pm}$ decays

In the partial reconstruction of a $B^0 \to D^{*\mp}\pi^{\pm}$ candidate, only the hard pion track from the B decay and the soft pion track π_s from the decays $D^{*-} \to \overline{D}^0\pi_s^-$ or $D^{*+} \to D^0\pi_s^+$ are reconstructed. The cosine of the angle between the momenta of the B^0 and the hard pion in the CM frame is then computed (see Equation 5.9):

$$\cos\theta_{Bh} = \frac{M_{D^{*-}}^2 - M_{B^0}^2 - M_\pi^2 + E_{\rm CM}E_h}{2p_{B^0}p_h}, \tag{6.3}$$

where E_h and $\mathbf{p}_h$ are the measured CM energy and momentum of the hard pion. Events are required to be in the physical region $|\cos\theta_{Bh}| < 1$. Given $\cos\theta_{Bh}$ and the measured momenta of the π_h and π_s, the B four-momentum can be calculated up to an unknown azimuthal angle ϕ around $\mathbf{p}_h$. For every value of ϕ, the expected D four-momentum $\mathcal{P}_D(\phi)$ is determined from four-momentum conservation, and the corresponding ϕ-dependent invariant mass $m(\phi) \equiv \sqrt{|\mathcal{P}_D(\phi)|^2}$ is calculated. One defines the missing mass $m_{\rm miss} \equiv \frac{1}{2}\left[m_{\rm max} + m_{\rm min}\right]$, where $m_{\rm max}$ and $m_{\rm min}$ are the maximum and minimum values that $m(\phi)$ may obtain. In signal events, $m_{\rm miss}$ peaks at the nominal D^0 mass M_{D^0}, with a spread of about 3 MeV/c^2 (Fig. 6.2). We find this choice of the azimuthal angle ϕ to be the most convenient for the further modelization of the signal (see Section 6.2.5). The distribution for combinatoric background events is significantly broader, making the missing mass the primary variable for distinguishing signal from background. With the arbitrary choice $\phi = 0$, one uses four-momentum conservation to calculate the CM D and B momentum vectors, which are used in the event selection as described below.

6.2.3 Backgrounds and event selection

In addition to $B^0 \to D^{*\mp}\pi^{\pm}$ events, the above procedure yields a sample containing the following kinds of events: $B \to D^{*\mp}\rho^{\pm}$; peaking $B\overline{B}$ background (other than $B \to D^{*\mp}\rho^{\pm}$), defined as pairs of tracks coming from the same B meson, with the soft pion originating from the decay of a charged D^*, including contributions from $B \to D^{**}\pi$ as well as non-resonant $B \to D^*\pi\pi$ decays; combinatoric B background, defined as all remaining $B\overline{B}$ background events; continuum $e^+e^- \to q\overline{q}$, where q represents a u, d, s, or c quark. Using the fact that B mesons are produced almost at rest, the $B\overline{B}$ events are spherical while the continuum events have a jet-like shape. This background can be significantly reduced.

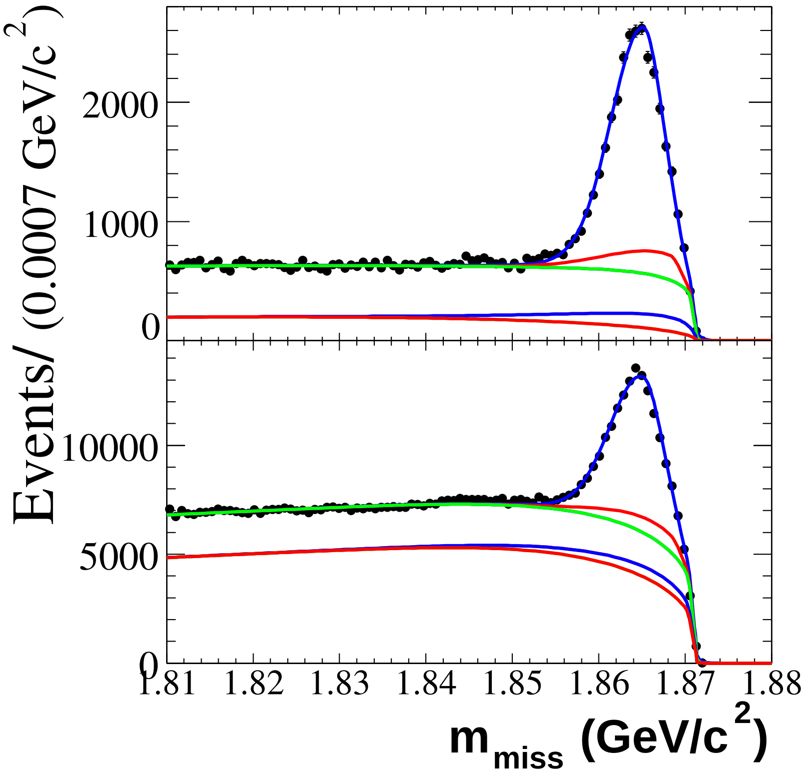

Figure 6.2: *The* m_{miss} *distributions for on-resonance lepton-tagged (top) and kaon-tagged (bottom) data. The curves show, from bottom to top, the cumulative contributions of the continuum, peaking* $B\overline{B}$*, combinatoric* $B\overline{B}$*,* $B \to D^{*\mp}\rho^{\pm}$*, and* $B^0 \to D^{*\mp}\pi^{\pm}$ *PDF components.*

To suppress the continuum background, the ratio of the second to the zeroth Fox-Wolfram moment [48], computed using all charged particles and EMC clusters not matched to tracks, is required to be smaller than 0.40. To further discriminate against continuum events, fifteen event shape variables are combined into a Fisher discriminant $\mathcal{F}$ [69]. Rather than applying requirements to the variable $\mathcal{F}$, it is included in the fits described below. This allows maximizing the reconstruction efficiency of the signal. Hard pion candidates are required to be reconstructed with at least twelve DCH hits. Kaons and leptons are rejected based on information from the IFR, DIRC, energy loss in the SVT and DCH, or the ratio of the candidate's EMC energy deposition to its momentum (E/p). Let us define the D^* helicity angle θ_{D^*} to be the angle between the flight directions of the D and the B in the D^* rest frame, calculated with $\phi = 0$. Taking advantage of the longitudinal polarization in signal events, to suppress the background yield, it is required $|\cos\theta_{D^*}|$ to be larger than 0.4. All candidates are required to be in the range $1.81 < m_{\mathrm{miss}} < 1.88$ GeV/c^2. When multiple candidates are found in the same event, only the one with the m_{miss} value closest to M_{D^0} is used.

6.2.4 Decay time measurement and flavor tagging

Let us define $z_{\rm rec}$ to be the decay position along the beam axis of the partially reconstructed B candidate. To find $z_{\rm rec}$, we fit the hard pion track with a beam spot constraint in the plane perpendicular to the beams, the (x, y) plane. The actual vertical beam spot size is approximately 5 μm, but the constraint is taken to be 30 μm in the fit in order to account for the B flight distance in the (x, y) plane. The soft pion is not used in the fit, since it undergoes significant multiple scattering.

The decay position $z_{\rm tag}$ of the other B in the event (the tag B) along the beam axis is obtained from all other tracks in the event, excluding all tracks whose CM momentum is within 1 rad of the D CM momentum. The remaining tracks are fit with a beamspot constraint in the (x, y) plane. The track with the largest contribution to the χ^2 of the vertex, if greater than 6, is removed from the vertex, and the fit is carried out again, until no track fails this requirement.

Then the decay distance and the decay-time difference are computed as $\Delta z = z_{\rm rec} - z_{\rm tag}$ and $\Delta t = \Delta z/(\gamma\beta c)$, respectively. The machine boost parameter $\gamma\beta$ is calculated from the beam energies, and its average value over the run period is 0.55. The vertex fits used to determine $z_{\rm rec}$ and $z_{\rm tag}$ also yield the Δz error $\sigma_{\Delta z}$ which is used to compute the event-by-event Δt error $\sigma_{\Delta t}$.

The flavor of the tag B is determined from lepton and kaon candidates. The lepton CM momentum is required to be greater than 1.1 GeV/c in order to suppress "cascade" leptons originating in charm decays. Electron candidates are identified using E/p, and the Cherenkov angle and number of photons detected in the DIRC. Muons are identified by the depth of penetration in the IFR. Kaons are identified using the ionization measured in the SVT and DCH, and the Cherenkov angle and number of photons detected in the DIRC. In either the lepton or kaon tagging category, if several tagging tracks are present, the track used for tagging is the one with the largest value of θ_{tag}, the CM-frame angle between the track momentum and the D momentum. This is done in order to minimize the impact of tracks originating from the unreconstructed D. If there are both identified leptons and kaons in the event, the event is tagged using the lepton tracks only.

The following criteria are applied in order to obtain good Δt resolution: the χ^2 probability of the $z_{\rm rec}$ vertex fit must be greater than 0.001; at least two tracks must be used for the tag B vertex fit; $\sigma_{\Delta t}$ is required to be less than 2 ps; and $|\Delta t|$ is required to be less than 15 ps. To minimize the impact of tracks coming from the unreconstructed D, only tagging leptons (kaons) satisfying $\cos\theta_{tag} < 0.75$ ($\cos\theta_{tag} < 0.50$) are retained.

6.2.5 Probability density function

The analysis is carried out with a series of unbinned maximum likelihood fits performed independently for the lepton-tagged and kaon-tagged events. The probability density function (PDF) depends on the variables $m_{\rm miss}$, Δt, $\sigma_{\Delta t}$, F, $s_{\rm t}$, and $s_{\rm m}$, where

$s_{\rm t} = 1$ (-1) when the $B_{\rm tag}$ is identified as a B^0 $(\overline{B}^0)$, and $s_{\rm m} = 1$ (-1) for "unmixed" ("mixed") events. An event is labeled unmixed if the π_h is a $\pi^-(\pi^+)$ and the $B_{\rm tag}$ is a $B^0(\overline{B}^0)$, and mixed otherwise. The PDF for on-resonance data is a sum over the PDFs of the different event types:

$$\mathcal{P} = \sum_i f_i\, \mathcal{P}_i, \tag{6.4}$$

where the index $i = \{D^*\pi, D^*\rho, \text{peak}, \text{comb}, q\overline{q}\}$ indicates one of the event types described above, f_i is the relative fraction of events of type i in the data sample, and $\mathcal{P}_i$ is the PDF for these events. The PDF for off-resonance data is $\mathcal{P}_{q\overline{q}}$. Each of the PDFs $\mathcal{P}_i$ is a product of the form,

$$\mathcal{P}_i = \mathcal{M}_i(m_{\rm miss})\, \mathcal{F}_i(F)\, \mathcal{T}'_i(\Delta t, \sigma_{\Delta t}, s_{\rm t}, s_{\rm m}), \tag{6.5}$$

where the functions appearing in the equation above, are motivated by MC studies and described below.

The $m_{\rm miss}$ PDF for each event type i is the sum of a bifurcated Gaussian plus an ARGUS function [47]. The proportionality constants are such that each of these functions is normalized to unit area. The Fisher discriminant PDF $\mathcal{F}_i$ for each event type is a bifurcated Gaussian. The parameter values of $\mathcal{F}_{D^*\pi}$, $\mathcal{F}_{D^*\rho}$, $\mathcal{F}_{\rm peak}$, and $\mathcal{F}_{\rm comb}$ are identical.

The Δt PDF $\mathcal{T}'_{D^*\pi}(\Delta t, \sigma_{\Delta t}, s_{\rm t}, s_{\rm m})$ for signal events corresponds to Equation 6.1 with $O(r^{*2})$ terms neglected, but has to be modified to account for several experimental effects. The first effect has to do with the origin of the tagging track. In some of the events, the tagging track originates from the decay of the missing D. These events are labeled "missing-D tags" and do not provide any information regarding the flavor of the $B_{\rm tag}$. In lepton-tagged events, we further distinguish between "direct" tags, in which the tagging lepton originates directly from the decay of the $B_{\rm tag}$, and "cascade" tags, where the tagging lepton is a daughter of a charmed particle produced in the $B_{\rm tag}$ decay. The second experimental effect is the finite detector resolution in the measurement of Δt. To address this effect, the distribution of the true decay time difference $\Delta t_{\rm tr}$ is convoluted with a detector resolution function. Putting these two effects together, the Δt PDF of signal events is

$$\begin{aligned} \mathcal{T}'_{D^*\pi}(\Delta t, \sigma_{\Delta t}, s_{\rm t}, s_{\rm m}) &= (1 + s_{\rm t}\, \Delta\epsilon_{D^*\pi}) \sum_j f^j_{D^*\pi} \times \\ \int d\Delta t_{\rm tr}\, \mathcal{T}^j_{D^*\pi}(\Delta t_{\rm tr}, s_{\rm t}, s_{\rm m})\, &\mathcal{R}^j_{D^*\pi}(\Delta t - \Delta t_{\rm tr}, \sigma_{\Delta t}), \end{aligned} \tag{6.6}$$

where $\Delta\epsilon_{D^*\pi}$ is half the relative difference between the detection efficiencies of positive and negative leptons or kaons, the index $j = \{\text{dir, cas, miss}\}$ indicates direct, cascade, and missing-D tags, and $f^j_{D^*\pi}$ is the fraction of signal events of tag-type j in the sample. One sets $f^{\rm dir}_{D^*\pi} = 1 - f^{\rm cas}_{D^*\pi} - f^{\rm miss}_{D^*\pi}$ for lepton tags, with the value $f^{\rm cas}_{D^*\pi} = 0.12 \pm 0.02$ obtained from the MC simulation. For kaon tags $f^{\rm dir}_{D^*\pi} = 0$. The function

$\mathcal{T}^j_{D^*\pi}(\Delta t_{\rm tr}, s_{\rm t}, s_{\rm m})$ is the $\Delta t_{\rm tr}$ distribution of tag-type j events, and $\mathcal{R}^j_{D^*\pi}(\Delta t - \Delta t_{\rm tr}, \sigma_{\Delta t})$ is their resolution function, which parameterizes both the finite detector resolution and systematic offsets in the measurement of Δz, such as those due to the origin of the tagging particle.

The $\mathcal{T}_{D^*\pi}(\Delta t_{\rm tr}, s_{\rm t}, s_{\rm m})$ function for signal events in Equation 6.6 has additional parameters to account for imperfect flavor tagging. Let us define ω_{B^0} ($\omega_{\overline{B}^0}$) to be the mistag probability of signal events whose tag B was tagged as a B^0 ($\overline{B}^0$), when the tagging track is a daughter of the tag B. Then $\omega = (\omega_{B^0} + \omega_{\overline{B}^0})/2$ is the average mistag rate, and $\Delta\omega = \omega_{B^0} - \omega_{\overline{B}^0}$ is the mistag rate difference. One further defines ρ to be the probability that the tagging lepton or kaon from the unreconstructed D produced in the $B^0 \to D^{*\mp}\pi^\pm$ decay, results in a mixed flavor tag. With these definitions, the signal PDF is written as

$$\begin{aligned}\mathcal{T}^j_{D^*\pi}(\Delta t_{\rm tr}, s_{\rm t}, s_{\rm m}) &= \frac{e^{-|\Delta t_{\rm tr}|/\tau}}{4\tau} \times \Big\{(1 - f^{\rm miss}_{D^*\pi})[1 - s_{\rm t}\,\Delta\omega^j_{D^*\pi} \\ &+ s_{\rm m}\,(1 - 2\omega^j_{D^*\pi})\,\cos(\Delta m_{D^*\pi}\Delta t_{\rm tr}) \\ &- \mathcal{S}^j_{D^*\pi}\,\sin(\Delta m_{D^*\pi}\Delta t_{\rm tr})] + f^{\rm miss}_{D^*\pi}(1 + s_{\rm m}\,(1 - 2\rho))\Big\}, \qquad (6.7)\end{aligned}$$

where $j = \{\text{dir},\ \text{cas}\}$. The last term accounts for the tags due to daughters of the unreconstructed D. The factor $\mathcal{S}^j_{D^*\pi}$ describes the effect of interference between $b \to u\bar{c}d$ and $b \to c\bar{u}d$ amplitudes in both the $B_{\rm rec}$ and the $B_{\rm tag}$ decays:

$$\mathcal{S}^j_{D^*\pi} = \quad (1 - 2\omega^j_{D^*\pi})\,(s_{\rm t} a_{D^*\pi} + s_{\rm m} c_{D^*\pi}) + s_{\rm t} s_{\rm m} b_{D^*\pi}(1 - s_{\rm t}\Delta\omega^j_{D^*\pi}), \qquad (6.8)$$

where $a_{D^*\pi}$, $b_{D^*\pi}$, and $c_{D^*\pi}$ are related to the physical parameters through

$$\begin{aligned} a_{D^*\pi} &\equiv 2r^* \sin(2\beta + \gamma)\cos\delta^*, \\ b_{D^*\pi} &\equiv 2r' \sin(2\beta + \gamma)\cos\delta', \\ c_{D^*\pi} &\equiv 2\cos(2\beta + \gamma)(r^* \sin\delta^* - r' \sin\delta'), \qquad (6.9)\end{aligned}$$

and r' (δ') is the effective magnitude of the ratio (effective strong phase difference) between the $b \to u\bar{c}d$ and $b \to c\bar{u}d$ amplitudes in the $B_{\rm tag}$ decay. This parameterization neglects terms of order r^{*2} and r'^2. Only $a_{D^*\pi}$ and $b_{D^*\pi}$ are related to *CP* violation, while $c_{D^*\pi}$ can be non-zero even in the absence of *CP* violation when $2\beta + \gamma = 0$. The inclusion of r' and δ' in the formalism accounts for cases where the $B_{\rm tag}$ undergoes a $b \to u\bar{c}d$ decay, and the kaon produced in the subsequent charm decay is used for tagging [70]. It is expected that $r' \sim 0.02$. In lepton-tagged events $r' = 0$ (and hence $b_{D^*\pi} = 0$) because most of the tagging leptons come from B semileptonic decays to which no suppressed amplitude with a different weak phase can contribute.

The Δt PDF of $B \to D^{*\mp}\rho^\pm$ has the same functional form and parameter values as the signal PDF, except that the weak phase parameters $a_{D^*\rho}$, $b_{D^*\rho}$, and $c_{D^*\rho}$ are set to 0 and are later varied to evaluate systematic uncertainties. The $\Delta t_{\rm tr}$ PDF for the combinatoric and the peaking $B\overline{B}$ background have the same functional form as Equation 6.7 and the subsequent expressions, Equations 6.8, 6.9, but with independent values for the parameters. The parameterization of the $\Delta t_{\rm tr}$ PDF for the peaking $B\overline{B}$ background accounts separately for charged and neutral B decays. The $\Delta t_{\rm tr}$ PDF for the continuum background is the sum of two components, one with a finite lifetime and one wit zero lifetime. To account for the finite detector resolution and systematic offsets in the measurement of Δz, all background PDFs are also convoluted with the resolution function.

The resolution function for events of type i and optional secondary type j ($j = \{\rm dir,\ cas,\ miss\}$ for lepton-tagged signal events and $j = \{+,\ 0\}$ for the peaking and combinatoric $B\overline{B}$ background types) is parameterized as the sum of three Gaussians:

$$\begin{aligned}\mathcal{R}^j_i(t_r, \sigma_{\Delta t}) &= f^{nj}_i\, \mathcal{G}^{nj}_i(t_r, \sigma_{\Delta t}) + (1 - f^{nj}_i - f^{oj}_i)\, \mathcal{G}^{wj}_i(t_r, \sigma_{\Delta t}) \\ &+ f^{oj}_i\, \mathcal{G}^{oj}_i(t_r), \qquad (6.10)\end{aligned}$$

where $t_r = \Delta t - \Delta t_{\rm tr}$ is the residual of the Δt measurement, and $\mathcal{G}^{nj}_i$, $\mathcal{G}^{wj}_i$, and $\mathcal{G}^{oj}_i$ are the "narrow", "wide", and "outlier" Gaussians. The narrow and wide Gaussians incorporate information from the Δt uncertainty $\sigma_{\Delta t}$, and account for systematic offsets in the estimation of $\sigma_{\Delta t}$ and the Δt measurement. The outlier Gaussian accounts for a small fraction of events with badly measured Δt.

6.2.6 Analysis procedure

The analysis takes place in four steps, each involving maximum likelihood fits, carried out simultaneously on the on- and off-resonance data samples:

1. *Kinematic-variable fit:* The data are fitted with the PDF in Equation 6.4, but with Equation 6.5 replaced by

   $$\mathcal{P}_i(m_{\rm miss}, F) = \mathcal{M}_i(m_{\rm miss})\, \mathcal{F}_i(F). \qquad (6.11)$$

   The parameters determined in this fit are $f_{D^*\rho} + f_{D^*\pi}$, $f_{\rm peak}$, and $f_{\rm comb}$ in Equation 6.4, the parameters of $\mathcal{M}_{q\overline{q}}(m_{\rm miss})$, and those of $\mathcal{F}_i(F)$ for both continuum and $B\overline{B}$ events.

2. $f^{\rm miss}_{D^*\pi}$ *and* ρ *fit:* The kinematic-variable fit is repeated to determine the number of signal events above and below the cut on $\cos\theta_{tag}$ (see section 6.2.4). These values are then used to compute the values of $f^{\rm miss}_{D^*\pi}$ and ρ in the Δt PDF (Equation 6.7). This is done using values for the efficiencies of the cut on $\cos\theta_{tag}$ determined from the Monte Carlo simulation. We calculate $f^{\rm miss}_{D^*\pi} = 0.011 \pm 0.001$ for lepton tagged events and $f^{\rm miss}_{D^*\pi} = 0.055 \pm 0.001$ for kaon-tagged events.

3. *Sideband fit:* To obtain the parameters of the combinatoric $B\overline{B}$ PDF $\mathcal{T}'_{\rm comb}$, the fit of the $m_{\rm miss}$ sideband $1.81 < m_{\rm miss} < 1.84$ GeV/c^2 is performed. The PDF in

Equation 6.4 is used in this fit, with $f_{D^*\rho} + f_{D^*\pi} + f_{\rm peak} = 0$ and $f_{\rm comb} + f_{q\overline{q}} = 1$, to account for the fact that the sideband is populated only by continuum and combinatoric $B\overline{B}$ events. The value of $f_{\rm comb}$ and the parameters of $\mathcal{T}'_{\rm comb}$, as well as those of $\mathcal{T}'_{q\overline{q}}$ in the sideband are also floated in this fit.

4. *Signal-region fit:* Using the parameter values obtained in the previous steps, the fit of the data in the signal region $1.845 < m_{\rm miss} < 1.880$ GeV/c^2 is performed. This fit determines all the floating parameters of the signal PDF $\mathcal{T}'_{D^*\pi}$, and the parameters of the continuum PDF $\mathcal{T}'_{q\overline{q}}$.

In steps 3 and 4 a possible difference between the B^0 and $\overline{B}^0$ tagging efficiencies which may be different for each event type, is also fitted. In order to minimize the possibility of experimenter bias, step 4 of the analysis is carried out in a "blind" manner, such that the values of $a_{D^*\pi}$, $b_{D^*\pi}$ and $c_{D^*\pi}$ are hidden from the analysts until all the systematic errors have been evaluated.

Several validity tests of the analysis procedure have been performed using the MC simulation. The entire analysis procedure is carried out on a MC sample containing four times the number of events observed in the data. The values of the most importantly parameters obtained in these MC fits are consistent with the input parameters to within the statistical uncertainties.

6.2.7 Results

Summarizing the values and uncertainties of the weak phase parameters, one obtains the following results from the lepton-tagged sample:

$$\begin{aligned} a^{\ell}_{D^*\pi} &= -0.042 \pm 0.019 \pm 0.010, \\ c^{\ell}_{D^*\pi} &= -0.019 \pm 0.022 \pm 0.013. \end{aligned} \tag{6.12}$$

The results from the kaon-tagged sample fits are

$$\begin{aligned} a^{K}_{D^*\pi} &= -0.025 \pm 0.020 \pm 0.013, \\ b^{K}_{D^*\pi} &= -0.004 \pm 0.010 \pm 0.010, \\ c^{K}_{D^*\pi} &= -0.003 \pm 0.020 \pm 0.015. \end{aligned} \tag{6.13}$$

Combining the results for lepton and kaon tags gives the amplitude of the time-dependent CP asymmetry,

$$\begin{aligned} a_{D^*\pi} &= 2r^* \sin(2\beta + \gamma) \cos\delta^* \\ &= -0.034 \pm 0.014 \pm 0.009, \end{aligned} \tag{6.14}$$

where the first error is statistical and the second is systematic. The systematic error takes into account correlations between the results of the lepton- and kaon-tagged samples coming from the systematic uncertainties related to detector effects, to interference between $b \to u\bar{c}d$ and $b \to c\bar{u}d$ amplitudes in the backgrounds and from $\mathcal{B}(B \to D^{*\mp}\rho^\pm)$. The dominant systematic error arises from the uncertainty in the weak phase parameters of the $B \to D^{*\mp}\rho^\pm$, peaking and combinatoric $B\overline{B}$ background. This value of $a_{D^*\pi}$ deviates from zero by 2.0 standard deviations. Although it is the most precise *CP* violation measurement in the decays of B mesons at this time, the statistical error is still dominant.

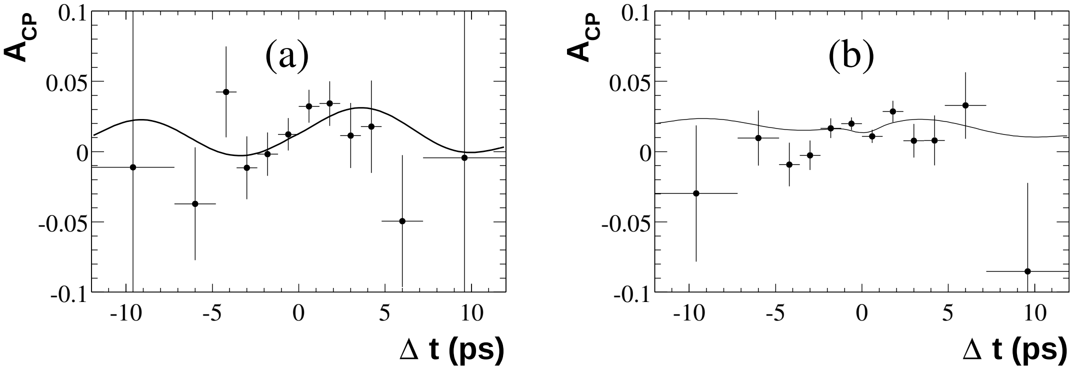

Figure 6.3: *Raw asymmetry for (a) lepton-tagged and (b) kaon-tagged events. The curves represent the projections of the PDF for the raw asymmetry.*

6.2.8 Constraint on $\sin(2\beta+\gamma)$

Two methods for interpreting these results in terms of constraints on $|\sin(2\beta+\gamma)|$ are used. Both methods involve minimizing a χ^2 function that is symmetric under the exchange $\sin(2\beta+\gamma) \to -\sin(2\beta+\gamma)$,

Due to the fact that the minimum value of the χ^2 may occur at the boundary of the physical region ($|\sin(2\beta+\gamma)| = 1$), the errors naively obtained from the variation of the χ^2 functions are not relevant. In order to give a probabilistic interpretation to the results, we apply the Feldman-Cousins method [71] to set limits on $|\sin(2\beta+\gamma)|$.

In the first method, no assumption regarding the value of r^* is made. The resulting 95% lower limit for the mode $B^0 \to D^{*\mp}\pi^\pm$ is shown as a function of r^* in Figure 6.4. The χ^2 function is invariant under the transformation $2\beta+\gamma \to \pi/2+\delta^*$ and $\delta^* \to \pi/2 - 2\beta+\gamma$. The limit shown in this figure is always the weaker of these two possibilities.

The second approach, originally proposed in Ref. [64], assumes SU(3) flavor symmetry to estimate r^* from the Cabibbo angle, the ratio of branching fractions $\mathcal{B}(B^0 \to$

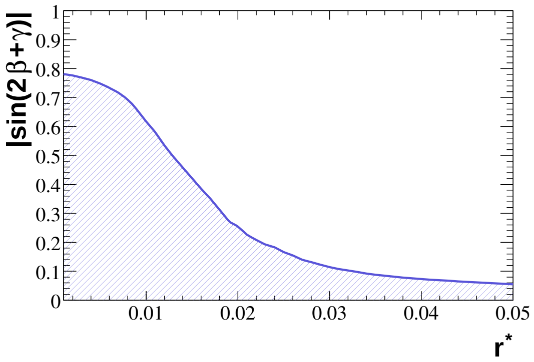

Figure 6.4: *Lower limit on* $|\sin(2\beta+\gamma)|$ *at 90% CL as a function of* r^**, for* $r^* > 0.001$.

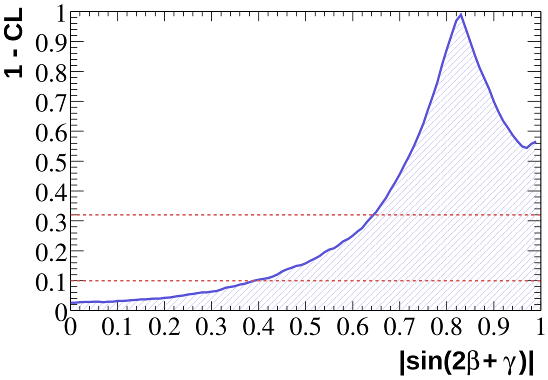

Figure 6.5: *The shaded region denotes the allowed range of* $|\sin(2\beta+\gamma)|$ *for each confidence level. The horizontal lines show, from top to bottom, the 68% and 90% CL.*

$D^{*+}_s\pi^-)/\mathcal{B}(B^0 \to D^{*-}\pi^+)$ [72], and the ratio of decay constants $f_{D^*}/f_{D^*_s}$ [73],

$$r^* \;=\; \tan\theta_C \sqrt{\frac{\mathcal{B}(B^0 \to D^{*+}_s\pi^-)}{\mathcal{B}(B^0 \to D^{*-}\pi^+)}}\frac{f_{D^*}}{f_{D^*_s}} \tag{6.15}$$

Using our measurement of $\mathcal{B}(D_s^+ \to \phi\pi^+)$ [54] (see also Section 5.4), one finds

$$r^{*meas} = 0.015^{+0.004}_{-0.006} \tag{6.16}$$

The approximation above takes into account the main (factorisable) SU(3) breaking effects by including the ratio of the decay constants $f_{D^*}/f_{D^*_s}$. However, to compute the confidence level, additional 30% relative error is attributed to the theoretical assumption in extraction of the value of r^* from Equation 6.16. Figure 6.5 shows the result of the frequentistic computation of the confidence level as a function of $|\sin(2\beta+\gamma)|$. This method yields the lower limits $|\sin(2\beta+\gamma)|>0.62$ (0.35) at 68% (90%) C.L. It is important to note that non factorisable SU(3) breaking corrections such as W-exchange contributions to the $B^0 \to D^{*-}\pi^+$ decay amplitude are expected to be small. Indeed, they were estimated to be of the order of 15% for r^* [74].

6.3 Status and perspectives

Study of the neutral B meson decay modes $B^0 \to D^{(*)\mp}h^\pm$, where h is a light hadron (π, ρ), are being actively pursued experimentally by *BABAR* [61, 75] and *BELLE* [76] experiments. Both experiments have used partial reconstruction techniques to increase the signal yields in the $D^{*\mp}\pi^\pm$ channel. In addition to $D^\mp\pi^\pm$ and $D^{*\mp}\pi^\pm$ decays, *BABAR* has also investigated $D^{\mp}\rho^{\pm}$ with a full reconstruction technique. Figure 6.6 shows the present experimental results obtained by *BABAR* and *BELLE* experiments for the *CP* violating parameter a. Although rather different techniques have been employed, most notably to deal with the troublesome possibility of *CP* violation effects on the flavor tagging side of the $\Upsilon(4S) \to B\bar{B}$ event, the results are consistent at the current level of precision. The combined result for *CP* violation in the most precisely measured decay channel $D^{*\mp}\pi^{\pm}$ is

$$a^{D^*\pi} = 2r^* \sin(2\beta+\gamma)\cos\delta = -0.037 \pm 0.011 \tag{6.17}$$

This measurement performed at the level of one per cent, deviates from zero by 3.4 standard deviations. Future updates are therefore of a great interest.

Figure 6.7 shows the constraint for the UT angle γ obtained from the different analysis measurements, described in Section 6.1. One can see, the $\sin(2\beta+\gamma)$ measurement provides remarkable contribution to the combined fit. As GGSZ method, it also allows excluding of the multiple solution $\gamma \to \pi - \gamma$ relevant to the ADS and GLW methods.

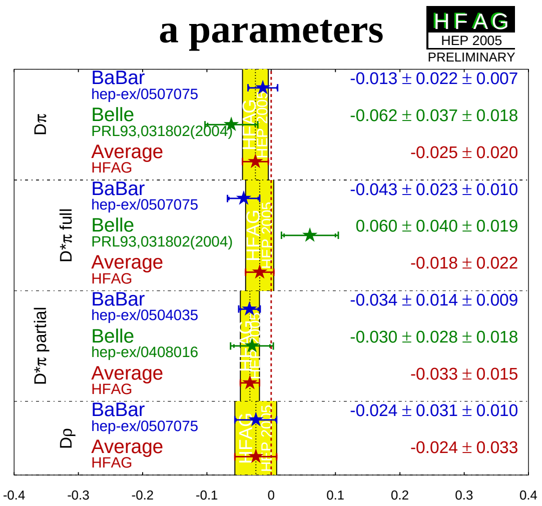

Figure 6.6: *Experimental results for CP parameter $a = 2r\sin(2\beta+\gamma)\cos\delta$ obtained by BABAR and BELLE experiments from the measurement of time-dependent CP asymmetries in $B^0 \to D^{(*)\mp}\pi^{\pm}(\rho^{\mp})$.*

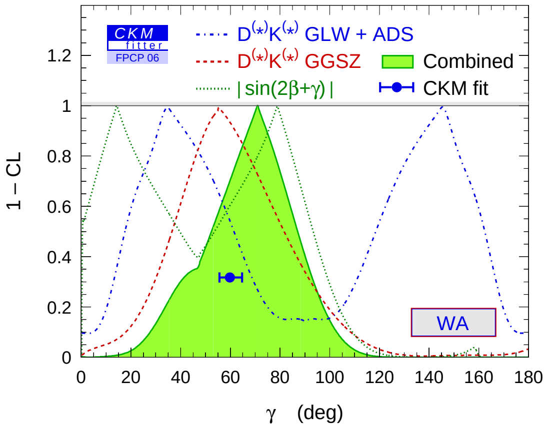

Figure 6.7: *Confidence level of the UT angle γ from the various measurements. The prediction from the standard CKM fit is also shown [74].*

Some related modes may also provide a measurement of $2\beta+\gamma$. $B^0 \to D^{*\mp}\rho^{\pm}$ has a vector-vector final state, and the interfering amplitudes result in an increased number of observables, so that all parameters can, in principle, be extracted from the data. However, this mode is experimentally challenging, e.g. the polarization measurement is sensitive to systematic effects, and recent results for the branching fraction measurements of the SU(3) partners suggest that the *CP* violation effect may be even smaller than expected.

Larger effects are expected to be found in modes mediated by the $b \to c\bar{u}s$ & $b \to u\bar{c}s$ transitions, such as $B^0 \to DK^{(*)}$ [77]. Due to relatively large $r_B \equiv |A(\overline{B}^0 \to \bar{D}^{(*)0}\bar{K}^0)|/|\overline{B}^0 \to D^{(*)0}\bar{K}^0)| \simeq 0.4$, these decay channels look very attractive for such a measurement. Since the parameter r_B can be measured with sufficient data sample by fitting the C coefficient in time distributions, the measured asymmetry can be interpreted in terms of $\sin(2\beta+\gamma)$ without additional assumptions. However, the branching fractions of such decays are relatively small ($\sim 5\cdot 10^{-5}$). The *BABAR* experiment has measured the branching fractions of $\overline{B}^0 \to D^{(*)0}\bar{K}^{(*)0}$ [78] and estimated the upper limit for $r_B < 0.40$ at the 90% C.L. Thus, the present signal yields suggest that a substantially larger data sample is needed for a competitive time-dependent measurement of $\sin(2\beta+\gamma)$ with these decay channels.

Recently it was proposed to consider the $B^0 \to D^{(*)\mp}a^{\pm}_{0(2)}$ decays for measurement of $\sin(2\beta+\gamma)$ [79]. The decay amplitudes of B mesons to light scalar or tensor mesons such as a_0^+ or a_2^+ are significantly suppressed due to the small decay constants $f_{a_{0(2)}}$. Thus, the absolute value of the CKM-suppressed and favored amplitudes become comparable. As a result, the *CP* asymmetry in such decays is expected to be large. However, the theoretical predictions of the branching fractions for $B^0 \to D^{(*)\mp}a^{\pm}_{0(2)}$ is expected of the order of $(1 \div 4)\cdot 10^{-6}$ [80]. The measured upper limits for the SU(3) partners $B^0 \to D_s^{(*)+}a^{-}_{0(2)}$ [81] suggest that the branching ratios of $B^0 \to D^{(*)+}a^{-}_{0(2)}$ are too small for *CP*-asymmetry measurements given the present statistics of the B-factories. The measurement of $\sin(2\beta+\gamma)$ in $B^0 \to D^{(*)+}a^{-}_{0(2)}$ decays could be an interesting program for the future experiments such as Super$B$-factories.

Another interesting mode is $B_s \to D_s^{(*)\pm}K^{\mp}$. In this case the B_s mixing phase ϕ_s replaces 2β, so the time-dependence probes $\phi_s + \gamma$. Since $r_{D_s^{(*)}K}$ is expected to be reasonably large, there will be sufficient observables to extract all parameters from the data and resolve the problem of multiple solutions [68]. This approach looks very promising for the LHCb experiment.

Conclusion

The *BABAR* experiment has been running very successfully since 1999. In 2001, *CP* violation in the system of neutral B mesons has been discovered. The measurement of the time-dependent *CP* asymmetry in the $B^0 \to J/\psi K_s^0$ decays allowed us to constrain the CKM parameter $\sin 2\beta$ and, therefore, claim the large *CP* violation in the system of B mesons predicted by the Standard Model. After this great success, further precise tests of the Standard Model through the measurements of the angles and the sides of the Unitarity Triangle have been performed. No significant discrepancy between experiment and theoretical expectations is observed up to now.

A powerful particle identification system over a large range of solid angle and momentum, in the development of which I have contributed, is an essential ingredient to meet the requirements of *CP* violation measurements. Indeed, the tagging of the B flavor and a high reconstruction efficiency for charmless $B \to hh$, $(h = \pi, K)$ decays require identification of kaons in the momentum range up to about 4 GeV/c. The achieved performances of the DIRC system provide an excellent possibility to perform the physics program of the *BABAR* experiment. Determination of the CKM angle α that exploits the charmless decays, observation of the direct *CP* violation in the $B^0 \to K^+\pi^-$ decays and discovery of the D^0-$\overline{D}^0$ mixing, are some examples of the highlights that would not occur without a dedicated particle identification system.

I have been involved in the design of the *BABAR* magnet system that plays a central role in the detector design. The *BABAR* magnet has been successfully commissioned without compromising the high luminosity of the accelerator. Operation disturbance of the PEP-II beam elements by the *BABAR* magnet was observed to be minimal. I have also contributed in the precision measurement of the magnetic field in the central tracking volume. The results of this work have been applied in the global reconstruction algorithm of the charged particles in the detector.

Two main methods of B meson reconstruction, full and partial reconstruction, are employed in *BABAR*. Being one of the conveners of the group which exploits the partial reconstruction technique, I have been deeply involved in the development of this reconstruction method. Due to high selection efficiency enhanced by non reconstructed meson, precise measurements of $B^0 \to D_s^{(*)+} D^{*-}$ and $D_s^+ \to \phi\pi^+$ branching fractions have been performed. It is important to note that the most precise measurements of such fundamental quantities as the B^0 lifetime ($\tau_{B_d^0}$) and the $B^0 - \overline{B}^0$ mixing frequency (Δm_d) have also exploited the method of partial reconstruction.

The key point of this report and of my research in *BABAR* is a precise *CP* violation measurement in the decays of B^0 mesons into $D^{*\mp}\pi^{\pm}$ final state. Due to low ratio of Cabibbo-favored over Cabibbo-suppressed amplitudes (about 2%) the expected *CP* asymmetry in this mode is very small. Thanks to the partial reconstruction technique, the *CP* asymmetry in this decay mode has been measured with a precision as good as about 1.5%. This allowed us to obtain a significant constraint on the CKM parameter $\sin(2\beta+\gamma)$. Together with the other measurements of the CKM angle γ that involve the $B \to D^{(*)}K^{(*)}$ decays, this provides a significant contribution to the test of the Standard Model.

Finally, I would like to characterize my scientific work in *BABAR* by two words: *complementary* and *coherent*. Complementary, because my commitment in the design and construction of the particle identification system allowed me to exploit its high performances in the study of the $B^0 \to D_s^{(*)+}D^{*-}$ decays and the kaon tagging of the B flavor in the time-dependent *CP* asymmetry measurements; my research experience in the magnetic field calculations and measurements of the fringe fields for the DIRC photomultipliers has subsequently been used for the field mapping in the volume of the central tracker and *BABAR* magnet simulations. Coherent, because, my deep involvement in the development of the method of a partial reconstruction technique is connected with the challenges of the $B^0 \to D^{*\mp}\pi^{\pm}$ decay reconstruction using this method and subsequently the measurement of *CP* asymmetry with it; the improved measurement of the $D_s^+ \to \phi\pi^+$ branching fraction provides a straightforward input in the $\sin(2\beta+\gamma)$ constraint using SU(3) flavor symmetry.

In summer 2005, I have joined the CMS collaboration to work on this LHC experiment. I am involved in the commissioning of the electromagnetic calorimeter (ECAL), where the CMS-Saclay group has the responsibility to build the laser-monitoring system that allows corrections for $PbWO_4$ crystal transparency changes due to irradiation. I have also performed a study of the feasibility to measure Triple Gauge Couplings with the $pp \to Z^0Z^0 \to 4l$ reaction at CMS. The result of this study has been included in the "Physics Technical Design Report" of CMS [82] in 2006 and published in Ref. [83]. I am looking forward to the LHC era, where my main scientific activity is related to the commissioning and the various physics searches in the CMS experiment.

Bibliography

[1] J. H. Christenson, J. W. Cronin, V. L. Fitch and R. Turlay, Phys. Rev. Lett. **13**, 138 (1964)

[2] S. Ganjour, "Study of $B \to D_s^{(*)+}X$ and $B^0 \to D_s^{(*)+}D^{*-}$ Decays with the *BABAR* Detector", *Dissertation zur Erlangung des Grades eines Doktors der Naturwissenschaften der Fakultät für Physik und Astronomie Institut für Experimentalphysik I der Ruhr-Universität Bochum*, Bochum, Germany (2002)

[3] "The *BABAR* Physics Book", D. Boutigny *et al.*, SLAC-R-504, October 1998, ed. by P. F. Harrison and H. R. Quinn.

[4] A.D. Sakharov, Pis'ma Zh.Eksp.Teor.Fiz **5** 32, (1967)

[5] A.G. Cohen, D.B. Kaplan and a.E. Nelson, Ann.Rev.Nucl.Part.Sci. **43**, 27 (1993)

[6] J. Schwingler, Phys. Rev. **82**, 914, (1951);G. Lüders, Mat. Fys. Medd. Kongl. Dan. Vid. Selsk. **28**, 5 (1954); W. Pauli, in "Niels Bohr and the development of physics", W. Pauli ed., Oxford (1955)

[7] K. Nishijima, *Fundamental particles*, W.A. Benjamin Inc., New Yotk, 1963; L.H. Ryder, *Elementary Particles and Symmetries*, Gordon and Breach Science Publishers, London, 1975.

[8] C.S. Wu *et al.* Phys. Rev. **105**, 1413 (1957)

[9] M. Kobayashi and T. Maskawa, Prog. Theor. Phys. **49**, 652 (1973)

[10] M. Gell-Mann and A. Pais, Phys. Rev. **97**, 1387 (1955)

[11] R. Aleksan, "Quark Mixing and *CP* violation", ed. T. Ferbel, Techniques and Consepts of High Energy Physics, Kluwer Academic Publishers, 487-596 (1999).

[12] I. Bigi, "*CP* Violation". ed. C.Jarlskog, World Scientific, Singapore (1992).

[13] Particle Data Group, W.-M. Yao *et al.*, J. Phys. **G33**, 1 (2006).

[14] N. Cabibbo, Phys. Rev. Lett. **10**, 531 (1963)

[15] P. Higgs, Phys. Rev. Lett. **13** 508 (1964).

[16] L. Wolfenstein, Phys. Rev. Lett. **51** 1945 (1983)

[17] J.Seeman *et al.* Status Report on PEP-II Performance, *Proceedings of 7th Europhaen Particle Accelerator Conferemce (EPAC 2000), Vienna, Austria (2000)*

[18] *BELLE* Collaboration, A. Abashian *et al.*,Nucl. Instr. Methods Phys. Res., Sect. A **479**, 117 (2002)

[19] *BELLE* Collaboration, K. Abe *et al.*, Phys. Rev. Lett. **87** 091802 (2001).

[20] *BABAR* Collaboration, B. Aubert *et al.*, Phys. Rev. Lett. **87** 091801 (2001).

[21] PEP-II Conceptual Design Report, SLAC-R-418 (1993).

[22] J.Seeman *et al.* The PEP-II Storage Rings, SLAC-PUB-8796 (2001)

[23] E.Antokhin *et al.* "Magnetic Field Calculations in the *BABAR* Detector", *BABAR note 344* (1996)

[24] E.Antokhin *et al.* "Field Measurements in the *BABAR* Solenoid", *BABAR note 514* (2000)

[25] *BABAR* Collaboration, B. Aubert *et al.*, Nucl. Instr. Methods Phys. Res., Sect. A **479**, 1 (2002)

[26] C. Bozzi *et al.*, "The *BABAR* Silicon Vertex Tracker", Nucl. Instr. Methods Phys. Res., Sect. A **435**, 25 (1999)

[27] Opera-2D, Vector Fields, Inc.,Aurora, IL, USA;ANSYS by ANSYS Inc.,Canonsburg, PA, USA; Mermaid (1994) by Sim Limited, Novosibirsk, Russia.

[28] E.Antokhin *et al.* "Magnetic Field Calculations in the *BABAR* Detector", *BABAR note 370* (1996)

[29] C. Newman-Holmes, E.E. Schmidt, R. Yamada, Nucl. Instr. Methods Phys. Res., Sect. A **274**, 443 (1989)

[30] *BABAR* Technical Design Report, D. Boutigny *et al.*, SLAC-R-95-457, March 1995.

[31] K.Arisaka *et al.*, "Recent results on Prototype Aerogel Threshold Counters for Particle Identification in the Region 0.5-4.3GeV/c", Nucl. Instr. Methods Phys. Res., Sect. A **379** 460-464 (1996); K.Arisaka *et al.*, "Four-layer aerogel Cherenkov counter", Journal of Non-Crystalline Solids 225(1998) 375-380; D.Boutigny *et al.*,

"Performance of an aerogel threshold particle identification detector readout by Hybrid Photon Detectors", IEEE Trans. Nucl. Sci. **44**, NO.4, August 1997, 1621-1629; K.Arisaka *et al.*, "Performance of a Prototype Aerogel Counter Readout by Fine Mesh Photo-tubes", Nucl. Instr. Methods Phys. Res., Sect. A **385** 74-80 (1997)

[32] B. Ratcliff, "The DIRC counter: A New Type of Particle Identification Device for the B Factory", Nucl. Instr. Methods Phys. Res., Sect. A **343**, 292(1994)

[33] A.R.Buzykaev *et al.* "Aerogel with high optical parameters for Cherenkov Counters", Nucl. Instr. Methods Phys. Res., Sect. A **379** 465-467 (1996).

[34] A.R. Buzykaev *et al.* "Measurement of optical parameters of aerogel", Nucl. Instr. Methods Phys. Res., Sect. A **433**, 396-400(1999)

[35] T. Iijima *et al.* "Aerogel Cherenkov counter for the BELLE detector", Nucl. Instr. Methods Phys. Res., Sect. A **453** 321-32 (2000).

[36] I. Adam *et al.*, Nucl. Instr. Methods Phys. Res., Sect. A **538**, 281 (2005)

[37] E. Antokhin *et al.*, "Simulation and measurement of the fringe field of the 1.5 T *BABAR* solenoid", Nucl. Instr. Methods Phys. Res., Sect. A **432**, 24 (1999)

[38] *BABAR* Collaboration, B. Aubert *et al.*, Phys. Rev. Lett. **93** 131801 (2004).

[39] *BABAR* Collaboration, B. Aubert *et al.*, Phys. Rev. Lett. **98** 211802 (2007).

[40] *BABAR* Collaboration, B. Aubert *et al.*, Phys. Rev. D **67** 092003 (2003).

[41] N. Isgur and M. B. Wise, Phys. Lett. B **232**, 113 (1989); Phys. Lett. B **237**, 527 (1990).

[42] H .Georgy, Phys. Lett. B **240**, 447 (1990).

[43] J.D. Bjorken, Nucl. Phys. Proc. Suppl. **11**, 325 (1989).

[44] M. Beneke *et al.*, Nucl. Phys. B **591**, 313 (2000).

[45] C.W. Bauer *et al.*, Phys. Rev. D **67**, 014010 (2003).

[46] Z. Luo and J. L. Rosner, Phys. Rev. D **64**, 094001 (2001).

[47] ARGUS Collaboration, H. Albrecht *et al.* Phys. Lett. B **241**, 278 (1990).

[48] G. Fox and S. Wolfram, Phys. Rev. Lett. **41**, 1581 (1978).

[49] Z. Luo and J. L. Rosner, Phys. Rev. D **64**, 094001 (2001).

[50] CLEO Collaboration, D. Gibaut *et al.*, Phys. Rev. D **53**, 4734 (1996).

[51] CLEO Collaboration, S. Ahmed *et al.*, Phys. Rev. D **62**, 112003 (2000).

[52] Particle Data Group, S. Eidelman *et al.* Phys. Lett. B **592**, 1 (2004).

[53] *BABAR* Collaboration, B. Aubert *et al.*, BABAR-CONF-03/021, hep-ex/0308017 (2003).

[54] *BABAR* Collaboration, B. Aubert *et al.*, Phys. Rev. D **71** 091104 (2005).

[55] $CB(m_{\rm ES}) = e^{-\alpha^2/2}(n/|\alpha|)^n(n/|\alpha| - |\alpha| - y)$ for $y < \alpha$, $CB(m_{\rm ES}) = e^{-y^2/2}$ for $y > \alpha$, where $y \equiv (m_{\rm ES} - \overline{m}_{\rm ES})/\sigma$. D. Antreasyan, Crystal Ball Note 321 (1983).

[56] CLEO Collaboration, M. Artuso *et al.* Phys. Lett. B **378**, 364 (1996).

[57] *BABAR* Collaboration, B. Aubert *et al.*, Phys. Rev. D **67** 091101 (2003).

[58] *BABAR* Collaboration, B. Aubert *et al.*, Phys. Rev. D **73** 012004 (2006).

[59] *BABAR* Collaboration, B. Aubert *et al.*, Phys. Rev. Lett. **95** 042001 (2005).

[60] *BABAR* Collaboration, B. Aubert *et al.*, Phys. Rev. Lett. **92** 251802 (2004).

[61] *BABAR* Collaboration, B. Aubert *et al.*, Phys. Rev. D **71** 112003 (2005).

[62] G. Cavoto *et al.* "Angles from B decays with charm", *Proceedings of the CKM 2005 Workshop (WG5), March 15-18, 2005, UC San Diego, San Diego, USA* hep-ph/0603019 (2007).

[63] S. Ganzhur, "Status and prospects for *CP* asymmetry measurements: $\sin(2\beta + \gamma)$", *Proceedings of the 4th International Workshop on the CKM Unitarity Triangle, December 12-16, 2006, Nagoya University, Nagoya, Japan* hep-ph/0703229 (2007).

[64] I. Dunietz, Phys. Lett. B **427**, 179 (1998).

[65] M.Gronau and D.Wyler, Phys. Lett. B **265** 172 (1991); M.Gronau and D.London, Phys. Lett. B **253**, 483 (1991)

[66] D.Atwood, I.Dunietz and A.Soni, Phys. Rev. Lett. **78**, 3257 (1997); Phys. Rev. D **63**, 036005 (2001).

[67] Giri, Grossman, A.Soffer and Zupan, Phys. Rev. D **68**, 054018 (2004); *BELLE* Collaboration, A. Poluektov *et al.*, Phys. Rev. D **70**, 072003 (2004).

[68] R. Fleischer, Nucl. Phys. B **591**, 459 (2003).

[69] R.A. Fisher, Annals of Eugenics **7**, 179 (1936); M.S. Srivastava and E.M. Carter, *An Introduction to Applied Multivariate Statistics* (North Holland, Amsterdam, 1983).

[70] O. Long *et al.*, Phys. Rev. D **68**, 034010 (2003).

[71] G. Feldman and R. Cousins, Phys. Rev. D **57**, 3873 (1998).

[72] *BABAR* Collaboration, B. Aubert *et al.*, Phys. Rev. Lett. **90**, 181803 (2003).

[73] D. Becirevic, Nucl. Phys. Proc. Suppl. **94**, 337 (2001).

[74] J. Charles *et al.* (CKMFitter Group), Eur. Phys. J. C **41**, 1 (2005)

[75] *BABAR* Collaboration, B. Aubert *et al.*, Phys. Rev. D **73**, 111101 (2006).

[76] *BELLE* Collaboration, F.J. Ronga *et al.*, Phys. Rev. D **73**, 092003 (2006).

[77] M. Gronau and D. London, Phys. Lett. B **253**, 483 (1991); D. Atwood, I. Dunietz, and A. Soni, Phys. Rev. Lett. **78**, 3257 (1997); B. Kayser and D. London, Phys. Rev. D **61**, 116013 (2000); A.I.Sandra, hep-ph/0108031.

[78] *BABAR* Collaboration, B. Aubert *et al.*, Phys. Rev. D **74** 031101 (2006)

[79] M. Diehl, G. Hiller, Phys. Lett. B **517**, 125 (2001).

[80] M. Diehl, G. Hiller, "New ways to explore factorization in B decays", hep-ph/0105194

[81] *BABAR* Collaboration, B. Aubert *et al.*, Phys. Rev. D **73** 071103 (2006)

[82] CMS Collaboration, CMS Physics TDR, vol 2, CERN/LHCC **2006/021** (2006)

[83] V. Brigljević *et al.* "Study of Di-Boson Production with the CMS Detector at LHC", J. Phys. **G34**, 269 (2007)

Publications

Appendix A

Field Measurement of the *BABAR* Solenoid

The `Mermaid` computing code has been successfully used to calculate the magnet system of the particle detector for a High Energy Physics experiment for the first time. The results of this work, in which I have participated, are described in *BABAR* Note#344 "Magnetic Field Calculations in the *BABAR* Detector".

This appendix summarizes the results of measurements and modeling of magnetic field of the *BABAR* solenoid in the central tracking region. They were obtained in collaboration with SLAC magnet group and described in *BABAR* Note#514 "Field Measurement of the *BABAR* Solenoid".

The *BABAR* experience of magnetic field calculations and field mapping in the central tracking volume has been shared with the other collaborations such as ATLAS and T2K. I have been invited to present the *BABAR* field map experience on the ATLAS magnetic field workshops held at CERN, March and November 2005 and meeting of the T2K tracker group. Due to a complex design of the magnetic system of the ATLAS detector cross checks of calculations are required. The experience of `Mermaid` calculations for *BABAR* has been successfully used to verify the TOSCA computations of the magnetic field in the toroid.

Field Measurements of the *BABAR* Solenoid

Abstract

The magnetic field within the BABAR super conducting solenoid (3.8 m *long by 3* m *diameter, at a field of 1.5 T) has been measured with a set of hall probes placed on a mechanical arm that rotated about, and moved along, the axis of the coil. The measurements were fit to a functional model which contains polynomial terms to order 40 for the B_z and B_r field components, a few trigonometric-Bessel terms having one-, two-, and six-fold ϕ symmetry, and 24 dipole terms positioned on the end plates to describe the non-uniform iron distribution of these plates. The measurements and the model agree to 1.7 G (rms) within the drift chamber tracking volume, and to 5 G in the fully mapped volume ($-1.8 < z < 1.8$ m, $r < 1.3$ m).*

A.1 Overview

The *BABAR* detector contains tracking and particle identifying devices that measure properties of tracks produced in the interaction region of the e^+e^- beams at PEP-II. Two subsystems in the detector, the drift chamber and the silicon vertex chamber, provide the positions and angles of the charged particles. These chambers are also immersed in a 1.5 T magnetic field so that the momentum of charged particles can be measured. The magnetic field is generated by a super conducting solenoid, 3.8 m long and 3.0 mm in diameter. The coil is surrounded by an iron return path that has a hexagonal cross section, and by end plates (doors) that provide the pole faces for the field. A schematic side view of the detector magnet is shown in Figure A.1. The doors can be moved out of the way for access to the chambers inside. The doors and the hexagonal sides are called the instrumented flux return (IFR) because they are constructed from multiple parallel plates of iron separated by spacers to provide gaps for tracking detectors that measure the trajectory and range of particles passing through the iron.

The magnetic field within the tracking volume (shaded region in Figure A.1) of the drift chamber ($r < 0.8$ m, $|z| < 1.4$ m, and particle production angles between 17 to 255°) must be known to high precision. The field outside of the tracking volume need not be known that precisely since the particle trajectories in this region are smeared by multiple scattering in the DIRC and calorimeter systems.

This document deals with the magnetic field produced by the solenoid in the absence of any PEP-II beam line components, namely the B1 and Q1 permanent magnets located on the axis within the solenoid. These permanent magnets produce fringe fields of approximately 100-200 G at the inner layers of the drift chamber [1]. Note that the z-coordinate system used in this document is zero at the center of the magnet. The interaction point is at -370 mm in this coordinate system.

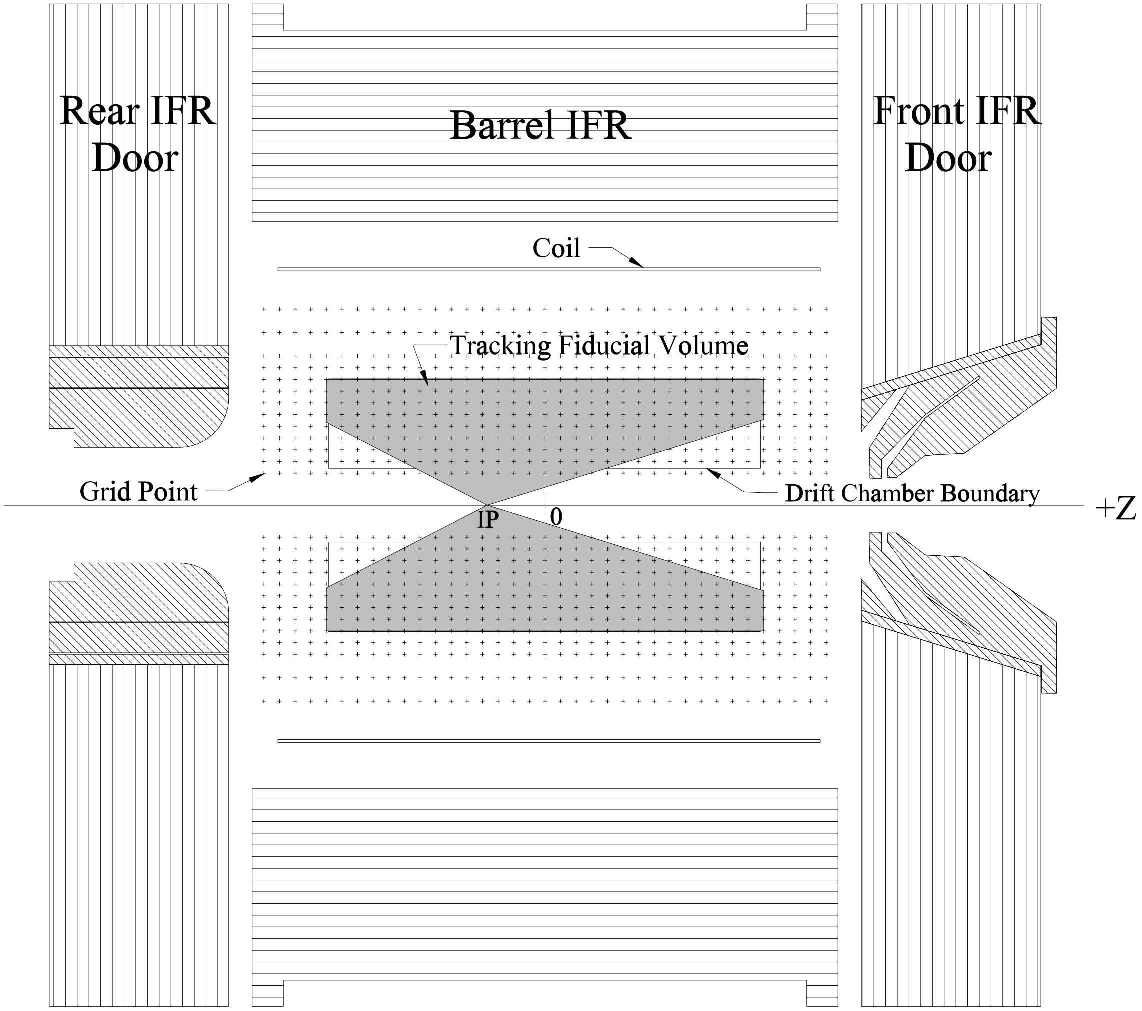

Figure A.1: *A schematic view of the BABAR magnet system. Shaded region shows the tracking fiducial volume. The grid points (plus signs) show the fully mapped region.*

The question arises as to how well the magnetic field must be known through out the tracking volume. The momentum resolution of the 40-layer drift chamber is at best approximately 0.3% if the field is known perfectly. This implies that the random errors in the field determination need not be better than about a tenth of a percent (15 G). However, systematic errors in the field determination can lead to momentum errors larger than the statistical error. Simulation studies [2] show that systematic field errors of only $1 \div 2$ G can produce visible changes in the parameters of reconstructed tracks, indicating that the field should be measured to better than 2 G within the tracking volume.

Another source of error in the field comes from the non-uniform distribution of iron in the end plates. Each end plate has a centrally located hole for placement of the PEP-II beam line components. The rear end plate also has through holes for signal cables from the drift chamber and vertex chamber, holes for the plug removal assembly (rails and screw leads), and slotted holes for the DIRC bar boxes. Iron has also been removed in the top portion of the rear end plate to provide a channel for cryogenic services to the super conducting coil. All these holes reduce the longitudinal field and increase the transverse fields in the vicinity of the holes. Finally, the IFR spacers add iron, thereby increasing the longitudinal field near the vicinity of these spacers.

A.2 The measuring apparatus

The magnetic field was measured by means of a transport mechanism that could move a set of Hall probes throughout the inside volume of the solenoid. Five probes were oriented in the z direction, five in the radial (r) direction, and two in the ϕ direction to measure the B_z, B_r, and B_ϕ field components respectively. These probes were equally spaced along a radial direction, each having the same ϕ. In addition, there was one NMR probe at a fixed r and a phi value 180° from that of the other probes that measured the total field near the central axis of the magnet.

The transport mechanism consisted of a long spindle with a rotating inner shaft held inside a pipe, with one end of the pipe rigidly attached to a cart on wheels. The cart moved on precision rails along the spindle axis such that the spindle could travel through the central hole of the front end plate. This allowed the tip of the spindle to be positioned anywhere along the axis inside the solenoid with the end plate doors closed. A narrow plate (propeller) mounted at right angles to the rotating shaft at the tip end provided a platform for the probes. The probes were mounted rigidly on a separate plate, and this probe plate was in turn mounted on the propeller plate. In this way, the z coordinate of the probes was controlled by the cart position on the rails, the ϕ coordinate by the rotation of the spindle shaft, and the r coordinate by the placement of the probe plate along the propeller arm. The z and ϕ placement was done under computer control. The probe plate could be manually installed to one of three radial positions. The radial placement of the probe plate and the nominal coordinates of each probe on the plate are shown in Figure A.2.

Each pair of high accuracy B_z and B_r probes [3] were encapsulated together in one unit, while the less accurate B_ϕ probe was an individual unit. The units had the shape of a square bar with a 14×14 mm cross section, and the field sensitive point was at the cross section center, 9 mm from one end of the bar. Signal cables came through the other end of the bar. These cables and the NMR signal cable were threaded through the spindle tube all the way to the cart and then to the digitizing electronics.

Predictions of the fields in the *BABAR* magnet were made using the `Mermaid` computer program. Comparisons of the measurements with the predictions gave comfort-

R (m)	Position 1	Position 2	Position 3
0.089	NMR	NMR	NMR
0.130	Bz1, Br1		
0.205		Bz1, Br1	
0.280	Bz2, Br2		
0.355		Bz2, Br2	
0.430	Bz3, Br3		
0.505	Bp1	Bz3, Br3	
0.580	Bz4, Br4	Bp1	
0.655	Bp2	Bz4, Br4	Bz1, Br1
0.730	Bz5, Br5	Bp2	
0.805		Bz5, Br5	Bz2, Br2
0.880			
0.955			Bz3, Br3
1.030			Bp1
1.105			Bz4, Br4
1.180			Bp2
1.255			Bz5, Br5

Figure A.2: *The nominal radial coordinates of the B_z, B_r and B_ϕ Hall probes at each of three positions of the probe plate.*

ing assurance that there were no gross errors in the measurements.

A.3 Data sets

At each plate position, the shaft and probe arm were moved in a sequence of steps to provide measurements over a grid of points in z and in ϕ. The z grid ranged from -1.8 m to +1.8 m in steps of 0.1 m, while ϕ ranged from 0° to 345° in steps of 15°. A data set consists of a full range over the z grid points, and a full range of the 24 ϕ-grid points at each z setting. At each $z - \phi$ grid point, the field readings from the 13 probes ($5 - B_z$, $5 - B_r$, $2 - B_\phi$, and 1−NMR) were recorded, together with the coil current and environmental temperatures. Thus, the full field map used in the fit model, consists of 46320 points.

The following table shows the data sets that were taken at nominal field settings of 1.5 T and 1.0 T. The repeated cases are also shown in this table.

Data Set	Plate Position	Field
1	1	1.5
2	2	1.5
2a	2	1.5
3	3	1.5
3a	3	1.5
2L	2	1.0
3L	3	1.0

Table A.1: *The data sets. Data set names ending with "a" are repeated cases, and sets ending with an "L" are measurements at the lower magnetic field.*

Measurements were made at a standard reference point at $z = 0$ and $\phi = 0$ between grid movements in z. This provided a quality check for the measurements. Two probes (B_{Z3}, B_{Z4}) were found to have started drifting during the course of the measurements. These probes were dropped from the fits in data sets that showed any drifting

A.4 Corrections to the data

Knowing the placement and the alignment of the probes is crucial for measuring the magnetic field. For example, a 1 mrad rotation of a B_r probe in the (r, z) plane results in an error of 15 G in that probe from the 15000 G B_z field. Corrections for the probe locations and the probe orientations were obtained from alignment measurements where possible, or from fits to the data when measurements were not possible.

A.4.1 Corrections from surveyed measurements

The SLAC alignment group positioned the axis of the mapping hardware on the axis of the detector. The plane of the propeller was also adjusted to be vertical to compensate for any droop from horizontal of the long spindle. However, as the spindle was moved in z, small deviations of the center of rotation of the propeller and of the tilt of the probe plate were observed. Alignment surveys of the probe plate were made every time the probe plate was moved. Two tooling balls placed along the radial length of the probe plate provided the tilt of the plate in the (r, z) plane (giving mostly a B_r probe correction from the B_z field, but also a B_z probe correction where the B_r field was large). Two other tooling balls placed across the width of the plate measured the rotation of the plate in the plane perpendicular to r (giving mostly a B_ϕ probe correction from the B_z field). These alignment corrections were applied both to the probe coordinates as well as the probe field measurements. The latter required the knowledge of the three field components at a grid point. If one of the field components was not available at that grid point (due to a bad probe, or the ϕ probes being interspersed between the z- and r-probes), then interpolation from other grid points was made. Later, as the fitting model improved, the missing field components were obtained from the fitting equations in an iterative fashion.

The following alignment measurements were made:

1. the x and y coordinates of the center of rotation of the spindle tip were surveyed as a function of z.

2. the deviations of the propeller's rotational axis (angles) from the detector axis in the horizontal and vertical planes were measured as a function of z.

3. the probe plate angles were measured at phi steps of 45°between 0° to 315°, and the plate angles at each of the ϕ grid point were found by interpolation from these.

4. the radial placement of the plate on the arm, and the relative z and r locations of the probes on the probe plate were measured.

All of the above measurements, and a few parameters from the fit (see next section), were used to correct and transform the probe coordinates, the probe angles, and the probe fields to the exact grid points.

A.4.2 Corrections by fitting

The orientation of the field sensitive volume in the Hall probes must be known to better than 0.1 mrad if the fields are to be measured to $\leq$2 G. Errors in the orientation come from the placement of the field sensitive volume within the probe, the positioning of the probe in its fixture, the fixture location on the plate, and the plate geometry (flexure). During the initial installation of the probes on the probe plate, the plate was put into a large dipole test magnet and the probe orientations were adjusted to null the B_r and B_ϕ signals. Even so, the correction angle of each B_r and B_ϕ probe was put as a parameter into the fit, with a set of such parameters for each data set (since the plate was moved between data sets). There is a steady progression of the angle from -1.0 mrad to 0.5 mrad with the probe number, i.e. r, for most data sets, implying that the plate is curved along the r direction.

Probe #	1	2	3	4	5
B_z(factor)	-0.00015	0.00048	0.00026	0.00015	0.00018
B_r(factor)	0.0071	0.0053	0.0041	0.0044	0.0044
B_ϕ(G)	2.35	-1.86			

Table A.2: *Calibration correction factors from the fit for the B_z and B_r probes, and offset corrections for the B_ϕ probes.*

The absolute probe calibration is unknown at the 0.01% level. The manufacturer states that 0.1% precision is assured but that 0.01% precision requires yearly calibration. Since the magnetic measurements lasted several weeks, it is not clear what precision to expect. Thus, a calibration parameter for each Hall probe was put into the fit. Note that since the NMR provides a very accurate absolute field measurement at the 0.1 G level, fitting for Hall probe calibrations cannot shift the overall field scale very much. For the B_ϕ probes, the field is small, and the offset was found to be more important than the calibration. Table A.2 shows the calibration correction factors and offsets found by the fit.

The z origin of the spindle and the ϕ origin of the propeller could change slightly during the process of moving the probe plate between data sets. These errors were found by fitting for four Δz and four $\Delta\phi$ parameters, one pair for each data set relative to data set 2. The fitted values are Δz=(0.3, 0., 0.2, 0.9, 0.3) mm and $\Delta\phi$=(8.1, 0.0, -13.1, 33.1, -13.8) mrad for data sets (1, 2, 3, 2a, 3a), respectively.

Finally, the measured B_r and B_ϕ fields showed an irregular pattern versus ϕ at many z and r points, as illustrated in Figure A.3 by the dotted data points. This irregularity was most evident near the center ($z = 0$), and could not be explained by irregularities in the iron structure. It is most likely due to flexing of the propeller as it rotates about the spindle, changing the probe orientation at each ϕ setting. The magnitude of the irregularity, seen in the residuals from the fit, increases approximately linearly with the r coordinate. Corrections were made to the data for this flexure by adding parameters at each ϕ grid point for the change in orientation of the probes. This required 26 parameters for the r orientations (24 ϕ parameters and 2 parameters for the linear r dependence) and 26 similar parameters for the ϕ orientations. The corrected data points are considerably smoother after the flex corrections are applied, as shown in Figure A.3. The solid curves show the fits to the corrected data.

All of the above corrections were done in an iterative manner. Values of the correction parameters were used to correct the data before the next fit iteration, and the fit in turn produced new correction parameters.

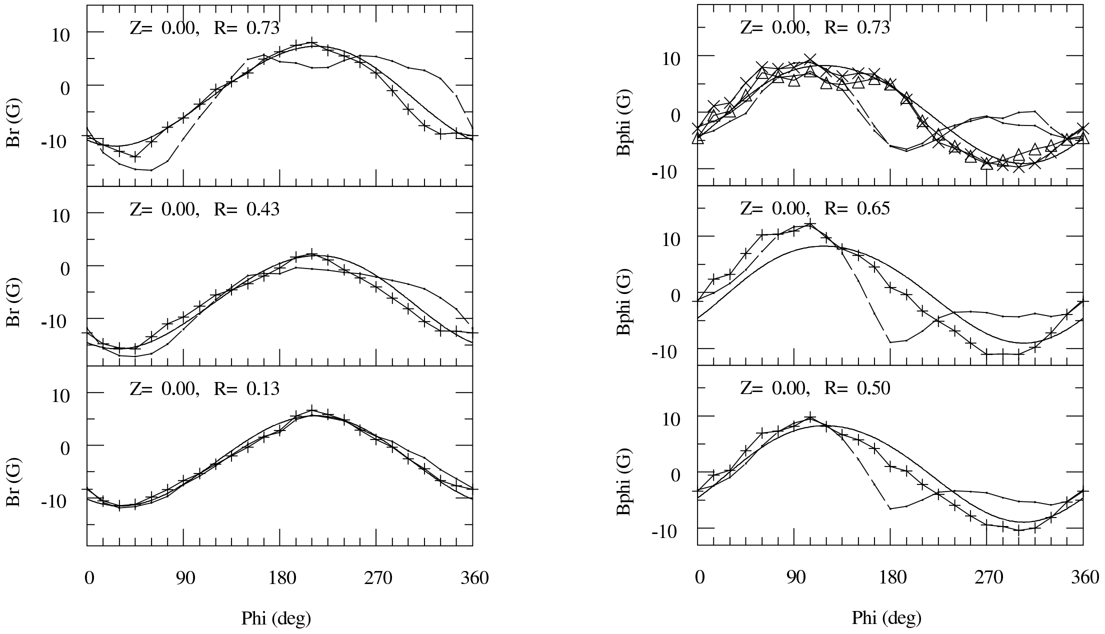

Figure A.3: *Distortions in the B_r and B_ϕ components due to flexure in the probe arm as a function of phi. The distortion increases approximately linearly with the radial location of the radial probe. The dots with dashed line show the data without any corrections for the arm flexure, while the plus signs show the corrected data points. The solid curve is the fit to the corrected data points.*

A.5 Magnetic field model

The equations for the magnetic field inside of the solenoid must satisfy Maxwell's equations. Since there are no magnetic sources within this volume, Maxwell's equations can be represented by a scalar potential satisfying the Laplace equation. The Laplace solutions are given in the next section for a cylindrical coordinate system based at the center of the solenoid. However, features such as holes in the *BABAR* iron end plates produce magnetic perturbations local to the end plate. It would require many terms to describe these perturbations by the centrally oriented Laplace solutions. These perturbations are better treated by functional terms located at each feature. These local functions (e.g. dipoles) are described in later sections.

A.5.1 The scalar magnetic potential

The magnetic field in a source-free region can be described by a scalar magnetic potential ψ satisfying the Laplace equation

$$\nabla^2\psi = 0 \tag{A.1}$$

When expressed in cylindrical coordinates, the solution $\psi(z, r, \phi)$ applicable to the inner volume of a solenoid is a linear combination of the following terms containing trigonometric, hyperbolic, and Bessel (I_n or J_n) functions,

$$\begin{array}{lll} (s_1 \sin(n\phi) + c_1 \cos(n\phi)) & \sin(kz) & I_n(kr) \\ (s_2 \sin(n\phi) + c_2 \cos(n\phi)) & \cos(kz) & I_n(kr) \\ (s_3 \sin(n\phi) + c_3 \cos(n\phi)) & \sinh(kz) & J_n(kr) \\ (s_4 \sin(n\phi) + c_4 \cos(n\phi)) & \cosh(kz) & J_n(kr) \end{array} \tag{A.2}$$

In these equations, n is an integer constant (0, 1, 2, ..), and $s_{1..4}$, $c_{1..4}$, k are arbitrary constants. Any field can be described by a sum of terms, each having its own set (s, c, n, k) constants.

The *BABAR* end plates have large holes along the axis for beam line components. These holes allow fields to extend in z outside of the end plates, with the fields decreasing at large z values. Field components with $\sin(kz)$ and $\cos(kz)$ terms are best suited to fit the decreasing field at large z, while terms with $\sinh(kz)$ and $\cosh(kz)$ that grow rapidly with z are not.

The Laplace potential function suitable for *BABAR* is then

$$\psi(z,r,\phi) = \sum_{n,i} \cos(n\phi - \phi_n)(s_{ni} \sin(k_{ni}z) + c_{ni} \cos(k_{ni}z))I_0(k_{ni}r) \tag{A.3}$$

If the field is symmetric in ϕ, then n and ϕ_n can be set to zero in the above equations. This is mostly the case for the *BABAR* magnet. However, it is found that a few terms with n values of 1, 2, and 6 are also required for the best fits to the data. The ϕ-symmetric Laplace potential function suitable for *BABAR* is

$$\psi(z,r,\phi) = \sum_{i} (s_i \sin(k_i z) + c_i \cos(k_i z))I_0(k_i r) \tag{A.4}$$

A.5.2 Laplace field functions.

The magnetic fields are given by the gradients of the magnetic scalar potential, $\vec{B} = - \bigtriangledown \psi$. In cylindrical coordinates, these are

$$B_z(z,r,\phi) = -\frac{d\psi}{dz},\ B_r((z,r,\phi) = -\frac{d\psi}{dr},\ B_z(z,r,\phi) = -\frac{d\psi}{rd\phi}. \tag{A.5}$$

The ϕ-symmetric field functions derived from the ϕ-symmetric Laplace potential function are

$$B_z(z,r) \ = \ \sum_{i} (s_i \cos(k_i z) - c_i \sin(k_i z))I_0(k_i r)$$

$$\begin{aligned} B_r(z,r) &= \sum_i (s_i \sin(k_i z) + c_i \cos(k_i z)) I_1(k_i r) \\ B_\phi(z,r) &= 0 \end{aligned} \tag{A.6}$$

These equations can be used to fit measured $B_z,\ B_r,\ B_\phi$ field values by choosing appropriate values for the k variables and fitting for the c coefficients. However, since the k values are arbitrary, it is difficult to pick an appropriate set that would minimize the number of terms required to fit the data. One attempt used the values $k_i = (i+1)/k_0$, with $k_0 \approx 0.5$ to match the approximate 2 meter detector size. It appeared that many terms were required to fit the data, and the computer time would be excessive.

An alternate method uses a set of polynomials to fit the data. Polynomials may be derived from the above set of equations by expanding each trigonometric or Bessel term into a series, collecting terms of equal rank, and replacing the resulting factors $\sum s_i k_i^n$ and $\sum c_i k_i^n$ by new fitting parameters P_n. It is then simple to fit these parameters for as many terms as needed to describe the data to a certain level of accuracy. These derived polynomial field functions are shown in the following section.

A.5.3 Polynomial field functions.

The series expansion of the ϕ-symmetric Laplace field functions in the previous section gives the following polynomial field functions, shown for terms up to order n

$$\begin{aligned} B_z(z,r) &= \sum_{i=0}^{n} P_i(i!)(-1)^{\frac{i+1}{2}} \sum_{k=0(2)}^{i} \frac{(-1)^{k/2} z^{i-k} r^k}{(i-k)!2^k((k/2)!)^2} \\ B_r(z,r) &= \sum_{i=1}^{n} P_i(i!)(-1)^{\frac{i+1}{2}} \sum_{k=1(2)}^{i} \frac{(-1)^{k/2} z^{i-k} r^k}{(i-k)!2^k((k/2)!)((k+1)/2)!} \\ B_\phi(z,r) &= 0 \end{aligned} \tag{A.7}$$

The $(i+1)/2,\ k/2$, and $(k+1)/2$ terms must be truncated to whole integers in the above expressions, and the k-summation is stepped by 2. Note that the same P_i fitting parameters appear in B_z and B_r in order to satisfy Maxwell's equations, since both equations are derived from the same magnetic potential.

The first few terms of each series are

$$\begin{aligned} B_z(z,r) &= P_0 - P_1 z - P_2\Big(\frac{z^2}{2} - \frac{r^2}{4}\Big) + P_3 \cdot 3\Big(\frac{z^3}{3} - \frac{zr^2}{2}\Big) + ... \\ B_r(z,r) &= P_1\Big(\frac{r}{2}\Big) - P_2(zr) + P_3 \cdot 3\Big(\frac{z^2 r}{2} - \frac{r^3}{8}\Big) + ... \\ B_\phi(z,r) &= 0 \end{aligned} \tag{A.8}$$

It was found that the fit was improved by using terms up to P_{40}.

A.5.4 ϕ-dependent fields.

Due to non ϕ symmetry of the *BABAR* magnet iron, the ϕ dependent field terms have to be added to the fitting model. These ϕ asymmetric features in the doors and barrel iron are:

1. The iron at the bottom region of the backward end plate has through holes for cable access and for the rails and lead screws of the plug removal mechanism.
2. The backward end plate has a vertically running channel at the top portion for services to the liquid helium cryostat.
3. Both front and back end plates are not solid iron but consist of many parallel plates of iron spaced apart for the RPC detectors. Iron spacers along the door boundaries and interior parts keep the plates separated, but these spacers also cause localized magnetic field concentrations on the end plate faces.
4. The front doors have vertically running channels at the top half where iron has been removed at the closing surfaces.
5. One of the front doors became warped during manufacture and was straightened by removing iron from the warped face.
6. The barrel iron has a hexagonal shape, which gives rise to distortion with six-fold symmetry at large radii.
7. Each hexagonal side in the barrel iron has access slots for cables, which distorts the field at large r and large z.

In order to fit the ϕ-dependent fields, other functional terms were added to the field model:

- A *magnetic dipole* term oriented along the Z-axis at each hole on the end plate gives an approximate representation of the field from the missing magnetized iron.
- For extended objects such as the linear RPC spacers, a rectangular shaped pole was used instead. A *rectangular pole* is achieved by placing a rectangular loop of current in the plane of the end plate that circumvents the object, giving a pole pointing along the z-axis over the length of the rectangle.
- The asymmetry due to the warped doors can be modeled in part by an *annular dipole* of varying width along its circumference. An annular dipole consists of two current loops in the plane of the end plate having opposite currents and origins slightly displaced from each other.

- The barrel iron surrounding the solenoid coil is in the shape of a hexagon, so a field component with six-fold symmetry in ϕ would be expected at large radii. This six-fold asymmetry can be modeled with a few trigonometric-Bessel terms (with $n = 6$) added to the fitting model. It was also found necessary to include trigonometric-Bessel terms with $n = 2$ and $n = 1$. The source for these fields is not precisely known, but a slightly flattened hexagonal barrel would give an $n = 2$ component, while a slightly off-centered component (coil or iron) could give an $n = 1$ component.

A.6 Fitting procedure

A non-linear least squares fitting program [4] was used to fit the model to the measured data. The fit varied parameters pertaining to the model as well as parameters that were corrections to the measured data. Some derivatives were computed analytically to reduce the computation time. The data from all good probes in all data sets (46320 total points) were used in the fit.

An assumed error of measurement of the probes for data points within the drift chamber tracking volume was as follows:

Probe	Precision
NMR	0.1 G
B_z Hall	1.0 G
B_r Hall	1.0 G
B_ϕ Hall	3.0 G

Because of the difficulty in modeling the field near the non-uniform iron, the assigned errors were increased (doubled) for points outside the tracking volume, and doubled again for the outer-most grid points in z and r.

A.6.1 Choice of fitting functions and parameters

The functional elements described above were included the fit. The number and placement of some of the elemental components such as the point dipoles for the holes and rectangular dipoles for the IFR spacer was straightforward. However, some of the elemental parameters like the number of polynomial terms or the placement of annular dipoles at the front door had to be determined by trial and error for best results (i.e. a decrease in χ^2 and improvement in residuals in the region of interest).

Fits were done with a varying number of polynomial terms to establish the minimum number that need be used. The χ^2 per degree of freedom decreases with the

Polynomial terms	χ^2/nDof
15	53.5
20	26.8
25	6.93
30	3.97
35	3.16
40	2.89
50	2.87

Table A.3: *The* χ^2 *per degree of freedom as a function of the number of polynomial terms used in the fit.*

number of polynomial terms below 40 terms, with little improvement beyond that as shown in Table A.3. Forty terms were used in the final fits.

Establishing the number of other functional elements and their parameters (e.g. coordinates and strengths of dipoles, coordinates, strengths, and area of rectangular poles, number of Bessel elements, etc.) required numerous fits to be done, adding a few components at a time. The final configuration included 80 fitting parameters, as follows:

4	Magnetic axis terms (X_0, Y_0, θ_{XZ}, θ_{YZ})
40	Polynomial strength
1	Bessel (n=1)
2	Bessel (n=2)
3	Bessel (n=6)
9	Dipole, (22 total)
14	Rectangular pole, (20 total)
7	Annular pole

The locations of all the poles on the front and rear end plates are shown graphically in Figures A.4, A.5, respectively.

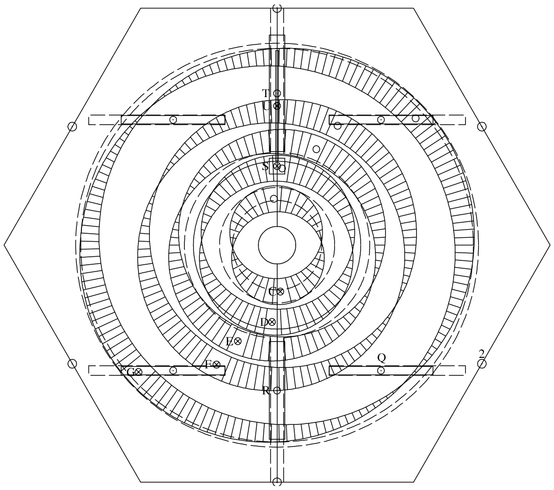

Figure A.4: *The locations of rectangular and annular poles on the front end plate.*

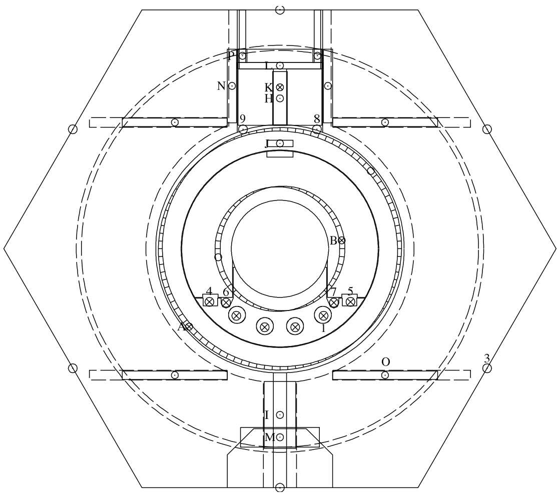

Figure A.5: *The locations of all poles on the rear end plate.*

A.7 Results

A resulting χ^2 per degree of freedom of 2.89 is found in the final fit. This implies that the model is not yet complete, or that the assumed measuring errors (e.g. 1.0 G for B_z probes) enumerated previously are too small, or some combination of the two. Increasing all the measuring errors by a factor of 1.7 is well within the estimate of the probe precision, and doing so would give the ideal fit with a χ^2 per degree of freedom of 1.0. The root mean square of the residuals is 1.7 G for points within the tracking fiducial volume and 4.8 G for all the measured points. Examples of the corrected measurements superimposed with the fitted curves for the B_z and B_r fields versus z at ϕ=0 are shown in Figure A.6.

A.8 Conclusions

The magnetic mapping data for the *BABAR* solenoid magnet has been fitted with a model containing polynomial terms for the coil field, and Bessel/trigonometric terms, dipoles, and other loops of currents that provide local field perturbations from the non-uniform distribution of iron on the end plates. The data and the model agree to 1.7 G (r.m.s.) for grid points within the tracking volume of the drift chamber, and to 4.8 G for the full measured volume ($|z| < 1.8\,\mathrm{m}$, $r < 1.3\,\mathrm{m}$). The above source files have also been combined with the model for the fringe fields from the beam line components [1].

Acknowledgments. We acknowledge the valuable help from Stepen Mikhailov in calculating

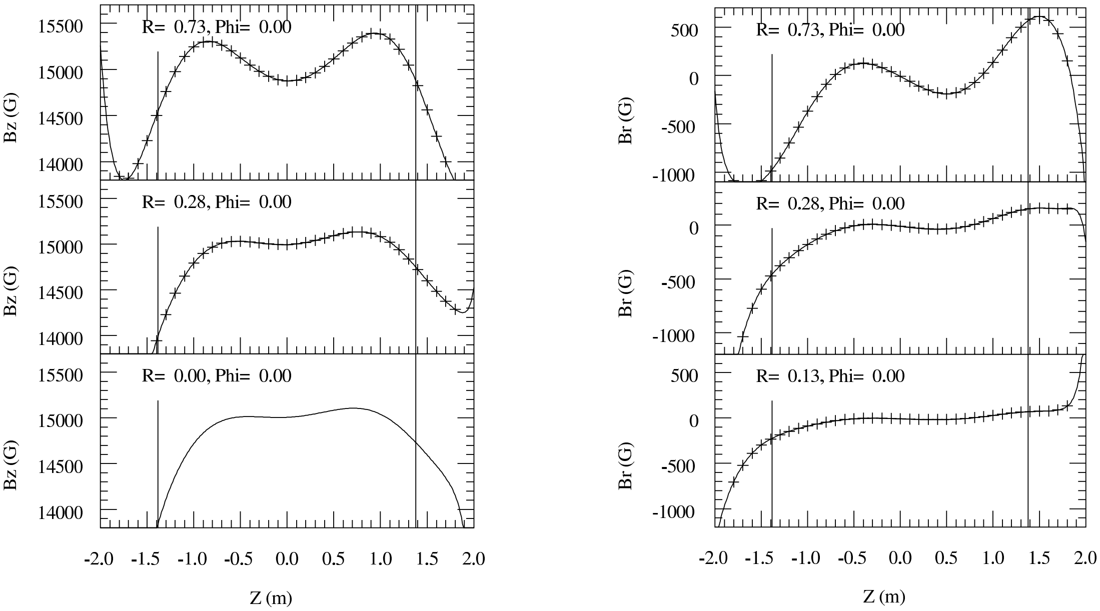

Figure A.6: *The B_z (B_r) field as a function of z at three values of r with $\phi = 0$. The plus signs show the corrected data points while the solid lines come from the fitted model. The vertical lines at $z = -1.4\,\mathrm{m}$ and $z = 1.4\,\mathrm{m}$ show the drift chamber bounds along the z coordinate. The top plot shows the field at $r = 0.73\,\mathrm{m}$ (between super layer 9 and 10), the middle plot is at $r = 0.28\,\mathrm{m}$ (middle of super layer 1), and the bottom plot is at $r = 0$ along the axis of the chamber.*

the field predictions for *BABAR* using the `Mermaid` computer program.

Bibliography

[1] Bill Dunwoodie, SLAC. The field measurements around the permanent B1 and Q1 magnets have been made, together with a fit to model equations. These results will be given in a future publication.

[2] Art Snyder, SLAC. Private communication.

[3] SENTRON AG, Two Axes very high accuracy Hall Probe, 2MR-4A/3B-14B25-20. The specification for the B_z component is 0.01% short term and $< 0.1\%$ long term, while the B_r component is 0.1%. Alignment tolerance for both components is $\pm 9\,\mathrm{mrad}$.

[4] SOLVE, A SLAC based least squares fitting program, C. Moore, SLAC, 1965.

Appendix B

Particle identification with ATC

This appendix presents a syntheses of my activity in period 1995-1997 being a member of *BABAR* Novosibirsk group. It was devoted to the research and development of the forward particle identification system based on Aerogel Threshold Counters (ATC) for *BABAR*. I summarize the results obtained with the prototypes of the 4-layer design developed by Novosibirsk group. These prototypes were tested with the pion and proton beams at CERN in 1995. The results of these tests are described in *BABAR* Note#290 "Prototype performance of a 4-layer aerogel Cherenkov detector". We developed a method to measure the optical parameters of aerogel samples in laboratory [1], which is also summarized in this appendix. One notes, that I am the author of a set of publications devoted to the research and development of the aerogel Cherenkov counters for the particle identification [2, 3, 4, 5, 6].

Prototype performance of a 4-layer aerogel Cherenkov detector

B.1 Project of 4-layer ATC system for *BABAR*

In the *BABAR* Technical Design Report [7], the particle identification system is completed in the forward region with an aerogel detector. Figure B.1 shows the proposed design for the 4-layer option of the ATC system of *BABAR*. A 4-layer design consists of 2 super-layers, where each one has two counters with low (n=1.008) and high (n=1.05) aerogel refractive indices. It allows us to perform the π/K identification between 0.4 and 4.3 GeV/c. The second super-layer is shifted (by a half of the counter size) with respect to the first one, in order to prevent a loss of signal when a particle crosses the photo-tube window in one of the layer. The aerogel blocks are placed inside a boxes wrapped with multiple layers of high reflectivity white PTFE film. Each high (low) index counter is read out by two (three) 2" (19 stages) Hamamatsu fine-mesh photomultipliers with UV glass window. The photomultipliers are parallel to the particle direction and has 20° with respect to the magnetic field vector. The 4-layer design of ATC system counts 280 photomultipliers in total.

In order to test the performances of such a detector, two prototypes: one with low and another with high aerogel indices were constructed. The dimensions of such prototypes were chosen to be close to the mechanical design of 4-layer system.

B.2 The prototype of 4-layer counters

Figures B.2, B.3 show the 4-layer prototypes with low and high aerogel indices, respectively.

Two sets of aerogel blocks with 69 mm thick were tested with low refractive index prototype: one set with n=1.012 produced by the Boreskov Catalysis Institute in Novosibrsk (SAN), and a second one with n=1.008 produced by the Jet Propulsion Laboratory (JPL). The counter is read out by three 2" Hamamatsu fine-mesh photomultipliers. The prototype with high aerogel index was filled with 21 mm thick aerogel produced in Boreskov Catalysis Institute in Novosibrsk (SAN-95) with the refractive index of 1.05. The high index aerogel counter is read out by two 2" Hamamatsu fine-mesh photomultipliers declined at 20° with respect to the counter surface. The walls of both counters were wrapped with three layers of 250μm PTFE film on top of aluminized mylar.

In order to remove water from the aerogel, all the blocks were baked before exposing them to the beam. A three stage annealing procedure has been applied for the

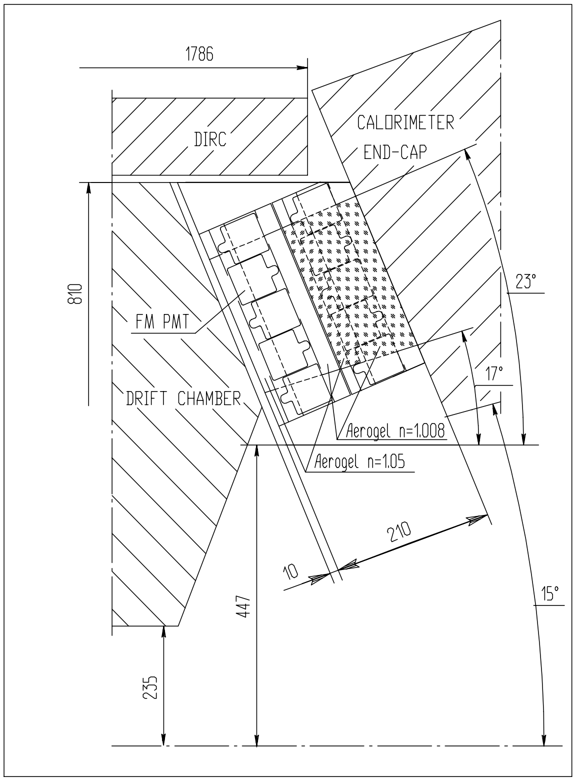

Figure B.1: *The BABAR ATC detector in the 4-layer option and fine mesh reading.*

aerogel placed in the special oven: slow increase by 1.6° C/min from room temperature up to 500° C with consequent 3 hours keeping of 500° C and slow return to room temperature with maximum decrease slope of 1.6° C/min.

B.3 Beam line

The prototypes of 4-layer design of ATC system has been tested at the CERN PS T10 test beam together with two other prototypes of 2-layer design: one with hybrid photodiode (HPD) readout [4] and a second one with fine-mesh readout [5].

The T10 beam line can provide positive and negative particle beams with momenta between 1 and 5 GeV/c. The beam composition were mainly pions and protons, with a small kaon and electron contamination. The beam line shown in Figure B.4, was equipped with two CO_2 Cherenkov counters, C1 and C2, filled to a pressure of 4.3 bar. The beam was defined by coincidence of three scintillator counters, its extension being limited by the third counter S3 ($1 \times 1\,\mathrm{cm}^2$). Another thick (1 cm) veto scintillator counter was read out in a CAMAC scaler, in order to count the number of particles crossing our setup in a $1 \mu\,\mathrm{s}$ gate. Three prototypes were placed on a horizontally and

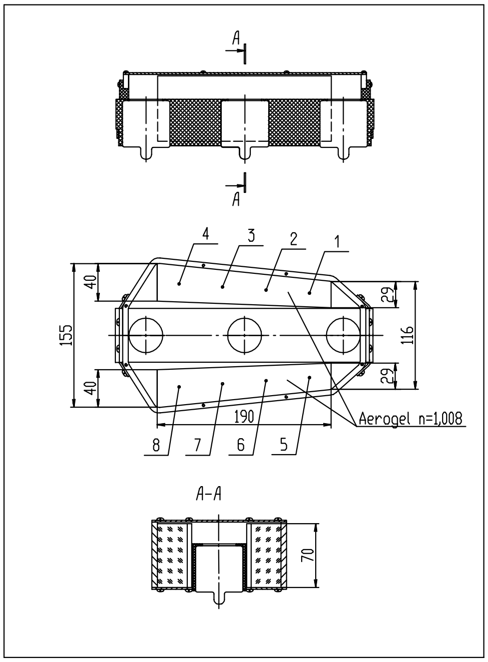

Figure B.2: *The prototype counter for low index aerogel*

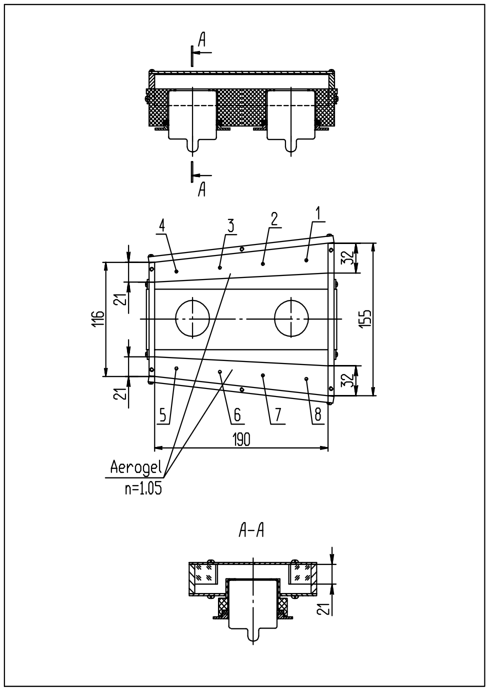

Figure B.3: *The prototype counter for high index aerogel*

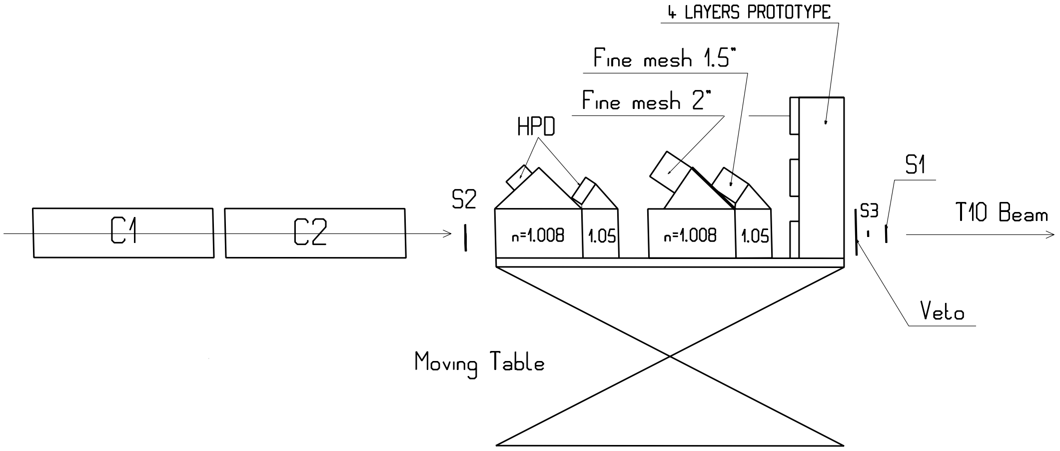

Figure B.4: *The T10 beam line with the apparatus*

vertically moving table.

Three kind of triggers were assembled:

- *Beam.* A beam event was the the coincidence of the 3 counters S1, S2, and S3. Two Cherenkov counters C1 and C2 were included in anti-coincidence for runs with protons;

- *Pedestal.* We recorded pedestal events inside and outside burst;
- *Calibration.* The photo-detectors were calibrated using a light emitting diode (LED).

B.4 Aerogel and reflector

Method described in [1] allows us to perform a measurement of absorption length in aerogel and quantity of the reflector.

A special code allows us to describe the processes of the light absorption and propagation in the aerogel counter. It assumes Rayleigh scattering phenomenon with an associated λ^4-dependent interaction length; this latter is 4.0 cm at 436 nm, and the diffusive emission according to the Lambert's low. The light monochromator is used to measure the light collection as a function of wavelength. Such a result is introduced in the code that solves the inverse problem. The light collection measured in the empty counter allows us to compute the absorption in the reflector. Figure B.5 shows the obtained reflection coefficient (R) as a function of wavelength. We also measure the light collection in the counter box filled with aerogel and introduce this result in the code. Using the previous result for the reflector, we compute the light absorption length in aerogel. Figure B.6 shows the results of such a measurement.

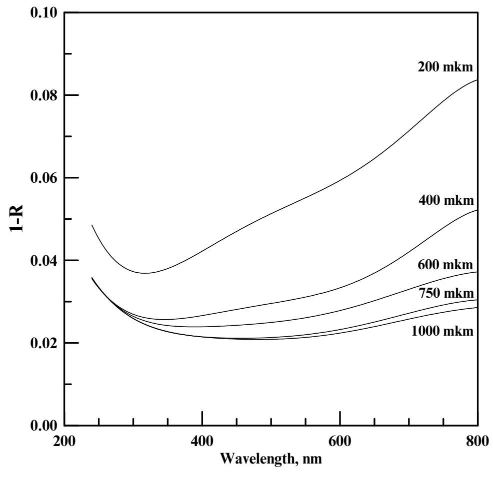

Figure B.5: *The absorption coefficient (1-R) of PTFE film as a function of wavelength. Curves present the different thickness of the wall coverage.*

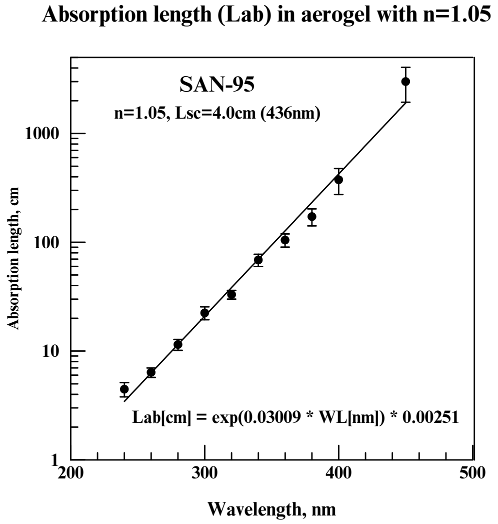

Figure B.6: *The absorption length of aerogel with n=1.05 (SAN-95) used in the prototypes.*

B.5 Photo-detectors

A study of particle identification performances of the threshold Cherenkov counters requires a knowledge of the single photoelectron and the noise frequency spectra of photomultiplier at small amplitude. We have measured these spectra for one of the fine-mesh photomultipliers used in the prototypes. It has a typical gain of 10^7 with absence of a magnetic field. Figure B.7 shows the results of such a measurement. We assumed 100% detection efficiency at the minimal possible threshold, while 1 photoelectron is defined at 50% efficiency level. Such a definition differs from the standard calibration described below about of 10%. One observes, a minimal applied threshold is about 100 times smaller then a single photoelectron amplitude. We estimate the contribution of 8 kHz noise at this threshold to the detection efficiency of particles with momentum below a Cherenkov threshold to be about 0.2%.

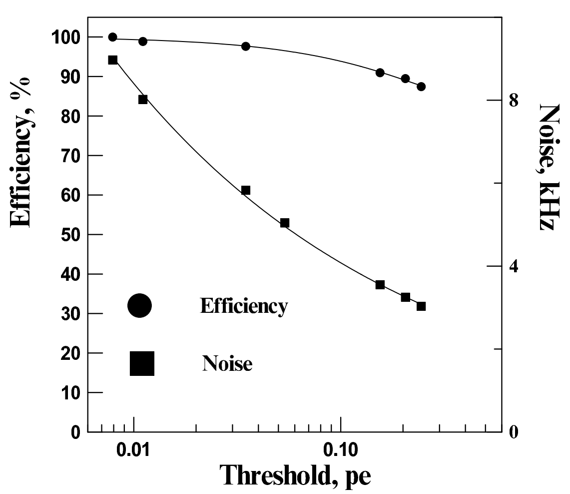

Figure B.7: *Detection efficiency of the single photoelectron and frequency of the noise as a function of threshold for Hamamatsu fine-mesh phototube.*

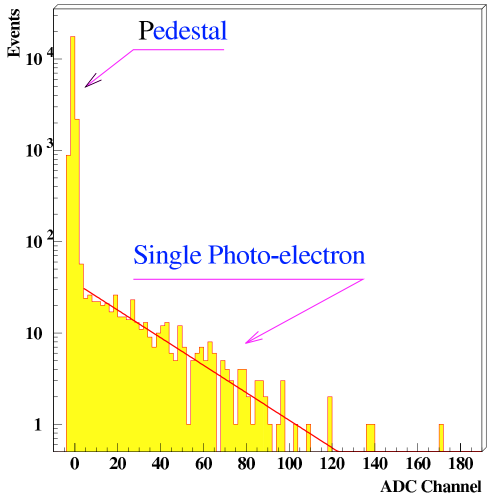

Figure B.8: *A LED run for 2" photo tubes. The peak at zero corresponds to a "0" photoelectron.*

A fine mesh photomultiplier calibration is a delicate procedure since this phototube does not permit to resolve the single photo-electron (p.e.) peak. We injected in the counter box the light pulses of a LED turned such that about 95% of the "calibration" trigger result "0" p.e. detected (pedestal). Figure B.8 shows a typical spectrum. The probability of 1 p.e. appearance is determined by Poisson distribution with an expected value:

$$\mu = -\ln \frac{n_0}{N}$$

where n_0 is the number of events contained in the pedestal and N the total number of events. We propagate the shape of the distribution in the pedestal region with a liner function. The calibration constant is computed by the mean value of such an extrapolated distribution between zero ADC channels and infinity. Contribution from more then 1 p.e. is determined by Poisson distribution. The calibration constant can be corrected by multiplying it by:

$$\xi = \frac{1 - e^{-\mu}}{\mu} = \frac{\frac{n_0}{N} - 1}{\ln \frac{n_0}{N}}$$

We estimate the total (statistics and systematic) error of the calibration to be about 4%.

B.6 Results

Aerogel counters were exposed to a 5 GeV/c negative pion beam ($\beta \simeq 1$). The events were selected by requiring a clean signal in both gas Cherenkov counters, and by asking only 1 count within 1μs in the veto counter to reduce pile up events. The observed number of photoelectrons in the prototypes are summarized in Table B.1. In order to investigate a non uniformity of the light collection in the counter, prototypes were exposed in four different points, shown in Figures B.2, B.3. We also present in this table a distribution of a total number of photoelectrons in each photomultiplier that readout the counter. The aerogel blocks produced by the Boreskov Catalysis Institute in Novosibrsk (SAN-95) were placed into high refractive index counter (n=1.050). Two sets of aerogel blocks were tested with low refractive index prototype: one set with n=1.012 produced by the Boreskov Catalysis Institute in Novosibrsk (SAN), and a second one with n=1.008 produced by the Jet Propulsion Laboratory (JPL).

A comparison of the light yield normalized on the same refractive index shows that the SAN aerogel has better optical parameters then the JPL one. Indeed, about 33% difference in intensities of Cherenkov light causes about 43% in the light yield. One has to note, a measured uniformity of the light collection in the counters for 4-layer ATC design is about 10%.

A signal induced by particles with momentum below the Cherenkov threshold contributes to the particle identification efficiency of the ATC counter as a background. We have studied such a signal with low aerogel index prototype by selecting a 5 GeV/c proton beam. Absence of signal in both gas Cherenkov counters was required to trigger such events. In order to diminish a kaon contamination, we eliminated the events that produce a signal in the low index (1.008) prototype readout by HPD and located in front of our counter.

The background is due to δ-rays, Cherenkov light in the PTFE wrapping, and scintillation in either aerogel or wrapping. From a Monte Carlo simulation of the beam line, we find that at 5 GeV/c, about 2% of the protons produce δ-rays above the Cherenkov threshold in the aerogel. To eliminate the contribution of the δ-rays produced in aerogel, a dedicated run with a 1 GeV/c proton beam has also been performed. We have used an amplitude information from S1 and S2 scintillator counters.

Point	n	PMT1	PMT2	PMT3	SUM
1	1.050 (SAN-95)	8.6	2.5	-	11.1
2	1.050 (SAN-95)	8.1	3.7	-	11.8
3	1.050 (SAN-95)	4.5	8.0	-	12.5
4	1.050 (SAN-95)	3.2	9.3	-	12.5
1	1.012 (SAN)	1.9	3.6	5.0	10.5
2	1.012 (SAN)	2.1	4.7	3.3	10.1
3	1.012 (SAN)	2.8	5.0	2.6	10.4
4	1.012 (SAN)	3.5	4.0	2.0	9.5
1	1.008 (JPL)	1.0	2.0	2.7	5.7
2	1.008 (JPL)	1.2	2.6	1.8	5.6
3	1.008 (JPL)	1.6	3.1	1.3	6.0
4	1.008 (JPL)	2.2	2.5	1.1	5.8

Table B.1: *Detected number of photoelectrons in the different exposing points of the prototypes. The impact points correspond to the positions indicated in Figures B.2, B.3. The aerogel blocks produced by the Boreskov Catalysis Institute (SAN) and by the Jet Propulsion Laboratory (JPL) were tested in the prototypes.*

A different energy loss for these spices (dE/dx) allowed us to suppress a non-proton contributions.

Figures B.9, B.10 show the proton contamination: $\mathcal{P}(p \rightarrow \pi)$ and the pion inefficiency: $\mathcal{P}(\pi \rightarrow p)$ as a function of the cut we apply to decide if an event corresponds to a pion or a proton. For convenience, the cross point of equal probabilities is considered as a merit of our detector and permits us to compare different configurations.

B.7 Conclusion

A test of aerogel Cherenkov counters based on 4-layer design of the ATC system of the *BABAR* detector has been performed. Two prototypes equipped with aerogel blocks of low (1.008) and a high (1.050) refractive indices have been exposed by pion and proton beams. The observed average number of photoelectrons for $\beta = 1$ particles is greater then 10 p.e. for the high aerogel index, about 8 p.e. for the low index. The walls of the counters were wrapped with three layers of 250μm PTFE film on top of

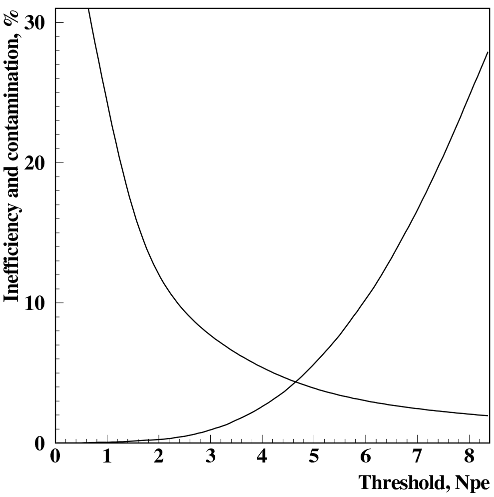

Figure B.9: *$\mathcal{P}(\pi \to p)$ and $\mathcal{P}(p \to \pi)$ as a function of the threshold in photoelectrons for the high index prototype.*

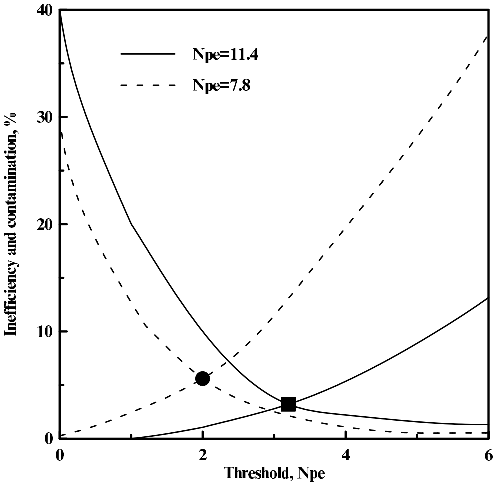

Figure B.10: *$\mathcal{P}(\pi \to p)$ and $\mathcal{P}(p \to \pi)$ as a function of the threshold in photoelectrons for the low index prototype. The different curves correspond to configuration with different average number of photoelectrons for $\beta = 1$ particles.*

aluminized mylar. A complete Monte Carlo simulation of the counter based on the measured optical parameters of aerogel and reflector shows a good agreement with the data.

The study of background induced by particles with momentum below the Cherenkov threshold has also been performed. The prototype with low aerogel index allows us to reach a pion efficiency of 96% for a proton misidentification as low as 4%.

We conclude that silica aerogel readout by fine mesh photomultipliers can be used to construct a powerful and compact particle identification device in the momentum range of 0.6-4.3 GeV/c.

Bibliography

[1] A.R. Buzykaev *et al.* “Measurement of optical papameters of aerogel”, Nucl. Instr. Methods Phys. Res., Sect. A **433**, 396-400 (1999)

[2] K.Arisaka *et al.*, ”Recent results on Prototype Aerogel Threshold Counters for Particle Identification in the Region 0.5-4.3GeV/c”, Nucl. Instr. Methods Phys. Res., Sect. A **379** 460-464 (1996)

[3] K.Arisaka *et al.*, ”Four-layer aerogel Cherenkov counter”, Journal of Non-Crystalline Solids 225(1998) 375-380.

[4] D.Boutigny *et al.*, ”Performance of an aerogel threshold particle identification detector readout by Hybrid Photon Detectors”, IEEE Trans. Nucl. Sci. **44**, NO.4, August 1997, 1621-1629.

[5] K.Arisaka *et al.*, ”Performance of a Prototype Aerogel Counter Readout by Fine Mesh Photo-tubes”, Nucl. Instr. Methods Phys. Res., Sect. A **385** 74-80 (1997)

[6] A.R.Buzykaev *et al.*, ”Project of Aerogel Cherenkov Counters for KEDR”, Nucl. Instr. Methods Phys. Res., Sect. A **379** 453-456 (1996); A.Buzykaev *et al.*, ”Aerogel Cherenkov counters with wavelength shifters and micro-channel plate phototubes”, Journal of Non-Crystalline Solids 225(1998) 381-384; M.Barnyakov *et al.*, ”Development of aerogel Cherenkov counter with wavelength shifter and phototubes”, Nucl. Instr. Methods Phys. Res., Sect. A **419** 584-589 (1998); M.Barnyakov *et al.*, ”Aerogel Cherenkov Counters for the KEDR Detector”, Nucl. Instr. Methods Phys. Res., Sect. A **453** 326-330 (2000)

[7] *BABAR* Technical Design Report, D. Boutigny *et al.*, SLAC-R-95-457, March 1995.

Appendix C

Simulation and Measurement of the Fringe Field

This appendix includes the complete report of “Simulation and Measurement of the Fringe Field of the 1.5 Tesla *BABAR* Solenoid” published in Nuclear Instruments and Methods (E.Antokhin et.al., Nucl. Instr. Methods Phys. Res., Sect. A **432**, 24 (1999)). Simulation and measurement of the fringe field of the *BABAR* solenoid have been performed in collaboration with G. London, E. Antokhin, and S. Singatulin in 1996-1998.

Simulation and Measurement of the Fringe Field of the 1.5 Tesla *BABAR* Solenoid

Abstract

In the context of the SLAC PEP-II asymmetric e$^+$*e*$^-$ *collider and the BABAR detector with its 1.5 Tesla solenoid, we have calculated and measured the fringe field at the nearby beam elements and at the position of the photomultipliers external to the return iron but within a specially designed iron shield. The comparisons of these measurements with the simulations based on finite element analysis are remarkably good, within about 5 G at the most critical beam element. The field at the photomultipliers is less than 1 Gauss, in agreement with the simulation. With a simple method of demagnetization of the shield, a maximum field of 0.6 G is obtained.*

C.1 Introduction

C.1.1 *CP* violation: PEP-II and *BABAR*

The study of B^0 decays and the resulting *CP*-violating asymmetries will test our understanding of the Standard Model. The SLAC PEP-II asymmetric e^+e^- collider [1] (9 GeV electrons interacting with 3.1 GeV positrons), now in construction, will produce the $\Upsilon(4S)$ state with a $\beta\gamma$=0.56. The boost of the decaying B^0 in the laboratory enables the measurement of the time order of the B^0-$\overline{B}^0$ pairs, crucial to detect *CP* violation.

The *BABAR* detector [2] will surround the interaction point, IP, in an asymmetric way to allow more flight path for the particles in the electron direction. In order to maximize the luminosity, the machine elements must be very close to this interaction point; therefore *BABAR* and the last elements are very close to each other.

The detector, which is in construction, consists of a 1.5 Tesla solenoid with an iron flux return in the form of a barrel closed by two end caps, consisting of two doors each, in addition to a number of sub-detector elements, namely from the IP radially out, the Silicon Vertex Tracker, Drift Chamber, *DIRC* (Detector of Internally Reflected Čerenkov light), CsI Calorimeter and Instrumented Flux Return for Muon Detection. It is shown in Figure C.1 with the nearby machine elements, and schematically in reffig:side which emphasizes the magnetic elements. Since the elements are symmetric about the interaction point, their relationship to the detector is quite different in the two directions; for example, notice the position of Q2 with respect to the flux return.

Notice also that since the detector and machine elements are in close proximity, the final elements are in a very strong fringe field. This field could degrade the performance of the quadrupoles, reducing the luminosity significantly and the possibility to detect *CP* violation.

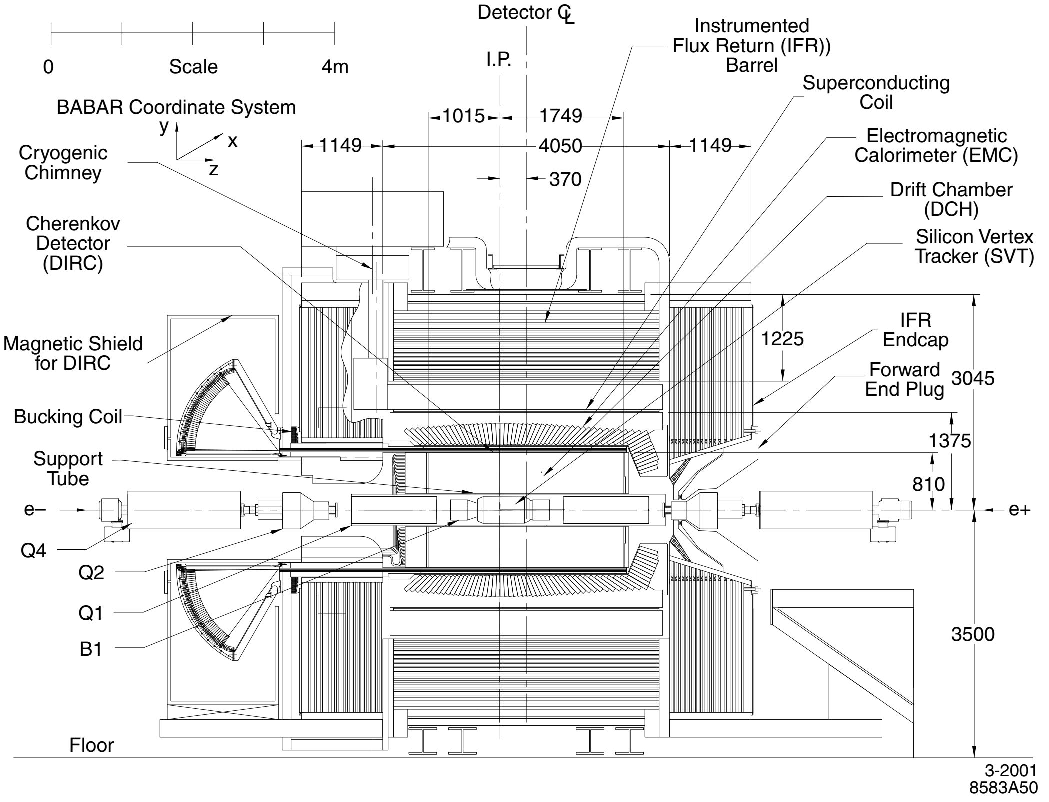

Figure C.1: *Side view of BABAR. The magnet right-handed coordinate system is given by the* $e^- = +Z$ *direction and the vertical direction* $= +Y$ *with the origin at the center of the magnet.*

C.1.2 *DIRC*

The *DIRC* [3] is the principle particle identification system of *BABAR*. It consists of quartz bars inside the detector and of a large pure water tank (the StandOff Box, or *SOB*) supporting photomultipliers outside the detector. The quartz bars and the *SOB* are supported by a complex mechanical structure which is attached to the outside of the barrel iron via an external support structure (ESS) composed of a structural element in the form of a "horsecollar" and a gusset plate.

Charged particles, produced at the interaction point inside the detector, traverse the quartz bars in which Čerenkov radiation is produced. The angle of this radiation with respect to the incident particles is a measure of the speed of these particles. The Čerenkov photons are propagated along the length of the rectilinear bars by total internal reflection, preserving the angular information and exiting outside the detector into the *SOB*. This water tank is composed of a cylinder, cone and 12 sectors which are cylindrical sections. The photomultipliers are mounted on the sectors placed at about 1.17 meters from the exit point to permit a precise measurement of the angle

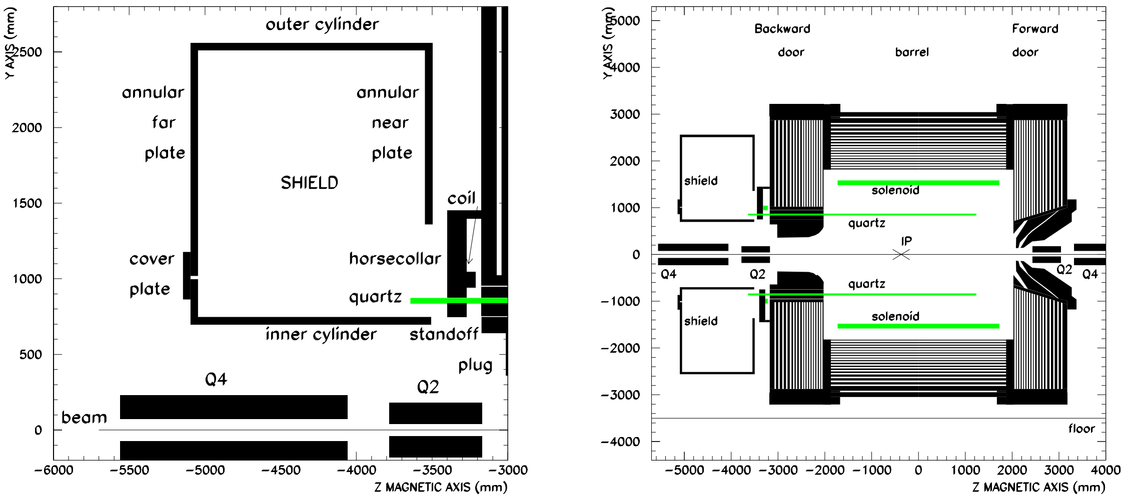

Figure C.2: *Schematic side view of the active and passive magnetic elements of the BABAR detector and nearby PEP-II machine elements, with a zoom on the shield concept. The quartz is included to indicate the reason for the big gap in the magnetic circuit. IP denotes the interaction point.*

for each photon. The tubes are arranged in a closely packed array to maximize the the number of detected photons, and light catchers are added to increase the effective solid angle for photon detection. The Čerenkov process is a weak source of photons which will be detected in the single photon counting mode.

The Q2 quadrupoles and the 10752 photomultipliers reside outside the main iron flux return but in the considerable fringe field of the 1.5 T solenoid magnet. In conjunction with a bucking coil in the backward direction, which is necessary to reduce the B_Z field at Q2 to less than about 100 G, a magnetic shield surrounding the SOB has been studied which reduces the fringe field at the photomultipliers to an acceptable level, less than 1 G. The field in the shield iron should be less than 0.1 T everywhere, though it might attain 0.8Tin some places in case of malfunctioning of the bucking coil or solenoid; a de-magnetization scheme must be envisioned.

C.1.3 Scope of article

In this article, we shall only consider the fringe field in the backward direction as it affects the quadrupoles, namely Q2, and the $DIRC$ photomultipliers.

We shall define the fringe field requirements (2), describe the simulation of the field (3), present the design and construction of the shield (4) and define the bucking coil (5). The mappers of the *DIRC* (6) and quadrupole (7) regions are then described. After presenting the results of the measurements (8), we conclude (9).

C.2 PMT and Q2 requirements from measurements

Measurements were made to determine the performance of the PMTs and the quadrupoles in a magnetic field, resulting in target limits.

C.2.1 PMT performance in a magnetic field

The PMT used in the *DIRC* is the Thorn-EMI 9125. It has a 28.2 mm diameter and a bialkali photocathode with a high blue response. It is well-suited for our single photon counting requirement. The dynodes are rectangular and thus the effects of a transverse magnetic field will depend on the orientation.

It has been tested with a pulsed blue light at a wavelength of 450 nm in magnetic fields up to 20 G, measured with an accuracy of 0.2 G [4]. The orientations of the field relative to the tube were longitudinal and transverse, with the latter in the direction: across the dynode ("favorable") and along the dynode ('unfavorable"). The PMT was operated at a high voltage such that the single photon peak was at 20 mV, i.e. as we shall run in *BABAR*. For a 95% efficiency, i.e. we lose 1/20 of the photoelectrons, the acceptable transverse field is about ±3(1) G in the favorable (unfavorable) direction, with about a 0.5 G asymmetry. The principal reason for the inefficiency is due to the perturbation of the electron multiplication,i.e. gain reduction, in the unfavorable orientation, and the decrease in the efficiency of photoelectron collection in the favorable orientation. The acceptable longitudinal field giving 95% efficiency is about 3 G, also asymmetric about 0, with the eciency falling more slowly than in the transverse direction.

From these measurements, we concluded that we would orient the PMTs transversely so that the anticipated lower field component, azimuthal with respect to the solenoid axis, is in the unfavorable transverse direction.

C.2.2 Quadrupole performance in a magnetic field

The major effect of the approximately axial solenoid fringe field on the quadrupoles is to induce higher order multipoles, in particular a skew octupole, due to flux concentration on the poles of the quadrupole. Beam studies have indicated that the multipole requirement is $\leq 10^{-4}$ for n=3 to 15 [5].

We will concentrate on the Q2 quadrupole since it is most acted by the solenoid fringe field. This water-cooled laminated iron quadrupole must accommodate both the high energy HER and low energy rings LER, as seen in Figure C.3. It is slightly offset, and therefore has a dipole component as well. The LER part has inner bore radius of 47.8 mm, and a length of 610 mm. In order to reduce the induced octupole, it has a mirror plate on the IP side, connected magnetically to the quadrupole iron. The opening in the mirror plate is 96.6 mm square with rounded corners. The solenoid field induces a skew octupole in the mirror plate of opposite sign to that induced in the quadrupole body providing cancellation. The plate is 9.5 mm thick and is placed at 38 mm from the main quadrupole iron, connected at the outer radius. The maximum design current is 1100A on 8 turns, with a current density of 57 A/mm^2. There are trim windings to cancel or reduce the n=3 term in the main quadrupole field, to buck the solenoid-induced dipole and skew octupole.

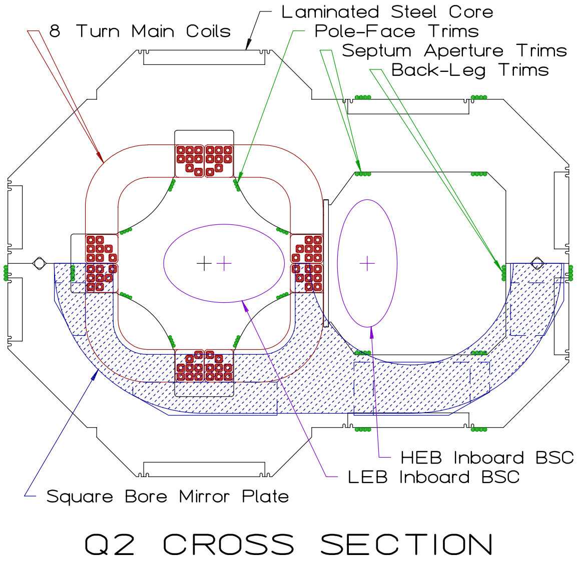

Figure C.3: *Schematic cross section for Q2. The LER is off-set as it goes through the quadrupole on the left, while the HER is in a "field-free" region, as shown on the right. The "beam-stay-clear" (BSC) regions are indicated. Only one half of the Mirror Plate is shown.*

An analytical calculation gives for the induced octupole: $\int_{Z_0}^{\infty} a_4(Z)dZ = \frac{a}{4}\bar{B}_Z R_i$ where Z_0 the offset from the pole face ($= R_i/4$), α the linkage coefficient =0.4-0.8 depending on the chamfer, $\bar{B}_Z$ is the average axial field integrated over the same limits, and R_i is the inner bore radius.

Harmonic measurements were made with a thin air-core solenoid placed at 170 mm from the core-edge of a Q2 model, which had the possibility to include mirror plates of varying shapes. The field was 360 G at the center of the solenoid, 216 G at the mirror plate and 71 Gauss at the core-edge. The skew octupole was measured between ±100 mm with respect to the Q2 core-edge. The results without a mirror plate are shown in Figure C.4, as well as those for two different shapes: annular and box opening. Without a mirror plate, the value was always negative, with a peak at the core-edge. With mirror plate, the value changed sign at the core-edge, with the integral closest to 0 for the box variation. The latter was adopted for the definitive design. (Annular mirror plates are used at both ends for Q4.)

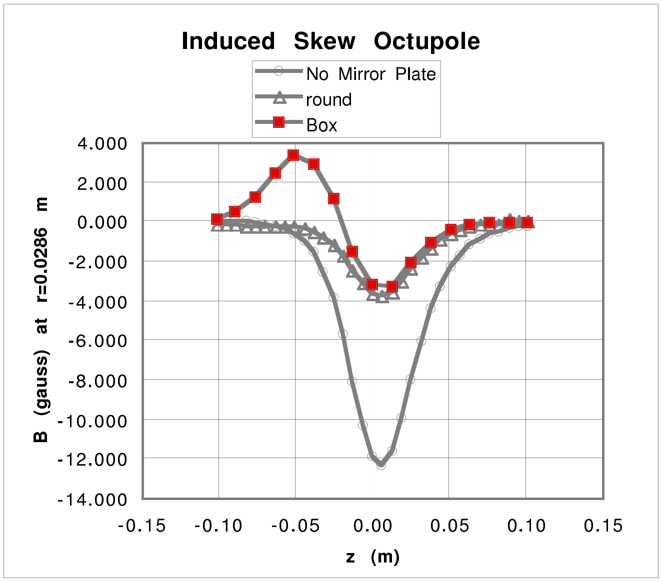

Figure C.4: *Skew-octupole vs. Z for different mirror plate configurations.*

C.3 Simulation with *BABAR* model

C.3.1 *BABAR* magnetic circuit

The *BABAR* magnetic circuit consists of 2 active elements: a thin 1.5 T cryogenic solenoid and a bucking coil in the backward direction. The mean radius of the solenoid is 1532 mm while its length is 3456 mm. The bucking coil is a warm magnet which can operate at ±1.5 times the expected operating current (see Section C.5).

Its passive elements consist of a barrel, forward and backward endcaps and plugs, part of the *DIRC* support structure (the Strong Support Tube, or SST radially between the backward door and the plug, and the ESS connection to the barrel iron) and the *DIRC* shield. The quadrupoles need to be treated as passive elements only. The ensemble of the elements is extremely complicated from a magnetic point-of-view, even for the axisymmetric approximation. This is mainly due to the varying thicknesses of the thin plates and narrow gaps which make up the instrumented flux return in the barrel and door regions, see Figure C.5. The other area of complication comes from the plugs which need careful shaping to obtain the uniform field requirements inside the drift chamber fiducial volume and to prevent too large of a leakage towards the quadrupoles especially in the forward direction. In the backward plug region, the *DIRC* support structure is part of the magnetic circuit, but the fragile quartz bars

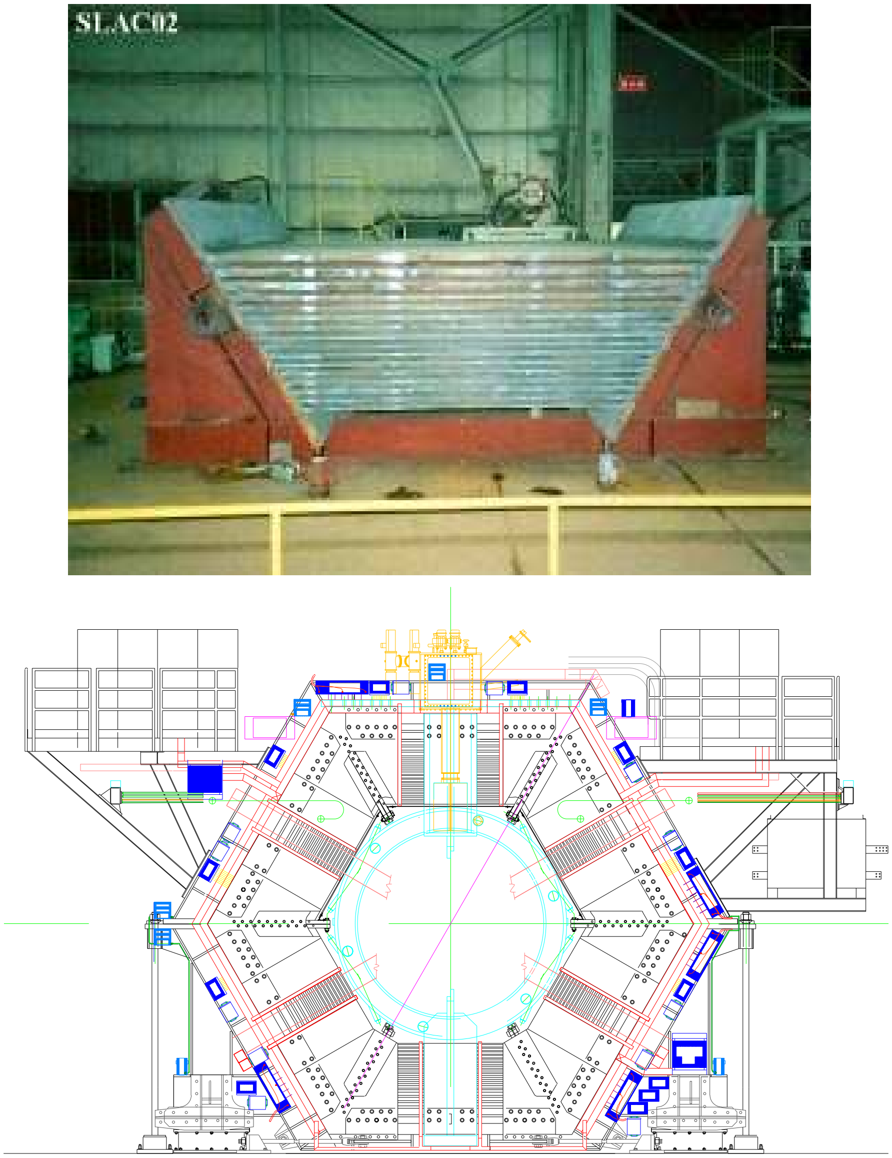

Figure C.5: *The BABAR iron: one of 6 barrel sectors of the instrumented flux return in construction, and end view design of barrel viewed from back.*

and bar boxes require holes in this part of the circuit, increasing the fringe field in the backward direction in a significant way, see Figure C.6. Note that the horsecollar is magnetically connected to the door iron; this is an approximation for the part which is not axi-symmetric.

In addition, there are the inevitable non-axisymmetric passive elements: the drift chamber cable holes in the backward plug, the upwards chimney passage for the cryogenics services, the skid plates under the two doors (to allow opening for access),

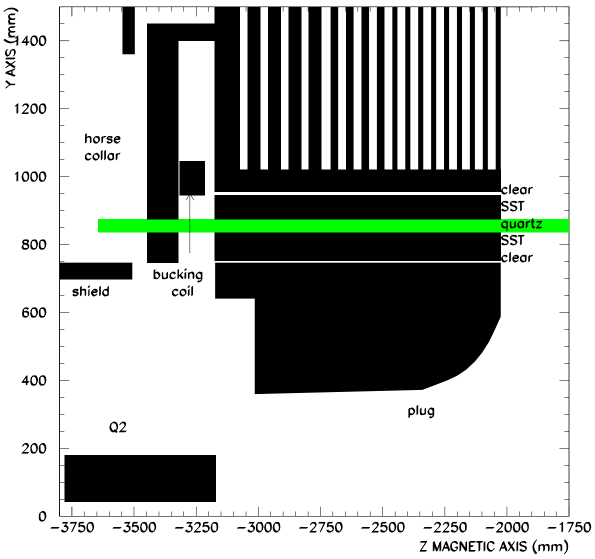

Figure C.6: *The BABAR iron: schematic details of the backward region, including the bottom part of door, the plug, SST and horsecollar. The quartz is included to indicate the reason for the big gap in the magnetic circuit.*

the ESS, the quadrupoles and some smaller features.

However, some of these elements have a left-right symmetry, making the analysis somewhat simpler. In addition, while the hexagonal shape of the barrel and door iron is not strictly axisymmetric, that approximation turns out to be a good one.

C.3.2 2D with Castem 2000 and Mermaid

In order to satisfy the PMT and Q2 requirements, it was recognized early that a combination of active (bucking coil) and passive elements (iron) was necessary.

There are external constraints on the shielding arrangement. They include:

- The shield is most strongly determined by the *SOB* which is shown in Figure C.7, cantilevered from the horsecollar. Part of the shield must consist of an inner cylinder at a radius inferior to that of the *SOB*.
- Beam elements will be contained within the shield cylinder. They are supported in cantilever, limiting the length of the shield along Z, i.e. $\geq$ -5000mm. The radial extent of the beam elements is determined by seismic considerations, and vary as a function of Z. The shield cylinder is thus sandwiched between these beam elements and the *SOB*.
- Access to the drift chamber is made inside the shield cylinder. This access is quite difficult because the beam elements fill a large fraction of the relatively

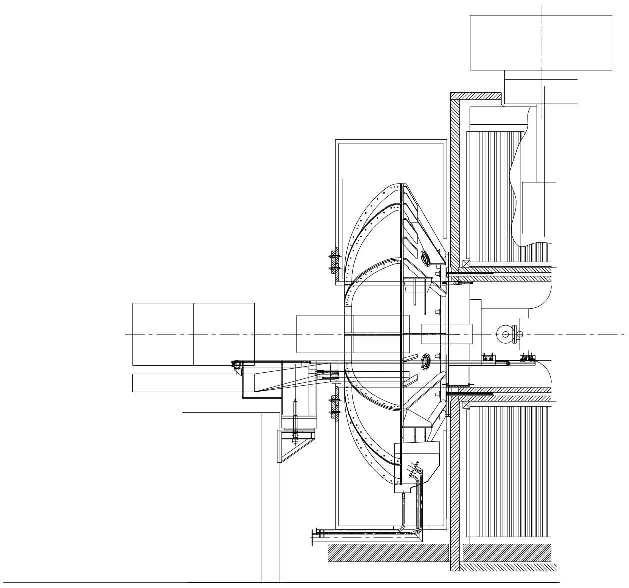

Figure C.7: *Side view of the DIRC SOB and shield, with BABAR iron. The SOB is cantilevered from the horsecollar which is connected to the BABAR iron, while the shield is supported by the skid plate which also supports the BABAR backward doors.*

small radial dimensions. However, only the upper part of the shield cylinder can be removed without moving the beam elements.

- Access to other parts of the detector requires that the *BABAR* doors open laterally on the moveable skid plates. The shield should also open laterally for *SOB* access. Since the opened *BABAR* doors are no longer bolted to the barrel iron, they are quite unstable due to their aspect ratio; therefore counterweights are required on the skid plates. Given the small radial space between the *SOB* and the skid plates, there is little room for a dedicated counterweight. Thus the magnetic shield and its support, resting on the skid plates, should also provide a counterweight for the *BABAR* doors, when opened.

- the shield should provide a stop for the backward plug against movements in the -Z direction due to a seismic event.

Studies were performed initially using Castem 2000 [6] and subsequently with Mermaid [7]. The comparison of the results of the two codes using the same geometry and magnetic properties was very good. The 2D results of Castem 2000 are presented since the code allows the use of more than three different regions with variable permeability.

The PMT closest to the beam line is more sensitive to the bucking coil current than the furthest PMT. In general, at the optimum bucking coil current, the maximum transverse field at the PMTs occurred at these two extremes, but with opposite sign.

An iterative series of studies were made minimizing the maximum transverse field at the photomultipliers at the optimum bucking coil current. The studies concerned:

- the position of the bucking coil: to be most effective in compensating the flux leakage, the bucking coil was placed at the exit of the hole for the quartz.
- the range of magnetic field for which the iron needed a high permeability: see Figure C.8 where the maximum field needed for the shield studies is H=100 A/m.
- the thickness of the iron: the influence of the thickness of the iron shield varied little between 40 and 60 mm and was chosen to be 50 mm.
- the magnetic gap between the shield iron and the plug/SST was found necessary but not very sensitive beyond a minimum distance.
- the dimensions of the horsecollar were increased to provide a path for the magnetic flux which avoided the inside of the shield
- the shape of the shield iron was varied between closely following the *SOB* and a cylindrical shape, easier to fabricate; the result was quite insensitive to this choice.
- the point at which the shield inner cylinder should connect to the remaining part of the shield was the closest to the null point at which the field changes sign. This latter point is quite delicate in that it is quite close to the PMTs closest to the beam line.

These studies resulted in a concept (see Figure C.2) with an inner cylindrical shell and an outer structure split in halves. The two halves consist of an outer cylindrical shell, two annular end-plates ("near" and "far"), an annular cover plate, support structures, and braces to the back door. The inner cylindrical shell is divided longitudinally into a fixed part (about 1/3) and a moveable part (about 2/3). The fixed part is connected to a standoff shell in cantilever from the backward plug.

For the shield design parameters, the simulation showed that, at the optimum bucking coil current for the PMTs, about 30.7 kA-turns, the transverse magnetic field at the PMTs is about 0.2 G as seen in Figure C.9. The optimum bucking coil current for Q2 is higher by about 15%, requiring a compromise. Since the optimization was done in 2D, the value of the current is only approximate; however the relative optima for the PMTs and Q2 should be verified.

The flux lines near the *DIRC* shield are shown in the same figure. Notice the influence of the horsecollar and the mirror plate of Q2, as well as the magnetic opening for the quartz and the cover plates. The reversal of the flux direction in the annular far plate is related to the zero in $B_\perp$ observed in the upper curve.

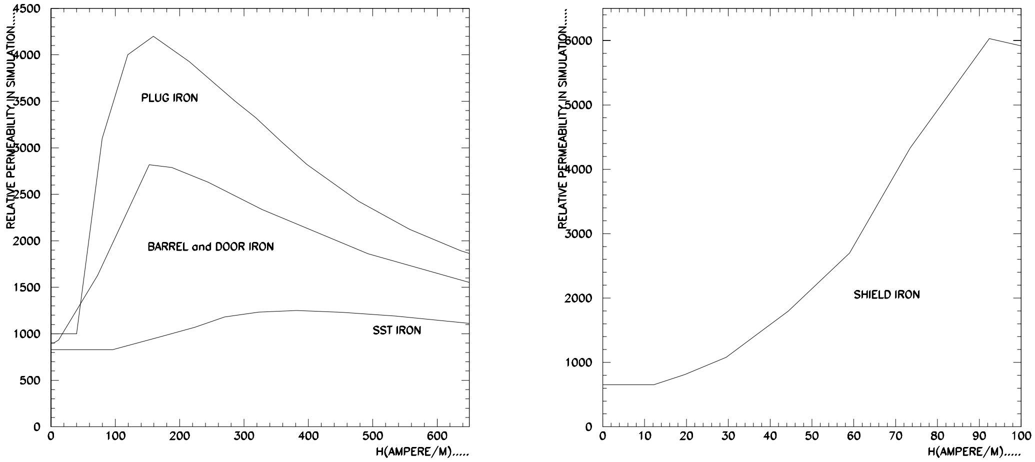

Figure C.8: *Magnetic properties assumed for different materials in the simulation. The left figure is for barrel, door, plug and SST iron, while the right figure is for the shield iron. Note the different scales, in particular the abscissa.*

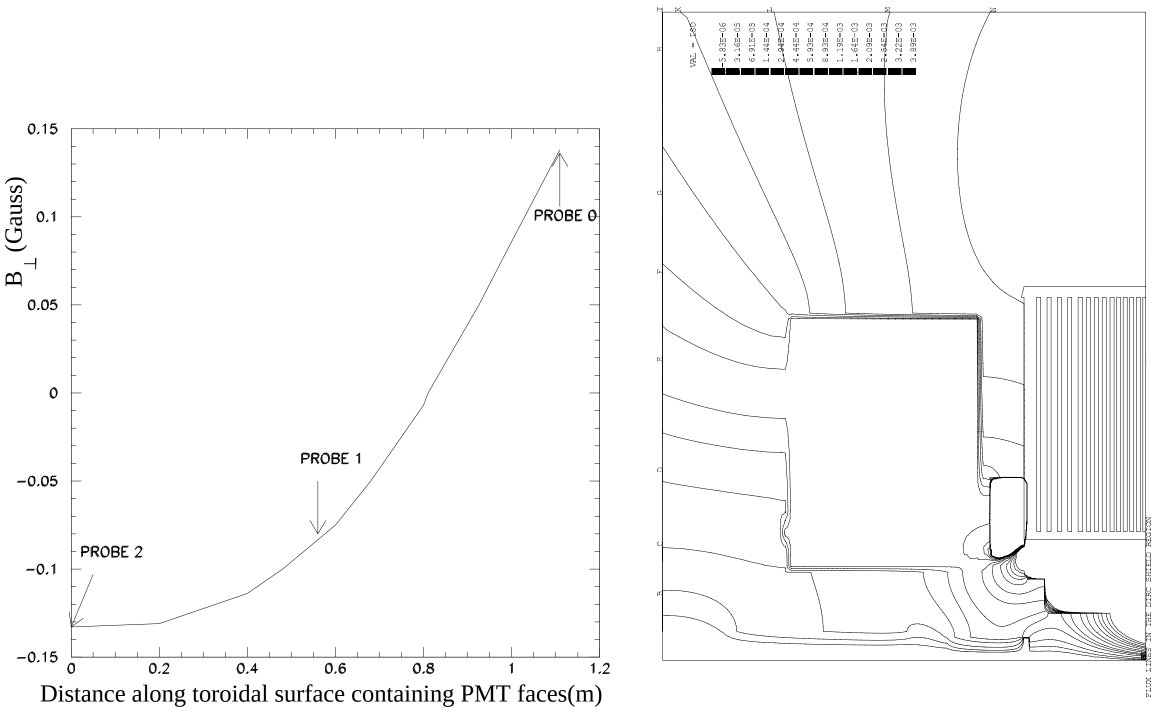

Figure C.9: *Results of the 2D modelization of BABAR using the measured permeability (see Section C.4). The figure on the left gives the $B_\perp$ along PMT face from probe 2 to probe 0 see 6 while the figure on the right gives the flux lines in the DIRC shield region.*

C.3.3 3D with Mermaid

Three-dimensional studies were made to study the effects of the different non-axisymmetric aspects of the *BABAR* iron [9]. In addition, they permitted an evaluation of the gaps between the two shield halves, necessary at the top for cable access, and at the bottom for water pipe access. The Mermaid 3D computer code was used for this purpose. This code allows us to have a mesh for calculations with up to 2×10^6 nodes at Pentium computer with 128 Mb memory core.

Simple axisymmetric version of *BABAR*

Before starting 3D calculations, we compared the results using the Mermaid 2D code with those obtained by Mermaid 3D for exactly the same axisymmetrical geometry. The comparison was performed in two regions of interest: inside the shield at the PMTs location and near Q2. The difference does not exceed 0.2 G for the PMT region and 5 G for the Q2 region. This accuracy could be improved by a finer meshing.

Due to the complexity of the *BABAR* magnetic circuit, it was not possible to make a 360° model within the memory limitations. Therefore, we considered two models with either left-right or top-bottom symmetry.

Left-right and top-bottom symmetric models of *BABAR*

In Figure C.10, one sees the *BABAR* model with left-right symmetry. It was used to study the effects of the top-bottom asymmetries, in particular

- the chimney for the cryogenics at the top
- the cable holes in the bottom of the plug
- non-symmetrical 5 mm split between the removeable and fixed parts of the backward plug
- the skid plate on the bottom

By using extreme values for the parameters, we have determined that the major effect is due to the ESS and the chimney cutout, i.e. the angular distribution reflects the angular variation of the magnetic reluctance between the near annular plate of the shield and the horsecollar. On the other hand, the angular variations due to the cable holes, split between removeable and fixed parts of the plug, and skid plates are very small. The $B_\perp$ for this model varies between 0.3 and 0.7 G as seen in Figure C.11

A *BABAR* model with top-bottom symmetry was used to study the effects of the left-right asymmetries, in particular Q2. Another left-right asymmetry was introduced to reflect an error in the mounting of the *BABAR*doors which produced an additional x-displacement of 7 mm. The model shows that the angular variations due to the Q2 asymmetry and the shift of one door are negligible [9].

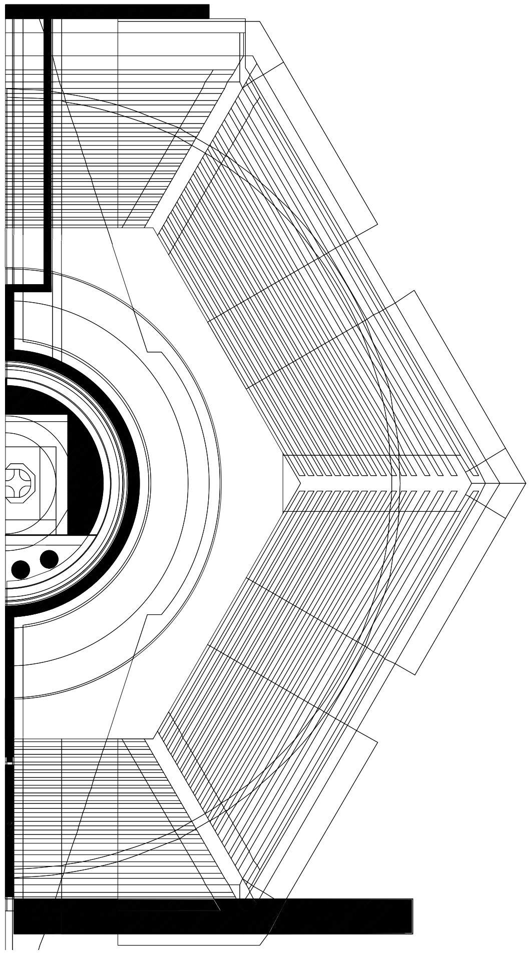

Figure C.10: *Cross-section of left-right symmetry model of BABAR. Note the shape of the horsecollar. The up-down asymmetric elements are in black.*

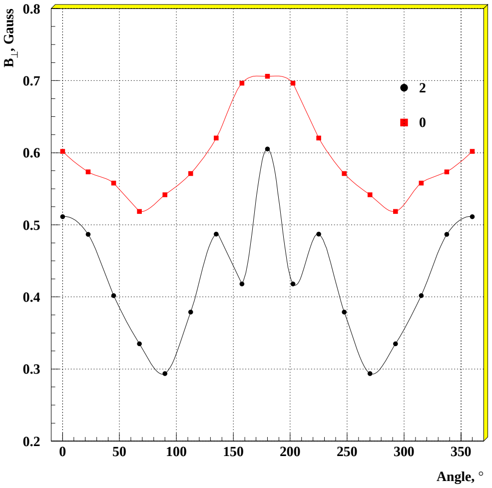

Figure C.11: $B_\perp$ *vs. azimuthal angle calculated in the left-right symmetry model of BABAR. The coordinate system has the downward direction at 0°.*

Therefore, the results of the 3D simulations show that the expected $B_\perp$ inside the *DIRC* shield is less than 1 G with angular variations of about 0.2 G. Since a possible residual field (see next section) was not included in the model, the measured azimuthal dependence can be different in detail from the prediction.

C.3.4 Necessity of demagnetization

The calculations by Castem 2000 and Mermaid show that in the case of the crash of the main solenoid or bucking coil, the field in the shield iron can reach 7 kG instead of 0.5 kG when both coils are on. The resulting coercive force is about 1 Oe for the very pure iron used in the shield construction. Therefore, the residual field of the iron will give an additional contribution to the fringe field in the PMTs region.

We estimated the residual field distribution inside the shield, simulating the magnetization of the iron by a coil applied to the shield iron from both inner and outer sides all along the contour of the shield. This coil inducing the magnetization field inside the iron should have a linear current density along the contour equal to the coercive force taken in A/cm. We assumed $j = 0.8$ A/cm corresponding to the value of the coercive force $H_c = 1$ Oe. The polarity of the current in the coil corresponded to the direction of the residual flux in the shield iron. This direction was taken from the calculation of the field at zero bucking coil current.

The value of the maximum perpendicular component at the PMTs, practically equal to the module of the field, reaches about 3 G on the upper PMTs and about 2 G on the lower PMTs. In this model, the residual field due to the coercive force exceeded the expected fringe field inside the shield. This led to a special effort to produce a shield with as small a coercive forces as possible, and to the consideration of the use of the bucking coil to demagnetize the shield. In this method, the amplitude of AC component of the bucking coil current should gradually decrease, for example (Figure C.12):

$$I^{BC} = I_0^{BC} + I_A^{BC} Sin(\frac{2\pi}{T_1}t)e^{-\frac{t}{T_2}}, T_1 << T_2$$

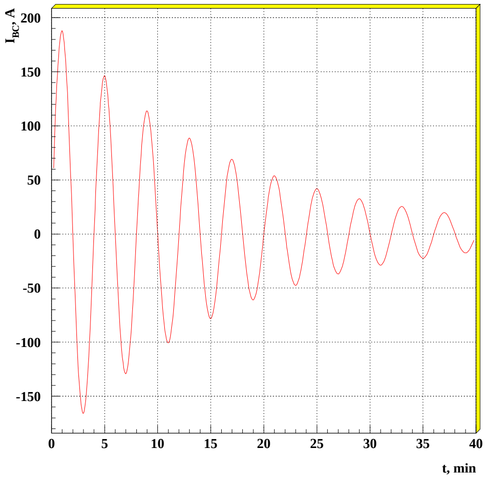

Figure C.12: *Possible degaussing procedure for the shield*

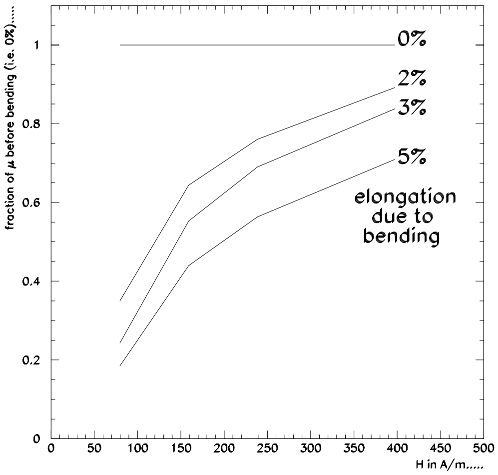

Figure C.13: *Measurements of the deterioration of the permeability at low fields due to bending. The region which is relevant for our studies is $H \leq 100$ A/m. The inner cylinder corresponds approximately to the 2% curve. Scaling by the radii, the outer cylinder corresponds approximately to 0.5%.*

Two different cases of the shield magnetization, due to main solenoid or bucking coil crashes, lead to two types of procedures. In the case when the main field cut, the demagnetization procedure has to have $I_0^{BC} = 0$, while $I_0^{BC} = I_{opt}^{BC}$ for the other case.

To estimate T_1, we have to take into account that the skin depth has to be at least half of the shield thickness:

$$T_1 = \frac{\pi \mu \delta^2}{\rho} \approx 20 sec,$$

for $\rho = 0.11 \mu$Hom/m and average μ=1000.

About ten cycles of bucking coil current would be enough to decrease the residual fields in a reasonable time.

C.4 Design and construction of the shield

The design of the shield was based on the following considerations:

- the outer part of the shield is cylindrical to minimize the number of elements to be connected.
- all connections are welded including the support structure, except for the cover plate to allow the opening of the shield doors and access to the Drift Chamber, and the flange on the fixed part of the inner cylinder to allow the opening of the *SOB*.
- since the necessary bending strongly affects the permeability, especially at low H (see Figure C.13 for measurement on a similar type of iron, [8]), the entire structure must be annealed after construction. The manufacturer studied two cases: annealing at 550° for 2 hours and at 850° for 4 hours. The latter gave better results.
- the shield structure is welded to the skid plate at the bottom, and is welded to the *BABAR* door at the top via braces to prevent movement during a seismic event.

The construction of the shield with its special low carbon steel was the responsibility of Kawasaki Heavy Industries (KHI). The material was EFE material, manufactured at Kawasaki Steel Corporation (KSC). The permeability and coercive force were measured at the manufacturer: see Figures C.14 and C.15. These values were better than specifications in general. In particular, the measured permeabilities were better than that used in the original simulation (the right part of Figure C.8) leading to a reduction of 1.5 in the maximum $B_\perp$ expected. The measured coercive forces were about one half that assumed in the calculation of Section C.3.3; therefore the expected residual field should not exceed about 1.5 G.

The design of the Saclay laboratory is shown in Figure C.16. The cover plate is made in 4 pieces to facilitate the opening of the shield. The turn buckles take up the

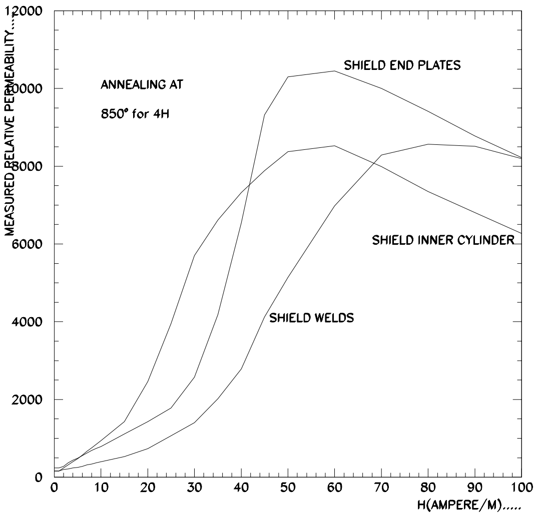

Figure C.14: *Relative permeability vs. field for the shield material as measured at KSC*

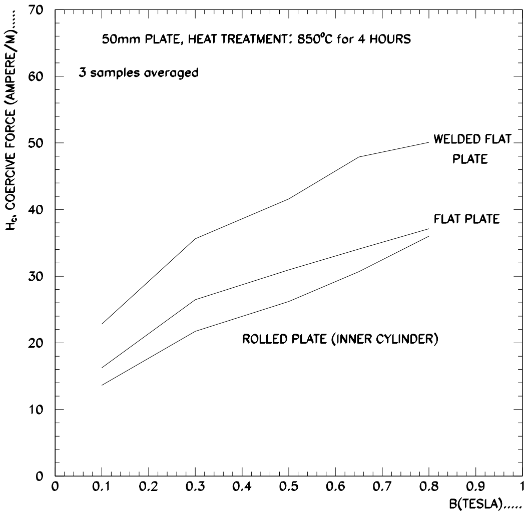

Figure C.15: *Coercive force vs. field for the shield material as measured at KSC*

construction tolerances and are made rigid to provide a "stop" for the upper part of the plug. A rail structure, not shown, enables us to remove the upper parts of the plug and inner shield cylinder to provided access to the drift chamber electronics.

The machining, bending, welding and annealing was done at KHI. Some construction processes are shown in Figures C.17-C.18, the latter also shows the shield as it is being aligned, and mounted and aligned, with half of the cover plate remaining to be mounted.

C.5 The bucking coil and its power supply

The bucking coil is constrained in the space between the moveable backward end doors and the horsecollar, and at a radius beyond the support of the quartz bars. The aim of the design is to allow for as many ampere-turns as possible in this restricted region, approximately 100 mm in Z, and 220 mm in radius, starting at a radius of about 945 mm.

The bucking coil, designed and built at SLAC, is a conventional magnet, water-cooled, with 140 turns of square hollow core copper, 0.375 inches on a side, insulated with polyester glass fiber. The bucking coil power supply consists of two off-the-shelf 15 KW switcher power supplies connected in parallel, a thyristor reversing switch, a zero-flux current measuring transductor, and a controller-regulator connected to the PEP-II Bit-Bus power supply control network. It has a combined maximum rating of ±300 A.

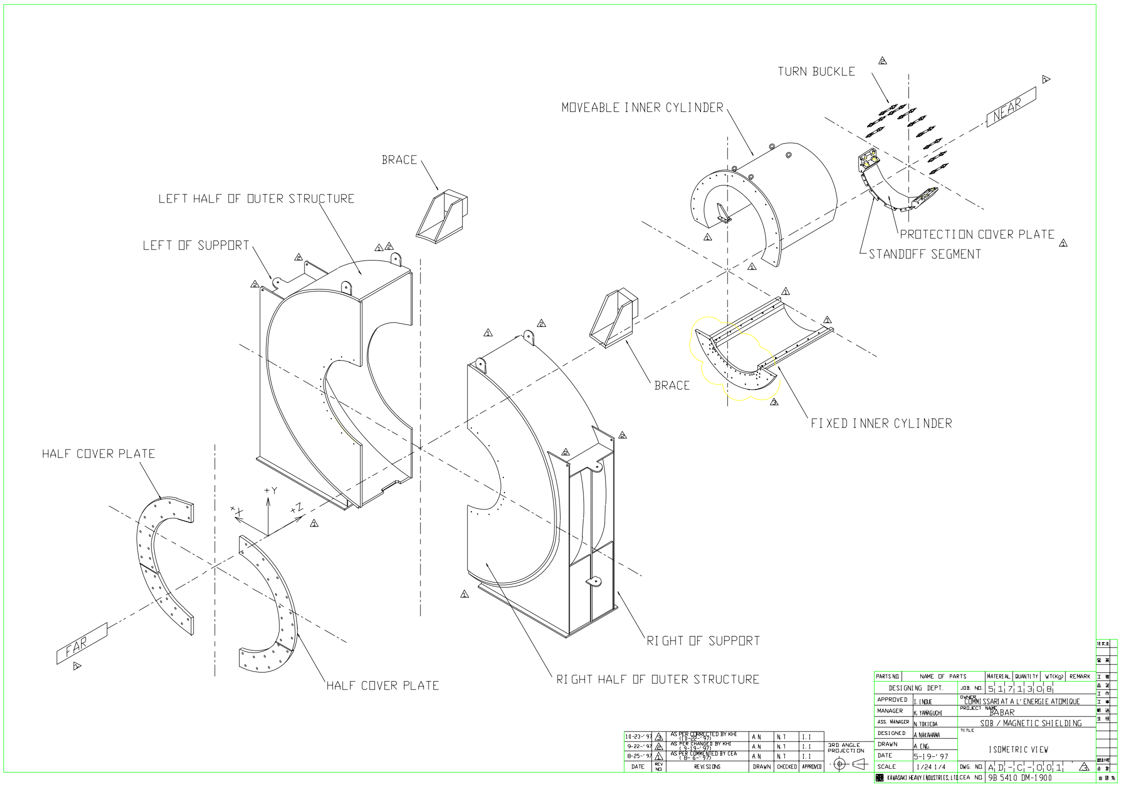

Figure C.16: *Exploded isometric view of the design of the DIRC shield design*

C.6 Design and construction of the *DIRC* mapper

The aim of the *DIRC* mapper is to measure the field components inside the shield at positions corresponding to the faces of the PMTs [10]. It was designed and built at the Budker Institute. It consists of a rigid support structure, mounted on the horsecollar, which can rotate about the beam axis. Three-dimensional probes are placed at three positions along the PMT rows, at the two extremes and in the middle. We will now describe the mechanics and the probes in some detail.

C.6.1 Mechanics

The mechanical design of the magnetic measurement system is shown in Figures C.19 and C.20.

A rigid frame is attached to the platform moving around the circular rail mounted on the Horsecollar. All elements, such as frame, removeable platform and circular rail are fabricated from aluminum alloy. The movement of the platform along the rail is provided by three rollers. Three 3D probes are fixed on the arc of the frame.

The step motor mounted on the platform provides the motion of the frame. The

(a) Rolling of outer cylinder (b) Rolling of inner cylinder

(c) Outer structure in two halves (d) Oven used to anneal each half

Figure C.17: *Construction of the DIRC shield: I*

motor has no permanent magnet inside. A worm gear is used to transfer the rotation momentum of the rotor.

The potentiometric method with the use of nichrome wire resistor of 0.8 mm diameter is used to measure the azimuthal angle ϕ. This wire is located in the groove on the rail. An electric contact attached to the platform moves along the rail together with the platform. The wire resistor is supplied by 100 mA current. The accuracy of the azimuthal angle measurement is about 0.2°.

C.6.2 Probes

Both ferro-probes (Magnetically Modulated Permalloy Probes or MMPP) and Hall probes are used. Each set of 3D probes consists of one 3D ferro-probe and one 3D

(a) Lower, or fixed, part of inner cylinder before short-blasting in factory

(b) Upper, or moveable, part of inner cylinder in machining

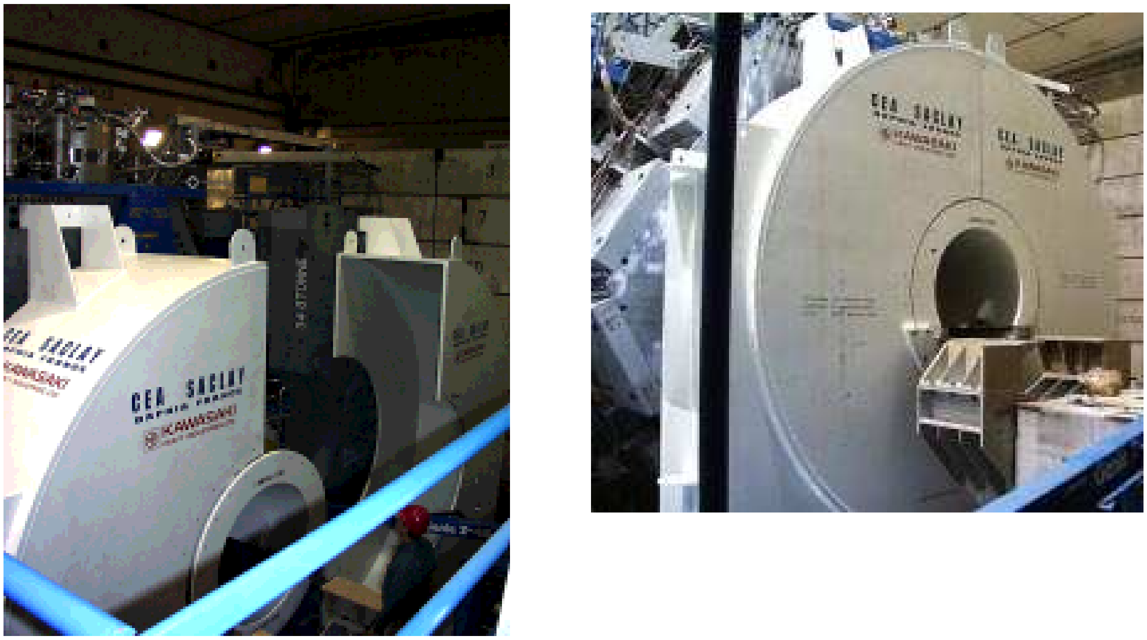

(c) Shield in process of being adjusted at *BABAR*

(d) Shield fully mounted at *BABAR*, except for the top of cover plate

Figure C.18: *Construction of the DIRC shield: II*

Hall probe located next to each other. The sensitive volume of a set is a cube of $20 \times 20 \times 20$ mm^3. The locations of the 3D probes on the rigid frame correspond to

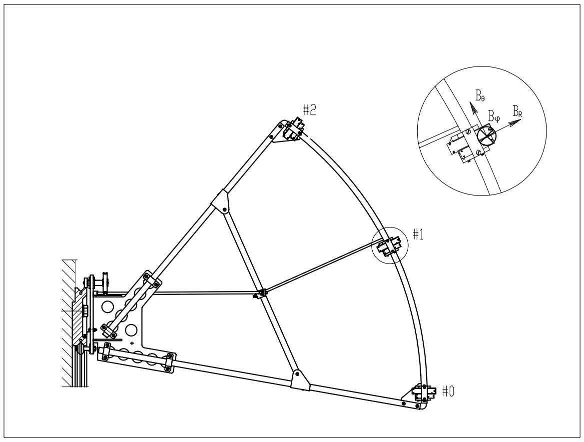

Figure C.19: *Side view of the mechanism. The location of probes is at the PMT faces with #0 the closest to the beam and #2 the furthest.*

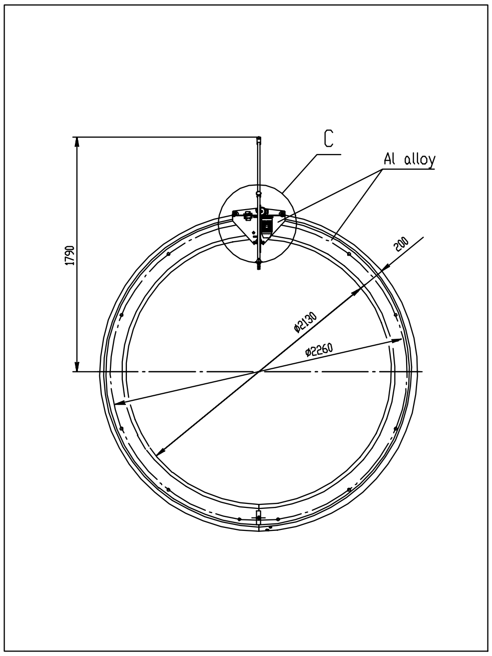

Figure C.20: *Front view of the mechanism. The mechanism rotates azimuthally about the beam direction.*

the faces of the PMTs as shown in Figure C.19, with the definitions:

- #2 probe - furthest PMT from beam line
- #1 probe - intermediary PMT
- #0 probe - closest PMT to beam line

The measurement coordinate system has 0° as the downward direction, rotating in the clockwise direction as viewed from the rear of *BABAR*.

Ferro-probes

Ferro-probes are used to measure relatively low fields up to about 10 G. The ferro-probe is supplied with a measuring electronic unit which transforms magnetic field into voltage with coefficient of about 0.5 V/Gauss. Each 3D ferro-probe is arranged inside a cube of $10 \times 10 \times 10$ mm^3.

The design of one coordinate ferro-probe is shown in Figure C.21. It consists of permalloy core of 20 μm diameter and 7 mm long located in the quartz tube. This core was annealed in advance and has very small coercive force. The common excitation and compensation coils are wound along the quartz tube. The signal coil is wound at the middle of the tube. Rectangular 16 kHz impulses from generator are applied to the excitation circuit. The signal in the signal coil is proportional to the B derivative in the core. The amplitude of the second harmonic (2f=32 kHz) of this signal is proportional to the measured B_{ext}. An integrating ADC with a multiplexer is used to read out the probes with 14-20 bit resolution for two scales: 8V and 0.5V. The long-term zero drift is less than 0.02 G within a 20-30°C temperature range.

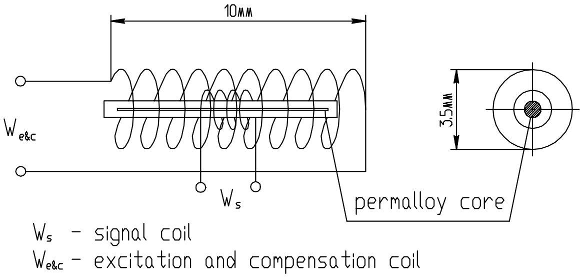

Figure C.21: *Design of ferro-probe or MMPP (one coordinate)*

Hall probes

Hall probes are used to measure relatively high fields exceeding 5 Gauss, thus overlapping the ferro-probe sensitive region. One 3D set of Hall probes consists of three probes glued on the sides of an aluminum cube, $3 \times 3 \times 3$ mm^3. This unit is assembled in a box $9 \times 15 \times 62$ mm^3. The stabilized DC current source which is used to supply the Hall probes has a stability of 10^{-5}.

Probe calibration

A special calibration system is used to measure zero offset and sensitivities of the probes. The calibration is performed with the help of Helmholtz coils located inside a zero field box (less then 0.01 G) manufactured from annealed permalloy. It can produce magnetic fields up to 50 G. We used a Hall probe calibrated by NMR probe to measure the coefficient between the current and magnetic field of this coils. The estimated error is 0.1%.

C.6.3 On-line for mapper

On-line code written on C^{++} runs under Linux operation system on IBM PC. We used a standard CAMAC interface PPI-2 and Crate Controller developed at the Budker Institute. This code allows one to drive the mechanics, calibrate the probes, measure the magnetic map and display the resulting curves during measurements.

OFF				
Radius	Z_h	Z_h-80	Z_h-160	Z_h-290
(cm)	B_{mod} (Gauss)	B_{mod} (Gauss)	B_{mod} (Gauss)	B_{mod} (Gauss)
0	220	50	20	7
70	175	25	15	7
105	30	20	9	
ON				
Radius	Z_h	Z_h-80	Z_h-160	Z_h-290
(cm)	B_Z (Gauss)	B_Z (Gauss)	B_Z (Gauss)	B_Z (Gauss)
0	-2.8	-0.2	-2.9	-2.6
70	-	-2.2	-3.1	-2.6
105	-7.6	-3.5	-3.6	-2.8

Table C.1: *Gaussmeter results for* $B_{mod}(B_Z)$ *with bucking coil OFF ON in the shield region.* Z_h *is the Z at the exit of the horsecollar. Solenoid current at 1.05 nominal=4830 A (nominal=4600 A)*

C.7 Field mapper at backward quadrupoles

A single Hall probe was used, which could be oriented to measure any component. It was placed in an aluminum channel, which had a 3 m scale graduated in mm. The channel was oriented on a line approximating either the LER or HER beam trajectory, or parallel to the beam axis at a radius=25 cm.

C.8 Results of measurements

C.8.1 Gaussmeter measurements with no shield

The solenoid was commissioned before the mounting of the *DIRC* shield. Measurements were taken at that time with a hand-held gaussmeter to obtain an order of magnitude of the fringe field with and without the bucking coil turned on. The reproducibility of the method was about ±10%. There was no coordination of the powering of two coils.

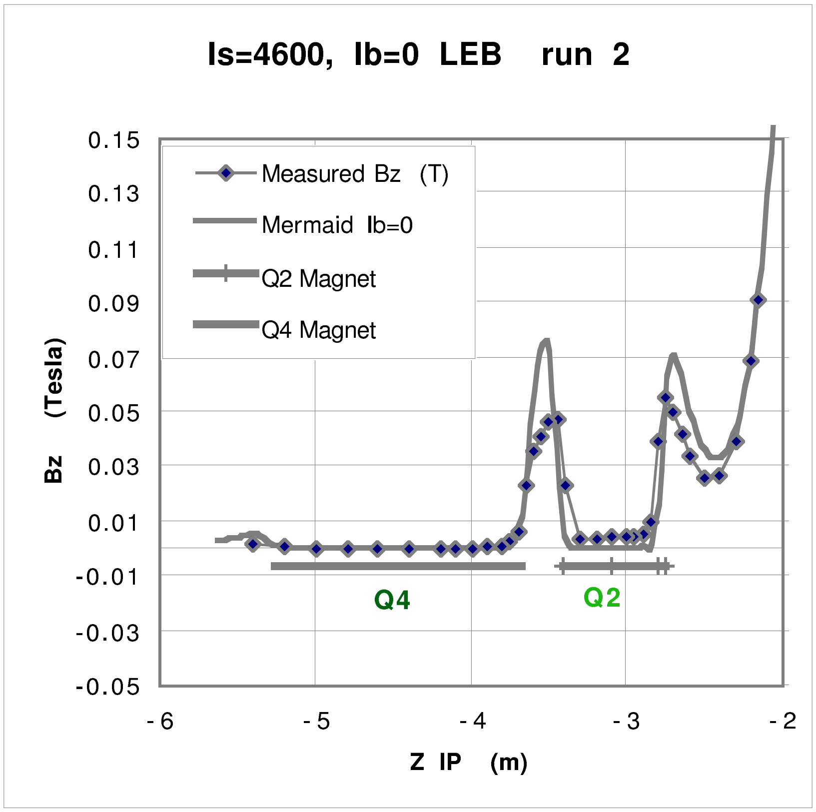

Figure C.22: *Gaussmeter results for B_Z in the Q2 region with the bucking coil off. The 2D Mermaid predictions are also shown. Note that Z refers to the distance from the interaction point.*

With the bucking coil off or on, the results for the shield region are given in Table C.1. They are valid for one azimuth and are difficult to compare to a 2D simulation. Note that the PMT closest furthest to the beam line is at R=83.7(186) cm and Z = Z_h-126(68) cm.

The results for the Q2 region as a function of Z on a straight-line approximation to the LER orbit are given in Figure C.22 and compared to the 2D Mermaid predictions. The results are quite accurate at the exit of the backward endcap as well as at the quadrupoles, while differing by about 20 Gauss at the mid-point between the quadrupoles. Note the large field at Q2 which the bucking coil must compensate.

C.8.2 Mapper measurements with “no” magnetization of shield

No field and minimal shield

Figure C.23 shows the measurements reflecting the remnant field in the *BABAR* doors, horsecollar and skid plates. The remnant field in the *BABAR* doors, horsecollar and skid plates was measured. The maximum B_{mod} was about 0.90 G, and was observed for probe 2 about the horizontal direction (90° and 270°). For this probe, it was a minimum in the vertical direction, about 0.55 G. The maximum and minimum values are approximately left-right and up-down symmetric.

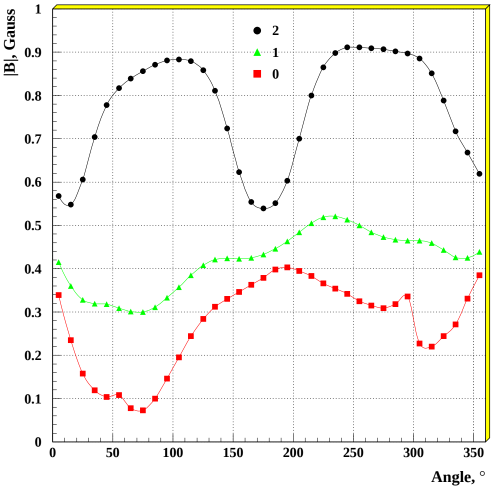

Figure C.23: B_{mod} *vs azimuthal angle with magnetized BABAR iron, only unmagnetized inner cylinder mounted and both coils turned off*

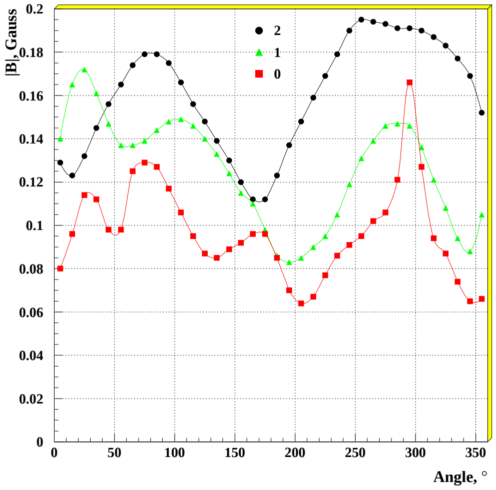

Figure C.24: B_{mod} *vs. azimuthal angle with magnetized BABAR iron, completed unmagnetized shield and both coils turned off*

No field and full shield

The mounting of the shield greatly reduced the influence of the remnant field of *BABAR* doors at the PMT positions. More important, the very low measured fields less than 0.2 G shown in Figure C.24 demonstrate that the iron used in the shield construction had a very low residual field.

Ramp to full field

The solenoid and bucking coils were ramped together in 5 steps to the nominal operating currents. Measurements were made at each step.

Inside the shield, the maximum $B_\perp$ was observed for probe 0 at around 60°. At the nominal currents, the maximum perpendicular component of the field at the PMTs is 0.8 G, quite reasonable for PMT operation. The fringe field is not linear (see Figure C.25) in that the *BABAR* iron is not saturated at low currents; at these currents, the bucking coil over-compensates the solenoid; It should also be noted that in simulations, a linear relationship between the ramping of the two coils leads to fields in the shield iron of about 1 kGauss at about mid-ramp, while an optimum relationship gives a maximum field of about 0.5 kGauss at the final, or nominal current. Therefore, a linear ramping function will lead to some extra magnetization of the iron.

Figure C.26 shows the measurements along the LER trajectory in the vicinity of Q2. Note the same effect of over-compensation due to the bucking coil before the iron becomes saturated.

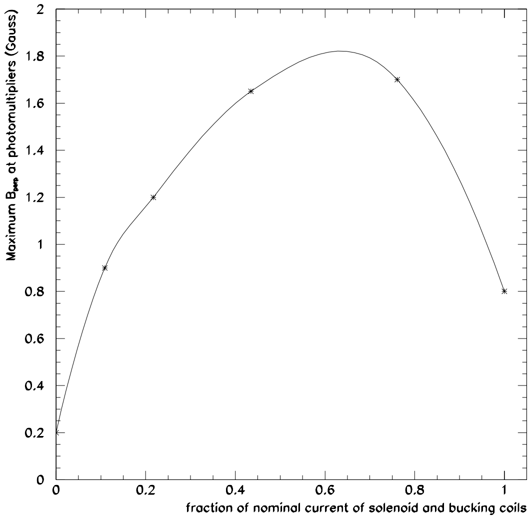

Figure C.25: *Maximum $B_\perp$ vs. fraction of nominal operation current for both coils, ramped together*

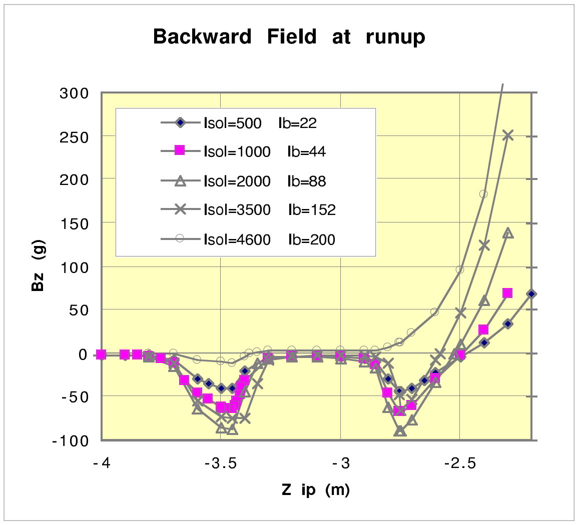

Figure C.26: *Results at Q2 as the solenoid and bucking coils were ramped together. Note that Z refers to the distance from the interaction point.*

Optimization of bucking coil current

The bucking coil current was varied to determine the optimum currents for PMT and quadrupole operation. It was increased to 230A in 10A steps and then was reduced to 200 A. The current was then reduced to 170 A in 10 A steps.

Figure C.27 shows the measurements along the LER trajectory in the vicinity of Q2. It is clear that the optimum is near 200 A. Note that this current is about 10% lower than the prediction (Section C.3.2). For the optimal current, a fine Z scan was performed along the LER direction from the exit of the backward end cap to beyond Q4; see Figure C.28 for the measurements. The 2D Mermaid results are also shown; they differ by less than about 5 G at and between the quadrupoles, and track quite well near the doors where B_Z rises rapidly.

For the PMTs, the value of $B_\perp$, measured at $\approx 60°$(the maximum point), differed in the two 200 A measurements due to hysteresis effects; it was reduced from 0.8 G to 0.6 G. At the 170 A, the three probes had the same maximum value, 0.5 G which

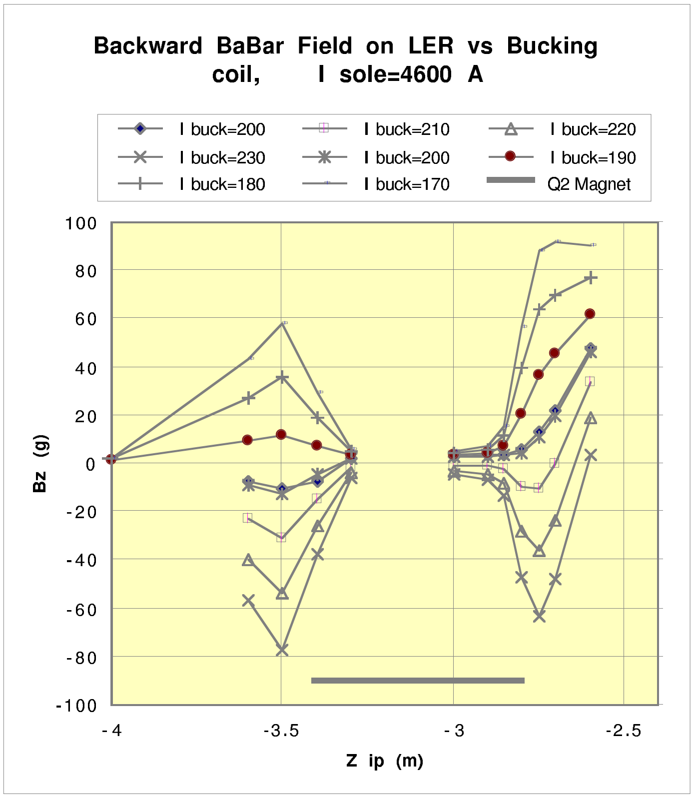

Figure C.27: *Results at Q2 as the bucking coil current was varied, while the solenoid was at nominal field. Note that Z refers to the distance from the interaction point.*

is the optimum for the PMTs. This value is about 15 lower than at 200A, the value that was determined as optimum for Q2, in good agreement with the calculation (Section C.3.2). The bucking coil current was cycled back to 200A as follows: 170A → 230A → 180A → 220A → 190A → 210A → 200A at which point we observed a reduction in the hysteresis. See Figure C.29 for the scan at the last current. The maximum $B_{\perp}$ is about 0.8 G and a left-right asymmetry is observed, probably due to residual shield magnetization. (No effects of shield magnetization were observed at Q2.)

C.8.3 Mapper measurements with magnetization of shield

A magnetization of the shield was induced by ramping down the bucking coil to 0, while the solenoid remained at its nominal value. The maximum $B_{\perp}$ was now over 5 G demonstrating the necessity of the bucking coil. See Figure C.30. This maximum point was at an angle $\approx 300^{\circ}$ and another local maximum was observed at $\approx 60^{\circ}$; it is notable that these angles correspond to the horizontal gaps in the cover plates.

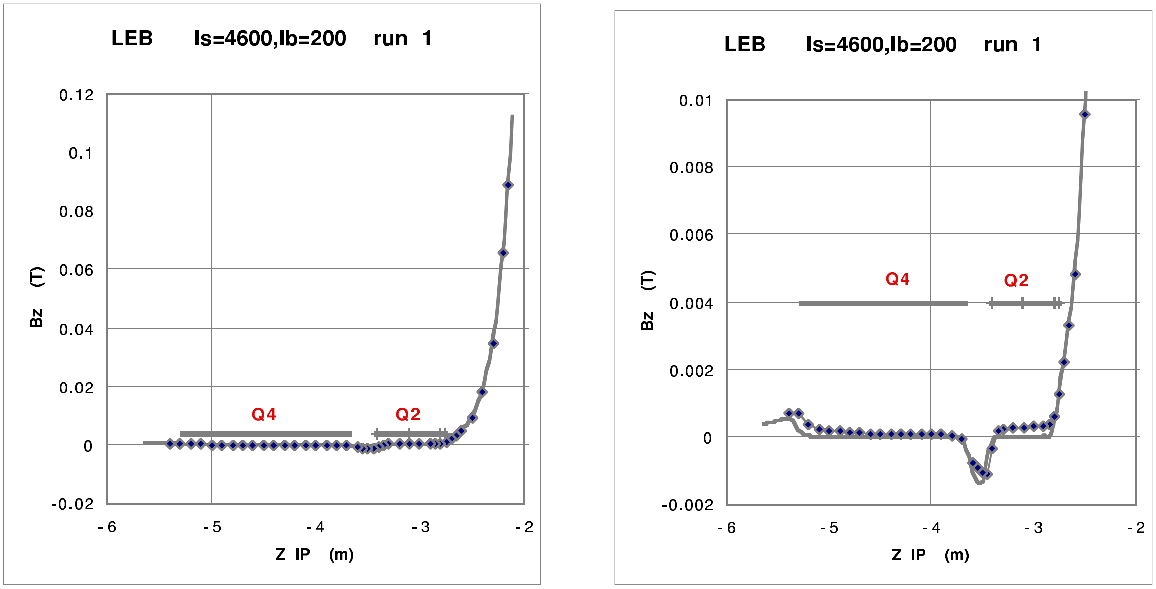

Figure C.28: *Fine scan in Z at Q2 at the optimum bucking coil current with two scales. The 2D Mermaid prediction with* I_b*=220 A is also shown. Note that Z refers to the distance from the interaction point.*

This coil was now ramped back up to 200A, and the maximum $B_\perp$ was reduced to about 2.1 G, as can be seen in Figure C.31. This maximum value corresponds to the limit set for the PMTs, see Section C.2.1, but leaves little margin. Since we want a more robust solution, we have investigated different demagnetization schemes.

C.8.4 Demagnetization

A typical demagnetization cycle is shown in Figure C.12, requiring a current reversal, e.g. when the solenoid is off, but it is also possible to use a demagnetization cycle about a finite current, e.g. when the solenoid is on.

A first incomplete demagnetization was performed by varying the bucking coil current around 200A with the following cycle: 200A → 250A → 155A → 240A → 165A → 230A → 175A → 220A 185A → 210A → 195A → 200A, each step performed in 2 minutes. While the shape was unchanged, the 2.1 G peak see in Figure C.31 was reduced to 1.15 G (to be compared to 0.8 G for the unmagnetized case). This already demonstrated that demagnetization using the bucking coil was feasible.

Solenoid "crash"

When the solenoid was discharged rapidly from full current (38 second time constant), the bucking coil power supply could not track, and the shield was re-magnetized.

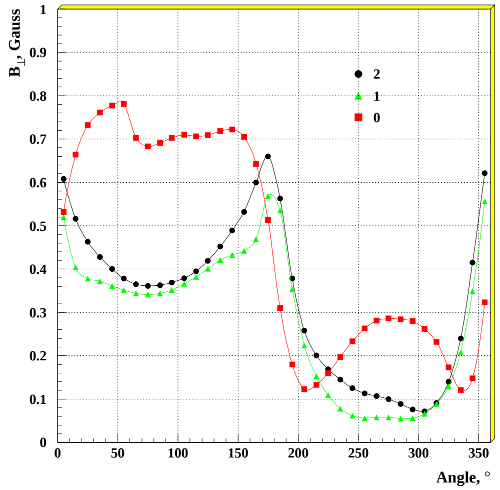

Figure C.29: $B_\perp$ *vs. azimuthal angle with the solenoid at its nominal current and the bucking coil at the optimum current for Q2.*

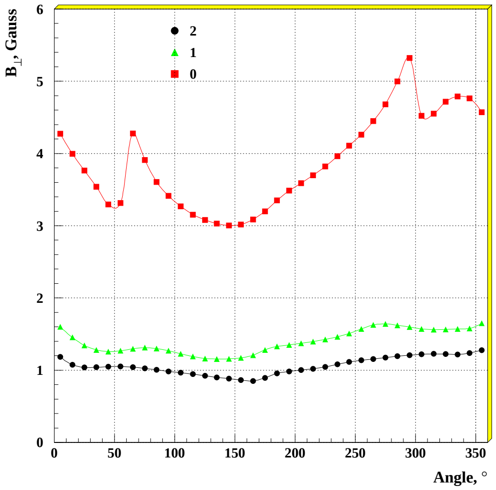

Figure C.30: $B_\perp$ *vs. azimuthal angle with the solenoid at its nominal current and the bucking coil turned off to induce a magnetization in the shield iron.*

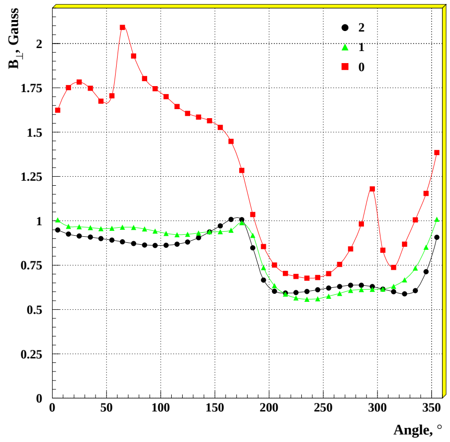

Figure C.31: $B_\perp$ *vs. azimuthal angle with the solenoid at its nominal current and the bucking coil at 200 A after the magnetization of the shield iron.*

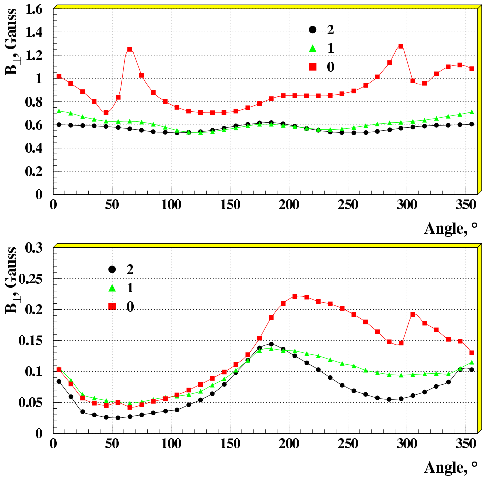

Figure C.32: *Comparison of* $B_\perp$ *vs. azimuthal angle after a solenoid "crash" and after a demagnetization cycle of the bucking coil around 0 A. Both coils are off*

A demagnetization cycle of the bucking coil current around 0 A was attempted as follows: 0A → -200A → 190A → -180A → 170A → -160A → 150A → -140A 130A →

-120A → 110A → -100A → 90A → -80A 70A → -60A → 50A → -40A → 30A → -20A → OA, each step performed in 2 minutes, and the result is shown in Figure C.32. The maximum $B_\perp$ is 0.22 G which is close to the one before the shield was put in a magnetic field (Figure C.24); we plan to use this scheme for demagnetization when the solenoid is off.

Bucking coil "crash"

While ramping up both power supplies, a problem caused the solenoid to be discharged rapidly again, and the shield was re-magnetized. The two power supplies were ramped up once again, and with the solenoid at full current, demagnetization was attempted with a cycle around 200A as follows: 200A → 300A → 105A → 290A → 115A → 280A → 125A → 270A 135A → 260A → 145A → 250A → 155A → 240A → 165A 230A → 175A → 220A → 185A → 210A → 195A → 200A, each step performed in 2 minutes. The result is shown in Figure C.33, and should be compared to Figure C.29. The maximum value is now 0.9 G, quite comparable to the 0.8 G previously attained.

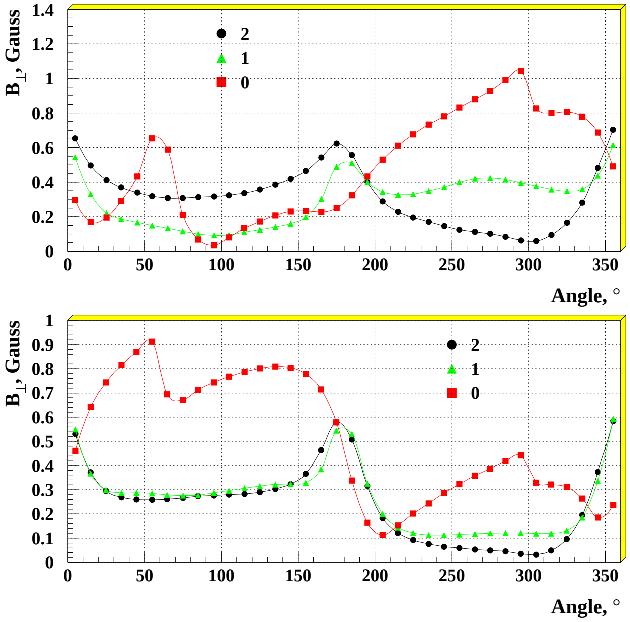

Figure C.33: *Comparison of $B_\perp$ vs. azimuthal angle after a bucking coil "crash" and after a demagnetization cycle of the bucking coil around 200 A with solenoid at full current. Both coils are on.*

While this scheme is satisfactory, it could possibly reduce the "on-time" of the experiment. Therefore, for a bucking coil "crash", another method of demagnetization was developed. We compensated for the magnetization by raising the bucking coil to a current above 200 A, called the overshoot current, and then lowering the current to the nominal 200 A current. We found that this was not only possible, but optimum in that the apparent *BABAR* left-right asymmetry could be compensated.

In Table C.2, we show the results of the optimization. Each I_{over} was obtained starting at a null bucking coil current.

I_{over}	max B_{perp}, left side	max B_{perp}, right side
200	1.9	1.2
250	0.68	0.56
260	0.61	0.61
275	0.58	0.72
300	0.54	0.88

Table C.2: *Optimization of the overshoot current,* I_{over}

In Figure C.34 we see the left-right compensation around the optimum value of $\mathrm{I}_o ver$=260 A. This result is in relatively good agreement with the calculation (Figure C.11) though some residual field probably still influences the probe 0 result. Nonetheless the results for probes 0 and 2 have about the same maximum value. In the experiment, we shall use this demagnetization scheme when the solenoid is at its nominal current.

Starting with a maximum $B_\perp$ of about 2 G when one of the two coils is inoperative and then is ramped up, the measurements with the simple demagnetization scheme show that a maximum $B_\perp$=0.6 G can be attained, in good agreement with the predictions, see Section C.3.4. This maximum field is quite robust for good PMT operation.

C.8.5 Conclusions

We have obtained low fringe fields in the backward part of the *BABAR* detector by using a bucking coil in conjunction with a very pure iron shield.

For the PMT region, within the shield, the measurements are in the sub-Gauss region, and a precise quantitative comparison with the simulation is masked somewhat by the magnetization of the shield which is difficult to avoid. As we have seen, this magnetization has a complicated azimuthal dependence.

For the quadrupole region, a more quantitative comparison can be made between the measurements and the 2D axisymmetric Mermaid model as shown on Figure C.28. The results are quite accurate at the exit of the backward endcap where the steep fall-off is very well-reproduced, even in the blown-up scale. Differences of the order of less than 5 G are seen at and between the quadrupoles.

The field in the PMT region is less than 1 G, in good agreement with the calculation. A simple method of demagnetization has been found, with a maximum $B_\perp = 0.6$ G in the PMT region. Demagnetization procedures have been investigated successfully and have become semi-automatic.

Acknowledgments. The authors are grateful for support by the Direction des Sciences de la Matière (CEA, France), SLAC and Budker Institute of Nuclear Physics (Novosibirsk). They would like to thank the solenoid/cryogenic group led by T. O'Connor and R. Burgess, the installation group led by R. Byers, and O. Fackler for his initial work on this subject.

The Saclay group would like to thank Kawasaki Heavy Industries, in particular Mr. Inoue and Mr. Numasawa, for their efficient and agreable collaboration on this project; in addition, the authors would like to thank KHI for its permission to use Figures C.5, C.17 and C.18.

One of the authors (GL) would like to thank J.-M. Baze for his initiation and help with Castem 2000. The Novosibirsk group would like to thank A. Dubrovin for his help with Mermaid.

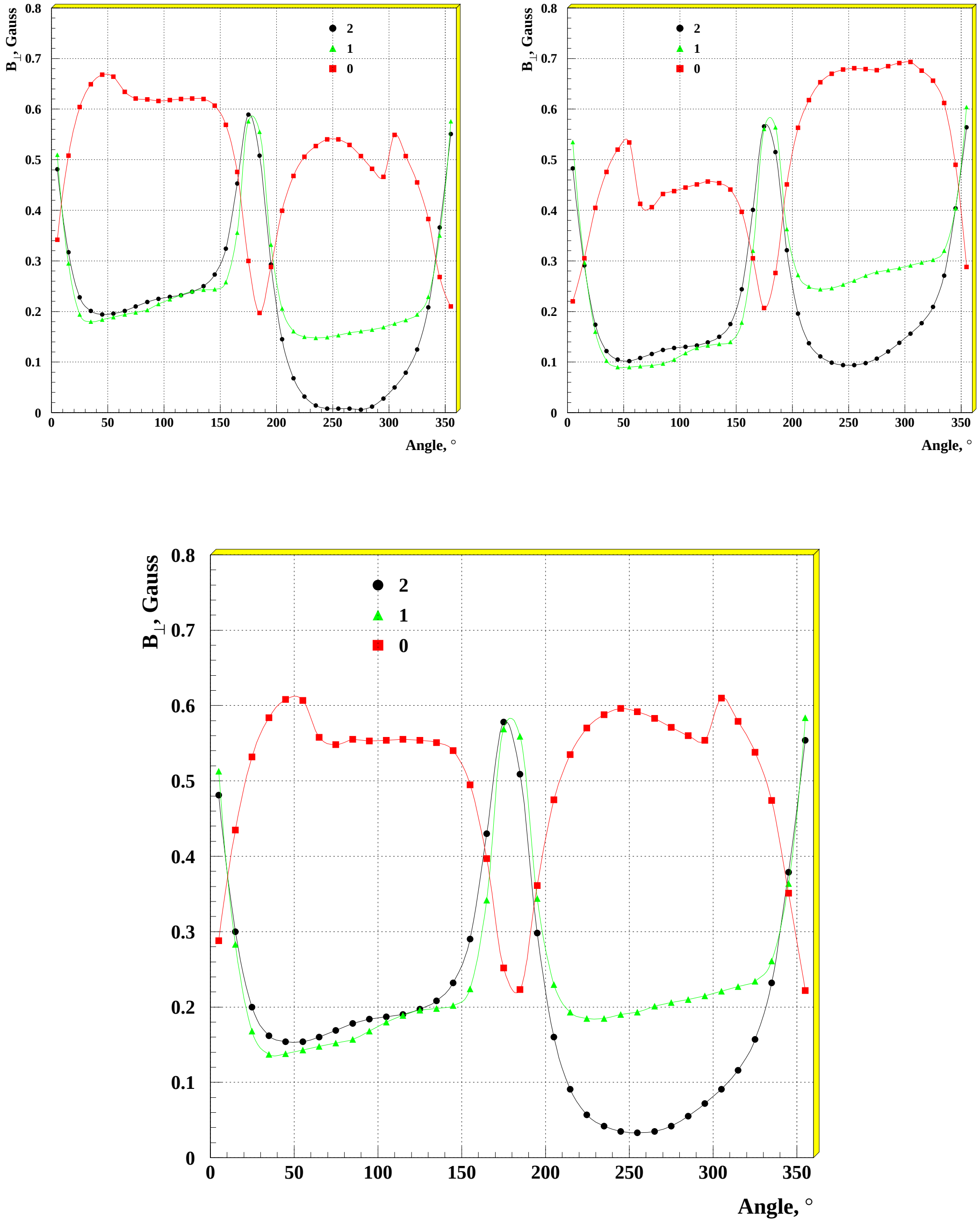

Figure C.34: *Comparison of $B_\perp$ vs. azimuthal angle for the overshoot currents = 250 A and 275 A, and the optimum current, 260 A.*

Bibliography

[1] An Asymmetric B Factory Based on PEP: *Conceptual Design Report*, *SLAC-REP-91-372* (1991)

[2] The *BABAR* collaboration, *Technical Design Report*, *SLAC-REP-95-457* (1995)

[3] H. Staengle *et al.* Nucl. Instr. Methods Phys. Res., Sect. C *A397* (1997) 261

[4] Ph. Bourgeois *et al. DIRC note 53* (1996), in particular, Figures 7 and 8

[5] Design of PEP-II Interaction Region Septum Quadrupole, J. Osborn, J. Tanabe, D. Yee, F. Younger, *97 Particle Accelerator Conference,* (Vancouver B. C. Canada, 12-16 May 1997)

[6] The Castem 2000 code was developed in the Saclay laboratory, P. Verpaux, T. Charras, A. Millard, "Castem 2000, une approche moderne du calcul des structures", *Calcul des structures et intelligences articielle* (J.M. Fouet, P. Ladeveze et R. Ohayon, Eds, Pluralis, 1988) 261-271

[7] The Mermaid code was developed in the Budker Institute, *Mermaid User's Guide,* (Novosibirsk, 1994)

[8] Kawasaki Heavy Industries, private communication.

[9] E.Antokhin *et al. BABAR note 344* (1996)

[10] A.Buzykaev *et al. DIRC note 101* (1998)

Appendix D

Study of $B^0 \to D_s^{(*)+} D^{*-}$ decays

This appendix includes the complete report of “Measurement of $B^0 \to D_s^{(*)+} D^{*-}$ Branching Fractions and $B^0 \to D_s^{*+} D^{*-}$ Polarization with a Partial Reconstruction Technique” published in Physical Revew D (*BABAR* Collaboration, B. Aubert *et al.* Phys. Rev. D **67** 092003 (2003))

Measurement of $B^0 \to D_s^{(*)+} D^{*-}$ Branching Fractions and $B^0 \to D_s^{*+} D^{*-}$ Polarization with a Partial Reconstruction Technique

BABAR Collaboratrion

Abstract

We present a study of the decays $B^0 \to D_s^{(*)+} D^{*-}$*, using* $20.8 fb^{-1}$ *of* e^+e^- *annihilation data recorded with the BABAR detector. The analysis is conducted with a partial reconstruction technique, in which only the* $D_s^{(*)+}$ *and the soft pion from the* D^{*-} *decay are reconstructed. We measure the branching fractions* $\mathcal{B}(B^0 \to D_s^+ D^{*-}) = (1.03 \pm 0.14 \pm 0.13 \pm 0.26)\%$ *and* $\mathcal{B}(B^0 \to D_s^{*+} D^{*-}) = (1.97 \pm 0.15 \pm 0.30 \pm 0.49)\%$*, where the first error is statistical, the second is systematic, and the third is the error due to the* $D_s^+ \to \phi\pi^+$ *branching fraction uncertainty. From the* $B^0 \to D_s^{*+} D^{*-}$ *angular distributions, we measure the fraction of longitudinal polarization* $\Gamma_L/\Gamma = (51.9 \pm 5.0 \pm 2.8)\%$*, which is consistent with theoretical predictions based on factorization.*

D.1 Introduction

Precise knowledge of the branching fractions of exclusive B decay modes provides a test of the factorization approach [1]. Factorization neglects final state interactions between the quarks of the two final state mesons. The pattern of branching fractions for two-body B decays to modes such as $D^{(*)}\pi$, $D^{(*)}\rho$ [2] can be successfully accommodated in such a model. However, it is possible that the factorization assumption is not applicable to the decays $B \to D^{(*)}X$, where the meson X contains a heavy quark. The current experimental uncertainties for $B \to D_s^{(*)+} \overline{D}^*$ branching fractions [3] do not allow us to perform a precise test of the factorization approach in this case.

Further tests of factorization are provided by measuring the polarization in decays of B mesons to vector-vector final states. Within experimental errors, polarization measurements are consistent with factorization predictions for the final states $\overline{D}^*\rho$ [4], $\overline{D}^*\rho(1450)$ [5], and $D_s^*\overline{D}^*$ [6].

In this paper we present measurements of the branching fractions[1] $\mathcal{B}(B^0 \to D_s^{(*)+} D^{*-})$. We also report a measurement of the D_s^{*+} polarization in the decay $B^0 \to D_s^{*+} D^{*-}$, obtained from an angular analysis. These results provide tests of factorization with increased precision.

---

[1] Reference to a specific decay channel or state also implies the charge conjugate decay or state. The notation $D_s^{(*)+}$ refers to either D_s^+ or D_s^{*+}.

D.2 The *BABAR* Detector and Data Set

The data used in this analysis were collected with the *BABAR* detector at the PEP-II storage ring. An integrated luminosity of $20.8\,\mathrm{fb}^{-1}$ was recorded in 1999 and 2000 at the $\Upsilon(4S)$ resonance, corresponding to about 22.7 million produced $B\overline{B}$ pairs.

A detailed description of the *BABAR* detector is presented in Ref. [7]. Only the components of the detector most relevant to this analysis are briefly described here. Charged particles are reconstructed with a five-layer, double-sided silicon vertex tracker (SVT) and a 40-layer drift chamber (DCH) with a helium-based gas mixture, placed in a 1.5 T solenoidal field produced by a superconducting magnet. The charged particle resolution is approximately $(\delta p_T/p_T)^2 = (0.0013\,p_T)^2 + (0.0045)^2$, where p_T is the transverse momentum given in GeV/c. The SVT, with a typical single-hit resolution of $10\,\mu$m, provides measurement of the impact parameters of charged particle tracks in both the plane transverse to the beam direction and along the beam. Charged particle types are identified from the ionization energy loss (dE/dx) measured in the DCH and SVT, and the Cherenkov radiation detected in a ring imaging Cherenkov device (DIRC). Photons are identified by a CsI(Tl) electromagnetic calorimeter (EMC) with an energy resolution $\sigma(E)/E = 0.023\cdot(E/\mathrm{GeV})^{-1/4}\oplus 0.019$.

D.3 Method of Partial Reconstruction

In selecting candidates for the decays $B^0 \to D_s^{(*)+}D^{*-}$ with $D^{*-} \to \overline{D}{}^0\pi^-$, no attempt is made to reconstruct the $\overline{D}{}^0$ decays. Only the $D_s^{(*)+}$ and the soft π^- from the D^{*-} decay are detected. In this way, the candidate selection efficiency is higher by almost an order of magnitude than that obtained with full reconstruction of the final state. Given the four-momenta of the $D_s^{(*)+}$ and π^-, and assuming they originate from a $B^0 \to D_s^{(*)+}D^{*-}$ decay, the four-momentum of the B^0 can be calculated up to an unknown azimuthal angle ϕ around the $D_s^{(*)+}$ flight direction. This calculation uses the constraint of the known center-of-mass (CM) energy and the masses of the B^0 and D^{*-} mesons. Energy and momentum conservation then allows a determination of the four-momentum of the $\overline{D}{}^0$, whose square yields the ϕ-dependent missing mass

$$m_{\text{miss}} = \sqrt{(\mathrm{P}_B - \mathrm{P}_{D_s^{(*)+}} - \mathrm{P}_\pi)^2}\ , \tag{D.1}$$

where P_B, $\mathrm{P}_{D_s^{(*)+}}$ and P_π are the four-momenta of the B^0, $D_s^{(*)+}$ and the soft pion, respectively. In this analysis the missing mass is defined with an arbitrary choice for the angle ϕ, such that the B^0 momentum $\mathbf{p}_B$ makes the smallest possible angle with $\mathbf{p}_\pi$ and $\mathbf{p}_{D_s^{(*)+}}$ in the CM frame.

D.4 Event Selection

For each event, we calculate the ratio of the second to the zeroth order Fox-Wolfram moments, using all observed charged tracks and neutral clusters. This ratio is required to be less than 0.35 in order to suppress continuum $e^+e^- \to q\overline{q}$ events, where $q = u, d, s, c$.

We reconstruct D_s^+ mesons in the decay modes $D_s^+ \to \phi\pi^+$, $D_s^+ \to \overline{K}^{*0}K^+$ and $D_s^+ \to K_S^0 K^+$, with subsequent decays $\phi \to K^+K^-$, $\overline{K}^{*0} \to K^-\pi^+$ and $K_S^0 \to \pi^+\pi^-$. These modes are selected since they offer the best combination of large branching fraction, good detection efficiency, and high signal-to-background ratio. Charged tracks from the D_s^+ are required to originate from within ±10 cm along the beam direction and ±1.5 cm in the transverse plane, and leave at least 12 hits in the DCH.

Kaons are identified using dE/dxinformation from the SVT and DCH, as well as the Cherenkov angle and the number of photons measured with the DIRC. For each detector component $d = \{\text{SVT, DCH, DIRC}\}$, a likelihood L_d^K (L_d^π) is calculated given the kaon (pion) mass hypothesis. A charged particle is classified as a "loose" kaon if it satisfies $L_d^K/L_d^\pi > 1$ for at least one of the detector components. A "tight" kaon classification is made if the condition $\prod_d L_d^K/L_d^\pi > 1$ is satisfied.

Three charged tracks consistent with originating from a common vertex are combined to form a D_s^+ candidate.

In the case of the decay $D_s^+ \to \phi\pi^+$, two oppositely charged tracks must be identified as kaons with both satisfying the loose criterion, and at least one, the tight criterion. No identification requirement is applied to the pion. The reconstructed invariant mass of the K^+K^- candidates must be within $8\,\text{MeV}/c^2$ of the nominal ϕ mass [8]. In the decay $D_s^+ \to \phi\pi^+$, the ϕ meson is polarized longitudinally, resulting in the kaons having a $\cos^2\theta_H$ distribution, where θ_H is the angle between the K^+ and D_s^+ directions in the ϕ rest frame. We require $|\cos\theta_H| > 0.3$, which retains 97% of the signal while rejecting about 30% of the background.

In the reconstruction of the $D_s^+ \to \overline{K}^{*0}K^+$ mode, the $K^-\pi^+$ invariant mass is required to be within $65\,\text{MeV}/c^2$ of the nominal $\overline{K}^{*0}$ mass [8]. This wider window leads to a larger fraction of combinatorial background than in the $D_s^+ \to \phi\pi^+$ mode. To reduce this background, we require $|\cos\theta_H| > 0.5$. In addition, substantial background arises from the decays $D^+ \to \overline{K}^{*0}\pi^+$ and $D^+ \to \overline{K}^0\pi^+$, which tend to peak around the nominal D_s^+ mass if the pion is misidentified as a kaon. This background is suppressed by requiring that the kaon daughter of the $\overline{K}^{*0}$ satisfy the loose kaon identification criterion and the other kaon, the tight criterion.

For the decay mode $D_s^+ \to K_S^0 K^+$, with $K_S^0 \to \pi^+\pi^-$, the $\pi^+\pi^-$ invariant mass must be within $15\,\text{MeV}/c^2$ of the nominal K_S^0 mass [8], and the charged kaon must satisfy the tight criterion. To improve the purity of the K_S^0 sample, we require the angle α between the K_S^0 momentum vector and the K_S^0 flight direction to satisfy $\cos\alpha > 0.98$.

The invariant mass M_{D_s} of D_s^+ candidates is required to be within three standard deviations (σ_{D_s}) of the signal distribution peak $M_{D_s}^{\mathrm{peak}}$ seen in the data.

D_s^+ candidates satisfying these selection criteria are combined with photon candidates to form $D_s^{*+} \to D_s^+\gamma$ candidates. Candidate photons are required to satisfy $E_\gamma > 50\,\mathrm{MeV}$, where E_γ is the photon energy in the laboratory frame, and $E_\gamma^* > 110\,\mathrm{MeV}$, where E_γ^* is the photon energy in the CM frame. When the photon candidate is combined with any other photon candidate in the event, the pair must not form a good π^0 candidate, defined by a total CM energy $E_{\gamma\gamma}^* > 200\,\mathrm{MeV}$ and an invariant mass $115 < M_{\gamma\gamma} < 155\,\mathrm{MeV}/c^2$.

The D_s^{*+} candidates must satisfy $|\Delta M - \Delta M^{\mathrm{peak}}| < 2.5\,\sigma_{\Delta M}$, where ΔM^{peak} is the peak of the signal $\Delta M = M(D_s^+\gamma) - M(D_s^+)$ distribution observed in the data. The CM momentum of the $D_s^{(*)+}$ candidate is required to be greater than $1.5\,\mathrm{GeV}/c$.

$D_s^{(*)+}$ candidates are combined with π^- candidates to form partially reconstructed $B^0 \to D_s^{(*)+}D^{*-}$ candidates. Since the transverse momentum of the pion in signal events is less than $210\,\mathrm{MeV}/c$, these tracks are not required to have DCH hits.

Due to the high combinatorial background in the ΔM distribution, more than one $D_s^{*+}\pi^-$ candidate pair is found per event, with about a 20% probability from signal Monte Carlo simulation. To select the best candidate in the event, the following χ^2 is calculated for each D_s^{*+} candidate

$$\begin{aligned}\chi^2 = {}& [(M_i - M_i^{\mathrm{peak}})/\sigma_i]^2 + [(M_{D_s} - M_{D_s}^{\mathrm{peak}})/\sigma_{D_s}]^2 \\ &+[(\Delta M - \Delta M^{\mathrm{peak}})/\sigma_{\Delta M}]^2,\end{aligned} \tag{D.2}$$

where M_i is the measured invariant mass of the intermediate $i = \phi$, K^{*0}, or K_S^0 candidate, depending on the D_s^+ decay mode, M_i^{peak} is the corresponding peak of the signal M_i distribution, and σ_i is its width obtained from data. The candidate with the smallest value of χ^2 in the event is retained.

D.5 Results

The missing mass distributions of candidates for partially reconstructed $B^0 \to D_s^{(*)+}D^{*-}$ decays are shown in Fig. D.1. A clear signal peak is observed in all modes. We perform a binned maximum likelihood fit to these distributions. The fit function is the sum of a Gaussian distribution and a background function given by

$$f_B(m_{\mathrm{miss}}) = \frac{C_1(M_0 - m_{\mathrm{miss}})^{C_2}}{C_3 + (M_0 - m_{\mathrm{miss}})^{C_2}}, \tag{D.3}$$

where C_i are parameters determined by the fit, and $M_0 \equiv M_{D^*} - M_\pi = 1.871\,\mathrm{GeV}/c^2$ is the kinematic end point. The fits find 3704 ± 232 and 1493 ± 95 events under the Gaussian peak in the sum of the $D_s^+\pi^-$ and $D_s^{*+}\pi^-$ distributions, respectively.

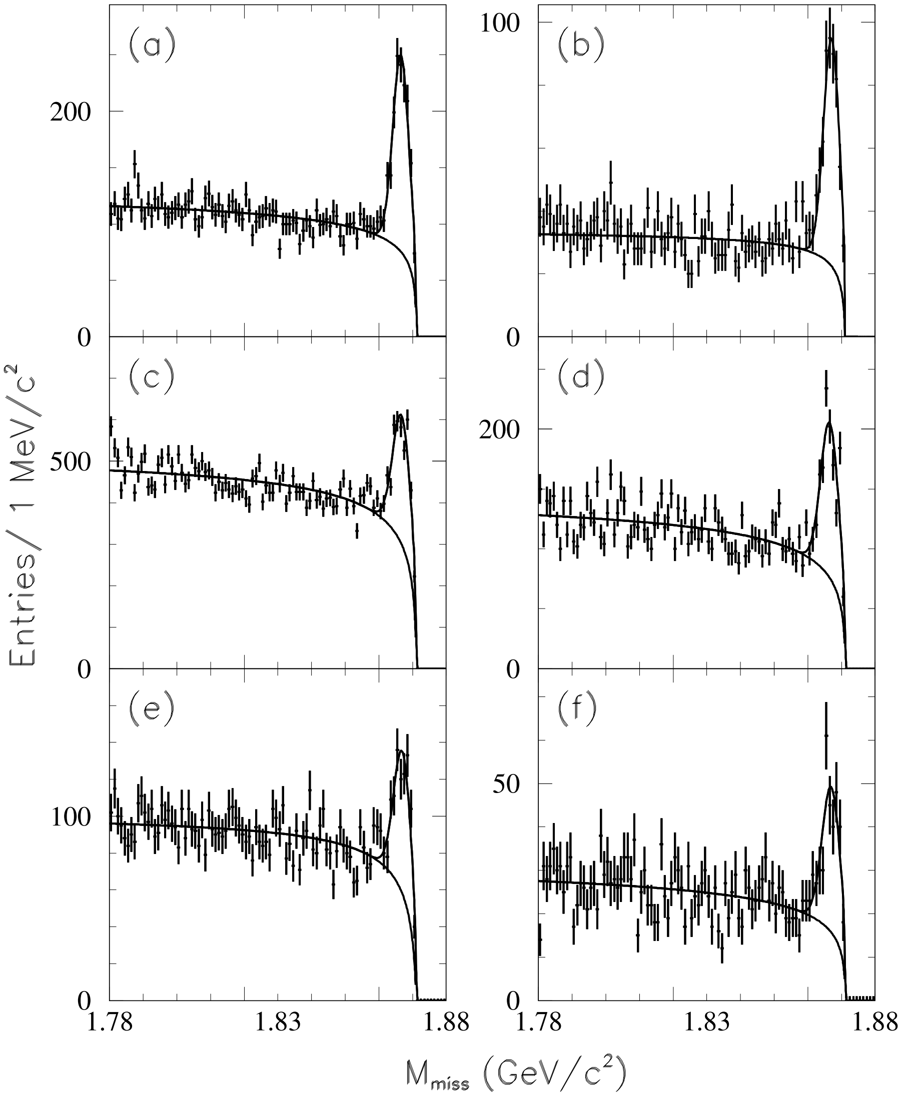

Figure D.1: *Missing mass distributions of B candidates in data. (a)* $D_s^+\pi^-$ *with* $D_s^+ \to \phi\pi^+$*, (b)* $D_s^{*+}\pi^-$ *with* $D_s^+ \to \phi\pi^+$*, (c)* $D_s^+\pi^-$ *with* $D_s^+ \to \overline{K}^{*0}K^+$*, (d)* $D_s^{*+}\pi^-$ *with* $D_s^+ \to \overline{K}^{*0}K^+$*, (e)* $D_s^+\pi^-$ *with* $D_s^+ \to K_S^0K^+$*, (f)* $D_s^{*+}\pi^-$ *with* $D_s^+ \to K_S^0K^+$*. The curves show the result of the fit (see text), indicating the signal and background contributions.*

However, due to the presence of cross feed and self-cross feed, discussed below, further analysis is needed in order to extract the signal yields and the branching fractions.

We use a Monte Carlo simulation, which includes both $B\overline{B}$ and $q\bar{q}$ continuum events, to study the missing mass distributions of the different background sources.

Table D.1: *Efficiencies for* $B^0 \to D_s^{(*)+}D^{*-}$ *decay modes to contribute to the* $D_s^+\pi^-$ *and* $D_s^{*+}\pi^-$ *missing mass distributions in the signal region* $m_{\rm miss} > 1.86\,{\rm GeV}/c^2$. *Two different* $B^0 \to D_s^{*+}D^{*-}$ *Monte Carlo samples have been used, one with longitudinal (long.) and the other with transverse (transv.) polarization.*

	Reconstructed mode	
Generated mode	$D_s^+\pi^-$	$D_s^{*+}\pi^-$
$B^0 \to D_s^+D^{*-}$	$(23.6 \pm 1.0)\%$	$(1.7 \pm 0.3)\%$
$B^0 \to D_s^{*+}D^{*-}$ (long.)	$(9.0 \pm 0.3)\%$	$(7.4 \pm 0.3)\%$
Self-Cross Feed		$(1.6 \pm 0.1)\%$
$B^0 \to D_s^{*+}D^{*-}$ (transv.)	$(10.4 \pm 0.3)\%$	$(6.9 \pm 0.3)\%$
Self-Cross Feed		$(1.4 \pm 0.1)\%$

We consider two kinds of backgrounds: a peaking component that contributes predominantly at the end of the missing mass distribution in the signal region and a non-peaking component that is more uniform. The non-peaking component is well modeled by the background function (D.3). The peaking component receives contributions from related channels due to

- **Cross Feed (CF):** if the soft photon from a $D_s^{*+} \to D_s^+\gamma$ decay is not reconstructed, $B^0 \to D_s^{*+}D^{*-}$ decays may lead to an enhancement under the signal peak of the $D_s^+\pi^-$ missing mass spectrum. Similarly, $B^0 \to D_s^+D^{*-}$ decays may lead to a peaking enhancement in the $D_s^{*+}\pi^-$ $m_{\rm miss}$ spectrum, due to the combination of a D_s^+ with a random photon.
- **Self-Cross Feed (SCF):** this is due to true $B^0 \to D_s^{*+}D^{*-}$ decays in which the D_s^+ is correctly reconstructed, but combined with a random photon to produce the wrong D_s^{*+} candidate, resulting in a peaking enhancement in the $D_s^{*+}\pi^-$ spectrum.

Table D.1 presents the reconstruction efficiency of correctly reconstructed signal $B^0 \to D_s^{(*)+}D^{*-}$ decays, as well as cross feed and self-cross feed, found for simulated events in the signal region $m_{\rm miss} > 1.86\,{\rm GeV}/c^2$.

In addition to these background sources, we also considered a possible contribution from the charged and neutral B decays $B \to D_s^{(*)+}\overline{D}^{**}$. These potential background sources were simulated with four $\overline{D}^{**}$ states: the observed $\overline{D}_1(2420)$ and $\overline{D}_2^*(2460)$ mesons, and the $\overline{D}_0^*(j=1/2)$ and $\overline{D}_1(j=1/2)$ mesons predicted by HQET [9]. Their contribution was determined to be negligible, mainly due to the $D_s^{(*)+}$ CM momentum

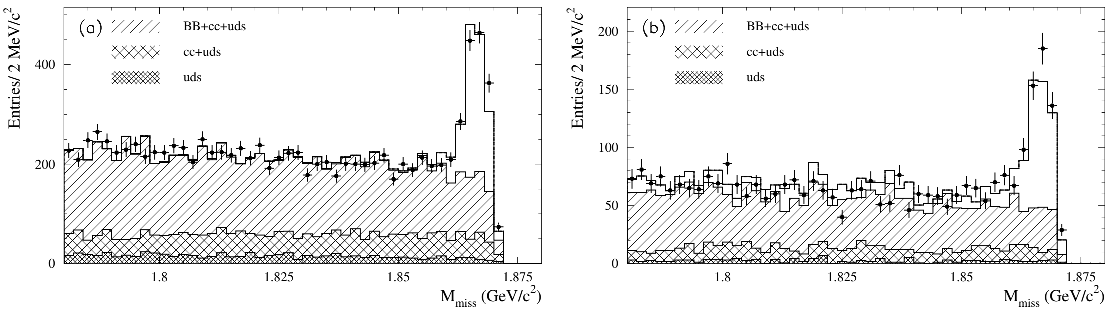

Figure D.2: *Missing mass distribution for (a)* $D_s^+\pi^-$ *and (b)* $D_s^{*+}\pi^-$ *combinations for data (points with error bars) and Monte Carlo (histogram). The contributions from the* $B\bar{B}$, $c\bar{c}$ *and* $q\bar{q}$ *with* $q = u,\ d,\ s$ *(labeled uds in the figure) are shown separately. The cross feed and self-cross feed backgrounds are included in the total histogram, but not in the hatched* $B\overline{B}$ *histogram.*

cut. Multi-body decays $B \to D_s^{(*)+}X$ are found not to contribute due to the same cut.

Figure D.2 shows a comparison of the missing mass distributions in data and Monte Carlo simulation. We assume 1.05% and 1.59% branching fractions for the $B^0 \to D_s^+ D^{*-}$ and $B^0 \to D_s^{*+} D^{*-}$ decays, respectively, in the Monte Carlo simulation.

The number of events in the peaks in the $D_s^+\pi^-$ and $D_s^{*+}\pi^-$ m_{miss} distributions is obtained from the fits described above. The branching fractions are computed from these yields correcting for cross feed and self-cross feed background. This is done by inverting the 2×2 efficiency matrix, whose diagonal elements correspond to the sum of signal and self-cross feed efficiencies presented in Table D.1, and whose off-diagonal terms are the cross-feed efficiencies. The efficiencies corresponding to transverse and longitudinal polarization of $B^0 \to D_s^{*+} D^{*-}$ have been weighted according to the measured polarization discussed below. With this procedure, the $B^0 \to D_s^{(*)+} D^{*-}$ branching fractions are determined to be

$$\mathcal{B}(B^0 \to D_s^+ D^{*-}) = (1.03 \pm 0.14 \pm 0.13 \pm 0.26)\%, \tag{D.4}$$

$$\mathcal{B}(B^0 \to D_s^{*+} D^{*-}) = (1.97 \pm 0.15 \pm 0.30 \pm 0.49)\%, \tag{D.5}$$

and their sum is

$$\mathcal{B}(B^0 \to D_s^{(*)+} D^{*-}) = (3.00 \pm 0.19 \pm 0.39 \pm 0.75)\%, \tag{D.6}$$

where the first error is statistical, the second is the systematic error from all sources other than the uncertainty in the $D_s^+ \to \phi\pi^+$ branching fraction, and the third error, which is dominant, is due the uncertainty in the $D_s^+ \to \phi\pi^+$ branching fraction $\mathcal{B}(D_s^+ \to \phi\pi^+) = (3.6 \pm 0.9)\%$ [8]. Correlations in the systematic errors between

Eqs. (D.4) and (D.5) are taken into account in Eq. (D.6). The sources of the systematic error are discussed in Sec. D.6.

The measurement of the fraction of the longitudinal polarization Γ_L/Γ in the $B^0 \to D_s^{*+} D^{*-}$ decay mode is performed for candidates having missing mass in the signal region ($M_{miss} > 1.86\,\mathrm{GeV}/c^2$). To minimize the systematic error due to large backgrounds, the polarization measurement involves only the $D_s^+ \to \phi\pi^+$ channel, which has the best signal to background ratio. Two angles are used: the helicity angle θ_γ between the D^{*-} and the soft photon direction in the D_s^{*+} rest frame, and the helicity angle θ_π between the D_s^{*+} and the soft pion direction in the D^{*-} rest frame. Since the B meson is not fully reconstructed, we compute θ_γ and θ_π by constraining m_{miss} to the nominal D^0 mass [8] to obtain a unique solution for the azimuth ϕ.

The two-dimensional distribution ($\cos\theta_\gamma$, $\cos\theta_\pi$) is divided into five ranges in each dimension, resulting in 25 bins. The combinatorial background, as well as the cross feed and the self-cross feed obtained from Monte Carlo simulation, are subtracted from this two-dimensional data distribution. The resulting signal distribution is corrected bin-by-bin for detection efficiency, which is obtained from the simulation separately for each bin. A two-dimensional binned minimum-χ^2 fit is then performed to the efficiency-corrected signal distribution with the fit function

$$\begin{aligned}\frac{d^2\Gamma}{d\cos\theta_\pi\ d\cos\theta_\gamma} &\propto \frac{\Gamma_L}{\Gamma}\ \cos^2\theta_\pi \sin^2\theta_\gamma + \\ &\quad (1\ -\ \frac{\Gamma_L}{\Gamma}\ )\sin^2\theta_\pi \frac{1+\cos^2\theta_\gamma}{4}. \end{aligned} \tag{D.7}$$

The resulting fit has a χ^2 of 23.1 for 25 bins with two floating parameters (Γ_L/Γ and total normalization). Figure D.3 shows the data and the result of the fit projected on the $\cos\theta_\gamma$ and $\cos\theta_\pi$ axes.

From the fit, the fraction of longitudinal polarization is determined to be

$$\Gamma_L/\Gamma = (51.9 \pm 5.0 \pm 2.8)\%, \tag{D.8}$$

where the first error is statistical and the second is systematic.

D.6 Systematic Uncertainties

The various contributions to the systematic errors on the branching fraction and polarization measurements are summarized in Table D.2. The dominant systematic error for the branching fractions is the uncertainty on the three D_s^+ branching fractions. To evaluate the uncertainty due to the background subtraction, the signal yield is determined using an alternative method in which the number of events is extracted directly from the histogram after subtraction of the background, which is estimated with the Monte Carlo simulation. The difference of the signal yields obtained in this

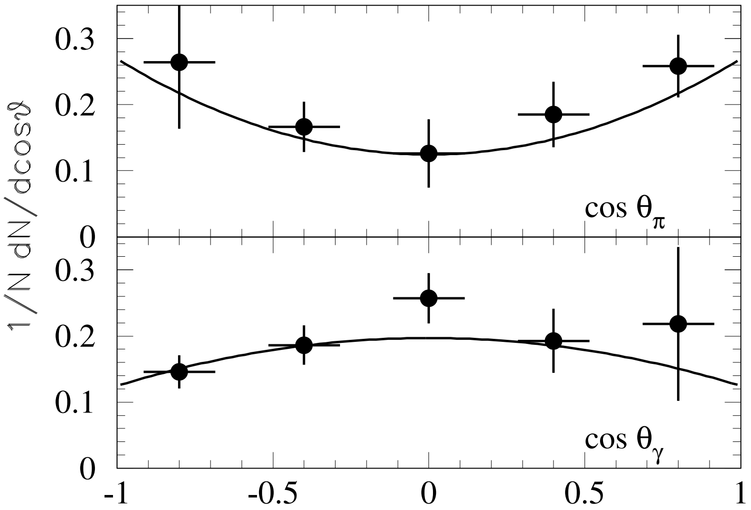

Figure D.3: *Projections of the number of background-subtracted data events on the* $\cos\theta_\pi$ *and* $\cos\theta_\gamma$ *axes. The result of the two-dimensional fit is overlaid.*

way from the results of the fit was taken as a systematic error. This also accounts for the systematic error due to a possible deviation of the signal shape from a Gaussian.

The Monte Carlo statistical errors in the determination of the signal and the cross feed efficiencies are included as a systematic error. The uncertainty in the calculation of the $B^0 \to D_s^{*+} D^{*-}$ polarization is propagated to the branching fraction systematic error. The systematic error due to the uncertainty on the efficiency for the reconstruction of charged particles is 1.2% times the number of charged particles in the decay. An additional error of 1.6% is added in quadrature to account for the uncertainty in the reconstruction efficiency of the soft pion. The systematic error due to the π^0 veto requirement was studied by measuring the relative D_s^{*+} yields in data and Monte Carlo with and without the π^0 veto.

In the polarization measurement, the level of the various backgrounds depends on the charged track, neutral cluster, and particle identification efficiencies. The fit was repeated varying the background according to the errors in these efficiencies, and the resulting variations in Γ_L/Γ were taken as the associated systematic error.

To check that the simulation accurately reproduces the background m_{miss} distributions in the data, a thorough data-Monte Carlo comparison is made in control samples containing no signal events. These samples are events with $1.78 < m_{\mathrm{miss}} < 1.85\,\mathrm{GeV}/c^2$; events in the D_s^+ sideband $1.89 < M_{D_s} < 1.95\,\mathrm{GeV}/c^2$ or $1.985 < M_{D_s} < 2.05\,\mathrm{GeV}/c^2$; events in the D_s^{*+} sideband $170 < \Delta M < 300\,\mathrm{MeV}/c^2$; wrong sign $D_s^{(*)+}\pi^+$ combinations in either the M_{D_s} and ΔM sidebands or signal regions determined above; and candidates in which m_{miss} was calculated with the inverse of the $D_s^{(*)+}$ center-of-mass momentum $p^*_{D_s^{(*)+}}$. The comparison between data

Table D.2: *Sources of systematic uncertainties (%) for the* $B^0 \to D_s^{(*)+} D^{*-}$ *branching fractions and* $B^0 \to D_s^{*+} D^{*-}$ *polarization measurements.*

Source	$D_s^+ D^{*-}$	$D_s^{*+} D^{*-}$	$\sigma(\Gamma_L/\Gamma)$
Background subtraction or modeling	2.7	5.9	0.5
Monte Carlo statistics	4.2	6.0	2.7
Polarization uncertainty	0.8	0.5	-
Cross feed	3.2	2.4	-
Number of B pairs	1.6	1.6	-
$\mathcal{B}(\phi \to K^+K^-)$	1.6	1.6	-
Particle identification	1.0	1.0	0.1
Tracking efficiency	3.6	3.6	0.5
Soft pion efficiency	2.0	2.0	0.2
Relative branching fractions	10.2	10.2	-
$\mathcal{B}(D_s^{*+} \to D_s^+\gamma)$	-	2.7	-
Photon efficiency	-	1.3	0.1
π^0 veto	-	2.7	0.3
Total systematic error	13.1	15.1	2.8

and Monte Carlo simulation for these control samples is shown in Table D.3. The average level of discrepancy is used to estimate the uncertainty in the modeling of the background.

Table D.3: *The fractional difference $\langle (N_{\rm D} - N_{\rm MC})/N_{\rm MC} \rangle$, averaged over all $m_{\rm miss}$ bins, where $N_{\rm D}$ ($N_{\rm MC}$) is the number of data (Monte Carlo) candidates in a given bin of the $m_{\rm miss}$ distribution of the given control sample. SB (SR) refers to the M_{D_s} or ΔM sideband (signal region) control sample. WS indicates wrong sign $D_s^{(*)+}\pi^+$ combinations, and $-p^*_{D_s^{(*)+}}$ indicates that $m_{\rm miss}$ was calculated from the negative of the $D_s^{(*)+}$ CM momentum. The missing mass range $1.78 < m_{\rm miss} < 1.87\,{\rm GeV}/c^2$ is used for the control sample, except for the first line.*

Sample type	$D_s^+\pi^-$	$D_s^{*+}\pi^-$
$1.78 < m_{\rm miss} < 1.85\,{\rm GeV}/c^2$	-0.009 ± 0.007	0.075 ± 0.014
SB	-0.075 ± 0.006	0.007 ± 0.022
SR, WS	0.006 ± 0.008	0.044 ± 0.015
SB, WS	-0.060 ± 0.007	-0.008 ± 0.024
SR, $-p^*_{D_s^{(*)+}}$	0.015 ± 0.009	0.075 ± 0.016
SB, $-p^*_{D_s^{(*)+}}$	-0.062 ± 0.007	-0.123 ± 0.022
Average	-0.038 ± 0.003	0.032 ± 0.007

D.7 Summary

In summary, based on a partial reconstruction technique, we have measured the branching fractions

$$\begin{aligned} \mathcal{B}(B^0 \to D_s^+ D^{*-}) &= (1.03 \pm 0.14 \pm 0.13 \pm 0.26)\% \,, \\ \mathcal{B}(B^0 \to D_s^{*+} D^{*-}) &= (1.97 \pm 0.15 \pm 0.30 \pm 0.49)\% \,, \\ \mathcal{B}(B^0 \to D_s^{(*)+} D^{*-}) &= (3.00 \pm 0.19 \pm 0.39 \pm 0.75)\% \,. \end{aligned}$$

The fraction of the longitudinal D_s^{*+} polarization in $B^0 \to D_s^{*+} D^{*-}$ decays is determined to be

$$\Gamma_L/\Gamma = (51.9 \pm 5.0 \pm 2.8)\%.$$

This measurement is consistent with theoretical predictions assuming factorization, which range from 50 to 55% [10, 11]. Our results are also in good agreement with previous experimental results [3, 6].

D.8 Acknowledgements

We are grateful for the excellent luminosity and machine conditions provided by our PEP-II colleagues, and for the substantial dedicated effort from the computing organizations that support *BABAR*. The collaborating institutions wish to thank SLAC for its support and kind hospitality. This work is supported by DOE and NSF (USA), NSERC (Canada), IHEP (China), CEA and CNRS-IN2P3 (France), BMBF and DFG (Germany), INFN (Italy), FOM (The Netherlands), NFR (Norway), MIST (Russia), and PPARC (United Kingdom). Individuals have received support from CONACyT (Mexico), A. P. Sloan Foundation, Research Corporation, and Alexander von Humboldt Foundation.

Bibliography

[1] M. Bauer, B. Stech, M. Wirbel, Z. Phys. C **34**, 103 (1987).

[2] CLEO Collaboration, M. S. Alam *et al.*, Phys. Rev. D **50**, 43 (1994).

[3] CLEO Collaboration, D. Gibaut *et al.*, Phys. Rev. D **53**, 4734 (1996).

[4] CLEO Collaboration, G. Bonvicini *et al.*, CLEO CONF 98-23, presented at the 29th International Conference on High Energy Physics, Vancouver, Canada (1998).

[5] CLEO Collaboration, J. P. Alexander *et al.*, Phys. Rev. D **64**, 092001 (2001).

[6] CLEO Collaboration, S. Ahmed *et al.*, Phys. Rev. D **62**, 112003 (2000).

[7] *BABAR* Collaboration, A. Palano *et al.*, Nucl. Instr. Methods Phys. Res., Sect. A **479**, 1 (2002).

[8] Particle Data Group, K. Hagiwara *et al.*, Phys. Rev. D **66**, 010001 (2002).

[9] A. F. Falk and M. Luke, Phys. Lett. B **292**, 119 (1992).

[10] J. D. Richman, in *Probing the Standard Model of Particle Interactions*, edited by R. Gupta, A. Morel, E. de Rafael, and F. David (Elsevier, Amsterdam, 1999), p.640.

[11] Z. Luo and J. L. Rosner, Phys. Rev. D **64**, 094001 (2001).

Appendix E

CP violation in $B^0 \to D^{*\mp}\pi^\pm$ decays

This appendix contains the report of *CP* violation measurement with $B^0 \to D^{*\mp}\pi^\pm$ decays and constraint on the $\sin(2\beta+\gamma)$ angle. It consists of three following sections:

- "First measurement of *CP* asymmetries in $B^0 \to D^{*\mp}\pi^\pm$ decays" published in Physical Review Letter (*BABAR* Collaboration, B. Aubert *et al.* "Measurement of Time-Dependent *CP* Asymmetries and Constraints on $\sin(2\beta+\gamma)$ with Partial Reconstruction of $B^0 \to D^{*\mp}\pi^\pm$ Decays" Phys. Rev. Lett. **92** 251802 (2004));
- "Precise measurement of *CP* asymmetries in $B^0 \to D^{*\mp}\pi^\pm$ decays" published in Physical Review D (*BABAR* Collaboration, B. Aubert *et al.* "Measurement of Time-Dependent *CP* Asymmetries and Constraints on $\sin(2\beta+\gamma)$ with Partial Reconstruction of $B^0 \to D^{*\mp}\pi^\pm$ Decays" Phys. Rev. D **71** 112003 (2005));
- "Status and prospects for *CP* asymmetry measurements: $\sin(2\beta+\gamma)$", proceedings of the CKM 2006 workshop in Nagoya University, December 2006, Nagoya, Japan (S. Ganzhur, "*BABAR* Status and prospects for *CP* asymmetry measurements: $\sin(2\beta+\gamma)$", hep-ph/0703229 (2007)).

The first section presents the results of the first measurement of *CP* violation in $B^0 \to D^{*\mp}\pi^\pm$ decays with about 82 million $B\overline{B}$ events recorded by the *BABAR* experiment. The second section reports the updated result of *CP* violation in this decay mode and constraint on $\sin(2\beta+\gamma)$ with about 232 million $B\overline{B}$ events. The measured *CP* asymmetry is

$$2r\sin(2\beta+\gamma)\cos\delta = -0.034 \pm 0.014 \pm 0.009,$$

where the first error is statistical and the second is systematic. This result indicates 2.0 standard deviations from zero and presents the most precise *CP* violation measurement in the decays of B mesons. It allows us to constraint the angles of the unitarity triangle using SU(3) symmetry assumption. This yields the limit $|\sin(2\beta+\gamma)| > 0.62(0.35)$ at 68% (90%) CL.

The last section describes the experimental status and future perspectives of $\sin(2\beta+\gamma)$ measurements with different decay channels and analysis techniques.

E.1 First measurement of *CP* asymmetries in $B^0 \to D^{*\mp}\pi^\pm$ decays

Measurement of Time-Dependent *CP* Asymmetries and Constraints on $\sin(2\beta+\gamma)$ with Partial Reconstruction of $B^0 \to D^{*\mp}\pi^\pm$ Decays

BABAR Collaboration

Abstract

We present a measurement of time-dependent CP-violating asymmetries in decays of neutral B mesons to the final states $D^{*\mp}\pi^\pm$*, using approximately* 82 *million* $B\overline{B}$ *events recorded by the BABAR experiment at the PEP-II* e^+e^- *storage ring. Events containing these decays are selected with a partial reconstruction technique, in which only the high-momentum* $\pi^\pm$ *from the B decay and the low-momentum* $\pi^\mp$ *from the* $D^{*\mp}$ *decay are used. We measure the amplitude of the asymmetry to be* -0.063 ± 0.024 *(stat.)* ± 0.014 *(syst.) and compute bounds on* $|\sin(2\beta+\gamma)|$*.*

The Cabibbo-Kobayashi-Maskawa (CKM) quark-mixing matrix [1] gives an explanation of *CP* violation and is under experimental investigation aimed at constraining its parameters. A crucial part of this program is the measurement of the angle $\gamma = \arg\left(-V_{ud}V_{ub}^*/V_{cd}V_{cb}^*\right)$ of the unitarity triangle related to the CKM matrix. The decay modes $B^0 \to D^{*\mp}\pi^\pm$ have been proposed for use in measurements of $\sin(2\beta+\gamma)$ [2], where $\beta = \arg\left(-V_{cd}V_{cb}^*/V_{td}V_{tb}^*\right)$ is well measured [3]. In the Standard Model the decays $B^0 \to D^{*+}\pi^-$ and $\overline{B}^0 \to D^{*+}\pi^-$ proceed through the $\overline{b} \to \overline{u}cd$ and $b \to c\bar{u}d$ amplitudes A_u and A_c. The relative weak phase between the two amplitudes in the usual Wolfenstein convention [4] is γ. When combined with $B^0\overline{B}^0$ mixing, this yields a weak phase difference of $2\beta+\gamma$ between the interfering amplitudes.

The decay rate distribution for $B \to D^{*\pm}\pi^\mp$ is

$$\begin{aligned}\mathcal{P}_\eta^\pm(\Delta t) \quad = \quad & \frac{e^{-|\Delta t|/\tau}}{4\tau} \times \Big[1 \mp S^\zeta \sin(\Delta m \Delta t) \\ & \mp \eta C \cos(\Delta m \Delta t)\Big]\,, \end{aligned} \tag{E.1}$$

where τ is the B^0 lifetime averaged over the two mass eigenstates, Δm is the $B^0-\overline{B}^0$ mixing frequency, and Δt is the difference between the time of the $B \to D^{*\pm}\pi^\mp$ ($B_{\rm rec}$) decay and the decay of the other B ($B_{\rm tag}$) in the event. The upper (lower) sign in Eq. E.1 indicates the flavor of the $B_{\rm tag}$ as a B^0 ($\overline{B}^0$), while $\eta = +1$ (-1) and $\zeta = +$ $(-)$ for the $B_{\rm rec}$ final state $D^{*-}\pi^+$ ($D^{*+}\pi^-$). The parameters C and $S^\pm$ are

$$C \equiv \frac{1-r^{*2}}{1+r^{*2}}\,, \qquad S^\pm \equiv \frac{2r^*}{1+r^{*2}}\sin(2\beta+\gamma\pm\delta^*). \tag{E.2}$$

Here δ^* is the strong phase difference between A_u and A_c and $r^* = |A_u/A_c|$. Since A_u is doubly CKM-suppressed with respect to A_c, one expects $r^* \sim 2\%$.

In this Letter we report a study of *CP*-violating asymmetries in $B^0 \to D^{*\mp}\pi^\pm$ decays using the technique of partial reconstruction, which allows us to analyze a large sample of signal events. Additional information about the techniques used in this analysis appears in Refs. [5, 6].

The data used in this analysis were recorded with the *BABAR* detector at the PEP-II storage ring, and consist of 76.4 fb^{-1} collected on the $\Upsilon(4S)$ resonance (on-resonance sample), and 7.6 fb^{-1} collected at an e^+e^- center-of-mass (CM) energy approximately 40 MeV below the resonance peak (off-resonance sample). Samples of simulated Monte Carlo (MC) events with an equivalent luminosity 3 to 4 times larger than the data are analyzed through the same analysis chain. The *BABAR* detector is described in detail in Ref. [7].

In the partial reconstruction of a $B^0 \to D^{*\mp}\pi^\pm$ candidate (B_{rec}), only the hard (high-momentum) pion track π_h from the B decay and the soft (low-momentum) pion track π_s from the decay $D^{*-} \to \overline{D}^0\pi_s^-$ are used. Applying kinematic constraints consistent with the signal decay mode, we calculate the four-momentum of the D, obtaining its flight direction to within a few degrees and its invariant mass m_{miss} [6]. Signal events peak in the m_{miss} distribution at the nominal D^0 mass M_D^0 with an r.m.s. of 3 MeV/c^2.

In addition to $B^0 \to D^{*\mp}\pi^\pm$ events, the selected event sample contains the following kinds of events: $B \to D^{*\mp}\rho^\pm$; $B\overline{B}$ background peaking in m_{miss}, composed of pairs of tracks coming from the same B meson, with the π_s originating from a charged D^* decay, excluding $B \to D^{*\mp}\rho^\pm$ decays; combinatoric $B\overline{B}$ background, defined as all remaining $B\overline{B}$ background events; and continuum $e^+e^- \to q\overline{q}$, where q represents a u, d, s, or c quark. We suppress the combinatoric background with selection criteria based on the event shape and the D^* helicity-angle. We reject π_h candidates that are identified as leptons or kaons. All candidates must satisfy $1.81 < m_{\text{miss}} < 1.88$ GeV/c^2. Multiple candidates are found in 5% of the events. In these instances, only the candidate with the m_{miss} value closest to M_{D^0} is used.

To perform this analysis, Δt and the flavor of the B_{tag} must be determined. We measure Δt using $\Delta t = (z_{\text{rec}} - z_{\text{tag}})/(\gamma\beta c)$, where z_{rec} (z_{tag}) is the decay position of the B_{rec} (B_{tag}) along the beam axis (z) in the laboratory frame, and the e^+e^- boost parameter $\gamma\beta$ is continuously calculated from the beam energies. To find z_{rec} we fit the π_h track with a beam spot constraint in the plane perpendicular to the beams. We obtain z_{tag} from a beam-spot-constrained vertex fit of all other tracks in the event, excluding all tracks within 1 rad of the D momentum in the CM frame. The Δt error $\sigma_{\Delta t}$ is calculated from the results of the z_{rec} and z_{tag} vertex fits.

We tag the flavor of the B_{tag} using lepton or kaon candidates. The lepton CM momentum is required to be greater than 1.1 GeV/c to suppress "cascade" leptons that originate from charm decays. If several flavor-tagging tracks are present in either the lepton or kaon tagging category, the only track of that category used for tagging is the one with the largest value of θ_T, the CM angle between the track momentum and the D momentum. The tagging track must satisfy $\cos\theta_T < C_T$, where $C_T = 0.75$ ($C_T = 0.50$) for leptons (kaons), to minimize the impact of tracks originating from the D decay. If both a lepton and a kaon satisfy this requirement, the event is tagged with the lepton only.

The analysis is carried out with a series of unbinned maximum-likelihood fits, performed simultaneously on the on- and off-resonance data samples and independently for the lepton-tagged and kaon-tagged events. The probability density function (PDF) depends on the variables $m_{\rm miss}$, Δt, $\sigma_{\Delta t}$, F, $s_{\rm t}$, and $s_{\rm m}$, where F is a Fisher discriminant formed from fifteen event-shape variables that provide discrimination against continuum events [6], $s_{\rm t} = 1$ (-1) when the $B_{\rm tag}$ is identified as a B^0 ($\overline{B}^0$), and $s_{\rm m} = 1$ (-1) for "unmixed" ("mixed") events. An event is labeled unmixed if the π_h is a $\pi^-(\pi^+)$ and the $B_{\rm tag}$ is a $B^0(\overline{B}^0)$, and mixed otherwise.

The PDF for on-resonance data is a sum over the PDFs of the different event types, $\mathcal{P} = \sum_i f_i \mathcal{P}_i$, where the index $i = \{D^*\pi, D^*\rho, {\rm peak}, {\rm comb}, q\overline{q}\}$ indicates one of the event types described above, f_i is the relative fraction of events of type i in the data sample, and $\mathcal{P}_i$ is the PDF for these events. The PDF for off-resonance data is $\mathcal{P}_{q\overline{q}}$. The parameter values for $\mathcal{P}_i$ are different for each event type, unless indicated otherwise. Each $\mathcal{P}_i$ is a product of the PDFs $\mathcal{M}_i(m_{\rm miss})$, $\mathcal{F}_i(F)$, and $\mathcal{T}'_i(\Delta t, \sigma_{\Delta t}, s_{\rm t}, s_{\rm m})$, defined below.

The $m_{\rm miss}$ PDF $\mathcal{M}_i$ for each event type i is the sum of a bifurcated Gaussian $B(x) \propto exp{-}\frac{(x-\mu)^2}{2\sigma_x^2}$, where $\sigma_x = \sigma_L(\sigma_R)$ for $x \leq \mu$ $(x > \mu)$, and an ARGUS function [6]. The Fisher PDF $\mathcal{F}_i$ is a bifurcated Gaussian. The parameter values for $\mathcal{F}_{D^*\pi}$, $\mathcal{F}_{D^*\rho}$, $\mathcal{F}_{\rm peak}$, and $\mathcal{F}_{\rm comb}$ are identical.

The Δt PDF, $\mathcal{T}'_i = \int d\Delta t_{\rm tr}\, \mathcal{T}_i(\Delta t_{\rm tr}, s_{\rm t}, s_{\rm m})\, \mathcal{R}_i(\Delta t - \Delta t_{\rm tr}, \sigma_{\Delta t})$, is a convolution, where $\mathcal{T}_i$ is the distribution of the true decay-time difference $\Delta t_{\rm tr}$ and $\mathcal{R}_i$ is a three-Gaussian resolution function that accounts for detector resolution and effects such as systematic offsets in the measured positions of vertices [6].

The PDF $\mathcal{T}_{D^*\pi}(\Delta t_{\rm tr}, s_{\rm t}, s_{\rm m})$ for signal events corresponds to Eq. E.1 with $O(r^{*2})$ terms neglected, and with additional parameters that account for imperfect flavor tagging:

$$\begin{aligned}
\mathcal{T}_{D^*\pi} \;=\; & \frac{e^{-|\Delta t_{\rm tr}|/\tau}}{4\tau}\, \{\alpha(1 + s_{\rm m}\kappa) + (1-\alpha)\,[(1 - s_{\rm t}\,\Delta\omega) \\
& + s_{\rm m}\,(1-2\omega)\,\cos(\Delta m \Delta t_{\rm tr}) \\
& - \mathcal{S}\,\sin(\Delta m \Delta t_{\rm tr})\,]\,\}\,,
\end{aligned} \tag{E.3}$$

where the mistag rate ω is the probability to misidentify the flavor of the $B_{\rm tag}$ averaged over B^0 and $\overline{B}^0$, $\Delta\omega$ is the B^0 mistag rate minus the $\overline{B}^0$ mistag rate, α is the probability that the tagging track is a daughter of the signal D meson, $\kappa = 1 - 2\rho$, where ρ is the probability that the daughter of the D results in a mixed flavor event, and $\mathcal{S} = s_{\rm t}\,(1-2\omega)\, S^{\zeta}$.

The $B_{\rm tag}$ may undergo a $b \to u\bar{c}d$ decay, and the kaon produced in the subsequent charm decay might be used for tagging. This effect is not described by Eq. E.3. To account for it, we use a different parameterization [8] for kaon tags, in which the coefficient of the $\sin(\Delta m \Delta t_{\rm tr})$ term $\mathcal{S} = [(1-2\omega)\,(s_{\rm t} a + s_{\rm m} c) + s_{\rm t} s_{\rm m} b(1 - s_{\rm t}\Delta\omega)]$, where $a \equiv 2r^* \sin(2\beta+\gamma)\cos\delta^*$, $b \equiv 2r' \sin(2\beta+\gamma)\cos\delta'$, and $c \equiv 2\cos(2\beta+\gamma)(r^*\sin\delta^* - r'\sin\delta')$. Here r' (δ') is the effective magnitude ratio (strong phase difference) between the $b \to u\bar{c}d$ and $b \to c\bar{u}d$ amplitudes in the tag-side decays. This parameterization is good to first order in r^* and r'.

The *CP* parameters ($S^\pm$, a, b, and c) of $\mathcal{T}_{D^*\rho}$, $T_{\rm peak}$, and $T_{\rm comb}$ are set to 0 and are later varied to evaluate systematic uncertainties. Otherwise, the PDF $\mathcal{T}'_{D^*\rho}$ for $B \to D^{*\mp}\rho^\pm$ events is taken to be identical to $\mathcal{T}'_{D^*\pi}$. The $B\overline{B}$ background PDFs $\mathcal{T}_{\rm comb}$ and $\mathcal{T}_{\rm peak}$ have the same functional form as Eq. E.3, with independent parameter values. The parameters of $\mathcal{T}'_{\rm peak}$ are determined from a fit to the MC simulation sample. The PDF $\mathcal{T}_{q\overline{q}}$ for the continuum background is the sum of two components, one with a finite lifetime and one with zero lifetime.

The analysis proceeds in three steps:

1. The parameters of $\mathcal{M}_i$ and the value of $f_{D^*\pi}/(f_{D^*\pi} + f_{D^*\rho})$ are obtained from the MC simulation with the branching fractions $\mathcal{B}(B^0 \to D^{*-}\pi^+)$ and $\mathcal{B}(B^0 \to D^{*-}\rho^+)$ from Ref. [9]. Using these parameter values, we fit the data with $\mathcal{P}_i = \mathcal{M}_i(m_{\rm miss})\,\mathcal{F}_i(F)$, to determine $f_{q\overline{q}}$, $f_{\rm comb}$, $f_{D^*\rho} + f_{D^*\pi}$, the parameters of $\mathcal{M}_{q\overline{q}}$, and the parameters of $\mathcal{F}_i$ for both continuum and $B\overline{B}$ events. This fit yields 6400 ± 130 (25160 ± 320) signal events for the lepton- (kaon-) tagged sample. The fit results for the $\mathcal{M}_i(m_{\rm miss})$ PDFs are shown in Fig. E.1. The fit is repeated to determine the signal yields requiring first $\cos\theta_T < C_T$ and then $\cos\theta_T > C_T$, in order to measure the values of α and ρ. We find $\alpha = (1.0 \pm 0.1)\%$ ($(5.6 \pm 0.2)\%$) for lepton- (kaon-) tagged events.

2. We fit the events in the sideband $1.81 < m_{\rm miss} < 1.84$ GeV/c^2 to obtain the parameters of $\mathcal{T}'_{\rm comb}$.

3. Using the parameter values obtained in the previous steps, we fit the data in the signal region $1.845 < m_{\rm miss} < 1.880$ GeV/c^2, determining the parameters of $\mathcal{T}'_{D^*\pi}$ and $\mathcal{T}'_{q\overline{q}}$.

We use the MC samples to verify the entire analysis procedure, as well as the validity of using the same non-*CP* parameters in $\mathcal{T}'_{D^*\rho}$ and $\mathcal{T}'_{D^*\pi}$ and of using the $\mathcal{T}'_{\rm comb}$ parameters obtained from the sideband in the signal region. For lepton-tagged events, we find a bias of ∓ 0.012 in $S^\pm$, due to the assumption that events tagged with direct and cascade leptons are described by the same resolution function. The results presented below are corrected for this bias.

The *CP* parameters $S^\pm$ for lepton tags and (a, b, c) for kaon tags are determined in step 3 to be $S^+ = -0.078 \pm 0.052 \pm 0.021$, $S^- = -0.070 \pm 0.052 \pm 0.019$, $a = -0.054 \pm 0.032 \pm 0.017$, $b = -0.009 \pm 0.019 \pm 0.013$, $c = +0.005 \pm 0.031 \pm 0.017$, where the first error is statistical and the second is systematic. The time-dependent, *CP*-violating asymmetry $\mathcal{A}_{CP} = (N_{B^0_{\rm tag}} - N_{\overline{B}^0_{\rm tag}})/(N_{B^0_{\rm tag}} + N_{\overline{B}^0_{\rm tag}})$ is shown in Fig. E.2. In the absence

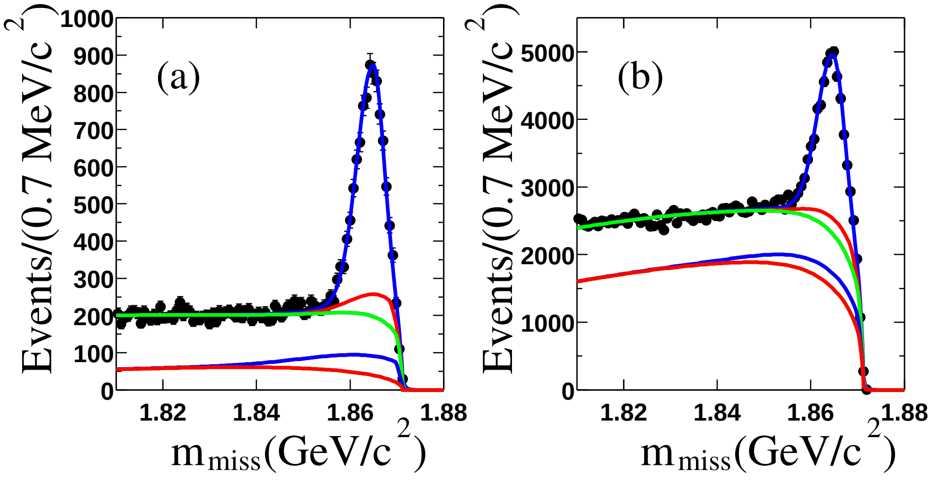

Figure E.1: *The* $m_{\rm miss}$ *distributions for (a) lepton-tagged and (b) kaon-tagged events. The curves show, from bottom to top, the cumulative contributions of continuum, peaking* $B\overline{B}$*, combinatoric* $B\overline{B}$*,* $B \to D^{*+}\rho^-$*, and* $B^0 \to D^{*+}\pi^-$ *events.*

of background and experimental effects, $\mathcal{A}_{CP} = 2r^* \sin(2\beta+\gamma)\cos\delta^* \sin(\Delta m \Delta t)$. The signal-region fit determines also the mistag rate $\omega = 0.102 \pm 0.008$ ($\omega = 0.217 \pm 0.006$) and the mixing frequency $\Delta m = 0.521 \pm 0.017$ (*stat.*) ps^{-1} ($\Delta m = 0.478 \pm 0.012$ (*stat.*) ps^{-1}), consistent with the world average [9], for lepton (kaon) tagged events.

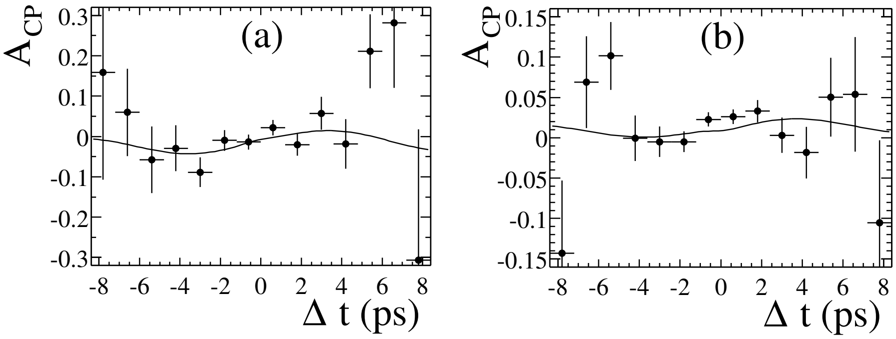

Figure E.2: *The asymmetry* $\mathcal{A}_{CP}$ *for (a) lepton- and (b) kaon-tagged events. The curves show the projection of the PDF from the unbinned fit.*

The systematic uncertainties on the CP parameters are summarized in Table E.1. They include (1) the statistical errors obtained from the fits of steps 1 and 2; (2) uncertainties due to the unknown values of the CP parameters in the background, the uncertainty in the ratio of branching fractions $\mathcal{B}(B^0 \to D^{*-}\pi)/\mathcal{B}(B^0 \to D^{*-}\rho)$, the modeling of $\mathcal{T}'_{\rm peak}$, and possible biases introduced by the presence of background;

(3) the uncertainty in the cascade lepton bias and possible biases due to the τ and Δm parameters; (4) uncertainties in the measurement of the beam spot position, the detector z length scale, and detector alignment; and (5) the statistical error in the parameters determined from the MC sample.

Table E.1: *The systematic uncertainties on the CP-violation parameters.*

Source	Error ($\times 10^{-3}$) in				
	S^+	S^-	a	b	c
(1) Step 1 & 2 statistics	1.7	0.9	1.0	0.5	0.6
(2) Backgrounds	12.1	10.0	13.7	8.4	14.2
(3) Fit procedure	6.6	5.3	5.2	1.7	0.8
(4) Detector effects	9.4	7.3	3.7	9.1	3.5
(5) MC statistics	12.8	12.8	8.0	4.0	9.0
Total	21	19	17	13	17

Combining a and $(S^+ + S^-)/2$, accounting for correlated errors, we obtain

$$2r^* \sin(2\beta+\gamma)\cos\delta^* = -0.063 \pm 0.024 \pm 0.014. \quad \text{(E.4)}$$

This measurement deviates from zero by 2.3 standard deviations. It can be used to provide bounds on $|\sin(2\beta+\gamma)|$ [10]. We use two methods for interpreting our results in terms of constraints on $|\sin(2\beta+\gamma)|$. Both methods involve minimizing a χ^2 function that is symmetric under the exchange $\sin(2\beta+\gamma) \to -\sin(2\beta+\gamma)$, and applying the method of Ref. [11].

In the first method we make no assumption regarding the value of r^*. For different values of r^* we minimize the function $\chi^2 = \sum_{j,k=1}^{3} \Delta x_j V_{jk}^{-1} \Delta x_k$, where Δx_j is the difference between the result of our measurement and the expression of S^+, S^-, and a as functions of r^*, δ^* and $\sin(2\beta+\gamma)$. The measurement error matrix V is nearly diagonal, and accounts for correlations between the measurements due to correlated statistical and systematic uncertainties. The parameters determined by this fit are $\sin(2\beta+\gamma)$, which is limited to lie in the range $[-1,1]$, and δ^*. We then generate many parameterized MC experiments with the same sensitivity as reported here for different values of $\sin(2\beta+\gamma)$ and with $\delta^* = 0$, which yields the most conservative lower limits. The fraction of these experiments in which $\chi^2(\sin(2\beta+\gamma)) - \chi^2_{\min}$ is smaller than in the data is interpreted as the confidence level (CL) of the lower limit on $|\sin(2\beta+\gamma)|$. The resulting 95% CL lower limit is shown as a function of r^* in

Fig. E.3. This limit is always the more conservative of the two possibilities implied by the ambiguity $|\sin(2\beta+\gamma)| \leftrightarrow |\cos\delta^*|$.

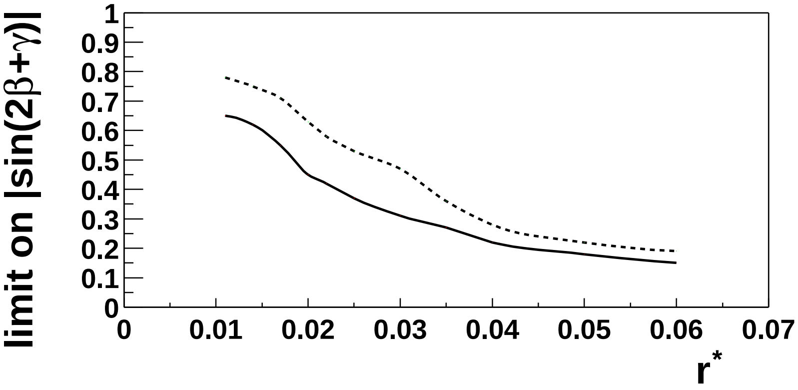

Figure E.3: *95% CL lower limit on* $|\sin(2\beta+\gamma)|$ *as a function of* r^**. The solid curve corresponds to this analysis; the dashed curve includes the results of Ref. [16] for* $B^0 \to D^{*\mp}\pi^{\pm}$ *only.*

The second method assumes that r^* can be estimated from the Cabibbo angle, the ratio of branching fractions $\mathcal{B}(B^0 \to D^{*+}_s\pi^-)/\mathcal{B}(B^0 \to D^{*-}\pi^+)$ [12, 13], and the ratio of decay constants $f_{D^*}/f_{D^*_s}$ [14], yielding ${r^*}_0 = 0.017^{+0.005}_{-0.007}$. We attribute an additional non-Gaussian 30% relative error to the theoretical assumptions involved in obtaining this value. We minimize $\tilde{\chi}^2 = \chi^2 + \Delta^2(r^*)$, where $\Delta^2(r^*) = 0$ for $|r^* - {r^*}_0|/{r^*}_0 \leq 0.3$ and is an offset quadratic function outside this range [15], corresponding to a χ^2 contribution with the uncertainties on ${r^*}_0$ given above. The parameters $\sin(2\beta+\gamma)$, δ^*, and r^* are determined in this fit. This method yields the limits $|\sin(2\beta+\gamma)| > 0.87$ (0.56) at 68 (95)% CL.

Combining this measurement with the *BABAR* results for fully reconstructed $B^0 \to D^{*\mp}\pi^{\pm}$ and $B^0 \to D^{\mp}\pi^{\pm}$ [16], taking into account correlations between the measurements, we find, using the second method, $|\sin(2\beta+\gamma)| > 0.87$ (0.58) at 68 (95) % CL. We use the same value of $r = |A_u/A_c|$ for $B^0 \to D^{\mp}\pi^{\pm}$ decays as Ref. [16] (Eq. 6). Due to the relatively low value of the asymmetry in $B^0 \to D^{\mp}\pi^{\pm}$ (Eq. (5), Ref. [16]), including this mode in the combination leads to almost no change in the lower limits. The lower limit on $|\sin(2\beta+\gamma)|$ obtained with the first method, including the results of Ref. [16] for $B^0 \to D^{*\mp}\pi^{\pm}$ only, is shown in Fig. E.3. The results of Ref. [16] for $B^0 \to D^{\mp}\pi^{\pm}$ were not included to avoid any assumption on the value of r.

We have studied time-dependent *CP*-violating asymmetries in $B^0 \to D^{*\mp}\pi^{\pm}$ using partial reconstruction. We interpret our results as a limit on $|\sin(2\beta+\gamma)|$ that can be used to set a constraint on the unitarity triangle.

We are grateful for the excellent luminosity and machine conditions provided by our PEP-II colleagues, and for the substantial dedicated effort from the computing organizations that support *BABAR*. The collaborating institutions wish to thank

SLAC for its support and kind hospitality. This work is supported by DOE and NSF (USA), NSERC (Canada), IHEP (China), CEA and CNRS-IN2P3 (France), BMBF and DFG (Germany), INFN (Italy), FOM (The Netherlands), NFR (Norway), MIST (Russia), and PPARC (United Kingdom). Individuals have received support from CONACyT (Mexico), A. P. Sloan Foundation, Research Corporation, and Alexander von Humboldt Foundation.

E.2 Precise measurement of *CP* asymmetries in $B^0 \to D^{*\mp}\pi^\pm$ decays

Measurement of Time-Dependent *CP*-Violating Asymmetries and Constraints on $\sin(2\beta+\gamma)$ with Partial Reconstruction of $B^0 \to D^{*\mp}\pi^\pm$ Decays

BABAR Collaboratrion

Abstract

We present a measurement of the time-dependent CP-violating asymmetries in decays of neutral B mesons to the final states $D^{*\mp}\pi^\pm$*, using approximately* 232 *million* $B\overline{B}$ *events recorded by the BABAR experiment at the PEP-II* e^+e^- *storage ring. Events containing these decays are selected with a partial reconstruction technique, in which only the high-momentum* $\pi^\pm$ *from the B decay and the low-momentum* $\pi^\mp$ *from the* $D^{*\mp}$ *decay are used. We measure the parameters related to* $2\beta+\gamma$ *to be* $a_{D^*\pi} = -0.034 \pm 0.014 \pm 0.009$ *and* $c^\ell_{D^*\pi} = -0.019 \pm 0.022 \pm 0.013$*. With some theoretical assumptions, we interpret our results in terms of the lower limits* $|\sin(2\beta+\gamma)| > 0.62\ (0.35)$ *at 68% (90%) confidence level.*

E.2.1 Introduction

The Cabibbo-Kobayashi-Maskawa (CKM) quark-mixing matrix [1] provides an explanation of *CP* violation and is under experimental investigation aimed at constraining its parameters. A crucial part of this program is the measurement of the angle $\gamma = \arg\left(-V_{ud}V^*_{ub}/V_{cd}V^*_{cb}\right)$ of the unitarity triangle related to the CKM matrix. The decay modes $B \to D^{*\mp}\pi^\pm$ have been proposed for use in measurements of $\sin(2\beta+\gamma)$ [2], where $\beta = \arg\left(-V_{cd}V^*_{cb}/V_{td}V^*_{tb}\right)$ is well measured [17]. In the Standard Model the decays $B^0 \to D^{*-}\pi^+$ and $\overline{B}^0 \to D^{*-}\pi^+$ proceed through the $\overline{b} \to \overline{c}u\overline{d}$ and $b \to u\overline{c}d$ amplitudes A_c and A_u. Fig. E.4 shows the tree diagrams contributing to these decays. The relative weak phase between A_u and A_c in the usual Wolfenstein convention [4] is γ. When combined with $B^0\overline{B}^0$ mixing, this yields a weak phase difference of $2\beta+\gamma$ between the interfering amplitudes.

In $\Upsilon(4S) \to B\overline{B}$ decays, the decay rate distribution for $B \to D^{*\mp}\pi^\pm$ is

$$\mathcal{P}^\pm_\eta(\Delta t) \;=\; \frac{e^{-|\Delta t|/\tau}}{4\tau} \times \left[1 \mp S^\zeta \sin(\Delta m \Delta t) \mp \eta C \cos(\Delta m \Delta t)\right], \qquad \text{(E.5)}$$

where τ is the B^0 lifetime averaged over the two mass eigenstates, Δm is the $B^0\overline{B}^0$ mixing frequency, and Δt is the difference between the time of the $B \to D^{*\mp}\pi^\pm$ ($B_{\rm rec}$) decay and the decay of the other B ($B_{\rm tag}$) in the event. The upper (lower) signs in

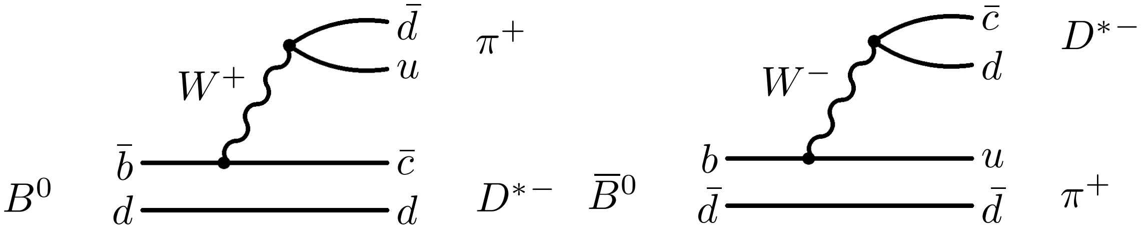

Figure E.4: *Feynman diagrams for the Cabibbo-favored decay $B^0 \to D^{*-}\pi^+$ (left), corresponding to the decay amplitude A_c, and the Cabibbo-suppressed decay $\overline{B}^0 \to D^{*-}\pi^+$ (right), whose amplitude is A_u.*

Eq. (E.5) indicate the flavor of the $B_{\rm tag}$ as a B^0 ($\overline{B}^0$), while $\eta = +1$ (-1) and $\zeta = +$ ($-$) for the $B_{\rm rec}$ final state $D^{*-}\pi^+$ ($D^{*+}\pi^-$). The parameters C and $S^\pm$ are given by

$$C \equiv \frac{1 - r^{*2}}{1 + r^{*2}}, \qquad S^\pm \equiv \frac{2r^*}{1 + r^{*2}} \sin(2\beta + \gamma \pm \delta^*). \tag{E.6}$$

Here δ^* is the strong phase difference between A_u and A_c, and $r^* = |A_u/A_c|$. Since A_u is doubly CKM-suppressed with respect to A_c, one expects $r^* \approx \left|\frac{V_{ub}V_{cd}^*}{V_{cb}^*V_{ud}}\right| = 0.02$.

We report a study of the *CP*-violating asymmetry in $B^0 \to D^{*\mp}\pi^\pm$ decays using the technique of partial reconstruction, which allows us to achieve a high efficiency for the selection of signal events. We use approximately twice the integrated luminosity of our previous analysis of this process [18], and employ an improved method to eliminate a measurement bias, as described in Sec. E.2.3. Many of the tools and procedures used in this analysis were validated in a previous analysis dedicated to the measurement of the B^0 lifetime [6].

In this analysis, terms of order r^{*2}, to which we currently have no sensitivity, have been neglected. The interpretation of the measured asymmetries in terms of $\sin(2\beta + \gamma)$ requires an assumption regarding the value of r^*, discussed in Sec. E.2.6.

E.2.2 The *BABAR* Detector and Dataset

The data used in this analysis were recorded with the *BABAR* detector at the PEP-II asymmetric-energy storage rings, and consist of 211 fb^{-1} collected on the $\Upsilon(4S)$ resonance (on-resonance sample), and 21 fb^{-1} collected at an e^+e^- center-of-mass (CM) energy approximately 40 MeV below the resonance peak (off-resonance sample). Samples of Monte Carlo (MC) [19] events with an equivalent luminosity approximately four times larger than the data sample were analyzed using the same reconstruction and analysis procedure.

The *BABAR* detector is described in detail in Ref. [7]. We provide a brief description of the main components and their use in this analysis. Charged-particle trajectories are measured by a combination of a five-layer silicon vertex tracker (SVT) and a 40-layer drift chamber (DCH) in a 1.5-T solenoidal magnetic field. Tracks with low transverse momentum can be reconstructed in the SVT alone, thus extending the charged-particle detection down to transverse momenta of about 50 MeV/c. We use a ring-imaging Cherenkov detector (DIRC) for charged-particle identification and augment it with energy-loss measurements from the SVT and DCH. Photons and electrons are detected in a CsI(Tl) electromagnetic calorimeter (EMC), with photon-energy resolution $\sigma_E/E = 0.023(E/\,\mathrm{GeV})^{-1/4} \oplus 0.014$. The instrumented flux return (IFR) is equipped with resistive plate chambers to identify muons.

E.2.3 Analysis Method

Partial Reconstruction of $B^0 \to D^{*\mp}\pi^\pm$

In the partial reconstruction of a $B^0 \to D^{*\mp}\pi^\pm$ candidate ($B_{\rm rec}$), only the hard (high-momentum) pion track π_h from the B decay and the soft (low-momentum) pion track π_s from the decay $D^{*-} \to \overline{D}^0\pi_s^-$ are used. The cosine of the angle between the momenta of the B and the hard pion in the CM frame is then computed:

$$\cos\theta_{Bh} = \frac{M_{D^{*-}}^2 - M_{B^0}^2 - M_\pi^2 + E_{\rm CM}E_h}{2p_B|\vec{p}_h|}, \tag{E.7}$$

where M_x is the nominal mass of particle x [20], E_h and $\vec{p}_h$ are the measured CM energy and momentum of the hard pion, $E_{\rm CM}$ is the total CM energy of the incoming e^+e^- beams, and $p_B = \sqrt{E_{\rm CM}^2/4 - M_{B^0}^2}$. Events are required to be in the physical region $|\cos\theta_{Bh}| < 1$. Given $\cos\theta_{Bh}$ and the measured momenta of the π_h and π_s, the B four-momentum can be calculated up to an unknown azimuthal angle ϕ around $\vec{p}_h$. For every value of ϕ, the expected D four-momentum $p_D(\phi)$ is determined from four-momentum conservation, and the corresponding ϕ-dependent invariant mass $m(\phi) \equiv \sqrt{|p_D(\phi)|^2}$ is calculated. We define the missing mass $m_{\rm miss} \equiv \frac{1}{2}\left[m_{\rm max} + m_{\rm min}\right]$, where $m_{\rm max}$ and $m_{\rm min}$ are the maximum and minimum values of $m(\phi)$. In signal events, $m_{\rm miss}$ peaks at the nominal D^0 mass M_{D^0}, with a gaussian width of about 3 MeV/c^2 (Fig. E.6). The $m_{\rm miss}$ distribution for combinatoric background events is significantly broader, making the missing mass the primary variable for distinguishing signal from background. The discrimination between signal and background provided by the $m_{\rm miss}$ distribution is independent of the choice of the value of ϕ. With the arbitrary choice $\phi = 0$, we use four-momentum conservation to calculate the CM D and B momentum vectors, which are used as described below. The various momenta and angles in the CM frame used in the partial reconstruction are illustrated in Fig. E.5.

Backgrounds

In addition to $B^0 \to D^{*\mp}\pi^\pm$ events, the selected event sample contains the following kinds of events:

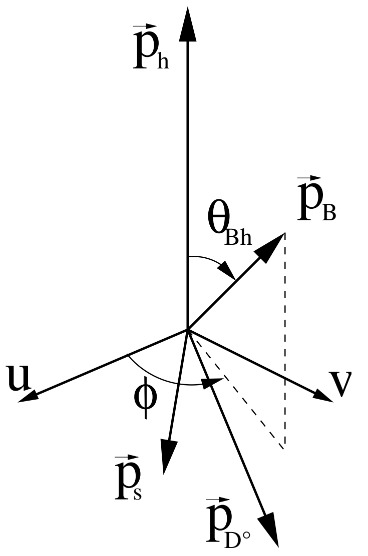

Figure E.5: *Momenta and angles in the CM frame used in the partial reconstruction. The orthogonal axes u and v are normal to the momentum $\vec{p}_h$ of the fast pion, and u lies in the plane defined by the momenta of the fast and slow pions, $\vec{p}_h$ and $\vec{p}_s$. The angle ϕ is measured in the $u - v$ plane.*

- $B \to D^{*\mp}\rho^\pm$.
- Peaking $B\overline{B}$ background, defined as decays other than $B \to D^{*\mp}\rho^\pm$, in which the π_h and π_s originate from the same B meson, with the π_s originating from a charged D^* decay. The m_{miss} distribution of these events peaks broadly under the signal peak.
- Combinatoric $B\overline{B}$ background, defined as all remaining $B\overline{B}$ background events.
- Continuum $e^+e^- \to q\overline{q}$, where q represents a u, d, s, or c quark.

Event Selection

To suppress the continuum background, we select events in which the ratio of the 2nd to the 0th Fox-Wolfram moment [21], computed using all charged particles and EMC clusters not matched to tracks, is smaller than 0.40. Hard-pion candidates are required to be reconstructed with at least twelve DCH hits. Kaons and leptons are rejected from the π_h candidate lists based on information from the IFR and DIRC, energy loss in the SVT and DCH, or the ratio of the candidate's EMC energy deposition to its momentum (E/p).

We define the D^* helicity angle θ_{D^*} to be the angle between the flight directions of the D and the B in the D^* rest frame. Taking advantage of the longitudinal polarization in signal events, we suppress background by requiring $|\cos\theta_{D^*}|$ to be larger than 0.4.

All candidates are required to satisfy $m_{\rm miss} > 1.81$ GeV/c^2. Multiple candidates are found in 5% of the events. In these instances, only the candidate with the $m_{\rm miss}$ value closest to M_{D^0} is used.

Fisher Discriminant

To further discriminate against continuum events, we combine fifteen event-shape variables into a Fisher discriminant [22] F. Discrimination originates from the fact that $q\overline{q}$ events tend to be jet-like, whereas $B\overline{B}$ events have a more spherical energy distribution. Rather than applying requirements to the variable F, we maximize the sensitivity by using it in the fits described below. The fifteen variables are calculated using two sets of particles. Set 1 includes all tracks and EMC clusters, excluding the hard and soft pion candidates; Set 2 is composed of Set 1, excluding all tracks and clusters with CM momentum within 1.25 radian of the CM momentum of the D. The variables, all calculated in the CM frame, are 1) the scalar sum of the momenta of all Set 1 tracks and EMC clusters in nine 20° angular bins centered about the hard pion direction; 2) the value of the sphericity, computed with Set 1; 3) the angle with respect to the hard pion of the sphericity axis, computed with Set 2; 4) the direction of the particle of highest energy in Set 2 with respect to the hard pion; 5) the absolute value of the vector sum of the momenta of all the particles in Set 2; 6) the momentum $|\vec{p}_h|$ of the hard pion and its polar angle.

Decay Time Measurement and Flavor Tagging

To perform this analysis, Δt and the flavor of the $B_{\rm tag}$ must be determined. We tag the flavor of the $B_{\rm tag}$ using lepton or kaon candidates. The lepton CM momentum is required to be greater than 1.1 GeV/c to suppress leptons that originate from charm decays. If several flavor-tagging tracks are present in either the lepton or kaon tagging category, the only track of that category used for tagging is the one with the largest value of θ_T, the CM angle between the track momentum and the momentum of the “missing” (unreconstructed) D. The tagging track must satisfy $\cos\theta_T < C_T$, where $C_T = 0.75$ ($C_T = 0.50$) for leptons (kaons), to minimize the impact of tracks originating from the decay of the missing D. If both a lepton and a kaon satisfy this requirement, the event is tagged with the lepton.

We measure Δt using $\Delta t = (z_{\rm rec} - z_{\rm tag})/(\gamma\beta c)$, where $z_{\rm rec}$ ($z_{\rm tag}$) is the decay position of the $B_{\rm rec}$ ($B_{\rm tag}$) along the beam axis (z) in the laboratory frame, and the e^+e^- boost parameter $\gamma\beta$ is calculated from the measured beam energies. To find $z_{\rm rec}$, we use the π_h track parameters and errors, and the measured beam-spot position and size in the plane perpendicular to the beams (the $x - y$ plane). We find the position of the point in space for which the sum of the χ^2 contributions from the π_h track and the beam spot is a minimum. The z coordinate of this point determines

$z_{\rm rec}$. The beam spot has an r.m.s. size of approximately 120 μm in the horizontal dimension (x), 5 μm in the vertical dimension (y), and 8.5 mm along the beams (z). The average B flight in the $x-y$ plane is 30 μm. To account for the B flight in the beam-spot-constrained vertex fit, 30 μm are added to the effective x and y sizes for the purpose of conducting this fit. The π_s track is not used in this fit, since it undergoes significant multiple Coulomb scattering and hence does not improve the $z_{\rm rec}$ measurement resolution.

In lepton-tagged events, the same procedure, with the π_h track replaced by the tagging lepton, is used to determine $z_{\rm tag}$. Using only the tagging lepton to determine $z_{\rm tag}$ eliminates a bias due to leptons produced in charm decays, as described in Sec. E.2.3.

In kaon-tagged events, we obtain $z_{\rm tag}$ from a beam-spot-constrained vertex fit of all tracks in the event, excluding π_h, π_s and all tracks within 1 radian of the D momentum in the CM frame, which are likely to originate from the D decay. If the contribution of any track to the χ^2 of the vertex is more than 6, the track is removed and the fit is repeated until no track fails the $\chi^2 < 6$ requirement.

The Δt error $\sigma_{\Delta t}$ is calculated from the results of the $z_{\rm rec}$ and $z_{\rm tag}$ vertex fits. We require $|\Delta t| < 15\,{\rm ps}$ and $\sigma_{\Delta t} < 2\,{\rm ps}$.

Probability Density Function

The probability density function (PDF) depends on the variables $m_{\rm miss}$, Δt, $\sigma_{\Delta t}$, F, $s_{\rm t}$, and $s_{\rm m}$, where $s_{\rm t} = 1$ (-1) when the $B_{\rm tag}$ is identified as a B^0 ($\overline{B}{}^0$), and $s_{\rm m} = 1$ (-1) for "unmixed" ("mixed") events. An event is labeled unmixed if the π_h is a $\pi^-(\pi^+)$ and the $B_{\rm tag}$ is a $B^0(\overline{B}{}^0)$, and mixed otherwise.

The PDF for on-resonance data is a sum over the PDFs of the different event types:

$$\mathcal{P} = \sum_i f_i\,\mathcal{P}_i, \tag{E.8}$$

where the index $i = \{D^*\pi, D^*\rho, {\rm peak}, {\rm comb}, q\overline{q}\}$ indicates one of the event types described above, f_i is the relative fraction of events of type i in the data sample, and $\mathcal{P}_i$ is the PDF for these events. The PDF for off-resonance data is $\mathcal{P}_{q\overline{q}}$. The parameter values for $\mathcal{P}_i$ are different for each event type, unless indicated otherwise. Each $\mathcal{P}_i$ is a product,

$$\mathcal{P}_i = \mathcal{M}_i(m_{\rm miss})\,\mathcal{F}_i(F)\,\mathcal{T}_i'(\Delta t, \sigma_{\Delta t}, s_{\rm t}, s_{\rm m}), \tag{E.9}$$

where the forms of the functions appearing in Eq. (E.9), which are motivated by MC studies, are described below.

$m_{\rm miss}$ and F PDFs

The $m_{\rm miss}$ PDF for each event type i is the sum of a bifurcated Gaussian plus an ARGUS function [23]:

$$\mathcal{M}_i(m_{\rm miss}) = f_i^{\hat{\mathcal{G}}}\,\hat{\mathcal{G}}_i(m_{\rm miss}) + (1 - f_i^{\hat{\mathcal{G}}})\mathcal{A}_i(m_{\rm miss}), \tag{E.10}$$

where $f_i^{\hat{\mathcal{G}}}$ is the fractional area of the bifurcated Gaussian function. The functions $\hat{\mathcal{G}}_i$ and $\mathcal{A}_i$ are

$$\hat{\mathcal{G}}_i(m) \propto \begin{cases} \exp\left[-(m - M_i)^2/2\sigma_{Li}^2\right] & , \quad m \le M_i \\ \exp\left[-(m - M_i)^2/2\sigma_{Ri}^2\right] & , \quad m > M_i \end{cases} \tag{E.11}$$

$$\begin{aligned} \mathcal{A}(m) \propto m\sqrt{1 - (m/M_i^A)^2} \; \times \\ \exp\left[\epsilon_i\left(1 - \left(m/M_i^A\right)^2\right)\right]\theta(M_i^A - m), \end{aligned} \tag{E.12}$$

where M_i is the peak of the bifurcated Gaussian, σ_{Li} and σ_{Ri} are its left and right widths, ϵ_i is the ARGUS exponent, M_i^A is its end point, and θ is the step function. The proportionality constants are such that each of these functions is normalized to unit area within the $m_{\rm miss}$ range. The $m_{\rm miss}$ PDF of each event type has different parameter values.

The Fisher discriminant PDF $\mathcal{F}_i$ for each event type is parameterized as the sum of two Gaussians. The parameter values of $\mathcal{F}_{D^*\pi}$, $\mathcal{F}_{D^*\rho}$, $\mathcal{F}_{\rm peak}$, and $\mathcal{F}_{\rm comb}$ are identical.

Signal Δt PDFs

The Δt PDF $\mathcal{T}'_{D^*\pi}(\Delta t, \sigma_{\Delta t}, s_{\rm t}, s_{\rm m})$ for signal events corresponds to Eq. E.5 with $O(r^{*2})$ terms neglected, modified to account for several experimental effects, described below.

The first effect has to do with the origin of the tagging track. In some of the events, the tagging track originates from the decay of the missing D. These events are labeled "missing-D tags" and do not provide any information regarding the flavor of the $B_{\rm tag}$. In lepton-tagged events, we further distinguish between "direct" tags, in which the tagging lepton originates directly from the decay of the $B_{\rm tag}$, and "cascade" tags, where the tagging lepton is a daughter of a charmed particle produced in the $B_{\rm tag}$ decay. Due to the different physical origin of the tagging track in cascade and direct tags, these two event categories have different mistag probabilities, defined as the probability to deduce the wrong B flavor from the charge of the tagging track. In addition, the measured value of $z_{\rm tag}$ in cascade-lepton tags is systematically larger than the true value, due to the finite lifetime of the charmed particle and the boosted CM frame. This creates a correlation between the tag and vertex measurements that we address by considering cascade-lepton tags separately in the PDF. In our previous analysis [18] we corrected for the bias of the $S^{\pm}$ parameters caused by this effect and included a systematic error due to its uncertainty. In kaon tags, $z_{\rm tag}$ is determined using all available $B_{\rm tag}$ tracks, so the effect of the tagging track on the $z_{\rm tag}$ measurement is small. Therefore, the overall bias induced by cascade-kaon tags is small, and there is no need to distinguish them in the PDF.

The second experimental effect is the finite detector resolution in the measurement of Δt. We address this by convoluting the distribution of the true decay time difference $\Delta t_{\rm tr}$ with a detector resolution function. Putting these two effects together, the Δt PDF of signal events is

$$\begin{aligned}\mathcal{T}'_{D^*\pi}(\Delta t, \sigma_{\Delta t}, s_{\rm t}, s_{\rm m}) = (1 + s_{\rm t}\, \Delta\epsilon_{D^*\pi}) \sum_j f^j_{D^*\pi} \times \\ \int d\Delta t_{\rm tr}\, \mathcal{T}^j_{D^*\pi}(\Delta t_{\rm tr}, s_{\rm t}, s_{\rm m})\, \mathcal{R}^j_{D^*\pi}(\Delta t - \Delta t_{\rm tr}, \sigma_{\Delta t}),\end{aligned} \tag{E.13}$$

where $\Delta\epsilon_{D^*\pi}$ is half the relative difference between the detection efficiencies of positive and negative leptons or kaons, the index $j = \{\text{dir, cas, miss}\}$ indicates direct, cascade, and missing-D tags, and $f^j_{D^*\pi}$ is the fraction of signal events of tag-type j in the sample. We set $f^{\rm dir}_{D^*\pi} = 1 - f^{\rm cas}_{D^*\pi} - f^{\rm miss}_{D^*\pi}$ for lepton tags, with the value $f^{\rm cas}_{D^*\pi} = 0.12 \pm 0.02$ obtained from the MC simulation. For kaon tags $f^{\rm dir}_{D^*\pi} = 0$. The function $\mathcal{T}^j_{D^*\pi}(\Delta t_{\rm tr}, s_{\rm t}, s_{\rm m})$ is the $\Delta t_{\rm tr}$ distribution of tag-type j events, and $\mathcal{R}^j_{D^*\pi}(\Delta t - \Delta t_{\rm tr}, \sigma_{\Delta t})$ is their resolution function, which parameterizes both the finite detector resolution and systematic offsets in the measurement of Δz, such as those due to the origin of the tagging particle. The parameterization of the resolution function is described in Sec. E.2.3.

The functional form of the direct and cascade tag $\Delta t_{\rm tr}$ PDFs is

$$\begin{aligned}\mathcal{T}^j_{D^*\pi}(\Delta t_{\rm tr}, s_{\rm t}, s_{\rm m}) &= \frac{e^{-|\Delta t_{\rm tr}|/\tau_{D^*\pi}}}{4\tau_{D^*\pi}} \times \\ &\Big\{1 - s_{\rm t}\, \Delta\omega^j_{D^*\pi} \\ &+ s_{\rm m}\, (1 - 2\omega^j_{D^*\pi})\, \cos(\Delta m_{D^*\pi}\Delta t_{\rm tr}) \\ &- \mathcal{S}^j_{D^*\pi}\, \sin(\Delta m_{D^*\pi}\Delta t_{\rm tr})\Big\},\end{aligned} \tag{E.14}$$

where $j = \{\text{dir, cas}\}$, the mistag rate $\omega^j_{D^*\pi}$ is the probability to misidentify the flavor of the $B_{\rm tag}$ averaged over B^0 and $\overline{B}^0$, and $\Delta\omega^j_{D^*\pi}$ is the B^0 mistag rate minus the $\overline{B}^0$ mistag rate. The factor $\mathcal{S}^j_{D^*\pi}$ describes the effect of interference between $b \to u\bar{c}d$ and $b \to c\bar{u}d$ amplitudes in both the $B_{\rm rec}$ and the $B_{\rm tag}$ decays:

$$\begin{aligned}\mathcal{S}^j_{D^*\pi} = \quad & (1 - 2\omega^j_{D^*\pi})\, (s_{\rm t} a_{D^*\pi} + s_{\rm m} c_{D^*\pi}) \\ & + s_{\rm t} s_{\rm m} b_{D^*\pi}(1 - s_{\rm t}\Delta\omega^j_{D^*\pi}),\end{aligned} \tag{E.15}$$

where $a_{D^*\pi}$, $b_{D^*\pi}$, and $c_{D^*\pi}$ are related to the physical parameters through

$$a_{D^*\pi} \equiv 2r^* \sin(2\beta + \gamma) \cos\delta^*,$$

$$
\begin{aligned}
b_{D^*\pi} &\equiv 2r' \sin(2\beta+\gamma)\cos\delta', \\
c_{D^*\pi} &\equiv 2\cos(2\beta+\gamma)(r^*\sin\delta^* - r'\sin\delta'),
\end{aligned}
\tag{E.16}
$$

and r' (δ') is the effective magnitude of the ratio (effective strong phase difference) between the $b \to u\bar{c}d$ and $b \to c\bar{u}d$ amplitudes in the $B_{\rm tag}$ decay. This parameterization is good to first order in r^* and r'. In the following we will refer to the parameters $a_{D^*\pi}$, $b_{D^*\pi}$, $c_{D^*\pi}$ and related parameters for the background PDF as the weak phase parameters. Only $a_{D^*\pi}$ and $b_{D^*\pi}$ are related to *CP* violation, while $c_{D^*\pi}$ can be non-zero even in the absence of *CP* violation when $2\beta+\gamma=0$. The inclusion of r' and δ' in the formalism accounts for cases where the $B_{\rm tag}$ undergoes a $b \to u\bar{c}d$ decay, and the kaon produced in the subsequent charm decay is used for tagging [8]. We expect $r' \sim 0.02$. In lepton-tagged events $r' = 0$ (and hence $b_{D^*\pi} = 0$) because most of the tagging leptons come from B semileptonic decays to which no suppressed amplitude with a different weak phase can contribute.

The $\Delta t_{\rm tr}$ PDF for missing-D tags is

$$
\begin{aligned}
\mathcal{T}^{\rm miss}_{D^*\pi}(\Delta t_{\rm tr}, s_{\rm t}, s_{\rm m}) &= \frac{e^{-|\Delta t_{\rm tr}|/\tau^{\rm miss}_{D^*\pi}}}{8\tau^{\rm miss}_{D^*\pi}}\Big\{1 + s_{\rm m}\,(1-2\rho_{D^*\pi}) \\
&- 2s_{\rm t}s_{\rm m}b_{D^*\pi}\,\sin(\Delta m_{D^*\pi}\Delta t_{\rm tr})\Big\},
\end{aligned}
\tag{E.17}
$$

where $\rho_{D^*\pi}$ is the probability that the charge of the tagging track is such that it results in a mixed flavor measurement. In this analysis, we have neglected the term proportional to $\sin(\Delta m_{D^*\pi}\Delta t_{\rm tr})$ of Eq. E.17. The systematic error on $b_{D^*\pi}$ due to this approximation is negligible due to the small value of $f^{\rm miss}_{D^*\pi}$ reported below.

Background Δt PDFs

The Δt PDF of $B \to D^{*\mp}\rho^\pm$ has the same functional form and parameter values as the signal PDF, except that the weak phase parameters $a_{D^*\rho}$, $b_{D^*\rho}$, and $c_{D^*\rho}$ are set to 0 and are later varied to evaluate systematic uncertainties. The validity of the use of the same parameters for $\mathcal{T}'_{D^*\rho}$ and $\mathcal{T}'_{D^*\pi}$ is established using simulated events, and stems from the fact that the π_h momentum spectrum in the $B \to D^{*\mp}\rho^\pm$ events that pass our selection criteria is almost identical to the signal spectrum.

The Δt PDF of the peaking background accounts separately for charged and neutral B decays:

$$
\begin{aligned}
&\mathcal{T}'_{\rm peak}(\Delta t, \sigma_{\Delta t}, s_{\rm t}, s_{\rm m}) = (1 + s_{\rm t}\,\Delta\epsilon_{\rm peak})\Big\{{\mathcal{T}^0}'_{\rm peak} \\
&+ \int d\Delta t_{\rm tr}\,\mathcal{T}^+_{\rm peak}(\Delta t_{\rm tr}, s_{\rm t}, s_{\rm m}) \times \\
&\quad \mathcal{R}^+_{\rm peak}(\Delta t - \Delta t_{\rm tr}, \sigma_{\Delta t})\Big\},
\end{aligned}
\tag{E.18}
$$

where ${\mathcal{T}^0}'_{\rm peak}$ has the functional form of Eq. (E.13) and the subsequent expressions, Eqs. (E.17-E.16), but with all $D^*\pi$-subscripted parameters replaced with their peak-subscripted counterparts. The integral in Eq. (E.18) accounts for the contribution of charged B decays to the peaking background, with

$$\mathcal{T}^{+}_{\rm peak}(\Delta t_{\rm tr}, s_{\rm t}) = \frac{e^{-|\Delta t_{\rm tr}|/\tau^{+}_{\rm peak}}}{4\tau^{+}_{\rm peak}} \Big(1 - s_{\rm t}\, \Delta\omega^{+}_{\rm peak}\Big)\,, \tag{E.19}$$

and $\mathcal{R}^{+}_{\rm peak}(\Delta t - \Delta t_{\rm tr}, \sigma_{\Delta t})$ being the three-Gaussian resolution function for these events described below.

The Combinatoric $B\overline{B}$ background PDF $\mathcal{T}'_{\rm comb}$ is similar to the signal PDF, with one substantial difference. Instead of parameterizing $\mathcal{T}'_{\rm comb}$ with the four parameters we use the set of three parameters

$$\begin{aligned} \omega'_{\rm comb} &= \omega^{\rm dir}_{\rm comb}\,(1 - f^{\rm dir}_{\rm comb}) + \frac{f^{\rm dir}_{\rm comb}}{2}, \\ \Delta\omega'_{\rm comb} &= \Delta\omega_{\rm comb}\,(1 - f^{\rm dir}_{\rm comb}), \\ \mathit{\Omega}_{\rm comb} &= f^{\rm dir}_{\rm comb}(1 - 2\,\rho_{\rm comb}). \end{aligned} \tag{E.20}$$

With these parameters and $f^{\rm cas}_{\rm comb} = 0$, the combinatoric $B\overline{B}$ background Δt PDF becomes

$$\begin{aligned} &\mathcal{T}'_{\rm comb}(\Delta t, \sigma_{\Delta t}, s_{\rm t}, s_{\rm m}) = (1 + s_{\rm t}\, \Delta\epsilon_{\rm comb}) \times \\ &\int d\Delta t_{\rm tr}\, \mathcal{T}_{\rm comb}(\Delta t_{\rm tr}, s_{\rm t}, s_{\rm m})\, \mathcal{R}_{\rm comb}(\Delta t - \Delta t_{\rm tr}, \sigma_{\Delta t})\,, \end{aligned} \tag{E.21}$$

where $\mathcal{R}_{\rm comb}(\Delta t - \Delta t_{\rm tr}, \sigma_{\Delta t})$ is the 3-Gaussian resolution function and

$$\begin{aligned} &\mathcal{T}_{\rm comb}(\Delta t_{\rm tr}, s_{\rm t}, s_{\rm m}) = \frac{e^{-|\Delta t_{\rm tr}|/\tau_{\rm comb}}}{4\tau_{\rm comb}} \Big\{ 1 - s_{\rm t}\, \Delta\omega'_{\rm comb} \\ &+ s_{\rm m}\mathit{\Omega}_{\rm comb} + s_{\rm m}\,(1 - 2\omega'_{\rm comb})\, \cos(\Delta m_{\rm comb}\Delta t_{\rm tr}) \\ &- \mathcal{S}_{\rm comb}\, \sin(\Delta m_{\rm comb}\Delta t_{\rm tr}) \Big\}, \end{aligned} \tag{E.22}$$

with

$$\begin{aligned} \mathcal{S}_{\rm comb} &= (1 - 2\omega'_{\rm comb})\,(s_{\rm t} a_{\rm comb} + s_{\rm m} c_{\rm comb}) \\ &+ s_{\rm t} s_{\rm m} b_{\rm comb}(1 - s_{\rm t}\, \Delta\omega'_{\rm comb}). \end{aligned} \tag{E.23}$$

As in the case of $\mathcal{T}_{D^*\rho}$, the weak phase parameters of the peaking and combinatoric background ($a_{\rm peak}$, $b_{\rm peak}$, $c_{\rm peak}$ and $a_{\rm comb}$, $b_{\rm comb}$, $c_{\rm comb}$) are set to 0 and are later varied to evaluate systematic uncertainties. Parameters labeled with superscripts "peak" or "comb" are empirical and thus do not necessarily correspond to physical parameters. In general, their values may be different from those of the $D^*\pi$-labeled parameters.

The PDF $\mathcal{T}_{q\overline{q}}$ for the continuum background is the sum of two components, one with a finite lifetime and one with zero lifetime:

$$\begin{aligned} \mathcal{T}'_{q\overline{q}}(\Delta t, \sigma_{\Delta t}, s_{\rm t}) &= (1 + s_{\rm t}\, \Delta\epsilon_{q\overline{q}}) \int d\Delta t_{\rm tr}\, \mathcal{T}_{q\overline{q}}(\Delta t_{\rm tr}, s_{\rm t}, s_{\rm m}) \\ &\times\ \mathcal{R}_{q\overline{q}}(\Delta t - \Delta t_{\rm tr}, \sigma_{\Delta t}), \end{aligned} \tag{E.24}$$

with

$$\begin{aligned}\mathcal{T}_{q\overline{q}}(\Delta t_{\rm tr}, s_{\rm t}) &= (1 - f^{\delta}_{q\overline{q}})\frac{e^{-|\Delta t_{\rm tr}|/\tau_{q\overline{q}}}}{4\tau_{q\overline{q}}}\,(1 - s_{\rm t}\,\Delta\omega_{q\overline{q}}) \\ &+ f^{\delta}_{q\overline{q}}\,\delta(\Delta t_{\rm tr}),\end{aligned} \tag{E.25}$$

where $f^{\delta}_{q\overline{q}}$ is the fraction of zero-lifetime events.

Resolution Function Parameterization

The resolution function for events of type i and optional secondary type j ($j = \{\text{dir, cas, miss}\}$ for lepton-tagged signal events and $j = \{+,\ 0\}$ for the peaking and combinatoric $B\overline{B}$ background types) is parameterized as the sum of three Gaussians:

$$\begin{aligned}\mathcal{R}^{j}_{i}(t_r, \sigma_{\Delta t}) &= f^{nj}_{\ i}\,\mathcal{G}^{nj}_{\ i}(t_r, \sigma_{\Delta t}) \\ &+ (1 - f^{nj}_{\ i} - f^{oj}_{\ i})\,\mathcal{G}^{wj}_{\ i}(t_r, \sigma_{\Delta t}) \\ &+ f^{oj}_{\ i}\,\mathcal{G}^{oj}_{\ i}(t_r),\end{aligned} \tag{E.26}$$

where $t_r = \Delta t - \Delta t_{\rm tr}$ is the residual of the Δt measurement, and $\mathcal{G}^{nj}_{\ i}$, $\mathcal{G}^{wj}_{\ i}$, and $\mathcal{G}^{oj}_{\ i}$ are the "narrow", "wide", and "outlier" Gaussians. The narrow and wide Gaussians incorporate information from the Δt uncertainty $\sigma_{\Delta t}$, and account for systematic offsets in the estimation of $\sigma_{\Delta t}$ and the Δt measurement. They have the form

$$\mathcal{G}^{kj}_{\ i}(t_r, \sigma_{\Delta t}) \equiv \frac{1}{\sqrt{2\pi}\,s^{kj}_{\ i}\,\sigma_{\Delta t}} \times \exp\left(-\frac{\left(t_r - b^{kj}_{\ i}\sigma_{\Delta t}\right)^2}{2(s^{kj}_{\ i}\,\sigma_{\Delta t})^2}\right), \tag{E.27}$$

where the index k takes the values $k = n, w$ for the narrow and wide Gaussians, and $b^{kj}_{\ i}$ and $s^{kj}_{\ i}$ are parameters determined by fits, as described in Sec. E.2.3. The outlier Gaussian, which accounts for a small fraction of events with badly measured Δt, has the form

$$\mathcal{G}^{oj}_{\ i}(t_r) \equiv \frac{1}{\sqrt{2\pi}\,s^{oj}_{\ i}} \exp\left(-\frac{\left(t_r - b^{oj}_{\ i}\right)^2}{2(s^{oj}_{\ i})^2}\right). \tag{E.28}$$

In all nominal fits the values of $b^{oj}_{\ i}$ and $s^{oj}_{\ i}$ are fixed to 0 ps and 8 ps, respectively, and are later varied to evaluate systematic errors.

Analysis Procedure

The analysis is carried out with a series of unbinned maximum-likelihood fits, performed simultaneously on the on- and off-resonance data samples and independently for the lepton-tagged and kaon-tagged events. The analysis proceeds in the following four steps, designed to enable the reliable determination of most parameters from the data:

1. In the first step, we determine the parameters $f_{D^*\rho} + f_{D^*\pi}$, f_{peak}, and f_{comb} of Eq. (E.8). In order to reduce the reliance on the simulation, we also obtain in the same fit the parameters $f_{q\overline{q}}^{\hat{\mathcal{G}}}$ of Eq. (E.10), $\epsilon_{q\overline{q}}$ of Eq. (E.12), σ_L for the signal m_{miss} PDF (Eq. (E.11)), and all the parameters of the Fisher discriminant PDFs. This is done by fitting the data with the PDF

$$\mathcal{P}_i = \mathcal{M}_i(m_{\mathrm{miss}})\, \mathcal{F}_i(F), \tag{E.29}$$

instead of Eq. (E.9); i.e. by ignoring the time dependence. The fraction $f_{q\overline{q}}$ of continuum events is determined from the off-resonance sample and its integrated luminosity relative to the on-resonance sample. All other parameters of the $\mathcal{M}_i$ PDFs and the value of $f_{D^*\pi}/(f_{D^*\pi} + f_{D^*\rho}) = 0.87 \pm 0.03$ are obtained from the MC simulation.

2. In the second step, we repeat the fit of the first step for data events with $\cos\theta_T \geq C_T$, to obtain the fraction of signal events in that sample. Given this fraction and the relative efficiencies for direct, cascade, and missing-D signal events to satisfy the $\cos\theta_T < C_T$ requirement, we calculate $f_{D^*\pi}^{\mathrm{miss}} = 0.011 \pm 0.001$ for lepton-tagged events and $f_{D^*\pi}^{\mathrm{miss}} = 0.055 \pm 0.001$ for kaon-tagged events. We also calculate the value of $\rho_{D^*\pi}$ from the fractions of mixed and unmixed signal events in the $\cos\theta_T \geq C_T$ sample relative to the $\cos\theta_T < C_T$ sample.

3. In the third step, we fit the data events in the sideband $1.81 < m_{\mathrm{miss}} < 1.84$ GeV/c^2 with the 3-dimensional PDFs of Eq. (E.9). The parameters of $\mathcal{M}_i(m_{\mathrm{miss}})$ and $\mathcal{F}_i(F)$, and the fractions f_i are fixed to the values obtained in the first step. From this fit we obtain the parameters of $\mathcal{T}'_{\mathrm{comb}}$, as well as those of $\mathcal{T}'_{q\overline{q}}$.

4. In the fourth step, we fix all the parameter values obtained in the previous steps and fit the events in the signal region $m_{\mathrm{miss}} > 1.845$ GeV/c^2, determining the parameters of $\mathcal{T}'_{D^*\pi}$ and $\mathcal{T}'_{q\overline{q}}$. Simulation studies show that the parameters of $\mathcal{T}'_{\mathrm{comb}}$ are independent of m_{miss}, enabling us to obtain them in the sideband fit (step 3) and then use them in the signal-region fit. The same is not true of the $\mathcal{T}'_{q\overline{q}}$ parameters; hence they are free parameters in the signal-region fit of the last step. The parameters of $\mathcal{T}'_{\mathrm{peak}}$ are obtained from the MC simulation.

E.2.4 Results

The fit of step 1 finds 18710 ± 270 signal $B^0 \to D^{*\mp}\pi^\pm$ events in the lepton-tag category and 70580 ± 660 in the kaon-tag category. The m_{miss} and F distributions for data are shown in Figs. E.6 and E.7, with the PDFs overlaid.

The results of the signal region fit (fourth step) are summarized in Table E.2, and the plots of the Δt distributions for the data are shown in Fig. E.8 for the lepton-tagged and the kaon-tagged events. The goodness of the fit has been verified with the

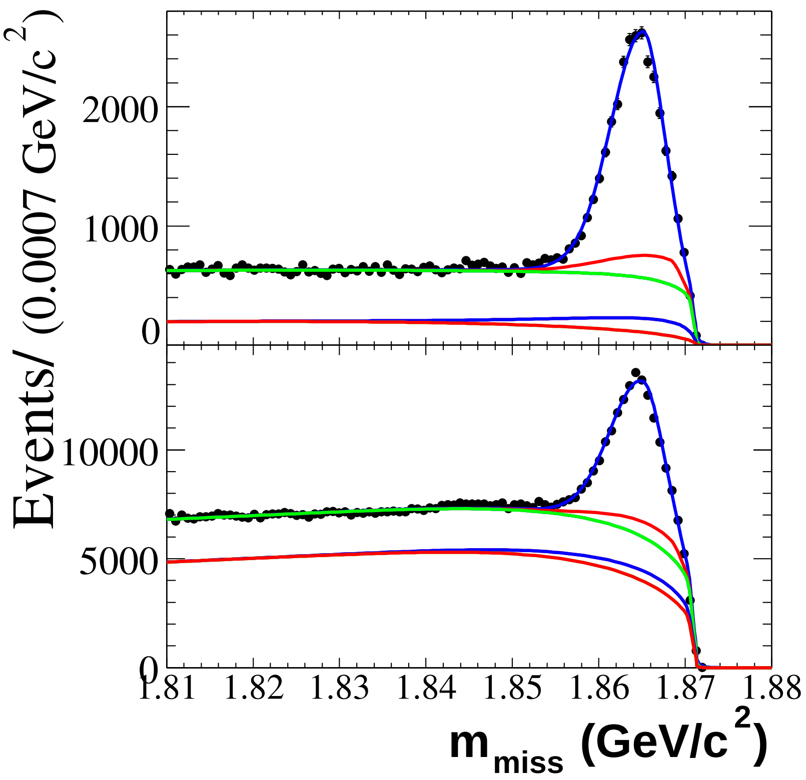

Figure E.6: *The* m_{miss} *distributions for on-resonance lepton-tagged (top) and kaon-tagged (bottom) data. The curves show, from bottom to top, the cumulative contributions of the continuum, peaking* $B\overline{B}$*, combinatoric* $B\overline{B}$*,* $B \to D^{*\mp}\rho^{\pm}$*, and* $B^0 \to D^{*\mp}\pi^{\pm}$ *PDF components.*

Kolmogorov-Smirnov test and by comparing the likelihood obtained in the fit with the likelihood distribution of many parameterized MC experiments generated with the PDF's obtained in the fit on the data. Fig. E.9 shows the raw, time-dependent CP asymmetry

$$A(\Delta t) = \frac{N_{s_{\mathrm{t}}=1}(\Delta t) - N_{s_{\mathrm{t}}=-1}(\Delta t)}{N_{s_{\mathrm{t}}=1}(\Delta t) + N_{s_{\mathrm{t}}=-1}(\Delta t)}. \tag{E.30}$$

In the absence of background and with high statistics, perfect tagging, and perfect Δt measurement, $A(\Delta t)$ would be a sinusoidal oscillation with amplitude $a_{D^*\pi}$. For presentation purposes, the requirements $m_{\mathrm{miss}} > 1.855$ GeV/c^2 and $F < 0$ were applied to the data plotted in Figs. E.8 and E.9, in order to reduce the background. These requirements were not applied to the fit sample, so they do not affect our results.

The fitted values of Δm reported in Table E.2 are in good agreement with the world average (0.502 ± 0.007) ps^{-1} [20]. The fitted values of the B^0 lifetime need

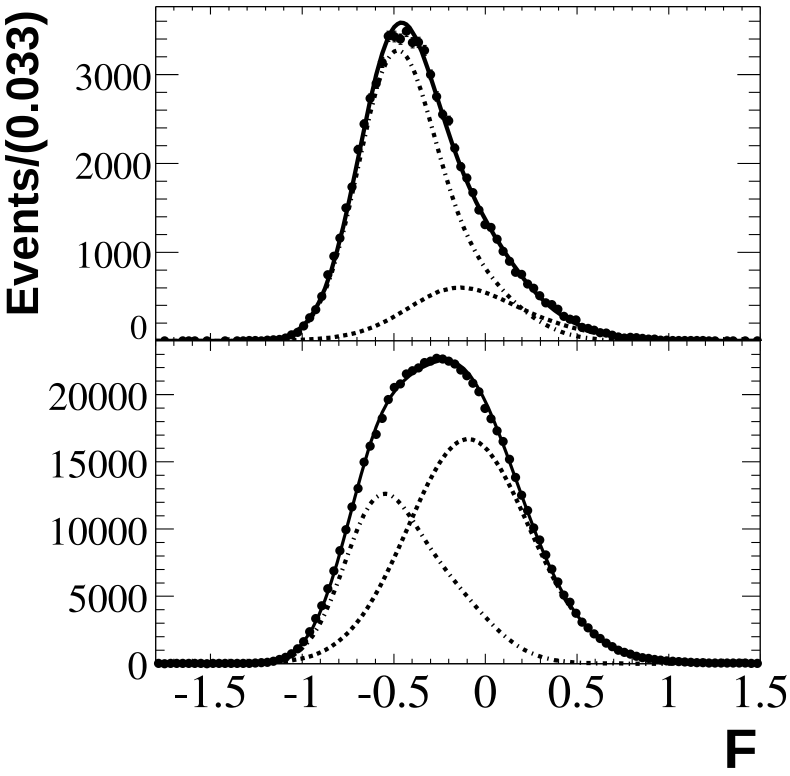

Figure E.7: *The F distributions for on-resonance lepton-tagged (top) and kaon-tagged (bottom) data. The contributions of the $B\overline{B}$ (dashed-dotted line) and the continuum (dashed line) PDF components are overlaid, peaking at approximately* -0.6 *and* -0.1*, respectively. The total PDF is also overlaid.*

to be corrected for a bias observed in the simulated samples, $\Delta\tau = \tau_{fit} - \tau_{gen} = (-0.03 \pm 0.02)$ ps for the lepton-tag and $\Delta\tau = (-0.04 \pm 0.02)$ ps for the kaon-tag events. After this correction, the measured lifetimes, $\tau(B^0) = (1.48 \pm 0.02 \pm 0.02)$ ps and $\tau(B^0) = (1.49 \pm 0.01 \pm 0.04)$ ps for the lepton-tag and kaon-tag, respectively, are in reasonable agreement with the world average $\tau(B^0) = (1.536 \pm 0.014)$ ps [20]. The correlation coefficients of $a^{\ell}_{D^*\pi}$ ($c^{\ell}_{D^*\pi}$) with Δm and $\tau(B^0)$ are -0.021 and 0.019 (-0.060 and -0.056).

E.2.5 Systematic Studies

The systematic errors are summarized in Table E.3. Each item below corresponds to the item with the same number in Table E.3.

1. The statistical errors from the fit in Step 1 are propagated to the final fit. This also includes the systematic errors due to possible differences between the PDF

Table E.2: *Results of the fit to the lepton- and kaon-tagged events in the signal region* $1.845 < m_{\rm miss} < 1.880$ GeV/c^2. *Errors are statistical only. See Sections E.2.3, E.2.3, and E.2.3 for the definitions of the symbols used in this table.*

	Lepton tags		Kaon tags	
Parameter description	Parameter	Value	Parameter	Value
Signal	$a^{\ell}_{D^*\pi}$	-0.042 ± 0.019	$a^{K}_{D^*\pi}$	-0.025 ± 0.020
weak phase par.			$b^{K}_{D^*\pi}$	-0.004 ± 0.010
	$c^{\ell}_{D^*\pi}$	-0.019 ± 0.022	$c^{K}_{D^*\pi}$	-0.003 ± 0.020
Signal Δt PDF	$\Delta m_{D^*\pi}$	0.518 ± 0.010 ps^{-1}	$\Delta m_{D^*\pi}$	0.4911 ± 0.0076 ps^{-1}
	$\tau_{D^*\pi}$	1.450 ± 0.017 ps	$\tau_{D^*\pi}$	1.449 ± 0.011 ps
	$\omega^{\rm dir}_{D^*\pi}$	0.010 ± 0.006	$\omega_{D^*\pi}$	0.2302 ± 0.0035
			$\Delta\omega_{D^*\pi}$	-0.0181 ± 0.0068
	$\Delta\epsilon_{D^*\pi}$	0.027 ± 0.010	$\Delta\epsilon_{D^*\pi}$	-0.0070 ± 0.0073
Signal resolution	${b^{n}_{D^*\pi}}^{\rm cas}$	-0.58 ± 0.16		
function	${b^{w}_{D^*\pi}}^{\rm cas}$	0.23 ± 2.01		
	${b^{n}_{D^*\pi}}^{\rm dir}$	0. (fixed)	$b^{n}_{D^*\pi}$	-0.255 ± 0.013
	${b^{w}_{D^*\pi}}^{\rm dir}$	0. (fixed)	$b^{w}_{D^*\pi}$	-2.07 ± 0.48
	${f^{n}_{D^*\pi}}^{\rm dir}$	0.978 ± 0.008	$f^{n}_{D^*\pi}$	0.969 ± 0.007
	${f^{o}_{D^*\pi}}^{\rm dir}$	0. (fixed)	$f^{o}_{D^*\pi}$	0.000 ± 0.001
	${s^{n}_{D^*\pi}}^{\rm dir}$	1.080 ± 0.033	$s^{n}_{D^*\pi}$	1.029 ± 0.023
	${s^{w}_{D^*\pi}}^{\rm dir}$	5.76 ± 1.44	$s^{w}_{D^*\pi}$	4.35 ± 0.40
Continuum	$\tau_{q\overline{q}}$	1.26 ± 0.32 ps	$\tau_{q\overline{q}}$	0.707 ± 0.048 ps
Δt PDF	$\omega_{q\overline{q}}$	0.340 ± 0.009	$\omega^{\tau}_{q\overline{q}}$	0.045 ± 0.022
			$\omega^{\delta}_{q\overline{q}}$	0.311 ± 0.006
	$f^{\delta}_{q\overline{q}}$	0.815 ± 0.064	$f^{\delta}_{q\overline{q}}$	0.820 ± 0.015
Continuum resolution	$b^{n}_{q\overline{q}}$	0.026 ± 0.048	$b^{n}_{q\overline{q}}$	0.017 ± 0.005
function	$b^{w}_{q\overline{q}}$	-0.39 ± 0.23	$b^{w}_{q\overline{q}}$	-0.043 ± 0.043
	$f^{n}_{q\overline{q}}$	0.65 ± 0.12	$f^{n}_{q\overline{q}}$	0.858 ± 0.014
	$f^{o}_{q\overline{q}}$	0.068 ± 0.014	$f^{o}_{q\overline{q}}$	0.018 ± 0.001
	$s^{n}_{q\overline{q}}$	0.929 ± 0.078	$s^{n}_{q\overline{q}}$	1.064 ± 0.008
	$s^{w}_{q\overline{q}}$	1.81 ± 0.28	$s^{w}_{q\overline{q}}$	2.267 ± 0.099

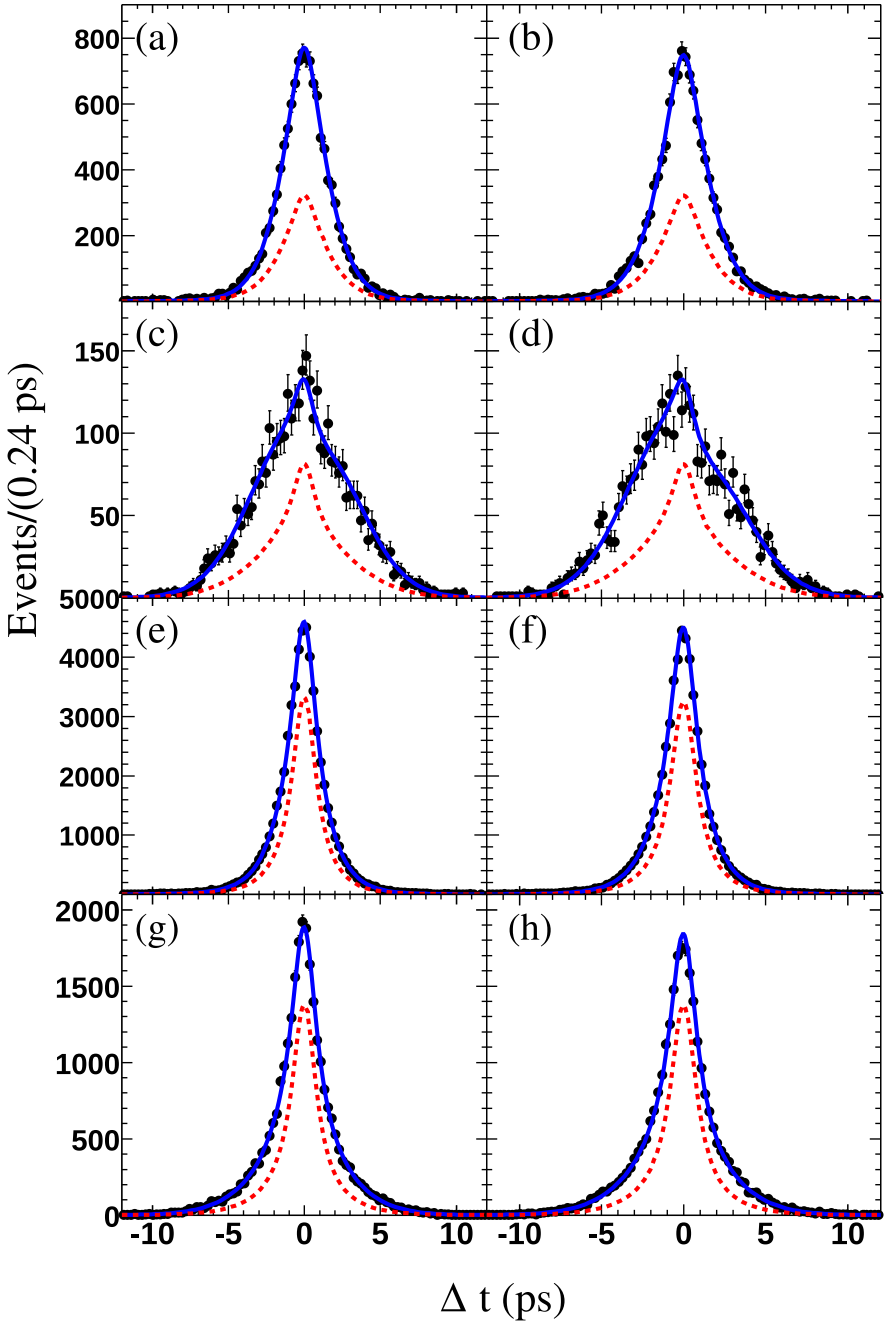

Figure E.8: Δt *distributions for the lepton-tagged (a-d) and kaon-tagged (e-h) events separated according to the tagged flavor of* $B_{\rm tag}$ *and whether they were found to be mixed or unmixed: a,e)* B^0 *unmixed, b,f)* $\overline{B}^0$ *unmixed, c,g)* B^0 *mixed, d,h)* $\overline{B}^0$ *mixed. The solid curves show the PDF, calculated with the parameters obtained by the fit. The PDF for the total background is shown by the dashed curves.*

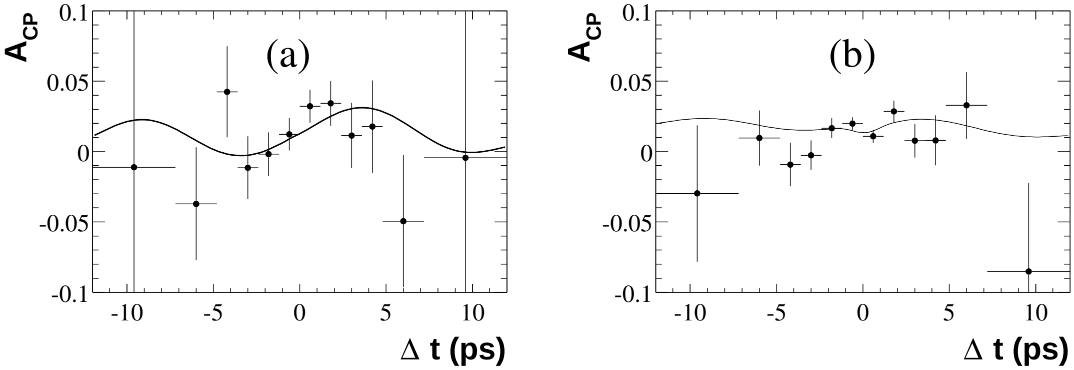

Figure E.9: *Raw asymmetry for (a) lepton-tagged and (b) kaon-tagged events. The curves represent the projections of the PDF for the raw asymmetry. A nonzero value of* $a_{D^*\pi}$ *would show up as a sinusoidal asymmetry, up to resolution and background effects. The offset from the horizontal axis is due to the nonzero values of* $\Delta\epsilon_{D^*\pi}$ *and* $\Delta\omega_{D^*\pi}$.

line shape and the data points.

2. The statistical errors from the $m_{\rm miss}$ sideband fit (Step 3) are propagated to the final fit (Step 4).

3-4. The statistical errors from the Step 2 fits are propagated to the final fit.

5. The statistical errors associated with the parameters obtained from MC are propagated to the final fit. In addition, the full analysis has been performed on a simulated sample to check for a possible bias in the weak phase parameters measured. No statistically significant bias has been found and the statistical uncertainty of this test has been assigned as a systematical error.

6. The effect of uncertainties in the beam-spot size on the vertex constraint is estimated by increasing the beam spot size by 50 μm.

7. The effect of the uncertainty in the measured length of the detector in the z direction is evaluated by applying a 0.6% variation to the measured values of Δt and $\sigma_{\Delta t}$.

8. To evaluate the effect of possible misalignments in the SVT, signal MC events are reconstructed with different alignment parameters, and the analysis is repeated.

9-11. The weak phase parameters of the $B \to D^{*\mp}\rho^\pm$, peaking, and combinatoric $B\overline{B}$ background are fixed to 0 in the fits. To study the effect of possible interference between $b \to u\bar{c}d$ and $b \to c\bar{u}d$ amplitudes in these backgrounds, their weak phase parameters are varied in the range ±0.04 and the Step-4 fit is repeated. We take the largest variation in each weak phase parameter as its systematic error.

12. In the final fit, we take the values of the parameters of $\mathcal{T}'_{\rm peak}$ from a fit to simulated peaking $B\overline{B}$ background events. The uncertainty due to this is evaluated by fitting the simulated sample, setting the parameters of $\mathcal{T}'_{\rm peak}$ to be identical to those of $\mathcal{T}'_{\rm comb}$.

13. The uncertainty due to possible differences between the Δt distributions for the combinatoric background in the $m_{\rm miss}$ sideband and signal region is evaluated by comparing the results of fitting the simulated sample with the $\mathcal{T}'_{\rm comb}$ parameters taken from the sideband or the signal region.

14. The ratio $f_{D^*\rho}/f_{D^*\pi}$ is varied by the uncertainty in the corresponding ratio of branching fractions, obtained from Ref. [20].

E.2.6 Physics Results

Summarizing the values and uncertainties of the weak phase parameters, we obtain the following results from the lepton-tagged sample:

$$\begin{aligned} a^{\ell}_{D^*\pi} &= -0.042 \pm 0.019 \pm 0.010, \\ c^{\ell}_{D^*\pi} &= -0.019 \pm 0.022 \pm 0.013. \end{aligned} \tag{E.31}$$

The results from the kaon-tagged sample fits are

$$\begin{aligned} a^{K}_{D^*\pi} &= -0.025 \pm 0.020 \pm 0.013, \\ b^{K}_{D^*\pi} &= -0.004 \pm 0.010 \pm 0.010, \\ c^{K}_{D^*\pi} &= -0.003 \pm 0.020 \pm 0.015. \end{aligned} \tag{E.32}$$

Combining the results for lepton and kaon tags gives the amplitude of the time-dependent CP asymmetry,

$$\begin{aligned} a_{D^*\pi} &= 2r^* \sin(2\beta+\gamma)\cos\delta^* \\ &= -0.034 \pm 0.014 \pm 0.009, \end{aligned} \tag{E.33}$$

where the first error is statistical and the second is systematic. The systematic error takes into account correlations between the results of the lepton- and kaon-tagged samples coming from the systematic uncertainties related to detector effects, to interference between $b \to u\bar{c}d$ and $b \to c\bar{u}d$ amplitudes in the backgrounds and from $\mathcal{B}(B \to D^{*\mp}\rho^{\pm})$. This value of $a_{D^*\pi}$ deviates from zero by 2.0 standard deviations.

Table E.3: *Systematic errors in* $a^\ell_{D^*\pi}$ *and* $c^\ell_{D^*\pi}$ *for lepton-tagged events and* $a^K_{D^*\pi}$, $b^K_{D^*\pi}$, *and* $c^K_{D^*\pi}$ *for kaon-tagged events.*

Source	Error ($\times 10^{-2}$)				
	Lepton tags		Kaon tags		
	$a^\ell_{D^*\pi}$	$c^\ell_{D^*\pi}$	$a^K_{D^*\pi}$	$b^K_{D^*\pi}$	$c^K_{D^*\pi}$
1. Step 1 fit	0.04	0.04	0.10	0.04	0.04
2. Sideband statistics	0.08	0.08	0.40	0.12	0.44
3. $f^{\text{miss}}_{D^*\pi}$	0.02	0.02	0.02	negl.	negl.
4. $\rho_{D^*\pi}$	0.02	0.02	0.02	negl.	negl.
5. MC statistics	0.60	0.82	0.68	0.34	0.70
6. Beam spot size	0.10	0.10	0.07	0.13	0.06
7. Detector z scale	0.03	0.03	0.02	negl.	0.03
8. Detector alignment	0.25	0.55	0.25	0.13	0.41
9. Combinatoric background weak phase par.	0.25	0.22	0.80	0.56	0.72
10. Peaking background weak phase par.	0.36	0.38	0.29	0.17	0.27
11. $D^*\rho$ weak phase par.	0.53	0.52	0.57	0.58	0.58
12. Peaking background	0.21	0.31	0.21	0.41	0.31
13. Signal region/sideband difference	negl.	negl.	0.04	0.03	0.05
14. $\mathcal{B}(B \to D^{*\mp}\rho^\pm)$	0.17	0.33	0.17	0.22	0.33
Total systematic error	1.0	1.3	1.4	1.0	1.5
Statistical uncertainty	1.9	2.2	2.0	1.0	2.0

Previous results of time-dependent *CP* asymmetries related to $2\beta+\gamma$ appear in Ref. [18, 24]. This measurement supersedes the results of the partial reconstruction analysis reported in Ref. [18] and improves the precision on $a_{D^*\pi}$ and $c_{D^*\pi}$ with respect to the average of the published results.

We use a frequentist method, inspired by Ref. [11], to set a constraint on $2\beta+\gamma$. To do this, we need a value for the ratio r^* of the two interfering amplitudes. This is done with two different approaches.

In the first approach, to avoid any assumptions on the value of r^*, we obtain the lower limit on $|\sin(2\beta+\gamma)|$ as a function of r^*.

We define a χ^2 function that depends on r^*, $2\beta+\gamma$, and δ^*:

$$\chi^2(r^*, 2\beta+\gamma, \delta^*) = \sum_{j,k=1}^{3} \Delta x_j V_{jk}^{-1} \Delta x_k, \qquad \text{(E.34)}$$

where Δx_j is the difference between the result of our measurement of $a^K_{D^*\pi}$, $a^\ell_{D^*\pi}$, or $c^\ell_{D^*\pi}$ (Eqs. (E.32) and (E.31)) and the corresponding theoretical expressions given by Eq. (E.16). We fix r^* to a trial value r^0. The measurements of $b^K_{D^*\pi}$ and $c^K_{D^*\pi}$ are not used in the fit, since they depend on the unknown values of r' and δ'. The measurement error matrix V is nearly diagonal, and accounts for correlations between the measurements due to correlated statistical and systematic uncertainties. We minimize χ^2 as a function of $2\beta+\gamma$ and δ^*, and obtain χ^2_{min}, the minimum value of χ^2.

In order to compute the confidence level for a given value x of $2\beta+\gamma$, we perform the following procedure:

1. We fix the value of $2\beta+\gamma$ to x and minimize χ^2 as a function of δ^*. We define $\chi'^2_{min}(x)$ to be the minimum value of the χ^2 in this fit, and δ^*_{toy} to be the fitted value of δ^*. We define $\Delta\chi^2(x) \equiv \chi'^2_{min}(x) - \chi^2_{min}$.

2. We generate many parameterized MC experiments with the same sensitivity as the data sample, taking into account correlations between the observables, expressed in the error matrix V of Eq. (E.34). To generate the observables $a^K_{D^*\pi}$, $a^\ell_{D^*\pi}$, and $c^\ell_{D^*\pi}$, we use the values $(2\beta+\gamma) = x$, $r^* = r^0$ and $\delta^* = \delta^*_{toy}$. For each experiment we calculate the value of $\Delta\chi^2(x)$, computed with the same procedure used for the experimental data.

3. We interpret the fraction of these experiments for which $\Delta\chi^2(x)$ is smaller than $\Delta\chi^2(x)$ in the data to be the confidence level (CL) of the lower limit on $(2\beta+\gamma) = x$.

The resulting 90% CL lower limit on $|\sin(2\beta+\gamma)|$ as a function of r^* is shown in Fig. E.10. The χ^2 function is invariant under the transformation $2\beta+\gamma \to \pi/2+\delta^*$ and $\delta^* \to \pi/2 - 2\beta+\gamma$. The limit shown in Fig. E.10 is always the weaker of these two possibilities.

In the second approach, we estimate r^* as originally proposed in Ref. [2], and assume SU(3) flavor symmetry. With this assumption, r^* can be estimated from the Cabibbo angle θ_C, the ratio of branching fractions $\mathcal{B}(B^0 \to D_s^{*+}\pi^-)/\mathcal{B}(B^0 \to D^{*-}\pi^+) = (5.4^{+3.4}_{-3.7} \pm 0.7) \times 10^{-3}$ [12], and the ratio of decay constants $f_{D_s^*}/f_{D^*} = 1.10 \pm 0.02$ [14],

$$r^* = \sqrt{\frac{\mathcal{B}(B^0 \to D_s^{*+}\pi^-)}{\mathcal{B}(B^0 \to D^{*-}\pi^+)}}\,\frac{f_{D^*}}{f_{D_s^*}}\tan(\theta_C), \qquad \text{(E.35)}$$

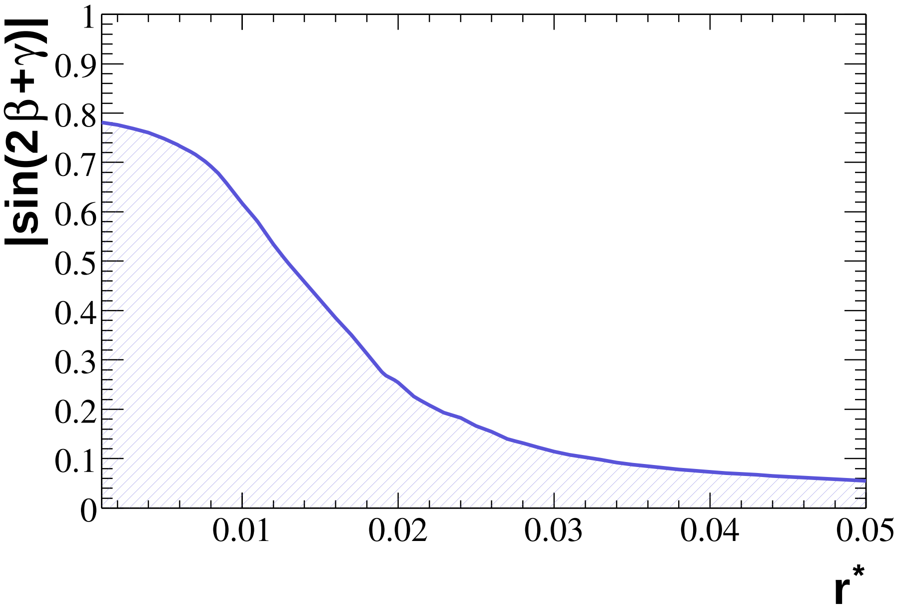

Figure E.10: *Lower limit on* $|\sin(2\beta+\gamma)|$ *at 90% CL as a function of* r^*, *for* $r^* > 0.001$.

yielding the measured value

$$r^{*\text{meas}} = 0.015^{+0.004}_{-0.006}. \tag{E.36}$$

This value depends on the value of $\mathcal{B}(D_s^+ \to \phi\pi^+)$, for which we use our recent measurement [25].

Equation (E.35) has been obtained with two approximations. In the first approximation, the exchange diagram amplitude E contributing to the decay $B^0 \to D^{*+}\pi^-$ has been neglected and only the tree-diagram amplitude T has been considered. Unfortunately, no reliable estimate of the exchange term for these decays exists. The only decay mediated by an exchange diagram for which the rate has been measured is the Cabibbo-allowed decay $B^0 \to D_s^- K^+$. The average of the *BABAR* and Belle branching fraction measurements [12, 13] is $(3.8 \pm 1.0) \times 10^{-5}$. This yields the approximate ratio $\mathcal{B}(B^0 \to D_s^- K^+)/\mathcal{B}(B^0 \to D^-\pi^+) \sim 10^{-2}$, which confirms that the exchange diagrams are strongly suppressed with respect to the tree diagrams. Detailed analyses [26] of the $B \to D\pi$ and $B \to D^*\pi$ decays in terms of the topological amplitudes conclude that $|E'/T'| = 0.12 \pm 0.02$ for $B^0 \to D^-\pi^+$ and $|\bar{E}/\bar{T}| < 0.10$ for $B^0 \to D^{*-}\pi^+$ decays, where E', $\bar{E}$ and T', $\bar{T}$ are the exchange and tree amplitudes for these Cabibbo-allowed decays. We assume that a similar suppression holds for the Cabibbo-suppressed decays considered here.

The second approximation involves the use of the ratio of decay constants $f_{D^*}/f_{D_s^*}$ to take into account SU(3) breaking effects and assumes factorization. We attribute a 30% relative error to the theoretical assumptions involved in obtaining the value of r^* of Eq. (E.36), and use it as described below.

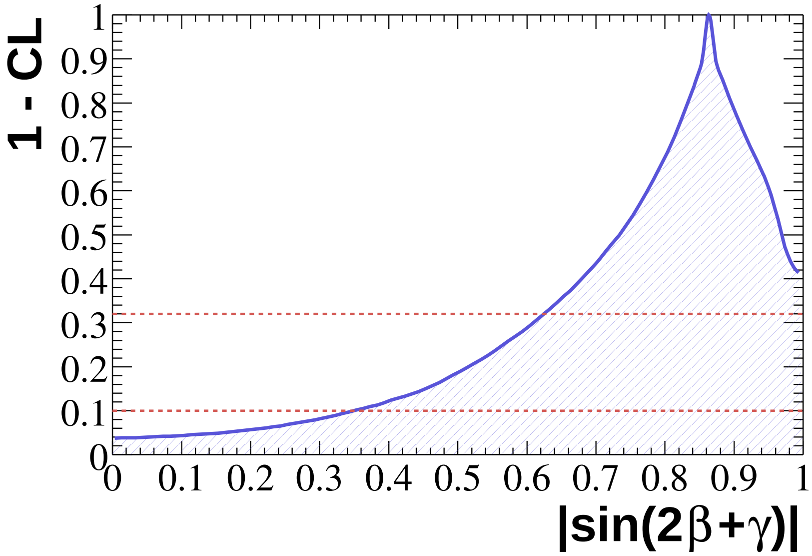

Figure E.11: *The shaded region denotes the allowed range of* $|\sin(2\beta+\gamma)|$ *for each confidence level. The horizontal lines show, from top to bottom, the 68% and 90% CL.*

We add to the χ^2 of Eq. (E.34) the term $\Delta^2(r^*)$ that takes into account both the Gaussian experimental errors of Eq. (E.36) and the 30% theoretical uncertainty according to the prescription of Ref. [15]:

where $\xi_{r^*} \equiv (r^* - r^{*\mathrm{meas}})/r^{*\mathrm{meas}}$.

To obtain the confidence level we have repeated the procedure described above with the following changes. To compute χ^2_{min} we minimize χ^2 as a function of $2\beta+\gamma$, r^* and δ^*. The value $\chi'^2_{min}(x)$ is obtained minimizing χ^2 as a function of r^* and δ^*, having fixed $2\beta+\gamma$ to a given value x. We define δ^*_{toy} and $r^*{}_{toy}$ to be the fitted value of δ^* and r^* in this fit. To generate the observables $a^K_{D^*\pi}$, $a^\ell_{D^*\pi}$, and $c^\ell_{D^*\pi}$ in the parameterized MC experiments, we use the values $(2\beta+\gamma) = x$, $r^* = r^*{}_{toy}$ and $\delta^* = \delta^*_{toy}$.

The confidence level as a function of $|\sin(2\beta+\gamma)|$ is shown in Fig. E.11. We set the lower limits $|\sin(2\beta+\gamma)| > 0.62$ (0.35) at 68% (90%) CL. The implied probability contours for the apex of the unitarity triangle, parameterized in terms of $\bar\rho$ and $\bar\eta$ defined in Ref. [4], appear in Fig. E.12.

E.2.7 Summary

We present a measurement of the time-dependent *CP* asymmetries in a sample of partially reconstructed $B^0 \to D^{*+}\pi^-$ events. In particular, we have measured the parameters related to $2\beta+\gamma$ to be

$$a_{D^*\pi} = 2r^* \sin(2\beta+\gamma)\cos\delta^* = -0.034 \pm 0.014 \pm 0.009 \qquad \text{(E.37)}$$

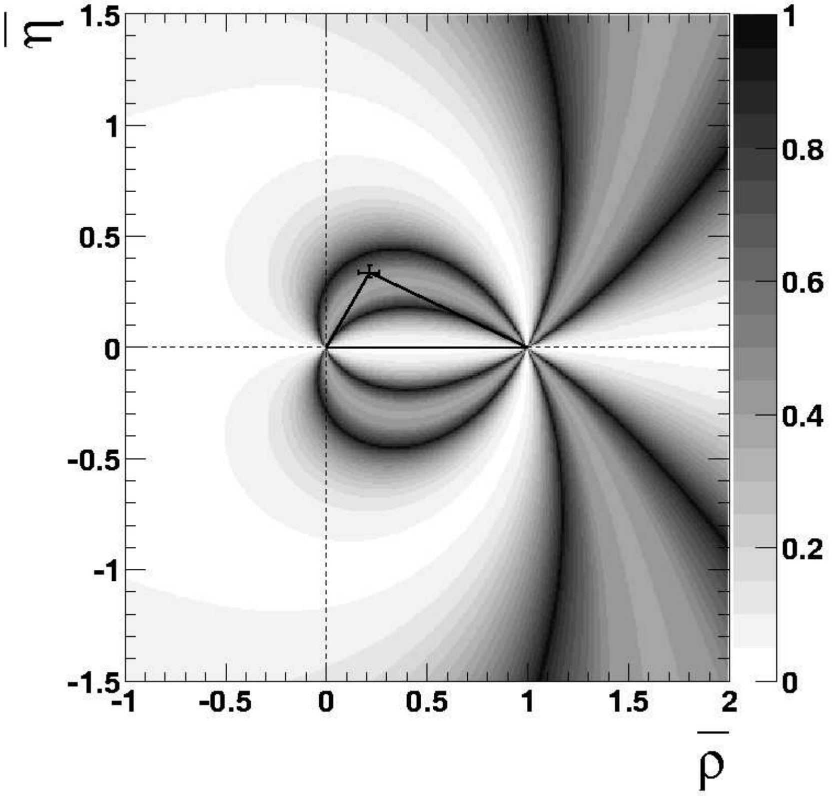

Figure E.12: *Contours of constant probability (color-coded in percent) for the position of the apex of the unitary triangle to be inside the contour, based on the results of Fig. E.11. The cross represents the value and errors on the position of the apex of the unitarity triangle from the CKMFitter fit using the "ICHEP04" results excluding this measurement [27].*

and

$$c^{\ell}_{D^*\pi} = 2r^* \cos(2\beta+\gamma)\sin\delta^* = -0.019 \pm 0.022 \pm 0.013, \tag{E.38}$$

where the first error is statistical and the second is systematic. We extract limits as a function of the ratio r^* of the $b \to u\bar{c}d$ and $b \to c\bar{u}d$ decay amplitudes. With some theoretical assumptions, we interpret our results in terms of the lower limits $|\sin(2\beta+\gamma)| > 0.62$ (0.35) at 68% (90%) CL.

E.2.8 Acknowledgements

We are grateful for the extraordinary contributions of our PEP-II colleagues in achieving the excellent luminosity and machine conditions that have made this work possible. The success of this project also relies critically on the expertise and dedication of the computing organizations that support *BABAR*. The collaborating institutions wish to thank SLAC for its support and the kind hospitality extended to them. This work is supported by the US Department of Energy and National Science Foundation, the Natural Sciences and Engineering Research Council (Canada), Institute of High Energy Physics (China), the Commissariat à l'Energie Atomique and Institut National de Physique Nucléaire et de Physique des Particules (France), the Bundesministerium für Bildung und Forschung and Deutsche Forschungsgemeinschaft (Germany), the Istituto Nazionale di Fisica Nucleare (Italy), the Foundation for Fundamental Research on Matter (The Netherlands), the Research Council of Norway, the Ministry of Science and Technology of the Russian Federation, and the Particle Physics and Astronomy Research Council (United Kingdom). Individuals have received support from CONACyT (Mexico), the A. P. Sloan Foundation, the Research Corporation, and the Alexander von Humboldt Foundation.

E.3 Status and prospects for *CP* asymmetry measurements: $\sin(2\beta+\gamma)$

S. Ganzhur
DSM/Dapnia, CEA/Saclay, F-91191 Gif-sur-Yvette Cedex, France

Abstract

The recent experimental results on CP violation related to the angles of the Cabibbo-Kobayashi-Maskawa (CKM) unitarity triangle $2\beta+\gamma$ *are summarized in these proceedings. These results are obtained with approximately* 232 *million* $\Upsilon(4S)\to B\overline{B}$ *events collected with the BABAR detector at the PEP-II asymmetric-energy B-factory at SLAC. Using the measurements on time-dependent CP asymmetries in* $B^0\to D^{(*)\mp}\pi^\pm$ *and* $B^0\to D^\mp\rho^\pm$ *decays and theoretical assumptions, one finds* $|\sin(2\beta+\gamma)|>0.64$ (0.40) *at* 68% (90%) *confidence level. The perspectives of* $\sin(2\beta+\gamma)$ *measurement with* $\overline{B}^0 \to D^{(*)0}\bar{K}^{(*)0}$ *and* $B^0 \to D^{(*)\mp}a^\pm_{0(2)}$ *decay channels are also discussed.*

Introductoin

A crucial part of the *CP* violation program in *B*-factories is the measurement of the angle $\gamma(\phi_3) = \arg\left(-V_{ud}V^*_{ub}/V_{cd}V^*_{cb}\right)$ of the unitary triangle related to the CKM matrix [1]. Decays of B_d mesons that allows one to constraint the CKM angle $2\beta+\gamma$, have either small *CP* asymmetry ($B \to D^{(*)}\pi$) or small branching fractions ($B \to D^{(*)}K^{(*)}$). This makes the *CP* violation effect hard to measure. Furthermore, due to presence of two hadronic parameters in the observables (r and δ, the amplitude ratio and the strong phase difference between two amplitudes) it is difficult to cleanly extract the weak phase information, although approaches based on SU(3) symmetry exists.

E.3.1 The *BABAR* detector and dataset

The data used in the presented analyzes were recorded with the *BABAR* detector at the PEP-II asymmetric-energy storage rings, and consist of 211 fb^{-1} collected on the Υ(4S) resonance (on-resonance sample), and 21 fb^{-1} collected at an e^+e^- center-of-mass (CM) energy approximately 40 MeV below the resonance peak (off-resonance sample). This corresponds to approximately 232 million $\Upsilon(4S)\to B\overline{B}$ recorded events.

The *BABAR* detector is described in detail in Ref. [7].

E.3.2 *CP* asymmetry in $B^0 \to D^{(*)\mp}\pi^\pm/\rho^\pm$ decays

The decay modes $B^0 \to D^{(*)\mp}\pi^\pm$ have been proposed to measure $\sin(2\beta+\gamma)$ [29]. In the Standard Model the decays $B^0 \to D^{(*)+}\pi^-$ and $\overline{B}^0 \to D^{(*)+}\pi^-$ proceed through the $\overline{b} \rightarrow \overline{u}cd$ and $b \rightarrow c$ amplitudes A_u and A_c, respectively. The relative weak phase between these two amplitudes is γ. When combined with $B^0\overline{B}^0$ mixing, this yields a weak phase difference of $2\beta+\gamma$ between the interfering amplitudes.

The decay rate distribution for $B \rightarrow D^{(*)\pm}\pi^{\mp}$ is

$$\begin{aligned}\mathcal{P}_{\eta}^{\pm}(\Delta t) &= \frac{e^{-|\Delta t|/\tau}}{4\tau} \times \Big[1 \mp S^{\zeta}\sin(\Delta m \Delta t) \\ &\quad \mp \eta C\cos(\Delta m\Delta t)\Big]\,, \end{aligned} \tag{E.39}$$

where τ is the B^0 lifetime averaged over the two mass eigenstates, Δm is the $B^0-\overline{B}^0$ mixing frequency, and Δt is the difference between the time of the $B \rightarrow D^{(*)\pm}\pi^{\mp}$ ($B_{\rm rec}$) decay and the decay of the other B ($B_{\rm tag}$) in the event. The upper (lower) sign in Eq. E.39 indicates the flavor of the $B_{\rm tag}$ as a B^0 ($\overline{B}^0$), while $\eta = +1$ (-1) and $\zeta = +$ ($-$) for the $B_{\rm rec}$ final state $D^{(*)-}\pi^+$ ($D^{(*)+}\pi^-$). The parameters C and $S^{\pm}$ are given by

$$C \equiv \frac{1-r^2}{1+r^2}\,, \qquad S^{\pm} \equiv \frac{2r}{1+r^2}\sin(2\beta+\gamma\pm\delta). \tag{E.40}$$

Here δ is the strong phase difference between A_u and A_c and $r \equiv |A_u/A_c|$. Since A_u is doubly CKM-suppressed with respect to A_c, one expects r to be small of order 2%. Due to the small value of r, large data samples are required for a statistically significant measurement of S.

Since the expected *CP* asymmetry in the selected B decays is small, this measurement is sensitive to the interference between the $b{\rightarrow}u$ and $b{\rightarrow}c$ amplitudes in the decay of $B_{\rm tag}$. To account for this "tagside interference", we use a parametrization which is described in Ref. [8]. The $S^{\pm}$ coefficient are replaced with three others

$$\begin{aligned} a &= 2r\sin(2\beta+\gamma)\cos\delta \\ b &= 2r'\sin(2\beta+\gamma)\cos\delta' \\ c &= 2\cos(2\beta+\gamma)(r\sin\delta - r'\sin\delta') \end{aligned} \tag{E.41}$$

For each tagging category, independent of the decay mode $\{D\pi, D^*\pi, D\rho\}$, the tagside interference is parametrized in terms of the effective parameters r' and δ'. One notes, $r'=0$ for the lepton tagging category.

Two different analysis techniques, full reconstruction [30] and partial reconstruction [18] were used for the $\sin(2\beta+\gamma)$ measurement with $B^0 \rightarrow D^{(*)\mp}\pi^{\pm}$.

The full reconstruction technique is used to measure the *CP* asymmetry in $B^0 \rightarrow D^{(*)\mp}\pi^{\pm}$ and $B^0 \rightarrow D^{*\mp}\rho^{\pm}$ decays [31]. From a time-dependent maximum likelihood fit the following parameters related to the *CP* violation angle $2\beta+\gamma$ are obtained:

$$\begin{aligned} a^{D\pi} &= -0.010 \pm 0.023 \pm 0.007 \\ c_{\rm lep}^{D\pi} &= -0.033 \pm 0.042 \pm 0.012 \\ a^{D^*\pi} &= -0.040 \pm 0.023 \pm 0.010 \end{aligned} \tag{E.42}$$

$$\begin{aligned} c_{\rm lep}^{D^*\pi} &= 0.049 \pm 0.042 \pm 0.015 \\ a^{D\rho} &= -0.024 \pm 0.031 \pm 0.009 \\ c_{\rm lep}^{D\rho} &= -0.098 \pm 0.055 \pm 0.018 \end{aligned}$$

where the first error is statistical and the second is systematic. The systematic error for $B^0 \to D^{*\mp}\rho^\pm$ includes the maximum bias of asymmetry parameters due to possible dependence of r on the $\pi\pi^0$ invariant mass. For the measurement of $2r\cos(2\beta+\gamma)\sin\delta$ parameter only the lepton-tagged events are used due to a presence of tag-side *CP* violation effect [8].

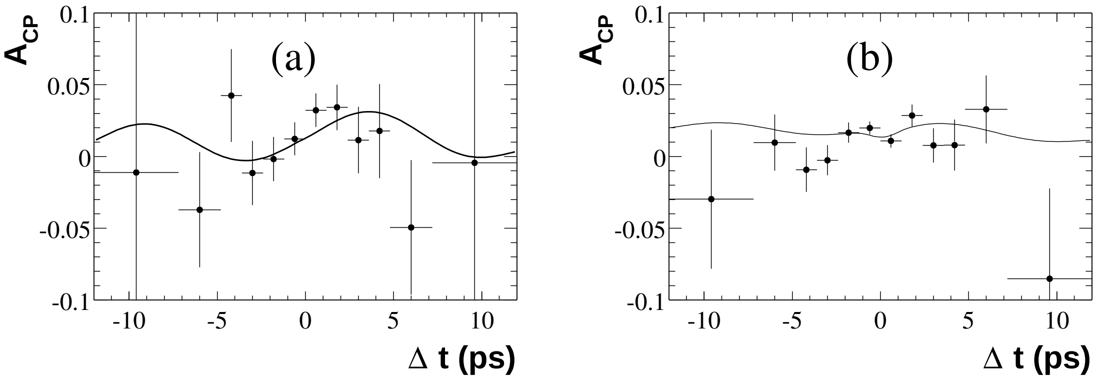

Figure E.13: *Raw asymmetry for (a) lepton-tagged and (b) kaon-tagged events of* $B^0 \to D^{*\mp}\pi^\pm$ *decay mode using the method of the partial reconstruction. The curves represent the projections of the PDF for the raw asymmetry.*

In the partial reconstruction of a $B^0 \to D^{*\mp}\pi^\pm$ candidate, only the hard (high-momentum) pion track π_h from the B decay and the soft (low-momentum) pion track π_s from the decay $D^{*-} \to \overline{D}^0\pi_s^-$ are used. Applying kinematic constraints consistent with the signal decay mode, the four-momentum of the non-reconstructed, “missing” D is calculated. Signal events are peaked in the $m_{\rm miss}$ distribution at the nominal D^0 mass. This method eliminates the efficiency loss associated with the neutral D meson reconstruction. The *CP* asymmetry independent on the assumption on $r^{D^*\pi}(r^*)$ measured with this technique is [32]

$$\begin{aligned} a^{D^*\pi} &= -0.034 \pm 0.014 \pm 0.009 \\ c_{\rm lep}^{D^*\pi} &= -0.019 \pm 0.022 \pm 0.013 \end{aligned} \tag{E.43}$$

where the first error is statistical and the second is systematic. This measurement deviates from zero by 2.0 standard deviations. Figure E.13 shows the raw, time-dependent *CP* asymmetry

$$A(\Delta t) = \frac{N_{B^0}(\Delta t) - N_{\overline{B}^0}(\Delta t)}{N_{B^0}(\Delta t) + N_{\overline{B}^0}(\Delta t)} \tag{E.44}$$

In the absence of background and with high statistics, perfect tagging, and perfect Δt measurement, $A(\Delta t)$ would be a sinusoidal oscillation with amplitude $2r\sin(2\beta+\gamma)\cos\delta$.

Two methods for interpreting these results in terms of constraints on $|\sin(2\beta+\gamma)|$ are used. Both methods involve minimizing a χ^2 function that is symmetric under the exchange $\sin(2\beta+\gamma) \to -\sin(2\beta+\gamma)$, and applying the method of Ref. [11]. In the first interpretation method, no assumption regarding the value of r^* is made. The resulting 95% lower limit for the mode $B^0 \to D^{*\mp}\pi^{\pm}$ is shown as a function of r^* in Figure E.14. The second interpretation assumes that $r^{(*)}$ can be estimated from the Cabibbo angle, the ratio of branching fractions $\mathcal{B}(B^0 \to D^{(*)+}_s\pi^-)/\mathcal{B}(B^0 \to D^{(*)-}\pi^+)$, and the ratio of decay constants $f_{D^*}/f_{D_s^*}$. The confidence level as a function of $|\sin(2\beta+\gamma)|$ is shown in Figure E.15. This method yields the lower limits $|\sin(2\beta+\gamma)|>0.64$ (0.40) at 68% (90%) C.L.

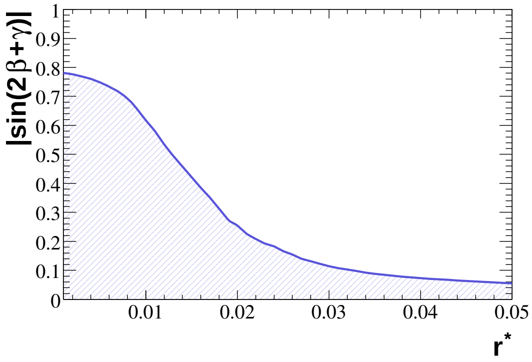

Figure E.14: *Lower limit on* $|\sin(2\beta+\gamma)|$ *a t 90% CL as a function of* r^**, for* $r^* >$ 0.001.

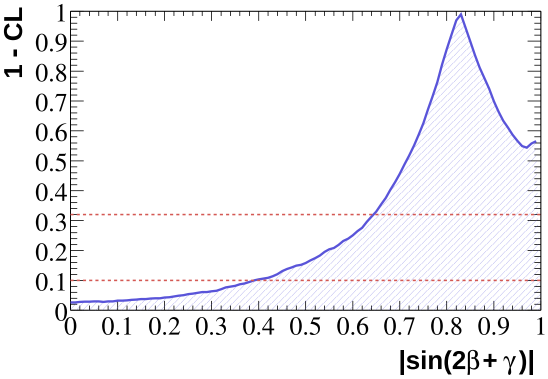

Figure E.15: *The shaded region denotes the allowed range of* $|\sin(2\beta+\gamma)|$ *for each confidence level. The horizontal lines show, from top to bottom, the 68% and 90% CL.*

E.3.3 $\overline{B}^0 \to D^{(*)0}\bar{K}^{(*)0}$ decays

The decay modes $\overline{B}^0 \to D^{(*)0}\bar{K}^0$ have been proposed for determination of $\sin(2\beta+\gamma)$ from measurement of time-dependent *CP* asymmetries [33]. In the Standard Model the decays of B^0 and $\overline{B}^0$ mesons into final state $D^{(*)0}K^0_S$ proceed through the $b \to c$ and $\overline{b} \to \overline{u}$ amplitudes, respectively. Due to relatively large *CP* asymmetry ($r_B \equiv |A(\overline{B}^0 \to \bar{D}^{(*)0}\bar{K}^0)|/|\overline{B}^0 \to D^{(*)0}\bar{K}^0)| \simeq 0.4$) these decay channels look very attractive for such a measurement. Since the parameter r_B can be measured with sufficient data sample by fitting the C coefficient in time distributions, the measured asymmetry can be interpreted in terms of $\sin(2\beta+\gamma)$ without additional assumptions. However, the branching fractions of such decays are relatively small ($\sim 5 \cdot 10^{-5}$). That is way the large data sample is still required.

From the measured signal yields [34], we find

$$\begin{aligned} \mathcal{B}(\overline{B}^0 \to D^0 \overline{K}^0) &= (5.3 \pm 0.7 \pm 0.3) \times 10^{-5} \\ \mathcal{B}(\overline{B}^0 \to D^{*0} \overline{K}^0) &= (3.6 \pm 1.2 \pm 0.3) \times 10^{-5} \\ \mathcal{B}(\overline{B}^0 \to D^0 \overline{K}^{*0}) &= (4.0 \pm 0.7 \pm 0.3) \times 10^{-5} \\ \mathcal{B}(\overline{B}^0 \to \overline{D}^0 \overline{K}^{*0}) &< 1.1 \times 10^{-5} \text{ at } 90\% \text{ C.L.} \end{aligned} \tag{E.45}$$

where the uncertainties are statistical and systematic, respectively. Figure E.16 shows the ΔE distributions of candidates with $|m_{\mathrm{ES}} - 5280| < 8$ MeV/c^2 for the sums of the reconstructed D^0 decay modes.

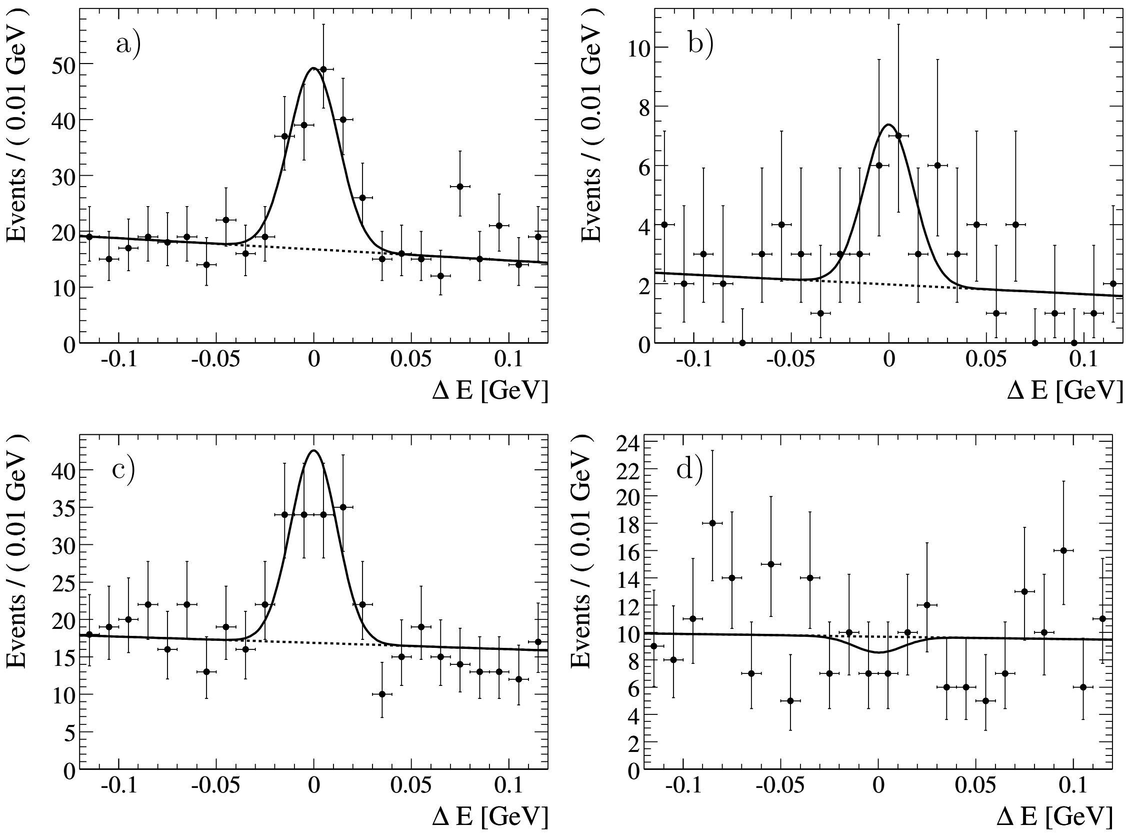

Figure E.16: *Distribution of* ΔE *for a)* $\overline{B}^0 \to D^0\overline{K}^0$*, b)* $\overline{B}^0 \to D^{*0}\overline{K}^0$*, c)* $\overline{B}^0 \to D^0\overline{K}^{*0}$*, and d)* $\overline{B}^0 \to \overline{D}^0\overline{K}^{*0}$ *candidates with* $|m_{\mathrm{ES}} - 5280\ \mathrm{MeV}/c^2| < 8\,\mathrm{MeV}/c^2$*. The points are the data, the solid curve is the projection of the likelihood fit, and the dashed curve represents the background component.*

The B decay dynamics can modify the expectation for the ratio r_B. The magnitude of this ratio can be probed by measuring the rate for the decays $\overline{B}^0 \to D^{(*)0}\bar{K}^{*0}$ and

$\overline{B}^0 \to \bar{D}^{(*)0}\bar{K}^{*0}$ using the self-tagging decay $\overline{K}^{*0} \to K^-\pi^+$. The $\overline{B}^0 \to D^0\overline{K}^{*0}$ and $\overline{B}^0 \to \overline{D}^0\overline{K}^{*0}$ decays are distinguished by the correlation between the charges of the kaons produced in the decays of the neutral D and the $\overline{K}^{*0}$. This charge correlation in the final state is diluted by the presence of the doubly-Cabibbo-suppressed decays $D^0 \to K^+\pi^-, K^+\pi^-\pi^0$, and $K^+\pi^-\pi^+\pi^-$. The ratio r_B is related to the experimental observable $\mathcal{R}$ defined for the $D^0 \to K^+\pi^-$ decay as

$$\begin{aligned}\mathcal{R} &= \frac{\Gamma(\overline{B}^0 \to (K^+\pi^-)_D\overline{K}^{*0})}{\Gamma(\overline{B}^0 \to (K^-\pi^+)_D\overline{K}^{*0})} \\ &= {r^*}^2_B + r_D^2 + 2{r^*}_B r_D\cos(\gamma+\delta), \qquad \text{(E.46)}\end{aligned}$$

where

$$\begin{aligned}r_D &= \frac{|\mathcal{A}(D^0 \to K^+\pi^-)|}{|\mathcal{A}(D^0 \to K^-\pi^+)|}, \qquad \text{(E.47)} \\ \delta &= \delta_B + \delta_D, \qquad \text{(E.48)}\end{aligned}$$

and δ_B and δ_D are strong phase differences between the two B and D decay amplitudes, respectively. From the measured B branching fractions (Eq. E.45), values of r_D [20] and Eq. E.46, one obtains $r < 0.40$ at the 90% C.L. To conclude, the present signal yields combined with this limit on r suggest that a substantially larger data sample is needed for a competitive time-dependent measurement of $\sin(2\beta+\gamma)$ in $\overline{B}^0 \to D^{(*)0}\overline{K}^0$ decays.

E.3.4 $B^0 \to D^{(*)\mp}a^{\pm}_{0(2)}$ decays

Recently it was proposed to consider the $B^0 \to D^{(*)\mp}a^{\pm}_{0(2)}$ decays for measurement of $\sin(2\beta+\gamma)$ [35]. The decay amplitudes of B mesons to light scalar or tensor mesons such as a_0^+ or a_2^+, emitted from a weak current, are significantly suppressed due to the small decay constants $f_{a_{0(2)}}$. Thus, the absolute value of the CKM-suppressed and favored amplitudes become comparable. As a result, the *CP* asymmetry in such decays is expected to be large. However, the theoretical predictions of the branching fractions for $B^0 \to D^{(*)\mp}a^{\pm}_{0(2)}$ is expected of the order of $(1 \div 4)\cdot 10^{-6}$ [36]. The main uncertainty in the branching fractions of these decay modes is due to unknown $B \to a_{0(2)}X$ transition form factors. One way to verify the expectations and test a validity of the factorization approach is to measure the branching fractions for the more abundant decay modes $B^0 \to D_s^{(*)+}a_{0(2)}$.

Using a sample of about 230 million $\Upsilon(4S) \to B\overline{B}$ no evidence for these decays were observed [37]. This allowed one to set upper limits at 90% C.L. on the branching fractions to be

$$\mathcal{B}(B^0 \to D_s^+a_0^-) < 1.9\cdot 10^{-5}$$

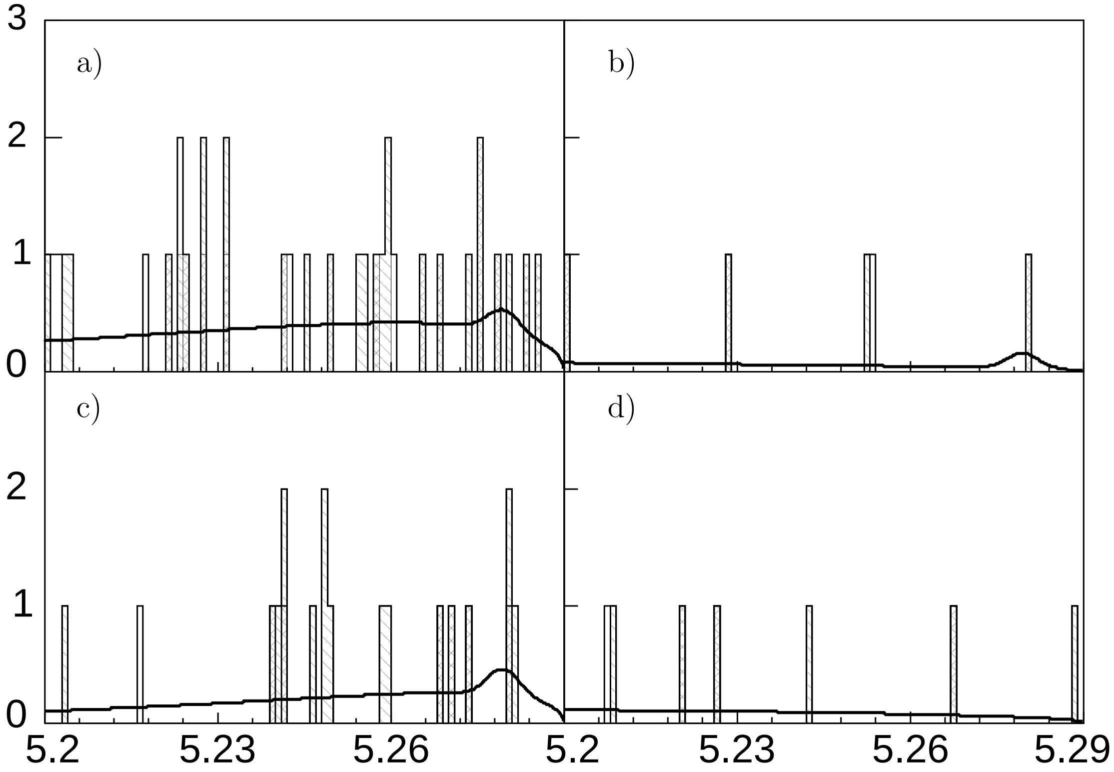

Figure E.17: *Distributions of* $m_{\rm ES}$ *for a)* $B^0 \to D_s^+ a_0^-$*, b)* $B^0 \to D_s^+ a_2^-$*, c)* $B^0 \to D_s^{*+} a_0^-$*, d)* $B^0 \to D_s^{*+} a_2^-$ *candidates overlaid with the projection of the maximum likelihood fit. Contributions from the three* D_s^+ *decay modes are shown with different hatching styles:* $\phi\pi^+$ *is cross hatched,* $\overline{K}^{*0}K^+$ *is hatched, and* $K_S^0 K^+$ *is white.*

$$\begin{aligned} \mathcal{B}(B^0 \to D_s^+ a_2^-) &< 1.9 \cdot 10^{-4} \\ \mathcal{B}(B^0 \to D_s^{*+} a_0^-) &< 3.6 \cdot 10^{-5} \\ \mathcal{B}(B^0 \to D_s^{*+} a_2^-) &< 2.0 \cdot 10^{-4} \end{aligned} \tag{E.49}$$

Figure E.17 shows the $m_{\rm ES}$ distributions for the reconstructed candidates $B^0 \to D_s^+ a_0^-$, $B^0 \to D_s^+ a_2^-$, $B^0 \to D_s^{*+} a_0^-$ and $B^0 \to D_s^{*+} a_2^-$. For each B decay mode, an unbinned maximum-likelihood fit is performed using the candidates from the three D_s^+ decay modes.

The upper limit value for $B^0 \to D_s^+ a_0^-$ is lower than the theoretical expectation, which might indicate the need to revisit the $B \to a_0 X$ transition form factor estimate. It might also imply the limited applicability of the factorization approach for this decay mode. The measured upper limits suggest that the branching ratios of $B^0 \to D^{(*)+} a_{0(2)}^-$ are too small for *CP*-asymmetry measurements given the present statistics of the B-factories. The measurement of $\sin(2\beta+\gamma)$ in $B^0 \to D^{(*)+} a_{0(2)}^-$ decays is an interesting program for the future experiments such as Super$B$-factories.

Conclusion

The substantial constraint on the CKM angles $2\beta+\gamma$ comes from the measurements of time-dependent *CP* asymmetry in the $B^0 \to D^{(*)\mp}\pi^\pm$ and $B^0 \to D^\mp\rho^\pm$ decays. The *BABAR* experiment has used two techniques such as full and partial reconstruction to increase the signal yields in the $D^{*\mp}\pi^\pm$ channel. The combined *BABAR*and *BELLE* results [38] for *CP* violation in the most precisely measured decay channel $D^{*\mp}\pi^\pm$ is

$$a^{D^*\pi} = 2r^* \sin(2\beta+\gamma)\cos\delta = -0.037 \pm 0.011 \tag{E.50}$$

This measurement performed at the level of one per cent deviates from zero by 3.4 standard deviations. Future updates are therefore of a great interest. We interpret the *BABAR* result in terms of $\sin(2\beta+\gamma)$ and find $|\sin(2\beta+\gamma)| > 0.64$ (0.40) at 68% (90%) C.L. using a frequentist method.

The *BABAR* experiment has measured the branching fractions of $\overline{B}^0 \to D^{(*)0}\bar{K}^{(*)0}$ and set up the limit on $B^0 \to D^{(*)\mp}a^\pm_{0(2)}$ decays. The present signal yields and established limits suggest that a substantially larger data sample is needed for a competitive time-dependent measurement of $\sin(2\beta+\gamma)$ with these decay channels.

Bibliography

[1] N. Cabibbo, Phys. Rev. Lett. **10**, 531 (1963); M. Kobayashi and T. Maskawa, Prog. Theoret. Phys. **49**, 652 (1973).

[2] I. Dunietz, Phys. Lett. **B427**, 179 (1998).

[3] *BABAR* Collaboration, B. Aubert *et al.*, Phys. Rev. Lett. **89**, 201802 (2002); Belle Collaboration, K. Abe *et al.*, Phys. Rev. D **66**, 071102 (2002).

[4] L. Wolfenstein, Phys. Rev. Lett. **51**, 1945 (1983).

[5] *BABAR* Collaboration, B. Aubert *et al.*, hep-ex/0307036.

[6] *BABAR* Collaboration, B. Aubert *et al.*, Phys. Rev. D **67**, 091101 (2003).

[7] *BABAR* Collaboration, B. Aubert *et al.*, Nucl. Instrum. Methods **A479**, 1 (2002).

[8] O. Long *et al.*, Phys. Rev. D **68**, 034010 (2003).

[9] Particle Data Group, K. Hagiwara *et al.*, Phys. Rev. D **66**, 010001 (2002).

[10] R. Fleischer, Nucl. Phys. B **591**, 459 (2003).

[11] G. Feldman and R. Cousins, Phys. Rev. D **57**, 3873 (1998).

[12] *BABAR* Collaboration, B. Aubert *et al.*, Phys. Rev. Lett. **90**, 181803 (2003).

[13] Belle Collaboration, P. Krokovny *et al.*, Phys. Rev. Lett. **89**, 231804 (2002).

[14] D. Becirevic, Nucl. Phys. Proc. Suppl. **94**, 337 (2001).

[15] A. Höcker *et al.*, Eur. Phys. J. C **21**, 225 (2001).

[16] The *BABAR* Collaboration, B. Aubert *et al.*, hep-ex/0308018, submitted to Phys. Rev. Lett.

[17] *BABAR* Collaboration, B. Aubert *et al.*, Phys. Rev. Lett. **89**, 201802 (2002); *BABAR* Collaboration, B. Aubert *et al.*, hep-ex/0408127, submitted to Phys. Rev. Lett.; Belle Collaboration, K. Abe *et al.*, Phys. Rev. D **66**, 071102 (2002).

[18] *BABAR* Collaboration, B. Aubert *et al.*, Phys. Rev. Lett. **92**, 251802 (2004).

[19] GEANT4 Collaboration, S. Agostinelli *et al.*, Nucl. Instrum. Meth. A **506**, 250 (2003).

[20] Particle Data Group, S. Eidelman *et al.*, Phys. Lett. B **592**, 1 (2004).

[21] G. Fox and S. Wolfram, Phys. Rev. Lett. **41**, 1581 (1978).

[22] R. A. Fisher, Annals of Eugenics **7**, 179 (1936); M.S. Srivastava and E.M. Carter, "An Introduction to Applied Multivariate Statistics", North Holland, Amsterdam (1983).

[23] ARGUS Collaboration, H. Albrecht *et al.*, Phys. Lett. B **254**, 288 (1991).

[24] *BABAR* Collaboration, B. Aubert *et al.*, Phys. Rev. Lett. **92**, 251801 (2004); Belle Collaboration, T. Sarangi *et al.*, Phys. Rev. Lett. **93**, 031802 (2004).

[25] *BABAR* Collaboration, B. Aubert *et al.*, hep-ex/0408040, submitted to Phys. Rev. Lett.

[26] C.W. Chiang and J.L. Rosner, Phys. Rev. D **67**, 074013 (2003); C.S. Kim, S. Oh, and C. Yu, hep-ph/0412418.

[27] J. Charles *et al.* (CKMFitter Group), hep-ph/0406184 (to appear in Eur. Phys. J. C).

[28] *BABAR* Collaboration, B. Aubert *et al.*, Phys. Rev. Lett. **92** 251801 (2004).

[29] R.G. Sachs, Enrico Fermi Institute Report, EFI-85-22 (1985) (unpublished); I. Dunietz and R.G. Sachs, Phys. Rev. **D37**, 3186 (1988) [E: Phys. Rev. **D39**, 3515 (1989)]; I. Dunietz, Phys. Lett. **B427**, 179 (1998); P.F. Harrison and H.R. Quinn, ed., "The *BABAR* Physics Book", SLAC-R-504 (1998), Chap. 7.6.

[30] *BABAR* Collaboration, B. Aubert *et al.*, Phys. Rev. Lett. **92**, 251801 (2004).

[31] *BABAR* Collaboration, B. Aubert *et al.*, Phys. Rev. D **73**, 111101 (2006).

[32] *BABAR*Collaboration, B. Aubert *et al.*, Phys. Rev. D **71**, 112003 (2005).

[33] M. Gronau and D. London, Phys. Lett. B **253**, 483 (1991); D. Atwood, I. Dunietz, and A. Soni, Phys. Rev. Lett. **78**, 3257 (1997); B. Kayser and D. London, Phys. Rev. D **61**, 116013 (2000); A.I.Sandra, hep-ph/0108031.

[34] *BABAR* Collaboration, B. Aubert *et al.*, Phys. Rev. D **74** 031101 (2006)

[35] M. Diehl, G. Hiller, Phys. Lett. B **517**, 125 (2001).

[36] M. Diehl, G. Hiller, "New ways to explore factorization in B decays", hep-ph/0105194

[37] *BABAR* Collaboration, B. Aubert *et al.*, Phys. Rev. D **73** 071103 (2006)

[38] *BELLE* Collaboration, F.J. Ronga *et al.*, Phys. Rev. D **73**, 092003 (2006).

Appendix F

CKM Phase Measurements

This appendix contains the report of "CKM Phase Measurement" I presented on the 15th International Topical Conference on Hadron Collider Physics, HCP2004 held at Michigan State University in June 2004 (S.Ganzhur, "CKM Phase Measurements", Proceedings of the 15th International Topical Conference on Hadron Collider Physics, HCP2004, 14-18 June 2004, East Lansing MI, USA, AIP Conf.Proc.753: 261-272 (2005), hep-ex/0409023).

This report summarizes the experimental results on *CP* violation in the *B* sector obtained by *BABAR* and *BELLE* before summer 2004. Different tests of the CKM interpretation of *CP* violation in the Standard Model by constraint of the apex of the Unitary Triangle from these measurements are discussed in details.

CKM Phase Measurements

Presented by Sergey Ganzhur
DSM/Dapnia, CEA/Saclay, F-91191 Gif-sur-Yvette Cedex, France

Abstract

Recent experimental results on CP violation in the B sector from BABAR and BELLE, experiments at asymmetric e^+e^- B-Factories, are summarized in these proceedings. The constraint on the position of the apex of the unitary triangle, obtained from these measurements allows a test of the CKM interpretation of CP violation in the Standard Model (SM).

F.1 Introduction

The violation of *CP* symmetry is a fundamental property of Nature which plays a key role in the understanding of the evolution of the Universe. The Cabibbo-Kobayashi-Maskawa (CKM) quark-mixing matrix [1] is a source of *CP* violation in the Standard Model and is under experimental investigation aimed over constraining its parameters. A crucial part of this program is the measurement of the three angles

$$\begin{aligned}\alpha(\phi_2) &= \arg\left(-V_{td}V_{tb}^*/V_{ud}V_{ub}^*\right)\\ \beta(\phi_1) &= \arg\left(-V_{cd}V_{cb}^*/V_{td}V_{tb}^*\right)\\ \gamma(\phi_3) &= \arg\left(-V_{ud}V_{ub}^*/V_{cd}V_{cb}^*\right)\end{aligned}$$

of the unitary triangle (UT), which represents the unitarity of the CKM matrix. These angles can be extracted from the measured time-dependent *CP* asymmetry in the different neutral B decay channels. The independent measurements of α, β and γ allows us to verify the unitary relation ($\alpha + \beta + \gamma = \pi$), resolve the several-fold ambiguity on the angles which usually arises from one single measurement, and search for New Physics (NP), comparing magnitudes of the same angle measured with modes dominated by either tree or penguin amplitudes [2].

The apex $(\bar{\rho}, \bar{\eta})$ [3] of the UT is already constrained from measurements which are not involve the *CP* violation in the B meson system. From the measured amplitudes of the CKM matrix elements, the mixing frequency of the B_d and B_s mesons, and the magnitude of indirect *CP* violation in the kaon system, one obtains a 95% confidence interval for the UT angles [4]:

$$\begin{aligned}20.2^\circ < \ &\beta < 26.0^\circ\\ 77^\circ < \ &\alpha < 120^\circ\\ 39^\circ < \ &\gamma < 80^\circ\end{aligned}$$

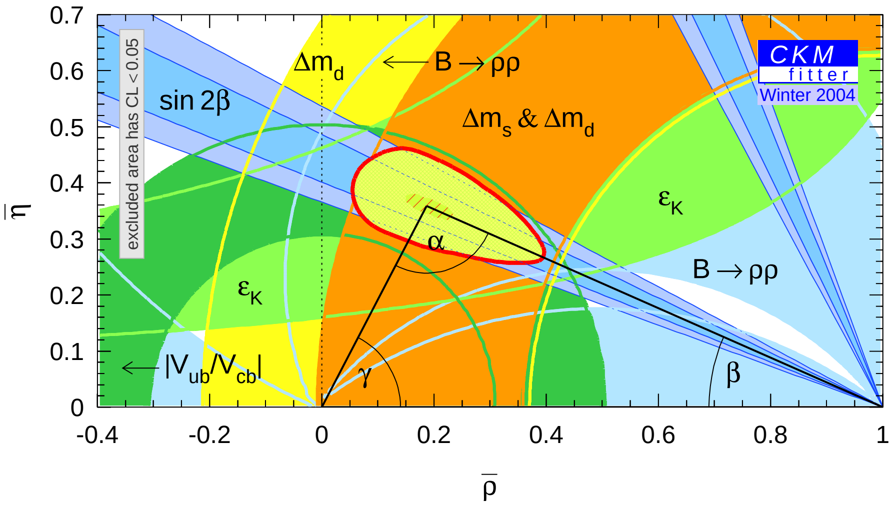

Figure F.1: *Confidence levels in the complex* $(\bar{\rho}, \bar{\eta})$ *plane obtained from the global fit. The constraint from the world average* $\sin(2\beta)/(\phi_1)$ *is not included in the fit and is overlaid.*

Figure F.1 shows the constraint in the $(\bar{\rho}, \bar{\eta})$ plane obtained from such a fit. Thus, the direct measurement of the unitary angles in B meson decays will allow us to check the CKM interpretation of the *CP* violation phenomenon in the SM.

F.2 Status of the B-Factories

It is fair to say that most of *CP* violation measurements in B meson decays are coming from e^+e^- energy-asymmetric machines (B-Factories). There are two B-Factories, PEP-II at SLAC (USA) and KEKB at KEK (Japan). Thanks to a recently incorporated technical feature known as “trickle” injection, both achieved luminosities of order $10^{34}\,\mathrm{cm}^{-2}s^{-1}$. Two similar asymmetric detectors, *BABAR* [5] and *BELLE* [6] operated at PEP-II and KEKB, respectively, measure charged tracks by a combination of a silicon vertex detector and a drift chamber embedded in a 1.5 T solenoidal magnetic field. A ring-imaging Cherenkov detector (DIRC) is used for charged particle identification in *BABAR* while *BELLE* uses aerogel cherenkov counters (ACC) and a time-of-flight system. Both detectors use a CsI(Tl) electromagnetic calorimeter (EMC) to detect photons and identify electrons. The detectors are also equipped with muon chambers to identify muons and reconstruct K_L^0 mesons. The key performances of the two experiments are summarized in the following table:

Experiment	Peak Lum.	Best month	Analyzed data sample
BABAR	$8.8 \times 10^{33}\,\mathrm{cm}^2 s^{-1}$	$15.4\,\mathrm{fb}^{-1}$	$115\,\mathrm{fb}^{-1}$ (123 M $B\bar{B}$ pairs)
BELLE	$13.0 \times 10^{33}\,\mathrm{cm}^2 s^{-1}$	$22.7\,\mathrm{fb}^{-1}$	$140\,\mathrm{fb}^{-1}$ (152 M $B\bar{B}$ pairs)

F.3 Experimental aspects

e^+e^- collisions at the $\Upsilon(4S)$ resonance is a way to produce $B\overline{B}$ pairs in a coherent state. Due to limited phase space, the B mesons from $\Upsilon(4S)$ are produced almost at rest in the center-of-mass (CM) frame. That is why the beam energies are different in order to boost the produced B mesons with a $\beta\gamma = 0.56(0.43)$ for *BABAR* (*BELLE*). This enables the measurement of the time-dependent *CP* asymmetry in the decays of neutral B mesons. The method is described in details elsewhere in [2].

The time-dependent *CP* asymmetry is obtained by measuring the proper time difference Δt between a fully reconstructed neutral B meson (B_{cp}) decaying into a given final state, and the partially reconstructed recoil B meson (B_{tag}). The asymmetry in the decay rate $\mathrm{f}_+(\mathrm{f}_-)$ when the tagging meson is a B^0 ($\overline{B}^0$) is given as

$$\mathrm{f}_\pm(\,\Delta t) \;=\; \frac{\mathrm{e}^{-|\Delta t|/\tau_{B^0}}}{4\tau_{B^0}}\,[\,1 \pm S\sin(\Delta m_d \Delta t) \mp C\cos(\Delta m_d \Delta t)], \qquad \text{(F.1)}$$

where τ_{B^0} is the B^0 lifetime and Δm_d is the B^0–$\overline{B}^0$ mixing frequency. The parameters C and S describe the magnitude of *CP* violation in the decay and in the interference between decay and mixing (mixing-induced), respectively. We expect $C = 0$ in the case of a single dominant decay amplitude, because the direct *CP* violation requires at least two comparable amplitudes with different *CP* violating phases, while S is linked to the CKM phases, e.g. $B^0 \to J/\psi K^0_S$. Presence of more than one decay amplitudes can lead to $C \neq 0$ and a non trivial relation of S with unitary angles, e.g. $B^0 \to \pi^+\pi^-$.

F.4 CKM phase $\beta/(\phi_1)$

F.4.1 Charmonium modes

The observation of *CP* violation in the B^0 system has been reported in 2000 by *BABAR* and *BELLE* collaborations. New precise measurements of $\sin 2\beta$ with a set of charmonium modes similar to the gold plated $J/\psi K^0_S$ decay channel were reported in [7, 8]. The data sample of 88 (152) millions $B\overline{B}$ pairs has been used by *BABAR* (*BELLE*) to fully reconstruct a sample of neutral B mesons decaying into *CP* eigenstates such as $J/\psi K^0_S$, $\psi(2S)K^0_S$, $\chi_{c1}K^0_S$, $\eta_c K^0_S$ (*CP*-odd) and $J/\psi K^0_L$ (*CP*-even) as well as vector-vector final state $J/\psi K^*$ which represents a mixture of *CP*-even and

Mode	*BABAR*	*BELLE*
	($88 \times 10^6 B\overline{B}$)	($152 \times 10^6 B\overline{B}$)
$J\psi K^0_S(K^0_S \to \pi^+\pi^-)$	0.82 ± 0.08	0.67 ± 0.08
$J\psi K^0_S(K^0_S \to \pi^0\pi^0)$	0.39 ± 0.24	0.72 ± 0.20
$\psi(2S)K^0_S(K^0_S \to \pi^+\pi^-)$	0.69 ± 0.24	0.89 ± 0.20
$\chi_{c1}K^0_S$	1.01 ± 0.40	1.54 ± 0.49
$\eta_c K^0_S$	0.59 ± 0.32	1.32 ± 0.29
All with $\eta_f = -1$	0.76 ± 0.07	0.73 ± 0.06
$J\psi K^0_L$	0.72 ± 0.16	0.80 ± 0.13
$J\psi K^{*0}(K^{*0} \to K^0_S\pi^0)$	0.22 ± 0.52	0.10 ± 0.45
All charmonium modes	$0.74 \pm 0.07 \pm 0.03$	$0.73 \pm 0.06 \pm 0.03$

Table F.1: *The CP asymmetry (*$\sin 2\beta$*) measured in the different charmonium decay channels.*

CP-odd states [1]. The obtained results are summarized in Table F.1, where the two experiments are in good agreement within experimental errors. It is interesting to note that the statistical error is still dominant. The average of the two experiments [10]

$$\sin 2\beta = 0.739 \pm 0.049 \tag{F.2}$$

is in a good agreement with Standard Model predictions.

The two vector final state $J/\psi K^*$ can also be used to measure the sign and magnitude of $\cos 2\beta$. Knowledge of the $\cos 2\beta$ sign allows us to reduce the four-fold ambiguity in the β angle. The simultaneous time-dependent and angular analysis for this decay channel obtained by *BABAR* where the $\sin 2\beta$ is fixed to the world average value Equation F.2 favors a positive sign for $\cos 2\beta$ [11]:

$$\cos 2\beta = +2.72^{+0.50}_{-0.79}(stat) \pm 0.27(syst)$$

F.4.2 Penguin dominated modes

In the SM decays like $B^0 \to \phi K^0_S$ are dominated by the $b \to s\bar{s}s$ gluonic penguin diagrams.We expect $C = 0$ in the SM because there is only one dominant decay mechanism. Since ϕK^0_S decays proceed through a *CP*-odd final state, we expect $S = \sin 2\beta$. The other contributions in the SM which can deviate the measured

---

[1] The angular analysis is required to determine the fraction of *CP*-even eigenstate [9]

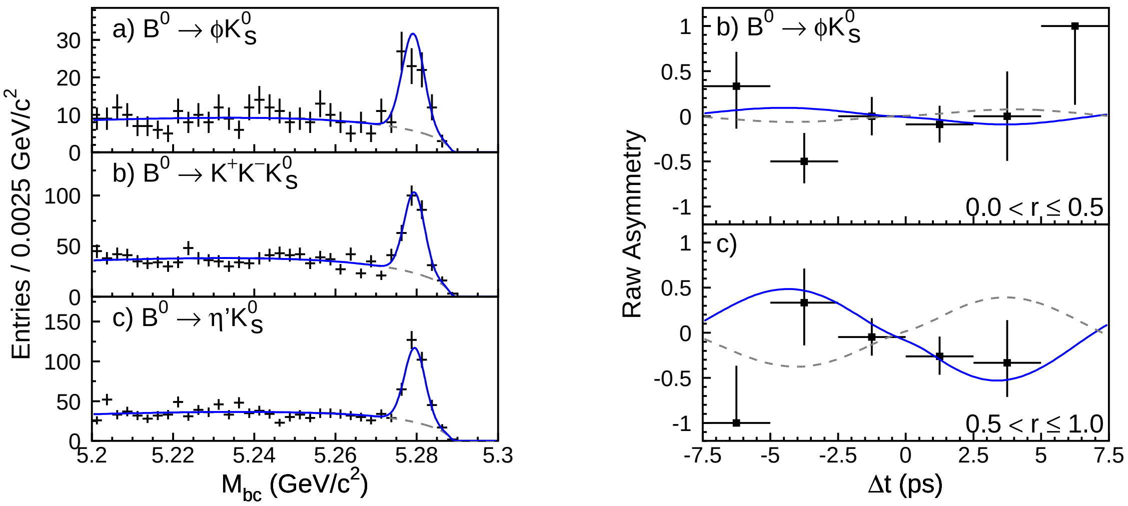

Figure F.2: *The beam-energy constrained mass distributions for three penguin dominated modes:* $\phi K_S^0, K^+K^-K_S^0,\ \eta' K_S^0$ *(left) and the raw asymmetry for* ϕK_S^0 *decay (right) mode measured by BELLE*

asymmetry from $\sin 2\beta$ are rather small and range from several percents for ϕK_S^0 to some tens percents for others [12]. However, contributions from physics beyond the Standard Model (NP), could invalidate these predictions [13]. Since $b \to s\bar{s}s$ decays involve one-loop transitions, they are especially sensitive to such contributions. Figure F.2 shows the beam-energy constrained mass distributions for the three modes: $\phi K_S^0, K^+K^-K_S^0,\ \eta' K_S^0$, obtained by *BELLE*. Clear peaks at the B mass demonstrate the ability to reconstruct modes with relatively small branching fractions of the order of $\sim 10^{-4}$ [14].

The *BELLE* CP violation result obtained with about 152 M $B\overline{B}$ pairs indicates a deviation from the $\sin 2\beta$ value obtained with charmonium modes of about 3.5σ:

$$S_{\phi K^0} = -0.96 \pm 0.50(stat)^{+0.09}_{-0.11}(syst)$$

Figure F.2 also shows the raw asymmetry for such a mode with the SM expectation overlaid. The *BABAR* results obtained with a similar data sample [15]

$$S_{\phi K^0} = +0.47 \pm 0.34(stat)^{+0.08}_{-0.06}(syst),$$

is consistent with $\sin 2\beta$. In addition to ϕK_S^0 this result includes the CP asymmetry measured with CP-even ϕK_L^0 decay mode. However, the two experiments are in marginal agreement within experimental errors for this decay. [2]

---

[2] The recent results presented in [16] solves this problem. The two results are now in good agreement.

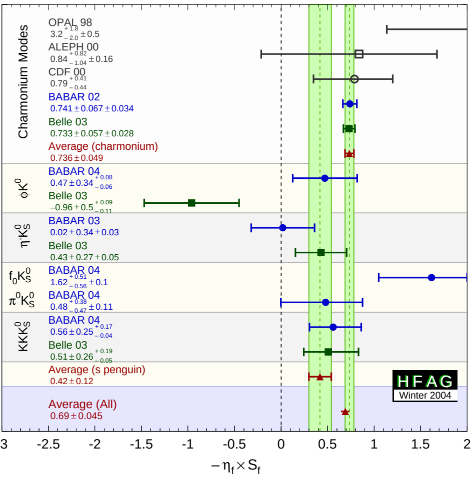

Figure F.3: *Compilation of the results for* $-\eta_f \times S$

A more accurate *CP* violation measurement can be made using all decays to KKK^0_S that do not contain a ϕ meson. This sample is several times larger than the sample of ϕK^0_S, but the *CP* content of the final state is not known. The *CP* content can be determined from isospin symmetry assumptions and measured branching fractions of KKK^0_S and $KK^0_S K^0_S$ decays. Using this approach [17] one observes that the *CP*-even state is strongly dominating decay channel ($f_{even} = 0.98 \pm 0.15 \pm 0.04$). It is fortunate because it maximizes the experimental sensitivity on *CP* violation. Two results reported in [14, 18] are in a good agreement with the SM expectation.

Figure F.3 summarizes the measured *CP* asymmetry relevant to $\sin 2\beta$ for the charmonium and penguin dominated modes [10]. The 2.4σ difference in average between the two types of decays does not allow us to state whether it is or is not an effect of NP. It is important to continue this study to improve the experimental uncertainty until it is resolved.

F.5 CKM phase $\alpha(\phi_2)$

In contrast to the theoretically clean measurements of $\sin 2\beta$ with charmonium final states, the extraction of $\sin 2\alpha$ is complicated by the presence of tree and gluonic penguin amplitudes in modes like $B \to hh$, where $h = \pi, \rho$. Neutral B decays to the *CP* eigenstate $\pi^+\pi^-$ can exhibit mixing-induced *CP* violation through interference between decays with and without B^0–$\overline{B}^0$ mixing, and direct *CP* violation through interference between the $b \to u$ tree and $b \to d$ penguin decay processes shown in Figure F.4. Both effects are observable in the time evolution of the asymmetry between B^0 and $\overline{B}^0$ decays to $\pi^+\pi^-$, where the interference between decay and mixing leads to a sine oscillation with amplitude $S_{\pi\pi}$ and direct *CP* violation leads to a cosine

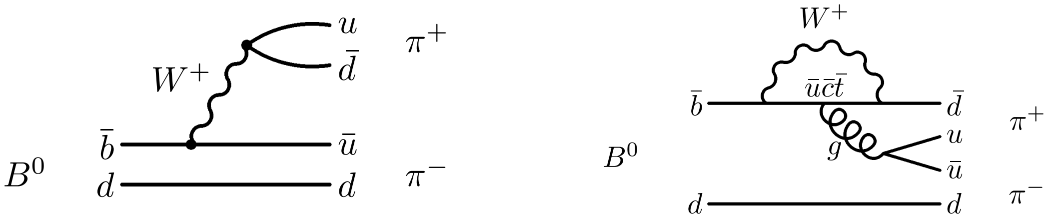

Figure F.4: *Tree (left) and gluonic penguin (right) diagrams contributing to the process* $B \to \pi\pi$

Parameter	*BABAR* (123 M $B\overline{B}$)	*BELLE* (152 M $B\overline{B}$)
$S_{\pi\pi}$	$-0.40 \pm 0.22(stat) \pm 0.03(syst)$	$-1.00 \pm 0.21(stat) \pm 0.07(syst)$
$C_{\pi\pi}$	$-0.19 \pm 0.19(stat) \pm 0.05(syst)$	$-0.58 \pm 0.15(stat) \pm 0.07(syst)$
$\rho(S, C)$	-0.02	-0.29

Table F.2: *Results on CP violation measurements in* $B^0, \overline{B}^0 \to \pi^+\pi^-$. $\rho(S, C)$ *is the correlation coefficient between* C *and* S *in the likelihood function.*

oscillation with amplitude $C_{\pi\pi}$. In the absence of the penguin process, $C_{\pi\pi} = 0$ and $S_{\pi\pi} = \sin 2\alpha$. while significant tree-penguin interference leads to $C_{\pi\pi} \neq 0$ and $S_{\pi\pi} = \sqrt{1 - C^2_{\pi\pi}} \sin 2\alpha_{\text{eff}}$. The presence of loop (penguin) contributions introduces additional phases which can shift the experimentally measurable parameter α_{eff} away from the value of α. The difference between α_{eff} and α can be determined from a model-independent analysis using the isospin-related decays $B^\pm \to \pi^\pm\pi^0$ and B^0, $\overline{B}^0 \to \pi^0\pi^0$ [19].

Results on *CP* violation in B^0, $\overline{B}^0 \to \pi^+\pi^-$ decay mode are summarized in Table. F.2 taken from Ref.[20, 21]. The *BELLE* experiment rule out the *CP*-conserving case, $S_{\pi\pi} = C_{\pi\pi} = 0$ at the 5.2σ level. It also finds evidence of direct *CP* violation with a significance of 3.2σ. The *BABAR* collaboration does not confirm the observation of large *CP* violation in this decay channel reported by *BELLE*. However, the two results are in agreement within experimental errors.

The difference between the measured α_{eff} and α is evaluated using measurements of the isospin-related decay $B^0, \overline{B}^0 \to \pi^0\pi^0$. The observation of this decay, 4.2σ significance, by the *BABAR* collaboration (Figure F.5 (left)) with relatively large branching fraction [22] demonstrates a large gluonic penguin contribution in this mode. However, this leads to essential difficulties for α extraction with $B \to \pi\pi$ decays.

Figure F.5 (right) shows a two-dimensional 68% and 95% C.L. for the experimental results in the (C,S) plane. For comparison, the colored regions shows the 95% C.L. obtained from the isospin analysis, the SU(3) $B^+ \to K^0\pi^+$ decay, and QCD factorization prediction. Large negative correlation between S and C observed in *BELLE* reflects the shape of the confidence region. One can state that experimental results

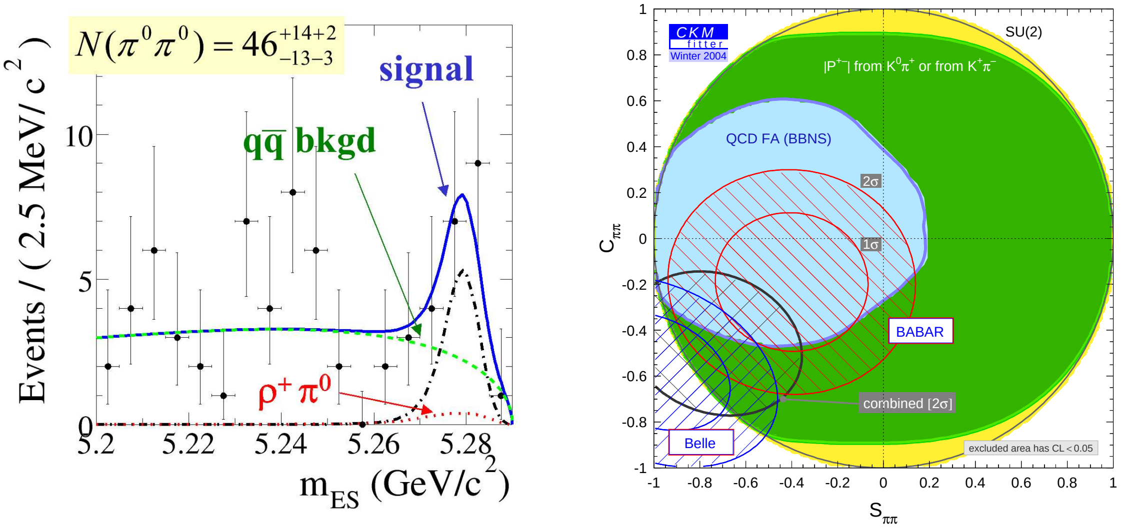

Figure F.5: *The observation of* B^0, $\overline{B}^0 \to \pi^0\pi^0$ *decay by BABAR (left). The* 1σ *and* 2σ *contours for the BABAR and BELLE in (C,S) plane obtained for* $B^0, \overline{B}^0 \to \pi^+\pi^-$ *decay (right).*

are consistent with isospin symmetry prediction, where knowledge of $\mathcal{B}(B^0 \to \pi^0\pi^0)$ is still a dominant uncertainty.

The measurement of the $B^\pm \to \rho^\pm\rho^0$ branching fraction and the upper limit for $B^0 \to \rho^0\rho^0$ [23] indicate small penguin contribution to the $B \to \rho\rho$ decay. Higher branching fraction and smaller shift of the measured parameters α_{eff} from α comparing to B^0, $\overline{B}^0 \to \pi^+\pi^-$ makes B^0, $\overline{B}^0 \to \rho^+\rho^-$ decays more attractive for the extraction of the CKM angle α. It is also fortunate for the sensitivity to α that this two-vector final state is almost longitudinally polarized as it was measured in [24] with an angular analysis.

Figure F.6 (left) shows the B mass distribution for the reconstructed $\rho^+\rho^-$ candidates [25]. The B candidates associated with only lepton tag, which provides the best signal-to-background ratio, are also shown. A clear peak at B^0 mass allows one to measure polarization and *CP* asymmetry. The new *BABAR* result for B^0, $\overline{B}^0 \to \rho^+\rho^-$ decay, obtained with 123 million $B\overline{B}$ pairs is the following:

$$\begin{aligned} f_L &= 1.00 \pm 0.02(stat)^{+0.04}_{-0.03}(syst) \\ C_{long} &= -0.23 \pm 0.24(stat) \pm 0.14(syst) \\ S_{long} &= -0.19 \pm 0.33(stat) \pm 0.11(syst) \end{aligned}$$

Ignoring the possible non-resonant contributions, interference, I=1 amplitudes and assuming isospin symmetry, by using the experimental data on $\mathcal{B}(B^0 \to \rho^0\rho^0)$, one can relate the *CP* parameters S_{long} and C_{long} to the CKM angle α up to a fourfold ambiguity. Selecting the solution closest to the CKM best fit average [4], this

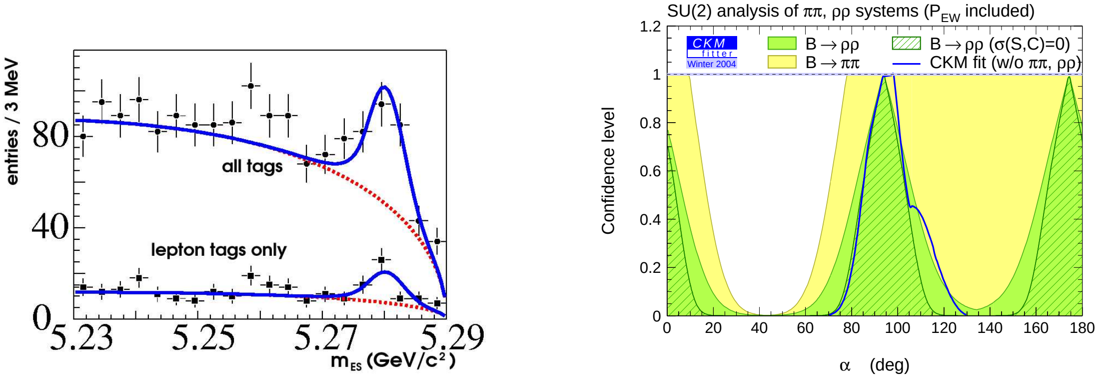

Figure F.6: *The* B *mass distribution for the* $B^0 \to \rho^+\rho^-$ *decay (left). Constrained on* α *obtained from the* $\pi\pi$ *and the* $\rho\rho$ *systems (right). The constraint assuming infinite precision for* C_{long} *and* S_{long} *is also shown. The plots are from* BABAR.

corresponds to

$$\alpha = 96^\circ \pm 10^\circ(stat) \pm 4^\circ(syst) \pm 13^\circ(peng)$$

where the last error is the additional contribution from penguins that is bounded at $< 13^\circ$ (68.3% C.L.)

Figure F.6 (right) shows the constraint on α from the $\pi\pi$ and the $\rho\rho$ systems. *BABAR* and *BELLE* average branching fractions, polarization in $\rho\rho$ (including the limit on $\rho^0\rho^0$, for which the polarization is unknown) and asymmetry C and S measurements are used to perform the Gronau-London isospin analysis. One can conclude that $\rho\rho$ system provides the most precise constraint on α, where the knowledge of penguin pollution is dominant.

F.6 CKM phase $\gamma(\phi_3)$

Decays of B_d mesons relevant to the CKM phase γ show either small *CP* asymmetry ($B \to D^{(*)}\pi$) or branching fractions ($B \to D^{(*)}K$). This produces essential difficulties for this measurement, where most of analyses are model dependent. That is why future experiments at Hadron Colliders are attractive for they will have access to the physics of the B_s mesons.

F.6.1 *CP* asymmetry with $B^0 \to D^{(*)\mp}\pi^\pm$

The decay modes $B^0 \to D^{(*)\mp}\pi^\pm$ have been proposed to measure $\sin(2\beta+\gamma)$ [26]. In the Standard Model the decays $B^0 \to D^{(*)+}\pi^-$ and $\overline{B}^0 \to D^{(*)+}\pi^-$ proceed through the $\overline{b} \to \overline{u}cd$ and $b \to c$ amplitudes A_u and A_c, respectively. The relative weak phase between these two amplitudes is γ. When combined with $B^0\overline{B}^0$ mixing, this yields a weak phase difference of $2\beta+\gamma$ between the interfering amplitudes. The decay rate distribution for $B \to D^{(*)\pm}\pi^{\mp}$ is described by an equation similar to Equation F.1, where the parameters C and S are given by

$$C \equiv \frac{1-r^{(*)2}}{1+r^{(*)2}}\,, \qquad S^{\pm} \equiv \frac{2r^{(*)}}{1+r^{(*)2}}\,\sin(2\beta+\gamma\pm\delta^{(*)}).$$

Here $\delta^{(*)}$ is the strong phase difference between A_u and A_c and $r^{(*)} \equiv |A_u/A_c|$. Since A_u is doubly CKM-suppressed with respect to A_c, one expects $r^{(*)}$ to be small of order 2%. Due to the small value of $r^{(*)}$, large data samples are required for a statistically significant measurement of S.

Two different analysis techniques, full reconstruction and partial reconstruction were used for the $\sin(2\beta+\gamma)$ measurement with $B^0 \to D^{(*)\mp}\pi^{\pm}$.

In the partial reconstruction of a $B^0 \to D^{*\mp}\pi^{\pm}$ candidate, only the hard (high-momentum) pion track π_h from the B decay and the soft (low-momentum) pion track π_s from the decay $D^{*-} \to \overline{D}{}^0\pi_s^-$ are used. Applying kinematic constraints consistent with the signal decay mode, the four-momentum of the non-reconstructed, “missing” D is calculated. Signal events are peaked in the m_{miss} distribution at the nominal D^0 mass. This method eliminates the efficiency loss associated with the neutral D meson reconstruction. The *CP* asymmetry independent on the assumption on r^* measured with this technique by *BABAR* is [27]

$$2r^*\sin(2\beta+\gamma)\cos\delta^* = -0.063 \pm 0.024 \pm 0.014$$

This measurement deviates from zero by 2.3 standard deviations. Both *BABAR* and *BELLE* also use the full reconstruction technique [28, 29] to extract the $\sin(2\beta+\gamma)$value.

Two methods for interpreting these results in terms of constraints on $|\sin(2\beta+\gamma)|$ are used. Both methods involve minimizing a χ^2 function that is symmetric under the exchange $\sin(2\beta+\gamma) \to -\sin(2\beta+\gamma)$, and applying the method of Ref. [30]. In the first interpretation method, no assumption regarding the value of r^* is made. The resulting 95% lower limit for the mode $B^0 \to D^{*\mp}\pi^{\pm}$ is shown as a function of r^* in Figure F.7 (left). The second interpretation assumes that $r^{(*)}$ can be estimated from the Cabibbo angle, the ratio of branching fractions $\mathcal{B}(B^0 \to D^{(*)+}_s\pi^-)/\mathcal{B}(B^0 \to D^{(*)-}\pi^+)$, and the ratio of decay constants $f_{D^*}/f_{D_s^*}$. This method yields the limits [27] $|\sin(2\beta+\gamma)| > 0.87$ at 68% C.L. and $|\sin(2\beta+\gamma)| > 0.58$ at 95% C.L. $|\sin(2\beta+\gamma)| = 0$ is excluded at 99.4 % C.L.

F.6.2 γ extraction with $B \to D^{(*)}K$

Several proposed methods for measuring γ exploit the interference between $B^- \to D^0K^-$ and $B^- \to \bar{D}^0K^-$, which occurs when D^0 and $\bar{D}^0$ decay into the same final state f. These methods are the following:

f= $\boldsymbol{K^+\pi^-}$ - CKM-suppressed (DCS) for D^0 and Cabibbo favored for $\overline{D}{}^0$ (ADS) [31];

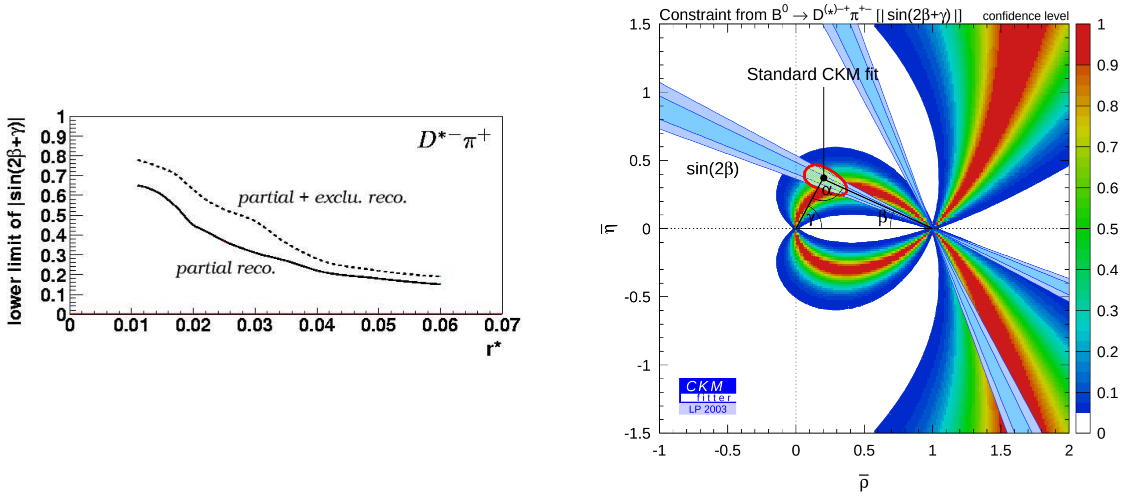

Figure F.7: *95% C.L. lower limit on* $|\sin(2\beta+\gamma)|$ *as a function of* r^* *with BABAR (left). The solid curve corresponds to the partial reconstruction analysis; the dashed curve includes the results of full reconstruction for* $B^0 \to D^{*\mp}\pi^\pm$ *only. Probability contours (right) for the position of the apex of the unitary triangle based on the* $B^0 \to D^{(*)\mp}\pi^\pm$ *decays.*

f= $\boldsymbol{\pi^+\pi^-,\ K^+K^-,\ K^0_s\pi^0}$ - *CP* eigenstate (GLW) [32];

f= $\boldsymbol{K^0_s\pi^+\pi^-}$ - 3-body Dalitz plot analysis [33].

Theoretically clean measurements of the angle γ can be obtained with ADS and GLW methods, while the Dalitz plot analysis relies on D^0 decay model.

The ADS method allows us to determine how large the suppression of $b \to u$ amplitude is. Assuming no *CP* violation in D meson decays, the measured quantity

$$R_{K\pi} = \frac{1}{2}R^+_{K\pi} + R^-_{K\pi} = r_B^2 + r_D^2 + 2r_B r_D \cos\gamma\cos(\delta_B + \delta_D),\ \ R^\pm_{K\pi} \equiv \frac{\Gamma([K^\mp\pi^\pm]_D K^\pm)}{\Gamma([K^\pm\pi^\mp]_D K^\pm)}$$

where $r_B =\equiv \frac{|A(B^-\to\bar{D}^0K^-)|}{|A(B^-\to D^0K^-)|} \simeq 0.2$, $r_D \equiv |\frac{A(D^0\to K^+\pi^-)}{A(D^0\to K^-\pi^+)}| = 0.060 \pm 0.003$ can be used to constraint γ. The analysis performed with 123 million $B\overline{B}$ pairs yields $N_{sig.} = 1.1 \pm 3.0$ signal ($B^+ \to [K^-\pi^+]_D K^+$) candidates [34]. This allows one to calculate the Bayesian limit $R_{K\pi} < 0.026$ at 90% C.L. assuming a constant prior for $R_{K\pi} > 0$. Figure F.8 shows the dependence of $R_{K\pi}$ on r_B. The area indicates the allowed region for any value of δ, with a $\pm 1\sigma$ variation on r_D and the restriction with (filled-in) and without (hatched) $48^\circ < \gamma < 73^\circ$ constraint suggested by global CKM fit [4]. The 90% C.L. upper limit on $r_B < 0.196(0.224)$ with (without) the constraint on γ. To conclude, the small value of r_B, as suggested by this analysis, makes determining γ from $B \to DK$ difficult.

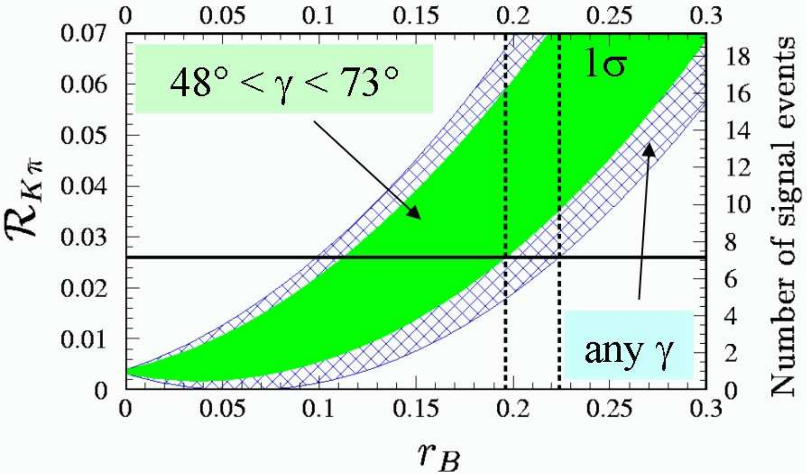

Figure F.8: *Expectation on $R_{K\pi}$ and N_{sig} versus r_B obtained with BABAR [34].*

CP-odd ($D^0 \to \pi^+\pi^-, K^+K^-$) [35, 36] and *CP*-even ($D^0 \to \pi^0 K^0_S$, ϕK^0_S, ωK^0_S, ηK^0_S, $\eta' K^0_S$) [36] decay modes were used to reconstruct $B^- \to D^0_{CP} K^-$. At the current precision of such measurements, γ can not be constrained yet.

The CKM phase γ, r_B and strong phase difference δ between the two amplitudes can be fitted in the Dalitz plot of $B^+ \to [K^0_S \pi^- \pi^+]_D K^+$. The decay model for Cabibbo allowed 3-body decay of D^0 is measured in D^*-tagged D^0 decays. By using 152 million $B\overline{B}$ pairs *BELLE* finds $35° < \gamma < 127°$, at 95% C.L. [37]. The fitted $r_B = 0.31 \pm 0.11$ is somewhat large, but in agreement with ADS method.

F.7 Conclusion

In conclusion, the two B-factories have been operating successfully since 1999 and the *BABAR* and *BELLE* experiments have already produced a lot of results relevant to the CKM phase measurements. Presence of *CP* violation is well established in the B-sector and its magnitude is in agreement with the CKM interpretation of this phenomenon in the Standard Model. Measurements of the three CKM angles provide very important constraints on the apex of the Unitary Triangle There are several “hot” modes such as $B^0 \to \phi K^0_S$ (penguin dominated) and $B^0 \to \pi^+\pi^-$ (presence of large penguin contribution), where statistical room for new effects exists.

Bibliography

[1] N. Cabibbo, Phys. Rev. Lett. **10**, 531 (1963); M. Kobayashi and T. Maskawa, Prog. Theor. Phys. **49**, 652 (1973).

[2] P.F. Harrison and H.R. Quinn, ed., "The *BABAR* Physics Book", SLAC-R-504 (1998).

[3] L. Wolfenstein, Phys. Rev. Lett. **51**, 1945 (1983).

[4] A. Höcker *et al.* , Eur. Phys. Jour. C **21**, 225 (2001);

[5] *BABAR* Collaboration, B. Aubert *et al.*, Nucl. Instrum. Methods **A479** 1 (2002).

[6] BELLE Collaboration, A. Abashian *et al.*, Nucl. Instrum. Methods **A479** 117 (2002).

[7] *BABAR* Collaboration, B. Aubert *et al.*, Phys. Rev. Lett. **89**, 201802 (2002).

[8] BELLE Collaboration, K. Abe *et al.*, BELLE-CONF-0353, (2003), presented at LP'03.

[9] S.Ganzhur, "Hadronic B decays with the *BABAR* detector", Results and Perspectives in Particle Physics, edited by M.Greco, proceedings of the Les Rencontres de Rhysique de la Vallé' d'Aoste, 4-11 March, 2001, La Thuile, Italy; *BABAR* Collaboration, B. Aubert *et al.*, Phys. Rev. Lett. **87**, 241801 (2001).

[10] Heavy Flavor Averaging Group: http://www.slac.stanford.edu/xorg/hfag

[11] *BABAR* Collaboration, B. Aubert *et al.*,

[12] D.London and A.Soni, Phys. Lett. B **407**, 61 (1997); Y.Grossman, Z.Ligeti, Y.Nir and H.Quinn, Phys. Rev. D **68**, 015004 (2003); M.Gronau, Y.Grossman and J.Rosner, Phys. Lett. B **579**, 331 (2004)

[13] Y. Grossman and M. P. Worah, Phys. Lett. B **395**, 241 (1997)

[14] BELLE Collaboration, K.Abe *et al.*, Phys. Rev. Lett. **91**, 261801 (2003).

[15] *BABAR* Collaboration, B. Aubert *et al.*, hep-ex/0403026, submitted to PRL.

[16] Y.Sakai, "Recent results of B decays" and M.Georgi "Recent results of CP violation in B decays", presented at the 32^{nd} International Conference on High-Energy Physics, ICHEP 04, 16-22 August, 2004, Beijing, China

[17] BELLE Collaboration, A.Garmash *et al.*, Phys. Rev. D **69**, 012001 (2004).

[18] *BABAR* Collaboration, B. Aubert *et al.*, hep-ex/0406005, submitted to PRL.

[19] M. Gronau and D. London Phys. Rev. Lett. **65**, 3381 (1990).

[20] BABAR-PLOT-0053 (Preliminary); *BABAR* Collaboration, B. Aubert *et al.*, hep-ex/0408089, submitted to the 32^{nd} International Conference on High-Energy Physics, ICHEP 04, 16-22 August, 2004, Beijing, China

[21] BELLE Collaboration, K. Abe *et al.*, Phys. Rev. Lett. **93**, 021601 (2004).

[22] *BABAR* Collaboration, B. Aubert *et al.*, hep-ex/0303028; BELLE Collaboration, K. Abe *et al.*, Phys. Rev. Lett. **91**, 261801 (2003).

[23] *BABAR* Collaboration, B. Aubert *et al.*, Phys. Rev. Lett. **91**, 171802 (2003).

[24] *BABAR* Collaboration, B. Aubert *et al.*, Phys. Rev. D **69**, 031102 (2004).

[25] *BABAR* Collaboration, B. Aubert *et al.*, hep-ex/0404029, submitted to PRL;
Update with 1999-2003 data set see: L.Roos for the *BABAR* collaboration,
http://moriond.in2p3.fr/EW/2004/transparencies/5_Friday/5_2_afternoon/5_2_4_Roos/Roos.pdf
presented at Recontres de moriond, EW session, 21-28 March, 2004, La Thuile, Italy

[26] R.G. Sachs, Enrico Fermi Institute Report, EFI-85-22 (1985) (unpublished); I. Dunietz and R.G. Sachs, Phys. Rev. **D37**, 3186 (1988) [E: Phys. Rev. **D39**, 3515 (1989)]; I. Dunietz, Phys. Lett. **B427**, 179 (1998); P.F. Harrison and H.R. Quinn, ed., "The *BABAR* Physics Book", SLAC-R-504 (1998), Chap. 7.6.

[27] *BABAR* Collaboration, B. Aubert *et al.*, Phys. Rev. Lett. **92**, 251802 (2004).

[28] *BABAR* Collaboration, B. Aubert *et al.*, Phys. Rev. Lett. **92**, 251801 (2004).

[29] BELLE Collaboration, K. Abe *et al.*, hep-ex/0308048

[30] G. Feldman and R. Cousins, Phys. Rev. D **57**, 3873 (1998).

[31] D.Atwood, I.Dunietz and A.Soni, Phys. Rev. Lett. **78**, 3257 (1997); M.Gronau, Phys. Lett. B **557**, 198 (2003)

[32] M.Gronau and D.Wyler, Phys. Lett. B **265** 172 (1991); M.Gronau and D.London, Phys. Lett. B **253**, 483 (1991)

[33] Giri, Grossman, A.Soffer and Zupan, hep-ph/0403187.

[34] *BABAR* Collaboration, B. Aubert *et al.*, hep-ex/0402024, submitted to PRL.

[35] *BABAR* Collaboration, B. Aubert *et al.*, hep-ex/0311033, submitted to PRL

[36] BELLE Collaboration, S.K. Swain, T.E.Browder *et al.*, Phys. Rev. D **68**, 051101 (2003).

[37] BELLE Collaboration, A. Poluektov *et al.*, hep-ex/0406067, submitted to PRD